RUPRECHT-KARLS-UNIVERSITÄT HEIDELBERG

Veit Lorenz Scharf

Measurement of $W\gamma\gamma$ production in proton-proton collisions and limits on anomalous quartic gauge couplings using the ATLAS detector

Dissertation

HD-KIP-14-14

KIRCHHOFF-INSTITUT FÜR PHYSIK

Dissertation

submitted to the

Combined Faculties of the Natural Sciences and Mathematics

of the Ruperto-Carola-University of Heidelberg, Germany

for the degree of

Doctor of Natural Sciences

Put forward by

Veit Lorenz Scharf

born in Kulmbach

Oral examination on January 21, 2014

Measurement of $W\gamma\gamma$ production in proton-proton collisions and limits on anomalous quartic gauge couplings using the ATLAS detector

Referees:	Prof. Dr. Hans-Christian Schultz-Coulon
	Prof. Dr. André Schöning

Abstract

The measurement of the joined production processes of three electroweak gauge bosons allows to probe the gauge structure of the electroweak interaction. In the analysis presented, W boson production in association with two high energetic photons has been measured for the first time using proton-proton collision data recorded in 2012 with the ATLAS detector. The dataset corresponds to an integrated luminosity of 20.3 fb^{-1} collected at a center-of-mass energy of $\sqrt{s} = 8$ TeV. Events are selected requiring the muonic decay channel of the W boson and two isolated photons. The production cross-section is measured in two restricted phase-space regions, with and without a requirement on the number of additional jets. It is found to be consistent with predictions at next-to-leading order precision in the strong coupling. The measurement is sensitive to new physics phenomena, namely anomalous quartic gauge boson couplings. In the absence of significant deviations from the Standard Model, 95 % C.L. frequentist CL_S limits on quartic electroweak gauge boson couplings are set.

Zusammenfassung

Die Messung der gemeinsamen Produktion von drei elektroschwachen Eichbosonen erlaubt es, die Eichstruktur der schwachen Wechselwirkung zu testen. In dieser Arbeit wird die erste Messung der Produktion von W-Bosonen zusammen mit zwei hochenergetischen Photonen in Proton-Proton-Kollision vorgestellt. Die Daten wurden mit dem ATLAS-Detektor im Jahr 2012 aufgezeichnet und entsprechen einer integrierten Luminosität von 20,3 fb^{-1} bei einer Schwerpunktsenergie von $\sqrt{s} = 8$ TeV. Die Ereignisse werden im muonischen Zerfallskanal des W-Bosons und zweier isolierter Photonen selektiert. Der Produktionswirkungsquerschnitt wird in zwei Phasenraumbereichen gemessen und stimmt mit der Vorhersage in nächstführender Ordnung in QCD überein. Die Messung wird dazu verwendet, die Daten auf die Präsenz von anomalen Vierboson-Kopplungen zu testen. Da keine signifikanten Abweichungen von der Standardmodell-Vorhersage aufgetreten sind, werden 95 % C.L. Ausschlussgrenzen auf die Kopplungsstärke anomaler Vierboson-Kopplungen gesetzt.

Contents

CHAPTER 1

Introduction

The Standard Model of particle physics (*SM*) is the theoretical framework for the calculation of particle physics phenomena. It describes very precisely most of the experimental data [1]. At the Large Hadron Collider (LHC) a new boson has recently been discovered by the ATLAS and CMS collaborations [2, 3]. It is compatible with the last missing piece of the Standard Model, the Higgs boson. Besides its properties as a discovery machine, the LHC provides the possibility for many other tests of the Standard Model. The self-interactions of electroweak gauge bosons are one interesting field through their sensitivity to the electroweak gauge structure.

Several measurements of di-boson production processes have been carried out at the LHC and have been found in agreement with the Standard Model expectations [4–6]. In this thesis the next step is taken: For the first time the tri-boson production process of a W boson in association with two highly energetic photons is measured. This processes directly tests the quartic gauge boson couplings predicted by the electroweak theory.

After more than two years of LHC data taking, the Standard Model has been confirmed rather than contested. Direct searches for new particles have found no evidence for physics beyond the Standard Model and no hints for new physics phenomena have been observed in inclusive as well as exclusive searches. The tri-boson production processes are directly sensitive to the electroweak gauge structure and thus sensitive to new physics phenomena in the electroweak sector. Deviations from the Standard Model can be parametrized in a model-independent way using higher-dimensional effective operators that give rise to anomalous quartic gauge couplings [7].

The Standard Model, details of the $W\gamma\gamma$ production process, and the mechanism of anomalous quartic gauge couplings are discussed in Chapter 2. The LHC and the ATLAS detector are described in Chapter 3. Details about the simulation of proton-proton collisions and the different simulation programs used in this thesis are given in Chapter 4. The algorithms used to reconstruct particles from their energy depositions in the ATLAS detector are discussed in Chapter 5.

After the theoretical and experimental framework for the analysis has been introduced, the cross-section measurement of the $pp \to W\gamma\gamma + X$ process is presented. Experimentally, the cross-section σ can be measured in data with an integrated luminosity L_{int}, using the well known formula

$$\sigma = \frac{N_{\text{obs}} - N_{\text{bkg}}}{A \cdot \epsilon \cdot L_{\text{int}}} \,.$$

The determination of each of the terms will be outlined in the following. The selection used to select the number of observed events N_{obs} is discussed in Chapter 6. The methods that are used to estimate the irreducible background N_{bkg} are introduced in Chapter 7. The corrections for the acceptance A and the efficiency ϵ, as well as the calculation of the cross-section and comparisons to the Standard Model prediction will be given in Chapter 8. In Chapter 9, the measurement will be used to constrain new physics phenomena in the context of anomalous quartic gauge couplings.

The author has carried out the analysis for the $W \to \mu\nu$ decay channel of the W boson from the initial sensitivity studies up to the final measurement and the limit setting. In parallel, the decay of the W boson into an electron-neutrino pair was studied within ATLAS.

CHAPTER 2

Theoretical background

The Standard Model of particle physics (*SM*) is the theoretical framework for the calculation of particle physics phenomena. It describes the fundamental particles and the forces that govern the interactions between them. Several theorists established it in the late sixties and early seventies of the last century and it agrees remarkably well with experiments carried out over the last decades. The success of the Standard Model was honored with several Nobel prizes and accumulated in the discovery of the long-sought after Higgs Boson at the LHC [2, 3] and the Nobel prize award to Englert and Higgs in October 2013 "for the theoretical discovery of a mechanism that contributes to our understanding of the origin of mass of subatomic particles, and which recently was confirmed through the discovery of the predicted fundamental particle, by the ATLAS and CMS experiments at CERN's Large Hadron Collider" [8]. However, there is reason to believe that the Standard Model is incomplete. For example it cannot describe the matter-antimatter asymmetry and it does not provide a viable candidate for *dark matter* [1]. Anomalous quartic gauge couplings provide the possibility to search for new physics phenomena in a model independent way.

The Standard Model will be briefly introduced in the first part of this chapter. Then, the $W\gamma\gamma$ production process and the physics at a hadron collider will be presented. At last the mechanism of anomalous quartic gauge couplings is introduced.

2.1 The Standard Model of particle physics

The Standard Model is a relativistic quantum field theory describing the strong, weak and electromagnetic interactions of fermions. It consists of fermions, gauge bosons and the scalar Higgs boson. The gauge bosons mediate the forces between the fermions, while the Higgs boson gives mass to the particles. The fermions can be further split into two groups, the leptons which do not interact via the strong force and the quarks which do. The leptons form three *families* of left-handed $\mathrm{SU(2)_L}$ doublets, each consisting of a lepton and a neutrino, and right-handed singlets only containing the lepton. The three leptons, electron (e^-), muon (μ^-) and tau (τ^-) carry negative electric charge, while the electron-, muon- and tau-neutrino, ν_e, ν_μ and ν_τ respectively, are neutral. The quarks can also be grouped into three families of doublets consisting of an *up*-type and *down*-type quark each. The up-type quarks, up (u), charm (c) and top (t) carry an electric charge of $q_e = +{}^2\!/\!_3$, while the down-type quarks, down (d), strange (s) and bottom (b), carry $q_e = -{}^1\!/\!_3$. The properties of the twelve fundamental fermions of the Standard Model are summarized in Table 2.1. Each of the fermions has a corresponding *antiparticle*

	Family			Charge q_e	Interaction
	I	II	III		
neutral leptons	ν_e	ν_μ	ν_τ	0	weak
charged leptons	e^-	μ^-	τ^-	-1	weak, electromagnetic
up-type quarks	u	c	t	$+^2/_3$	weak, electromagnetic, strong
down-type quarks	d	s	b	$-^1/_3$	weak, electromagnetic, strong

Table 2.1: The properties of the twelve fundamental fermions of the Standard Model.

which has opposite charge, parity and color but otherwise the same quantum numbers. Antiparticles are denoted by using a plus instead of a minus for the charged leptons, e.g. the anti-electron is e^+, also known as positron, and with a bar for the other fermions, i.e. the anti-up is denoted as $\bar{u}$.

The force carriers of the Standard Model are gauge bosons corresponding to the generators of the symmetry groups of the interactions. The electromagnetic interaction is described by "Quantum Electro Dynamics" (QED) with the symmetry group $\mathrm{U(1)_{EM}}$. It is mediated by a single massless gauge boson, the photon (γ), that couples to the electric charge. The theory of the weak interaction follows an $\mathrm{SU(2)_L}$ symmetry group. The three massive gauge bosons, $W^\pm$ ($m_W = 80.4\,\mathrm{GeV}$) and Z^0 ($m_Z = 91.2\,\mathrm{GeV}$) [1], couple to the weak charge. The electromagnetic and the weak interaction have been unified by Glashow, Weinberg and Salam [9–11] as the local symmetry of $\mathrm{SU(2)_L \times U(1)_Y}$. This unified interaction is called the *electroweak* interaction. The Higgs-mechanism gives mass to the particles through the mechanism of *spontaneous symmetry breaking*.

The strong force is described by "Quantum Chromo Dynamics" (QCD) which obeys an $\mathrm{SU(3)_C}$ symmetry. It is mediated by eight massless gluons coupling to *color*-charge. Only quarks and gluons carry color and interact under the strong force. Up to now only color singlets have been observed (*color confinement*) meaning that quarks either appear in bound quark-antiquark states called mesons (e.g. the charged pion $\pi^+ = |u\bar{d}\rangle$) or in three-quark states called baryons (e.g. the proton $p = |uud\rangle$). Both together are called hadrons.

The combination of QCD with the electroweak interaction yields the Standard Model, which is invariant under local $\mathrm{SU(3)_C \times SU(2)_L \times U(1)_Y}$ gauge transformations.

2.1.1 The electroweak theory

The weak interaction follows a local $\mathrm{SU(2)_L}$ gauge symmetry. Invariance under the non-abelian local gauge transformation of $\mathrm{SU(2)_L}$ gives rise to self interactions between the gauge bosons of the electroweak interaction. Since the $W\gamma\gamma$ production process is interesting through its possibility to study the coupling between the gauge bosons $W^\pm$ and γ the theory of electroweak interactions will be briefly introduced following the discussion in [12, 13].

The electroweak theory is a spontaneously broken local gauge theory with $\mathrm{SU(2)_L \times U(1)_Y}$ as symmetry group. $\mathrm{SU(2)_L}$ is the group of the weak isospin with the gauge fields W^i_μ that couple only to left-handed fermions causing the maximum parity violating behaviour. The generator of the $\mathrm{U(1)_Y}$ group is the weak hypercharge Y defined as $Q = I_3 + \frac{\mathrm{Y}}{2}$, with the electric charge Q and third component of the weak isospin I_3. With the gauge field of $\mathrm{U(1)_Y}$, B_μ the $\mathrm{SU(2)_L \times U(1)_Y}$ group gives rise to four gauge fields.

The fermions are described as left-handed doublets (denoted by a subscript L) and right-handed singlets of the weak isospin (subscript R).The left-handed lepton doublets are

$$\begin{pmatrix}\nu_e\\ e\end{pmatrix}_{\mathrm{L}},\ \begin{pmatrix}\nu_\mu\\ \mu\end{pmatrix}_{\mathrm{L}},\ \begin{pmatrix}\nu_\tau\\ \tau\end{pmatrix}_{\mathrm{L}}, \tag{2.1}$$

and the right-handed lepton singlets are

$$e_{\mathrm{R}},\ \mu_{\mathrm{R}},\ \tau_{\mathrm{R}}\,. \tag{2.2}$$

For quarks a small complication arises from the fact that the weak interaction does not couple to the mass eigenstates of the down-type quarks. Therefore the left-handed quark doublets are given as

$$\begin{pmatrix}u\\ d'\end{pmatrix}_{\mathrm{L}},\ \begin{pmatrix}c\\ s'\end{pmatrix}_{\mathrm{L}},\ \begin{pmatrix}t\\ b'\end{pmatrix}_{\mathrm{L}}\,. \tag{2.3}$$

The primed quarks are linear combinations of the mass eigenstates, which are specified by the Cabibbo-Kobayashi-Maskawa (CKM) matrix [14, 15].

To obtain local gauge invariance the derivative ∂_μ is replaced with the covariant derivative D_μ. Since the right-handed fermions do not participate in the weak interaction the covariant derivatives D_μ are different for left- and right-handed fermions:

$$D_\mu \psi_{\mathrm{L}} = \left(\partial_\mu + i\frac{g}{2}W^i_\mu \sigma^i + i\frac{g'}{2}B_\mu\right)\psi_{\mathrm{L}} \tag{2.4}$$

$$D_\mu \psi_{\mathrm{R}} = \left(\partial_\mu + i\frac{g'}{2}B_\mu\right)\psi_{\mathrm{R}}\,. \tag{2.5}$$

Here, σ^i are the Pauli matrices and g and g' are the coupling constant of $\mathrm{SU(2)_L}$ and $\mathrm{U(1)_Y}$, respectively. As expected the covariant derivative for right-handed fermions does not contain terms with the gauge fields of $\mathrm{SU(2)_L}$, i.e. they do not couple to the weak interaction.

The Lagrangian containing the dynamical terms and the $\mathrm{SU(2)_L} \times \mathrm{U(1)_Y}$ gauge terms can be written as

$$\begin{aligned}\mathcal{L} &= \bar{\psi}_{\mathrm{L}}\gamma^\mu \left(\partial_\mu + i\frac{g}{2}W^i_\mu \sigma^i + i\frac{g'}{2}B_\mu\right)\psi_{\mathrm{L}} \\ &+ \bar{\psi}_{\mathrm{R}}\gamma^\mu \left(\partial_\mu + i\frac{g'}{2}B_\mu\right)\psi_{\mathrm{R}} \\ &- \frac{1}{4}W^i_{\mu\nu}W^{\mu\nu}_i - \frac{1}{4}B_{\mu\nu}B^{\mu\nu}\,.\end{aligned} \tag{2.6}$$

The first two terms are the dynamical terms for the left-handed and right-handed fermions, respectively. They contain the kinetic energy of the fermions and their interaction with the gauge bosons. The last two terms are the kinetic terms and the self interaction of the gauge fields, where $B_{\mu\nu} = \partial_\mu B_\nu - \partial_\nu B_\mu$ and $W^i_{\mu\nu} = \partial_\mu W^i_\nu - \partial_\nu W^i_\mu - g\epsilon_{ijk}W^j_\mu W^k_\nu$.

The Lagrangian in the form of Equation 2.6 does not contain mass terms for the fermions and electroweak gauge bosons, yet we know that both are massive particles. Simply adding a mass term for these particles, e.g. $m\bar{\psi}\psi = m\left(\bar{\psi}_{\mathrm{L}}\psi_{\mathrm{R}} + \bar{\psi}_{\mathrm{R}}\psi_{\mathrm{L}}\right)$ for the fermions, will not suffice since it violates the gauge invariance of the $\mathrm{SU(2)_L}$ group. One mechanism to generate the masses is the *Higgs-Brout-Englert-Guralnik-Hagen-Kibble mechanism* [16–21] which introduces an additional scalar field ϕ. The choice of a specific potential for this field leads to spontaneous symmetry breaking of the $\mathrm{SU(2)_L}\times\mathrm{U(1)_Y}$ invariance as explained below.

A general scalar field is introduced as a complex scalar SU(2) doublet

$$\phi = \begin{pmatrix} \phi^+ \\ \phi^0 \end{pmatrix} , \tag{2.7}$$

and the Lagrangian for this field is

$$\mathcal{L}_{\text{Higgs}} = \left(D_\mu \phi\right)^\dagger \left(D^\mu \phi\right) - V(\phi) , \tag{2.8}$$

with the covariant derivative defined as above. If the potential, $V(\phi)$, takes the special form

$$V(\phi) = -\mu\phi^\dagger\phi + \lambda\left(\phi^\dagger\phi\right)^2 \tag{2.9}$$

with μ^2, $\lambda > 0$, the minimum of the potential is not at $\phi = 0$ but at

$$|\phi_0| = \sqrt{\frac{\mu^2}{2\lambda}} . \tag{2.10}$$

Perturbative calculations require expansions around the minimum of the potential. If one arbitrary, but fixed point satisfying Equation 2.10 is chosen, the SU(2) symmetry is broken. One common choice is

$$\phi = \frac{1}{\sqrt{2}} \begin{pmatrix} 0 \\ v \end{pmatrix} , \tag{2.11}$$

with $v = \sqrt{\frac{\mu^2}{\lambda}}$. If the field expanded around its minimum, i.e.

$$\phi = \frac{1}{\sqrt{2}} \begin{pmatrix} 0 \\ v + H \end{pmatrix} , \tag{2.12}$$

is inserted into the Lagrangian 2.8, it contains mass terms for linear combinations of the four gauge bosons:

$$\begin{aligned} \mathcal{L}_{\text{Higgs}} =& \frac{1}{2}\left(\partial_\mu H\right)^2 - \frac{1}{2} m_H^2 H^2 - \sqrt{\frac{\lambda}{2}} m_H H^3 - \frac{1}{4} H^4 \\ &+ \left(m_W^2 W_\mu^+ W^{-\mu} + \frac{1}{2} m_Z^2 Z_\mu Z^\mu\right)\left(1 + \frac{H}{v}\right)^2 . \end{aligned} \tag{2.13}$$

Here,

$$W_\mu^\pm = \frac{1}{\sqrt{2}}\left(W_\mu^1 \mp i W_\mu^2\right) \tag{2.14}$$

$$Z_\mu = \frac{1}{\sqrt{g^2 + g'^2}}\left(g W_\mu^3 - g' B_\mu\right) \tag{2.15}$$

$$A_\mu = \frac{1}{\sqrt{g^2 + g'^2}}\left(g W_\mu^3 + g' B_\mu\right) \tag{2.16}$$

are the mass eigenstates of the gauge bosons with masses $m_W = \frac{gv}{2}$ and $m_Z = \frac{\sqrt{g^2+g'^2}}{2} v$ and the massless photon. The first two terms of the Lagrangian 2.13 describe a scalar field of mass $m_H = \sqrt{2\lambda} v$ known as

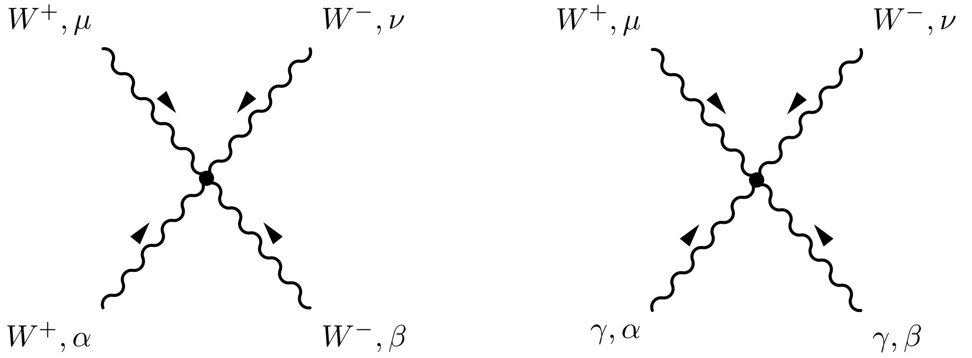

(a) $-ig^2\left(-2g_{\alpha\beta}g_{\mu\nu} + g_{\alpha\mu}g_{\beta\nu} + g_{\alpha\nu}g_{\beta\mu}\right)$ (b) $ig^2\sin^2\theta_W\left(-2g_{\alpha\beta}g_{\mu\nu} + g_{\alpha\mu}g_{\beta\nu} + g_{\alpha\nu}g_{\beta\mu}\right)$

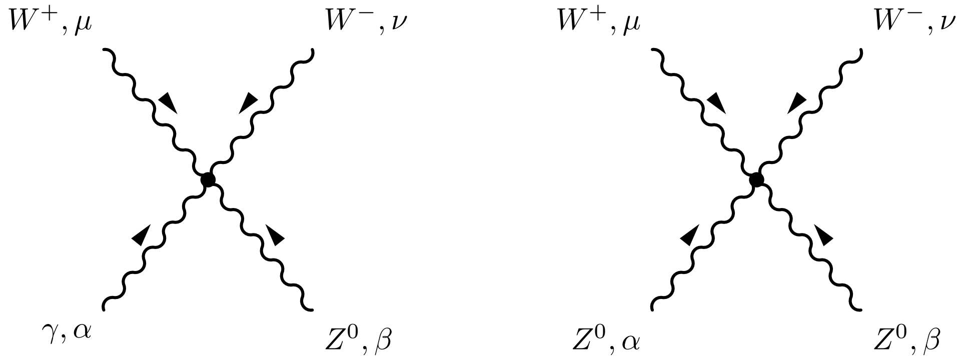

(c) $-ig^2\sin\theta_W\left(-2g_{\alpha\beta}g_{\mu\nu} + g_{\alpha\mu}g_{\beta\nu} + g_{\alpha\nu}g_{\beta\mu}\right)$ (d) $ig^2\cos^2\theta_W\left(-2g_{\alpha\beta}g_{\mu\nu} + g_{\alpha\mu}g_{\beta\nu} + g_{\alpha\nu}g_{\beta\mu}\right)$

Figure 2.1: The four quartic gauge boson interactions of the Standard Model and their Feynman rules in unitary gauge. The arrows indicate the momentum flow.

the *Higgs field*. By adding a scalar field with a specially crafted potential the masses of the heavy gauge bosons have been added in a gauge invariant way. The - still missing - masses of the fermions are added by Yukawa couplings between the Higgs boson and the fermions.

The electroweak theory predicted several particles years before they had been discovered at a collider and withstood all experimental tests in the last decades. One of the least tested sectors of the Standard Model are the quartic couplings of the electroweak gauge bosons. They just started to be directly accessible by experiments at the LHC. After the spontaneous symmetry breaking the Lagrangian of the electroweak interaction can be written in terms of the physical fields $W^\pm_\mu$, Z_μ and A_μ. The resulting Lagrangian for four-point self interactions between the gauge bosons is

$$\begin{aligned}\mathcal{L}_{WWVV} = &-\frac{g^2}{4}\Bigg(\left(2W^+_\mu W^{-\mu} + \left(A_\mu \sin\theta_W - Z_\mu \cos\theta_W\right)^2\right)^2 - \\ &\left(W^+_\mu W^-_\nu + W^+_\nu W^-_\mu + \left(A_\mu \sin\theta_W - Z_\mu \cos\theta_W\right)\left(A_\nu \sin\theta_W - Z_\nu \sin\theta_W\right)\right)^2\Bigg)\end{aligned} \tag{2.17}$$

yielding four physically distinct cases, $W^+W^-\gamma\gamma$, $W^+W^-\gamma Z$, W^+W^-ZZ and $W^+W^-W^+W^-$. The corresponding Feynman diagrams and the Feynman rules in unitary gauge are given in Figure 2.1.

2.2 General aspects of pp-scattering

The cross-section as well as the kinematic properties of a scattering process at a hadron collider do not only dependent on the matrix elements calculated using perturbation theory. In addition, long-distance processes, which are dominated by non-perturbative QCD and therefore can not be calculated directly, have to be considered. These two parts of the cross-section can be treated separately according to the *factorization theorem* [22]. The dominant non-perturbative effect for the $W\gamma\gamma$ production process is the momentum distribution of the partons inside the proton, which is described by the *parton distribution functions* (PDFs). These will be introduced in this section.

2.2.1 Parton distribution functions

The factorization theorem allows to treat the *hard scatter*, i.e. the partonic cross-section $\hat{\sigma}_{ab\to X}$, separately from soft, non-perturbative effects which cannot be calculated but have to be described using phenomenological models tuned to experimental data. Typically these soft long-distance processes include the fragmentation and hadronization of quarks and gluons into jets and the parton distribution functions describing the structure of the proton. The following description will focus on the latter, since the $W\gamma\gamma$ processes, which a subsequent decay of the W boson into a muon-neutrino pair, does not yield quarks and gluons in the final state at leading order.

The proton is not an elementary particle. In the quark model the quantum numbers of the proton are described by the color singlet $|uud\rangle$ of two up- and one down quark. This picture provides a good description of the proton as long as it is probed at small energies. If the energy of the particle used to probe the proton is increased, it can resolve finer structures. Therefore it becomes sensitive to spontaneous gluon exchange between the constituent quarks and gluons that split into quark-antiquark pairs. The former gives raise to the gluon content of the proton, while the latter yields the so-called *sea quarks* inside the proton. By this mechanism the structure of the proton depends on the momentum scale of the interaction Q^2.

The structure is described by parton distribution functions $f_p\left(x, Q^2\right)$ that give the probability to find a parton p with a fraction x of the total proton momentum in an interaction at the scale Q^2. The Q^2 dependence of $f_p\left(x, Q^2\right)$ is determined by the DGLAP equations [24–27], while the x dependence has to be determined experimentally. It is measured in fixed-target and collider experiments using either lepton-proton deep inelastic scattering or hard-scattering in proton-(anti-)proton interactions. Several groups use all or parts of the available data to determine the PDF of the proton, for example MSTW [28], CTEQ [29] or HERAPDF [30].

A hard-scattering process in proton-proton collision can be imagined as the partonic cross-section, $\hat{\sigma}_{ab\to X}$, for the interaction of two partons a and b, folded with their momentum distribution inside the proton. This is illustrated in Figure 2.2: A and B are the incoming protons whose constituents a and b participate in the hard scatter. The momentum distributions and the relative

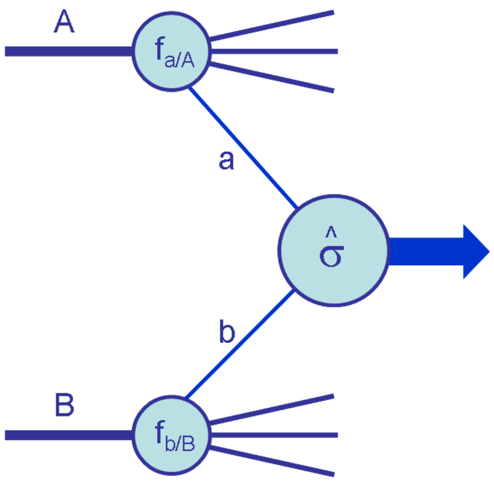

Figure 2.2: Diagram of the structure of a hard scattering process. From [23].

frequency of occurrence for the different constituents is determined by the PDFs $f_{a/A}$ and $f_{b/B}$.

More quantitatively the cross-section for the production of a final state X in proton-proton collisions, $\sigma_{pp\to X}$, can be schematically written as [23]

$$\begin{aligned}\sigma_{pp\to X} = &\int \mathrm{d}x_a \mathrm{d}x_b f_a\left(x_a, \mu_\mathrm{F}^2\right) f_b\left(x_b, \mu_\mathrm{F}^2\right)\\ &\cdot \left(\hat{\sigma}_0 + \alpha_\mathrm{S}\left(\mu_\mathrm{R}\right)\hat{\sigma}_1 + \ldots\right)_{ab\to X} .\end{aligned}$$

Here, $\hat{\sigma}_i$ are the partonic cross-sections for the process under study, where i indicates the order in perturbation theory at which the cross-section is evaluated. The *factorization scale*, μ_F, is the scale that separates the long- from the short distance physics and μ_R, the *renormalization scale*, is the scale at which the renormalization that cancels the UV divergences of QCD is done. A typical choice for these scales is $\mu_\mathrm{F} = \mu_\mathrm{R} = Q^2$, where Q^2 is the momentum scale that characterizes the hard interaction, e.g. the invariant mass of the $W\gamma\gamma$ system, $m_{W\gamma\gamma}$, for the process $pp \to W\gamma\gamma$. In a calculation to all orders in perturbation theory the physical observables are independent of these scales, since higher orders in the partonic cross-section cancel the scale dependence. However, at finite order unknown higher order corrections are absorbed in different choices of μ_F and μ_R. Therefore the *scale dependence*, i.e. the change of the cross-section with μ_F and μ_R, is a measure on the uncertainty associated with the finite order calculation of the cross-section.

2.3 The $W\gamma\gamma$ production process

At the parton level and in leading order the $pp \to W(\to l\nu)\gamma\gamma + X$[1] process is described by 21 Feynman diagrams [31], four of them are shown in Figure 2.3. Besides the diagrams involving two connected triple ($WW\gamma$) or one quartic $WW\gamma\gamma$ vertex, also ordinary W production contributes. In this case the photons either stem from radiation of the incoming quarks or the outgoing lepton or a mixture of both. In addition, photons coming from the hard fragmentation of a quark or gluon contribute to the $W\gamma\gamma$ final state if they appear in association with a W boson. Two example diagrams for the fragmentation contribution are depicted in Figure 2.4. Here, $D_{q/g\to\gamma}\left(z, Q^2\right)$ are the quark- and gluon-to-photon fragmentation functions respectively. They describe the probability that a photon is created and carries away the fraction z of the parton momentum. Q^2 is the scale fixed by the hard process. Experimentally photons from a hard fragmentation cannot be distinguished from other photons and are considered as part of the signal in this analysis.

The cross-section for the process $pp \to l\nu\gamma\gamma$ has been calculated at leading order in the strong coupling [31] and next-to-leading order in the strong coupling [32] and [33]. The former calculation includes the contribution from $q \to q\gamma$ fragmentation, but treats the W boson as stable. The latter calculation includes leptonic decays of the W boson and, in particular, photon radiation from the charged lepton, but does not include photons from fragmentation processes. Therefore special care has to be taken to reject events with a photon emitted collinear to a quark, which would leads to infrared singularities. These events are treated properly "by construction" when using the fragmentation functions $D_{q/g\to\gamma}$ to describe real photon emissions below a fragmentation scale μ_frag. The rejection of such events in case the fragmentation functions are not used is commonly achieved by a so-called *photon isolation* criterion.

The simple prescription for the photon isolation that rejects events containing partons within a cone around the photon is theoretically not well defined [34]. If no energy is allowed in the cone around the photon the cone-based isolation is not infrared safe: no soft-gluon emission into the isolation cone

---

[1] In the following $pp \to W(\to l\nu)\gamma\gamma + X$ will be referred to as $pp \to W(\to l\nu)\gamma\gamma$ process, or simply $W\gamma\gamma$ production process.

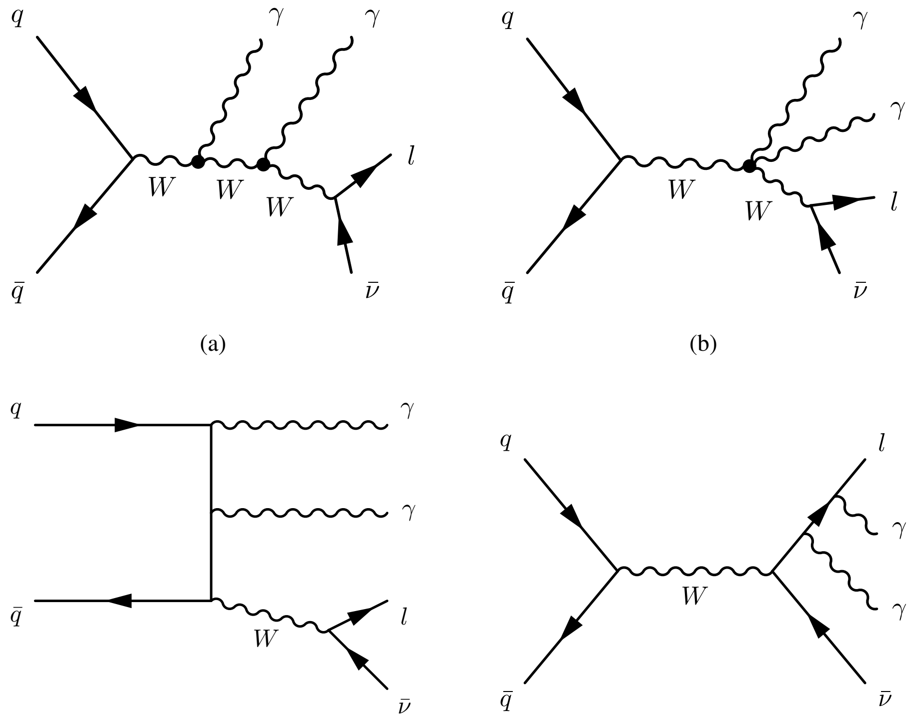

(a) (b) (c) (d)

Figure 2.3: Typical Feynman diagrams for the process $q\bar{q} \to l\nu\gamma\gamma$.

is allowed and thus the cancellation of the infrared singularities is spoiled. Therefore the cone-based isolation requirement is replaced by the so-called *Frixione isolation* [34] which does not suffer from the problems described above. A photon is considered isolated if it fulfills

$$\sum_i E_{\mathrm{T}}^i \theta(\delta - R_{i\gamma}) \leq \epsilon E_{\mathrm{T}}^{\gamma} \frac{1 - \cos\delta}{1 - \cos\delta_0} \qquad \forall \delta < \delta_0\,, \tag{2.18}$$

with parameters δ_0 and ϵ, that describe the cone size and the allowed energy fraction of the photon, respectively. Here, i is the parton with transverse energy E_{T}^i and a separation $R_{i\gamma}$ from a photon with transverse energy E_{T}^{γ}. This definitions allows soft partons that are arbitrarily close to the photons. However, a parton that is exactly collinear to the photon is required to have vanishing energy.

Throughout this work the calculations from [33] will be used for the theory predictions. The calculation is available as a part of the VBFNLO program [35]. VBFNLO is a parton level Monte Carlo program for the simulation of various processes at next-to-leading order in the strong coupling constant.

Properties of $W\gamma\gamma$ at next-to-leading order in QCD

In the following the properties of the $W\gamma\gamma$ process at next-to-leading order in QCD will be discussed. The predictions have been derived using the VBFNLO program [35], version `2.7.0-beta4`, with a minimal set of selection criteria that represent the typical experimental requirements of a general purpose

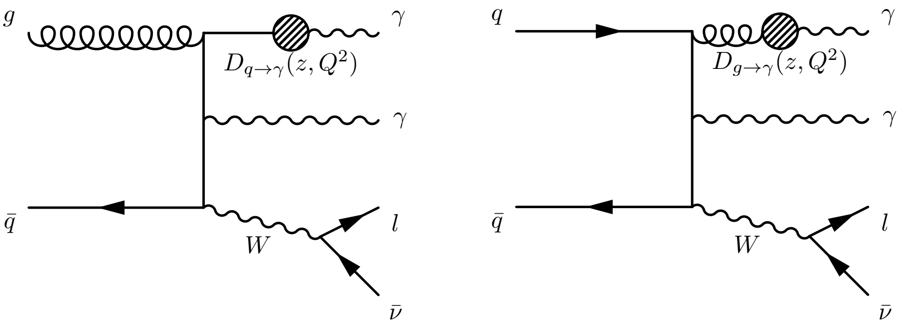

(a) (b)

Figure 2.4: Feynman diagrams illustrating the fragmentation component of the $W\gamma\gamma$ process.

detector at the LHC. These selections are

$$\begin{aligned} p_{\mathrm{T}}^{l,\gamma} > 20\,\mathrm{GeV}, \quad \left|y_{l,\gamma}\right| < 2.5, \quad p_{\mathrm{T}}^{j} > 30\,\mathrm{GeV}, \quad \left|y_{j}\right| < 4.4, \\ R_{\gamma,\gamma} > 0.4, \quad R_{l,\gamma} > 0.7, \quad R_{l,j} > 0.3, \quad R_{\gamma,j} > 0.3\,, \end{aligned} \tag{2.19}$$

where p_{T} is the transverse momentum and y is the rapidity of the lepton (l), photon (γ) and parton (j), respectively. The distance in the rapidity-azimuthal angle plane between the different particles is denoted by R. As explained above the calculations do not include the fragmentation contribution. Therefore a photon isolation requirement has to be applied to get rid of infrared singularities. The isolation is based on the Frixione prescription given in Equation 2.18 with the parameters $\delta_0 = 0.4$ and $\epsilon = 0.5$.

Since the properties of the $W\gamma\gamma$ process are studied at a hadron collider, the prediction for the cross-section does not only depend on the matrix element calculation. In addition, the momentum distribution of the partons in the proton has to be folded into the cross-section. This is done using parton distribution functions (PDFs) derived from data. Details how the calculation of the matrix element and the PDFs are combined are given below in Section 2.2. For the calculations presented here, the MSTW2008NLO PDF set [28] has been used.

The results for the cross-section in this phase-space for the process $pp \to W^{\pm}\gamma\gamma \to l^{\pm}\nu\gamma\gamma$ at a center-of-mass energy $\sqrt{s} = 8\,\mathrm{TeV}$ are given in Table 2.2 for leading order (LO) and next-to-leading order (NLO) in the strong coupling. In addition the k-factor defined as $k = \sigma^{\mathrm{NLO}}/\sigma^{\mathrm{LO}}$ is given. The NLO corrections enhance the cross-section by more than a factor of three. This extraordinary large correction has two reasons, one associated with general features of three boson production processes and the other one specific to the $W\gamma\gamma$ final state, which will be discussed later.

The individual contributions of the channels depicted in Figure 2.3 cannot be separated in a gauge-invariant way. However, the contribution from diagrams where one or both photons are radiated from the

LO [fb]	NLO [fb]	k-factor
3.66	10.97	2.99

Table 2.2: Cross-section for $pp \to l^{\pm}\overset{(-)}{\nu}\gamma\gamma$ at leading (LO) and next-to-leading order (NLO) in the strong coupling for a center-of-mass energy $\sqrt{s} = 8\,\mathrm{TeV}$. In addition the ratio between the next-to-leading order and leading order cross-section is given as the k-factor. The statistical uncertainty on the calculation is below one per-mil.

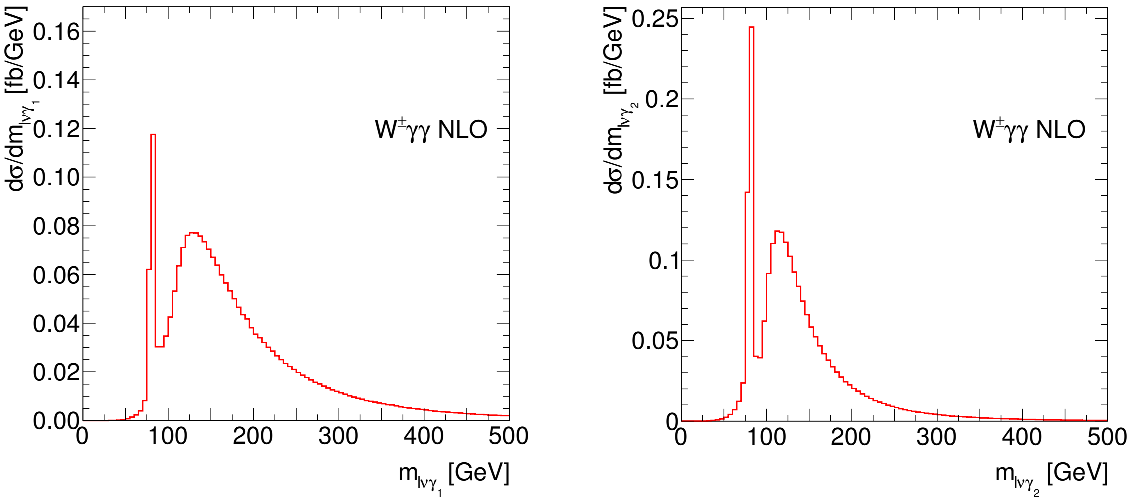

(a) (b)

Figure 2.5: Invariant mass of the $l\nu\gamma_1$ system (a) for the photon with the larger transverse momentum, γ_1, and invariant mass of the $l\nu\gamma_2$ system (b) for the photon with the second largest transverse momentum, γ_2.

lepton can be assessed exploiting the invariant mass distribution of the $l\nu\gamma$ and $l\nu\gamma\gamma$ system, respectively. The $m_{l\nu\gamma}$ distribution is shown in Figure 2.5a for the photon with the larger transverse momentum and in Figure 2.5b for the photon with the second largest transverse momentum. The peak around $m_W = 80.4\,\text{GeV}$ is caused by events where the photon is radiated of the lepton and carried away a part of its momentum. The continuum above the mass of the W boson is created by events where the photon originates from another source. Therefore the fraction of events where the invariant mass of the $l\nu\gamma$ system is close to m_W for one of the two photons in the final state, gives a handle on the contribution of processes where one of the photons is radiated of the lepton. For the phase-space considered here, this is the case for around 26 % of the events. The same argument can be applied to the invariant mass distribution of the $l\nu\gamma\gamma$ system. Two photons are emitted by the lepton in roughly 0.1 % of the events.

The scale dependence of the theory prediction is evaluated by changing the factorization scale, μ_F and the renormalization scale, μ_R, independently by a factor $\xi \in \{0.5, 1, 2\}$. The envelope of the resulting eight variations is then taken as the uncertainty. The scale dependence of the prediction for the di-photon invariant mass distribution is shown in Figure 2.6a and the prediction for the transverse momentum of the $l\gamma\gamma$ system is shown in Figure 2.6b. Both distributions show a moderate scale dependence. The uncertainty on the total cross-section is around 6 %.

Large QCD corrections

The NLO corrections for other triple vector production cross-sections are sizable and generally between a factor of 1.5 and 2 [36–39]. In these channels NLO corrections open up completely new topologies for the production of the three vector bosons in the final state. This is illustrated in Figure 2.7, which shows one example of a Feynman diagram contributing only at next-to-leading order for the calculation of $W\gamma\gamma$ production. In addition, the process now is sensitive to the gluon PDFs as can been seen from the incoming gluon line. Especially at small x the contribution of the gluon PDFs is substantial and leads to an increased cross-section.

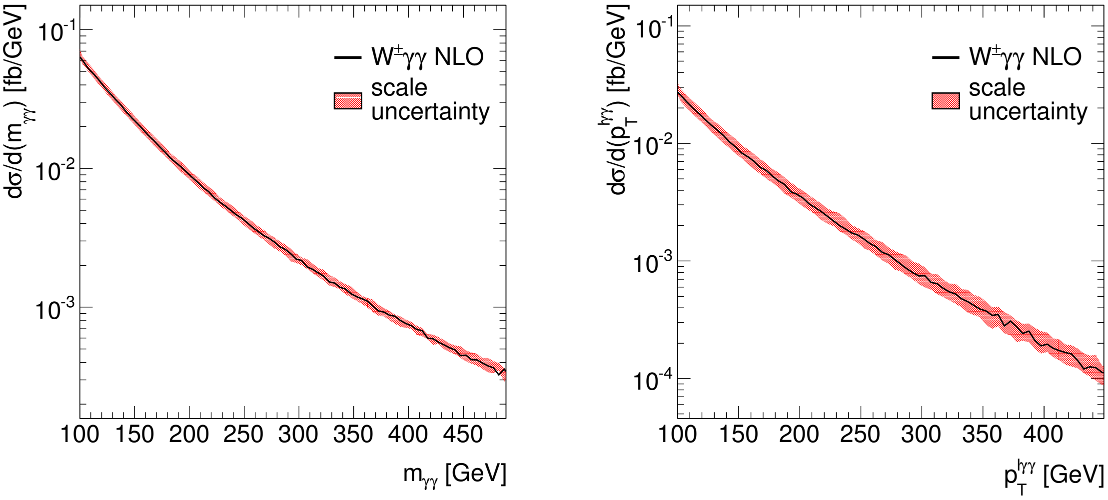

(a) (b)

Figure 2.6: Scale dependence of the prediction for the di-photon invariant mass, $m_{\gamma\gamma}$, and the transverse momentum of the $l\gamma\gamma$ system, $p_T^{l\gamma\gamma}$.

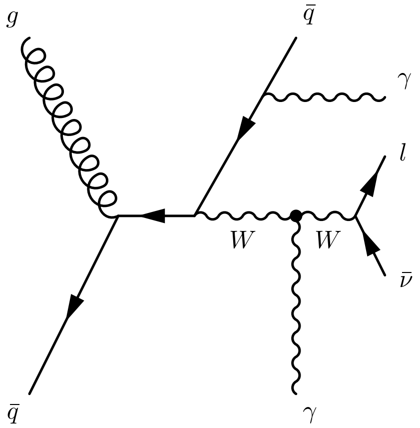

Figure 2.7: Example of a Feynman diagram at next-to-leading order in QCD.

The remaining difference between the $W\gamma\gamma$ and other triple vector production processes can be explained by a feature called *radiation zero* [40]. It predicts that the amplitude of the $q\bar{q} \to W^{\pm}\gamma\gamma$ process vanishes for $\cos\theta^*_W = \pm 1/3$ and collinear photons. Here, θ_W denotes the angle between the incoming quark and the W boson and the $*$ implies that the angle is calculated in the parton center-of-mass frame. However, this does not hold for gluon-induced channels like the one in Figure 2.7, which appear in next-to-leading order calculations. Thus the radiation zero is expected to be weakened in the NLO predictions.

This can be seen in Figure 2.8, which shows the rapidity difference between the W boson and the photon pair, which is a useful variable to observe radiation zero at a hadron collider according to [31]. At leading order (a) a dip around 0 is observed. This dip is not present anymore if next-to-leading order corrections are included in the calculation (b). Therefore the extraordinary large k-factor of $W\gamma\gamma$ production compared to other three boson production processes can be explained by the cancellation of the radiation zero only present for the $W\gamma\gamma$ process

The QCD corrections show a large phase-space dependence as illustrated in Figure 2.9, which shows the k-factor as a function of the transverse momentum of the lepton-photons system. The correction increases from about 2 to more than 10 with increasing transverse momentum. This especially affects the search for anomalous quartic gauge couplings described below. In general, searches for physics beyond the Standard Model are carried out in an extreme phase-space region to suppress the Standard Model background and enhance the sensitivity. With NLO QCD corrections of $\mathcal{O}(10)$ it is not clear that higher orders of perturbation theory give tiny corrections and can be neglected.

Currently, no calculation for the $W\gamma\gamma$ process considering next-to-next-to-leading order (NNLO) cor-

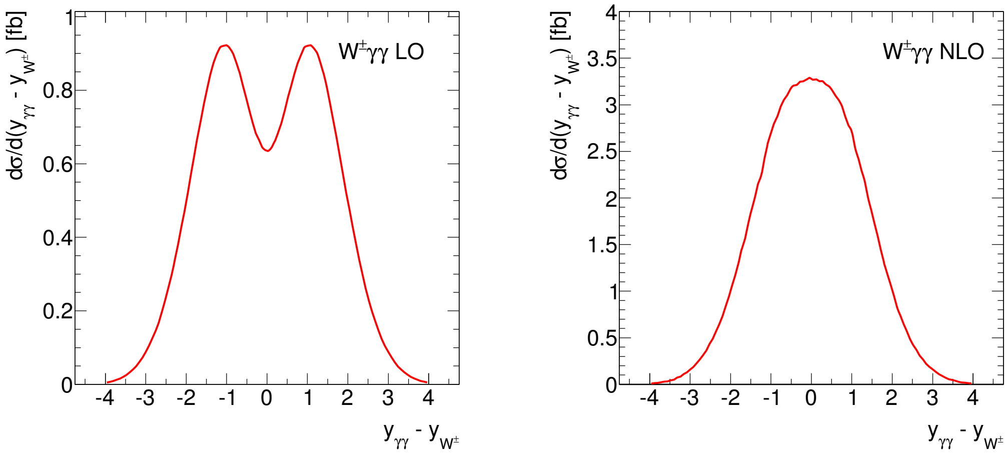

(a) (b)

Figure 2.8: Rapidity difference between the W boson and the di-photon system at LO (left) and NLO (right).

rections is available. However, the calculation of the $W\gamma\gamma$+jet at NLO QCD was published recently [41], which is an important step towards an NNLO calculation [42]. The k-factor of $W\gamma\gamma$ + jet is around 1.4 for a similar phase-space as used above. This indicates once again that the extraordinarily large k-factor for $W\gamma\gamma$ occurs due to the cancellation of the radiation zero and that NNLO corrections may be sizable. When comparing the data to Monte Carlo simulations without these corrections, the difference may be misinterpreted as a sign for physics beyond the Standard Model.

This can be partly prevented by employing a *jet veto*, i.e. not considering events that contain real emissions of quarks or gluons. This reduces the contribution of higher orders to diagrams that contain only pure-virtual corrections, which are expected to be smaller. However, the jet veto is plagued by large theoretical and experimental uncertainties and the scale dependence is artificially small [42]. Nevertheless in the work presented here, physics beyond the Standard Model will be searched for in a phase-space without additional jets.

2.4 Searches for anomalous quartic gauge couplings

The sensitivity of the $W\gamma\gamma$ process to quartic vector boson couplings that are not tightly constrained by previous measurements makes it a viable candidate for the search for physics beyond the Standard Model (BSM physics). Even if no deviations from the Standard Model are observed, the measurement will help to constrain models that predict new physics scenarios which modify the quartic vector boson couplings. In general, searches for BSM physics can be performed using two distinct approaches. One is a *model-dependent* search which tries to falsify a specific model based on its predictions. One example for this type is the search for the minimal super-symmetric extension of the Standard Model (MSSM). The other approach is a *model-independent* search which tries to exploit general features of yet undiscovered processes. One way to determine these general features is the so-called *effective field theory* approach suggested in [43].

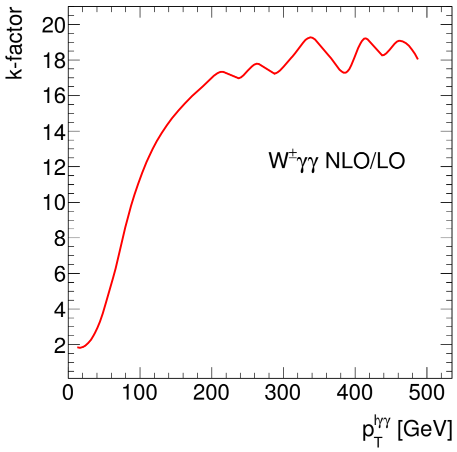

Figure 2.9: QCD correction (k-factor) as a function of the transverse momentum of the lepton-photons system, $p_{\mathrm{T}}^{l\gamma\gamma}$.

2.4.1 Effective field theory

The effective field theory approach is based on the assumption that the yet undiscovered processes (in the following referred to as *new physics phenomena*) are not directly accessible with the current experiments. That means that the energy scale Λ at which new physics phenomena manifest themselves is larger than the energy scales of the Standard Model and out-of-reach of current collider experiments. This is a reasonable assumption, since no new physics phenomena have been discovered at the current energies. Therefore the current experiments are only sensitive to low-energy effects of new physics phenomena.

In general, the Lagrangian, L, that describes new physics phenomena can be written as the sum of the Standard Model Lagrangian, $\mathcal{L}_{\mathrm{SM}}$, and new Lagrangians describing the effects of the new physics phenomena

$$\mathcal{L} = \mathcal{L}_{\mathrm{SM}} + \mathcal{L}_{\mathrm{EFT}} + \mathcal{L}_{\mathrm{NEW}} \,. \tag{2.20}$$

Here, $\mathcal{L}_{\mathrm{EFT}}$ describe the part of the new theory which modifies the interaction between the particles of the Standard Model, and $\mathcal{L}_{\mathrm{NEW}}$ contains the yet unknown interactions and fields. The latter term is negligible, since far below the energy scale of the new theory no new particles can be produced directly.

The *effective Lagrangian*, $\mathcal{L}_{\mathrm{EFT}}$, is required to fulfill the same symmetry as the Standard Model Lagrangian, i.e. invariance under $\mathrm{SU(3)_C} \times \mathrm{SU(2)_L} \times \mathrm{U(1)_Y}$ gauge transformations. The low energy effects of new physics phenomena come into play by allowing operators with a dimension larger than four. In the Standard Model these operators are not allowed since their presence renders the theory unrenormalizable [13]. In the low-energy limit of an effective theory that is known to be valid only up to an energy scale Λ non-renormalizable operators do not spoil the predictive power. The operators in $\mathcal{L}_{\mathrm{EFT}}$ can be ordered according to their dimension, yielding

$$\mathcal{L}_{\mathrm{EFT}} = \frac{1}{\Lambda}\mathcal{L}_5 + \frac{1}{\Lambda^2}\mathcal{L}_6 + \ldots \tag{2.21}$$

with

$$\frac{1}{\Lambda^d}\mathcal{L}_d = \sum_i \frac{f_i^{(d)}}{\Lambda^d} O_i^{(d)} . \tag{2.22}$$

Here, $O_i^{(d)}$ is an operator with dimension d and coupling $f_i^{(d)}$, and i runs over all possible operators of this dimension. The Lagrangian $\mathcal{L}_d$ contains therefore all operators with dimension d. Equation 2.21 can be seen as an expansion in powers of $\frac{1}{\Lambda}$, thus if an experiment is carried out at an energy E, the terms of $\mathcal{L}_{\mathrm{EFT}}$ are suppressed by $\left(\frac{E}{\Lambda}\right)^d$. This has two important consequences. Firstly, in the limit of low energies or high new physics phenomena scales the Standard Model is recovered and all current experimental data is well described. Secondly, only the lowest dimension operators have to be considered.

2.4.2 Anomalous quartic gauge couplings

The Feynman diagrams that describe the three boson $W\gamma\gamma$ final state measured in this work comprise the $WW\gamma\gamma$ vertex. Therefore effective operators modifying the quartic gauge boson couplings of the electroweak theory are of special interest. The lowest dimensions operators yielding anomalous quartic gauge couplings (AQGC) are of dimension six. However, these operators additionally modify the trilinear gauge couplings (TGC), which are far more constrained by the experimentally better accessible di-boson production processes. Operators of dimension eight are the lowest-dimension operators that only modify quartic gauge couplings. All parity conserving operators, which obey $\mathrm{SU(2)_L} \times \mathrm{U(1)_Y}$ gauge symmetry and lead to pure quartic couplings between the weak gauge bosons have been listed by [44]. They identified in total 18 operators, 14 of them modify the $WW\gamma\gamma$ coupling relevant to the $W\gamma\gamma$ final state. They are named $\mathcal{L}_{\mathrm{T}}$ and $\mathcal{L}_{\mathrm{M}}$. One example for such an operator is

$$\mathcal{L}_{\mathrm{T},0} = \mathrm{Tr}\left[\hat{W}_{\mu\nu}\hat{W}^{\mu\nu}\right] \times \mathrm{Tr}\left[\hat{W}_{\alpha\beta}\hat{W}^{\alpha\beta}\right] . \tag{2.23}$$

Here, $\hat{W}_{\mu\nu} = \sum_j W^j_{\mu\nu}\frac{\sigma_j}{2}$ and the rest is as defined above. Thus the effective Lagrangian that can be constrained by measurements of the $W\gamma\gamma$ final state can be written as

$$\mathcal{L} = \sum_i \frac{f_{\mathrm{M},i}}{\Lambda^4}\mathcal{L}_{\mathrm{M},i} + \sum_i \frac{f_{\mathrm{T},i}}{\Lambda^4}\mathcal{L}_{\mathrm{T},i} \tag{2.24}$$

and limits can be set on the coupling parameters $\frac{f_{\mathrm{M},i}}{\Lambda^4}$ and $\frac{f_{\mathrm{T},i}}{\Lambda^4}$ with the dimension of TeV^{-4}.

In previous measurements of anomalous quartic gauge boson couplings carried out at LEP [45–48] and TeVatron [49] a slightly different parametrization has been used. These measurements set limits on the couplings a_0^W, a_C^W which can be associated with above parameters [50]:

$$\frac{f_{\mathrm{M},2}}{\Lambda^4} = -\frac{g^2 g'^2}{2m_W^2}\frac{a_0^w}{\Lambda^2} \tag{2.25}$$

and

$$\frac{f_{\mathrm{M},3}}{\Lambda^4} = \frac{g^2 g'^2}{2m_W^2}\frac{a_C^w}{\Lambda^2} . \tag{2.26}$$

Comparing the dimension of $a_{0/C}^W$, TeV^{-2}, to the dimension TeV^{-4} of $f_{\mathrm{M},i}$, it seems like the former couplings belong to dimension six operators. This would contradict the previous observation that pure quartic couplings can only be achieved by dimension eight operators. However, according to [51] the definition of these operators suffers from poor power-counting, rendering them effectively dimension eight and resolving the contradiction.

2.4.3 Unitarity violation

Every effective field theory violates the unitarity of the S-matrix, if the scale at which the theory is probed gets close to the scale of new physics phenomena. A prominent historical example is the effective theory Fermi introduced to describe the β-decay [52, 53]. Fermi postulated a four fermion interaction that gave a satisfying description in an energy regime far below the W mass. However, when going to higher energies the theory predicted that the total cross-section rises with the center-of-mass energy leading to a violation of unitarity above $\Lambda \sim \frac{m_W}{2g\sqrt{\pi}}$. Today, the reason for this behaviour is known. At these scales the interaction resolves the heavy W boson mediating the interaction turning the effective four-fermion vertex into two three-point vertices connected by the W boson. Therefore the inclusion of the, at the time Fermi developed the theory, unknown electroweak interaction, regularized the bad high-energy behaviour and made the theory UV-complete.

This example can be transferred to the effective field theories considered in this thesis. If a measurement probes scales to close to that of the new physics phenomena, the unitarity of the S-matrix will be violated. This renders the predictions obtained from the effective theory unphysical and therefore the limits meaningless. Current limits on these couplings are on the order of $\mathcal{O}(1\,\mathrm{TeV}^{-4})$ [54, 55]. Therefore assuming a coupling $\mathcal{O}(1)$ the current measurements probe scales $\Lambda \sim 1\,\mathrm{TeV}$ in reach of the LHC. This implies that the assumption that the new physics scale is well above the current experimental reach might already be violated.

To approach the possible unitarity violation more quantitatively, the unitarity bound is calculated using a tool from the VbfNlo authors [56]. The calculation is based on a partial wave decomposition of the S-matrix of $VV \to VV$ scattering (with $V = W^\pm, Z$ or γ). The unitarity criterion is defined such that the real part of the zeroth partial wave has to be below 0.5 [57]. Although the calculation is based on $2 \to 2$ scattering processes and therefore not strictly valid for the $1 \to 3$ processes encountered in three boson production, it provides an estimate of the unitarity bound.

The unitarity bound can be seen in Figure 2.10a which shows it as a function of the effective center-of-mass energy, $\sqrt{\hat{s}}$, and for three different operators. The region to the right of the unitarity bound violates unitarity, while the region above the dotted lines is excluded by experiments. It is clear that the unitarity bound crosses the experimental limits far below $\sqrt{\hat{s}} < 8\,\mathrm{TeV}$. More precisely the unitarity bound is between 600 GeV for $f_{\mathrm{T},0}$ and 1.4 TeV for $f_{\mathrm{M},2}$ using the current experimental limits on the couplings. These effective center-of-mass energies are easily reachable in the data recorded at the LHC with a proton-proton center-of-mass energy of $\sqrt{s} = 8\,\mathrm{TeV}$. Therefore it is necessary to *unitarize* the effective Lagrangians before using their predictions as inputs for the limit setting.

2.4.4 Unitarization

Several methods exist to obtain meaningful theory predictions and thus meaningful limits at energy scales which might already violate unitarity. One class of methods is the *form-factor* approach. It modifies the couplings with a form-factor $\mathcal{F}(s)$, which depends on the scale of the interaction, s:

$$f_i \to f_i \cdot \mathcal{F}(s)\,. \tag{2.27}$$

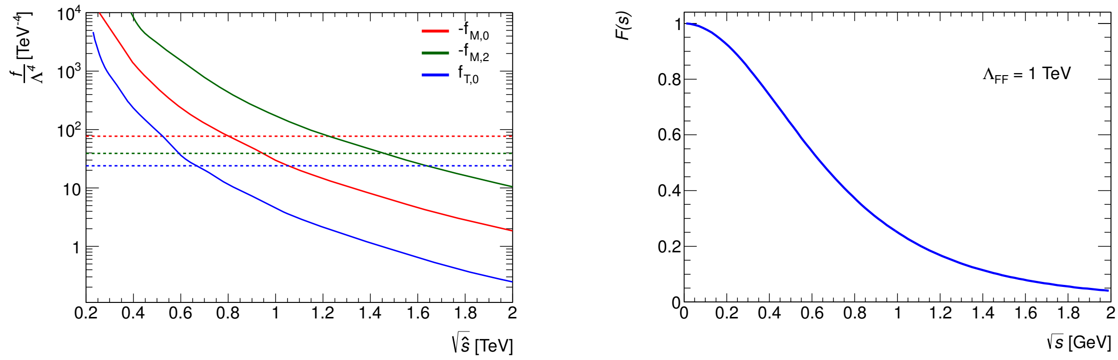

(a)

(b)

Figure 2.10: (a): Unitarity bounds as a function of $\sqrt{\hat{s}}$ for three different operators and current experimental limits (dotted lines). (b): Dipole form-factor, $\mathcal{F}(s)$, with $\Lambda_{\mathrm{FF}} = 1\,\mathrm{TeV}$ as a function of $\sqrt{s}$.

The form-factor can be an arbitrary function of s as long as it suppresses contributions from processes with $s \sim \Lambda$. One trivial choice would be

$$\mathcal{F}(s) = \Theta(\Lambda_{\mathrm{FF}}^2 - s)\,, \tag{2.28}$$

with the Heaviside Function Θ and a form-factor scale Λ_{FF}. This choice of the form-factor suppresses contributions above a scale Λ_{FF} completely and is therefore often called *cutoff* or *trimming*. The scale can be arbitrarily chosen but it must guarantee that unitarity is conserved up to all scales s the experiment can reach, i.e. up to $\sqrt{s}$ in case of a collider experiment. A common choice for Λ_{FF} is to use the smallest scale that ensures unitarity.

Another choice of $\mathcal{F}$ often used in the literature due to its larger reach and smoother form is the *dipole form-factor* defined as

$$\mathcal{F}(s) = \left(1 + \frac{s}{\Lambda_{\mathrm{FF}}^2}\right)^{-2}\,. \tag{2.29}$$

It effectively suppresses the contribution from anomalous couplings already at scales below Λ_{FF} as can be seen in Figure 2.10b, which shows the dipole form-factor as a function of the energy, $\sqrt{s}$, for $\Lambda_{\mathrm{FF}} = 1\,\mathrm{TeV}$.

In this work the unitarization of the results will be obtained using the dipole form-factor from Equation 2.29. The form-factor scale is chosen as the largest value such that new physics phenomena with a coupling equal to the expected limit still conserves unitarity up to $\sqrt{s} = 8\,\mathrm{TeV}$.

The application of a form-factor is necessary to obtain physically meaningful results, but it has a drawback. It introduces a dependence on another parameter, the form-factor scale. This can be thought of as choosing a specific model in an up-to-now model independent prescription of new physics phenomena.

CHAPTER 3

The ATLAS experiment at the LHC

This analysis was carried out using proton-proton collision data recorded with the ATLAS[1] experiment located at the Large Hadron Collider (LHC). This chapter provides an overview over the experimental setup. At first, the LHC will be introduced and then the ATLAS experiment will be discussed. The overview given here covers the main features of both machines, more details can be found in [58] and [59], respectively.

3.1 The Large Hadron Collider

The Large Hadron Collider is currently the world's highest-energy particle accelerator, having reached a center-of-mass energy $\sqrt{s}$ of 8 TeV. It is designed to collide proton beams at $\sqrt{s} = 14\,\text{TeV}$ with a peak instantaneous luminosity of $10^{34}\,\text{cm}^{-2}\,\text{s}^{-1}$. In addition, heavy ion beams can be collided with an energy of 2.8 TeV per nucleon and a peak instantaneous luminosity of $10^{27}\,\text{cm}^{-2}\,\text{s}^{-1}$. It is built in the former tunnel of the Large Electron Positron Collider (LEP), located at the European Organization for Nuclear Research (CERN) near Geneva. The tunnel which has a circumference of 26.7 km was built between 1984 and 1989 and lies between 45 m and 170 m below the surface. It consists of eight straight sections connected by eight arcs. Two tunnels link the LHC with the accelerator complex located at CERN, which is used to inject the proton beams with an energy of 450 GeV into the LHC.

From the eight possible interaction points located around the tunnel, four have been equipped with large-scale experiments. The two general-purpose experiments ATLAS and CMS[2] [60] have been designed for a diverse physics program, including the discovery of the Higgs boson, precision measurements of the Standard Model, and searches for physics beyond the Standard Model. Two specialized experiments have been installed in other interaction points. One of them, ALICE[3] [61], is specialized on heavy ion collisions and studies the formation of the quark-gluon plasma at extreme energy densities and temperatures. The other, LHCb[4] [62], is focused on precision measurements of processes including b quarks to better understand CP violation and the matter-antimatter asymmetry in the universe.

In contrast to electron-positron colliders where synchrotron radiation limits the achievable beam energies, the maximum beam energy at a proton collider depends on the magnetic field that bends the

---

[1] **A** **T**oroidal **L**HC **A**pparatu**s**

[2] **C**ompact **M**uon **S**olenoid

[3] **A** **L**arge **I**on **C**ollider **E**xperiment

[4] **L**arge **H**adron **C**ollider **b**eauty experiment

protons around the ring. To reach a beam energy of 7 TeV at the LHC, the required dipole field strength is 8.33 T. This field strength is obtained by using superconducting Nb-Ti magnets operated at a temperature of 1.9 K, cooled using super-fluid helium. As the LHC is a particle-particle collider, two beam pipes that host the counter-rotating beams are necessary. A magnet design that hosts two coils and beam lines in the same mechanical structure and cryostat has been adopted, due to limited space and to reduce cost.

The instantaneous luminosity provided by the LHC is proportional to the beam intensities, the revolution frequency of the beam around the ring, and further factors describing the geometry of the beams at the interaction point. To achieve the design luminosity, these parameters have to be tuned to the edge of the presently available technologies. The revolution frequency is obtained by the circumference of the ring and the speed of light and is thus fixed to 11.2 kHz due to the decision to reuse the LEP tunnel. Each proton beam is divided into 3500 bunches, of which 2808 bunches are occupied at full intensity. Each of these bunch positions is separated by 25 ns from the following. This gives rise to a 40 MHz bunch-crossing rate of the two counter-rotating beams in the interaction points. At each of the bunch crossings, not only one proton-proton collision takes place, but several, depending on the beam intensity and the size of the interaction region. On average 23 proton-proton collisions will happen in one bunch crossing at design luminosity.

The operation of the LHC started in September 2008, but was abruptly stopped only nine days later due to a faulty electrical connection that caused mechanical damage due to a subsequent release of helium. The operation was resumed in November 2009 with a reduced center-of-mass energy of 900 GeV. The energy was raised to 3.5 TeV per beam in March 2010, and data was recorded until November 2011 yielding an integrated luminosity of about 5.6 fb^{-1} delivered by the LHC. During this time the bunch spacing was reduced from 75 ns to 50 ns.

The physics program of the LHC restarted in March 2012 with an increased center-of-mass energy of 8 TeV. Data was taken until December, at which point the LHC had delivered an integrated luminosity of 23.3 fb^{-1} with a peak instantaneous luminosity of $7.73 \times 10^{33}\ \mathrm{cm}^{-2}\,\mathrm{s}^{-1}$. Currently, the LHC is in the *Long Shutdown 1*, during which it is prepared for a center-of-mass energy of 14 TeV.

3.2 The ATLAS experiment

The ATLAS experiment is a general-purpose experiment at the LHC built in a cavern at the interaction point 1. It was built by thousands of collaborators in a period over fifteen years, before the installation was finished in 2008.

To guide the design, requirements on the detector have been identified using several benchmark processes that represent the wide range of the intended physics program [63]. These benchmark processes included the discovery of the Higgs boson, as well as the discovery of potential new physics phenomena, like the decay of hypothesized super-symmetric particles, or new heavy gauge bosons. The requirements are as follows:

- A tracking system with a high granularity embedded in a strong magnetic field to be able to provide good track momentum resolution and vertex reconstruction.

- A large coverage calorimetry that allows high resolution energy measurements provides the ability to identify electrons and photons. The large-coverage is necessary to allow an accurate measurement of the missing transverse momentum.

- A muon system that provides excellent resolution for muons over a large range of momenta.

- A highly efficient trigger and data acquisition system that allows to reduce the 40 MHz collision rate to a level that can be stored permanently.

The general design of the detector was guided by a few basic choices on the layout of the magnetic fields used to bent the particles in the tracking and muon system. The inner tracking devices are immersed in a 2 T solenoidal field, generated by a thin superconducting solenoid located in front of the calorimeters. Three air-core, superconducting toroids generate the magnetic field that bends the particle tracks inside the muon system. They are arranged around the calorimeter in an eight-fold azimuthal symmetry.

The layout of the ATLAS detector is shown in Figure 3.1. It is forward-backward symmetric with respect to the interaction point and covers the full angle around the beam axis. It consists of a barrel-shaped central part and two disc-shaped endcaps, one on either side. The diameter of the detector is 25 m. With a total length of 40 m and a weight of approximately 7000 t, it is the world's largest detector built at a particle collider. The different detector systems are arranged layer-wise around the interaction point. The innermost detector is the *inner detector*, which is used to measure the trajectory and momentum of charged particles produced in the collision. The next layer is comprised of the calorimetry that measures the energy of incident particles. The outermost system is the muon spectrometer dedicated to the measurement of the trajectory of muons.

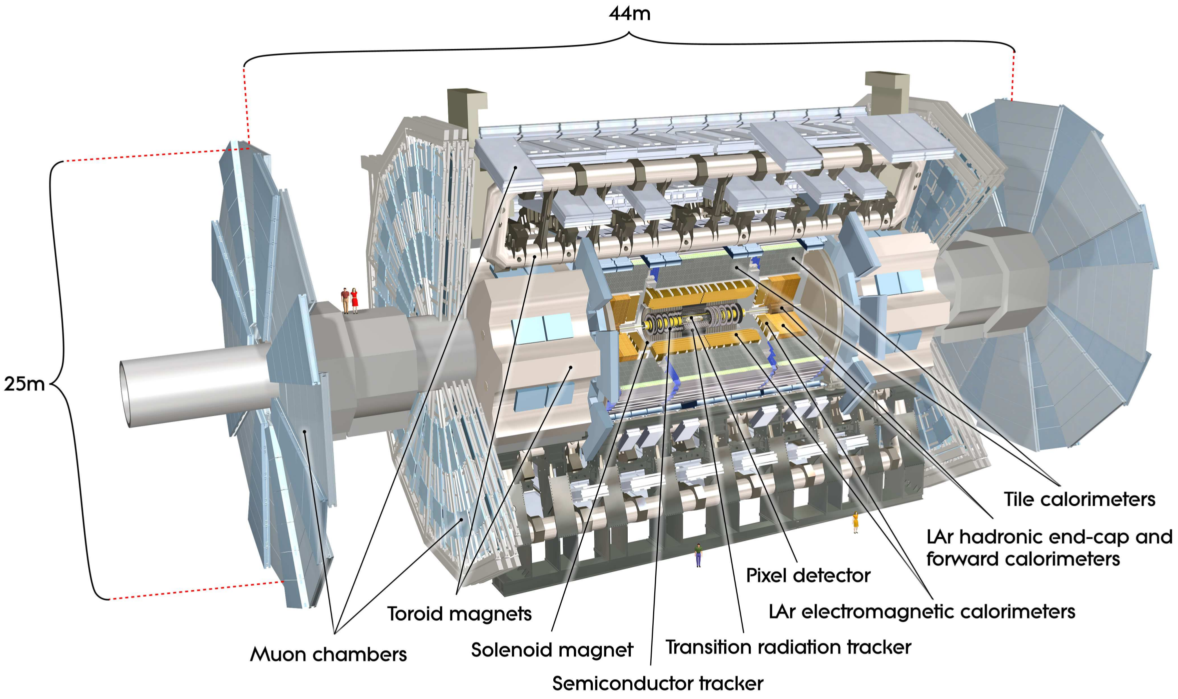

Figure 3.1: Layout of the ATLAS detector. From [59].

The reference coordinate system used in ATLAS is defined as follows. The origin of the a right-handed coordinate system is defined as the nominal interaction point. The beam line defines the z-axis, and the x-y-plan is transverse to the beam direction. The positive x-axis points from the interaction point towards the center of the LHC, and the positive y-axis points upwards. The azimuthal angle, ϕ, is measured in the plane perpendicular to the beam axis, and the polar angle, θ, is defined from the beam axis. The transverse quantities, p_{T}, E_{T} and $E_{\mathrm{T}}^{\mathrm{miss}}$, are defined in the x-y-plane. The pseudo-rapidity is defined as $\eta = -\ln\tan(\theta/2)$, and the distance in pseudo-rapidity-azimuthal angle space is defined as $\Delta R = \sqrt{\Delta\eta^2 + \Delta\phi^2}$.

This section is organized as follows: At first, the inner detector is briefly introduced. Afterwards, the calorimeters and the muon spectrometer are outlined. Then, the trigger system is summarized. At last, the principle of the luminosity measurement is explained.

3.2.1 Inner detector

The inner detector (ID) is designed to measure the trajectory of charged particles with $p_{\mathrm{T}} > 0.5\,\mathrm{GeV}$ and $|\eta| < 2.5$, created in the collision or subsequent decays. As it is immersed in a 2 T solenoidal magnetic field, the curvature of the trajectories allows to measure the momentum of the particles. The primary vertex and additional secondary vertices, originating from the decay of a long-lived particle within the beam pipe, can be reconstructed using the intersection of two or more trajectories. Finally, the inner detector has particle identification capabilities, which allow to separate electrons and hadrons with transverse momenta between 0.5 GeV and 150 GeV and with $|\eta| < 2.0$.

The inner detector consist of three subsystems which can be operated independently. From inside out, these are the Semiconductor Pixel Detector, the Silicon Microstrip Detector (SCT) and the Transition Radiation Tracker (TRT). The first two sub-detectors cover the region $|\eta| < 2.5$, while the TRT only extends up to $|\eta| < 2.0$. The length of the cavity housing all three sub-detector systems is 6.2 m, and its diameter is 2.1 m. The layout of the inner detector is shown in Figure 3.2.

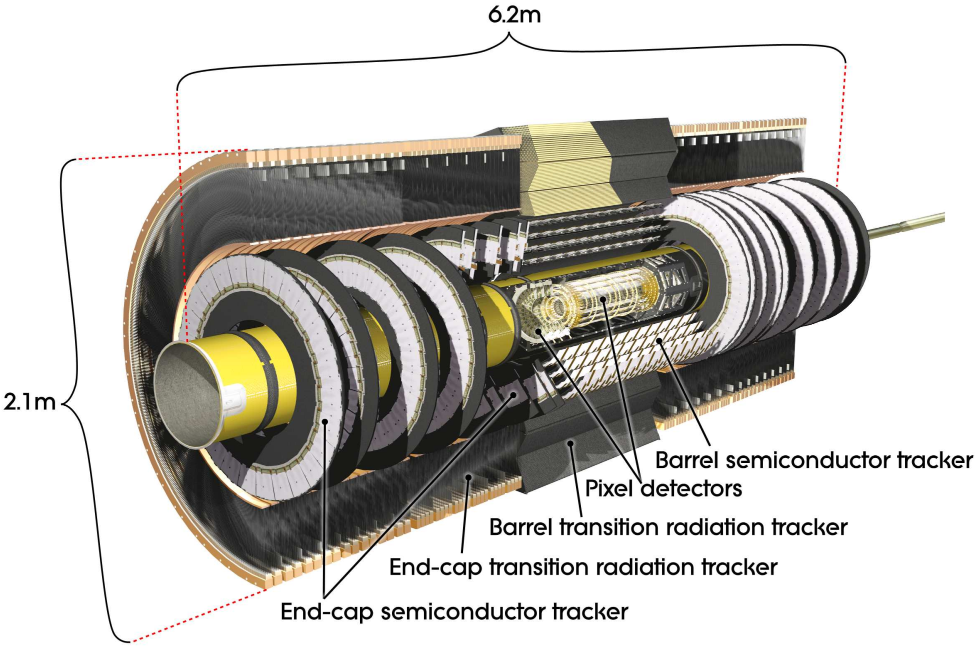

Figure 3.2: The layout of the ATLAS inner detector. From [59].

The innermost subsystem, the Semiconductor Pixel Detector, consist of 80.4 million pixels, most of which have a size of $(50 \times 400)\,\mu\mathrm{m}^2$. The pixels are grouped in 1744 sensors placed on three cylindrical layers in the barrel and five discs on either side. The intrinsic accuracy of the pixel system is 10 µm in the transverse, and 115 µm in the z- and R-direction for the barrel and endcap discs, respectively.

The Silicon Microstrip Detector, which is the intermediate sub-detector system, is equipped with

15912 sensors hosting 768 active silicon strips each with a length of 12 cm and a pitch of 80 µm. The intrinsic accuracy in the R-ϕ-plane is 17 µm. The intrinsic accuracy in the z- and R-plane for the barrel and endcap, is 580 µm and is achieved by an 40 mrad stereo angle between the SCT sensors.

The outermost system is the Transition Radiation Tracker, which is comprised of polymide straw tubes of 4 mm diameter, a length of 144 cm in the barrel and 37 cm in the endcap. The barrel tubes are aligned in parallel to the beam direction, while the tubes in the endcap are pointing outwards. Inside the tubes a 31 µm diameter gold-plated tungsten wire serves as anode. The tubes are filled with a gas mixture consisting of 70 % Xe, 27 % CO_2 and 3 % O_2. The TRT provides 36 hits per track on average with an intrinsic accuracy of 130 µm in the plane perpendicular to the beam and enhances the pattern recognition on the trajectories. As mentioned above it only covers the region $|\eta| < 2.0$. The straw tube are interleaved with material that provokes transition radiation consisting of low energy photons. These are absorbed in the gas mixture and give rise to larger signal amplitudes than minimum ionising particles. Therefore the TRT hits are classified as either low-threshold (typically larger than 250 eV) or high-threshold (typically larger than 6 keV) hits directly at the front-end electronics. This information is later used to discriminate tracks from electrons and hadrons.

3.2.2 Calorimetry

The purpose of the ATLAS calorimeters is to measure the energy and direction of incident particles, and to determine the missing transverse energy. The missing transverse energy is an energy imbalance in the plane transverse to the beam direction, caused by the presence of particles that escape the detector undetected. In addition, the calorimeter must provide spatial information about the energy deposition that can be used to identify the particle type.

Sufficient precision of the energy measurement can only be achieved if the induced shower from the incident particles is stopped within the calorimeter. This necessitates a large radial depth of the calorimeter. The direction and shape of the shower is measured by segmenting the calorimeter into many small cells whose measured energy can be read out individually. At the same time, the calorimeter should provide almost full coverage of the solid angle to obtain a precise measurement of the missing transverse energy.

To achieve these goals at reasonable cost, the ATLAS calorimeters are divided laterally and longitudinally into different subsystems. The innermost layer is the electromagnetic calorimeter (EM), which is thick enough to stop electrons and photons. Other particles that induce hadronic showers are stopped in the outer part, the hadronic calorimeter (HAD). The central part of the calorimeters that covers the region $|\eta| < 2.5$ is dedicated to high precision measurements and hence was built with a fine segmentation. The calorimeters which cover the region $2.5 < |\eta| < 4.9$ are built with a coarser granularity and are designed to provide reasonable precision for jet and missing transverse energy measurements.

All calorimeters are sampling calorimeters, which means that they are built using two different alternating materials, one acting as absorber and the other one helps to measure the energy. Primary particles interact with the absorber material giving rise to secondary particles, which are detected in the active material. The ATLAS calorimeters are built with a variety of different technologies. The electromagnetic layer uses liquid argon as active and lead as absorber material in the barrel ($|\eta| < 1.475$) and endcap ($1.375 < |\eta| < 3.2$) calorimeters. For the hadronic calorimeter, steel is the absorber material and polystyrene-based scintillators are the active material in the barrel part ($|\eta| < 1.7$). The hadronic calorimeter endcaps ($1.5 < |\eta| < 3.2$) use LAr as active material with copper as absorber. The forward calorimeters ($3.1 < |\eta| < 4.9$) also employ LAr as active material and copper or tungsten as absorber for the electromagnetic and hadronic part, respectively. The layout of the ATLAS calorimeters is shown in Figure 3.3.

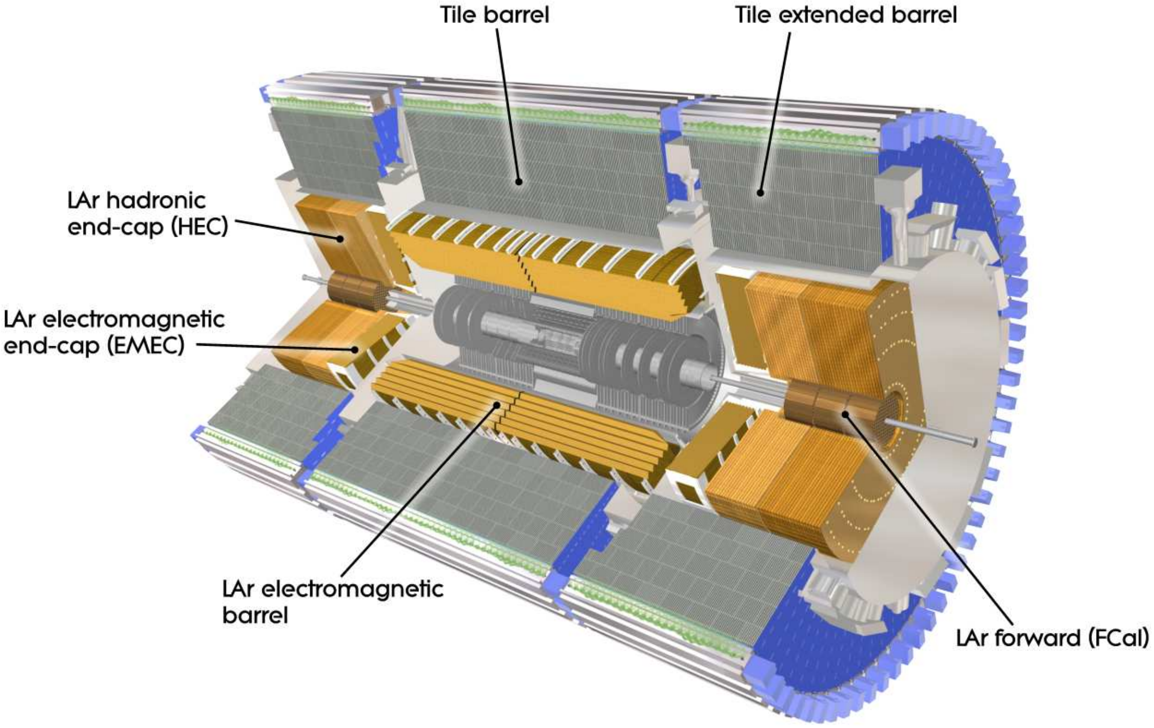

Figure 3.3: The layout of the ATLAS calorimeter system. From [59].

Electromagnetic calorimeter

The electromagnetic calorimeter is a sampling calorimeter using lead as absorber and liquid argon as the active material. The barrel part is divided into two identical half-barrels, one for the positive and negative z-direction, respectively. The endcap calorimeters consist of two wheels each, the outer wheel covering the region $1.375 < |\eta| < 2.5$ and the inner wheel which covers the region $2.5 < |\eta| < 3.2$. The absorber material as well as the electrodes are accordion-shaped to provide full coverage in the azimuthal angle.

The electromagnetic calorimeter shares a common vacuum vessel with the solenoid magnet to reduce the amount of material in front of the calorimeter. In addition, a thin layer of active material (the presampler) is placed in front of the calorimeter inside the cryostat to provide information about energy lost upstream of the calorimeter. The material budget in front of the presampler and the electromagnetic calorimeter is shown in Figure 3.4. The amount of material corresponds to a radiation length between $2\,X_0$ and $5\,X_0$, with the notable exception of the transition region between the barrel and endcap calorimeters at around $|\eta| = 1.4$, where it reaches up to $11\,X_0$. The large material budget poses a challenge for the reconstruction of photons, since a significant fraction undergoes a conversion into an e^+e^- pair before reaching the calorimeters.

In the region $|\eta| < 2.5$, the electromagnetic calorimeter is segmented into three longitudinal layers. The innermost layer is finely segmented in η and dedicated to a precise position measurement of photons. In addition, it provides detailed information about the shower shape, which helps to identify photons and electrons. The layout of the electromagnetic barrel calorimeter is illustrated in Figure 3.5. The three layers and the accordion-shaped geometry are clearly visible.

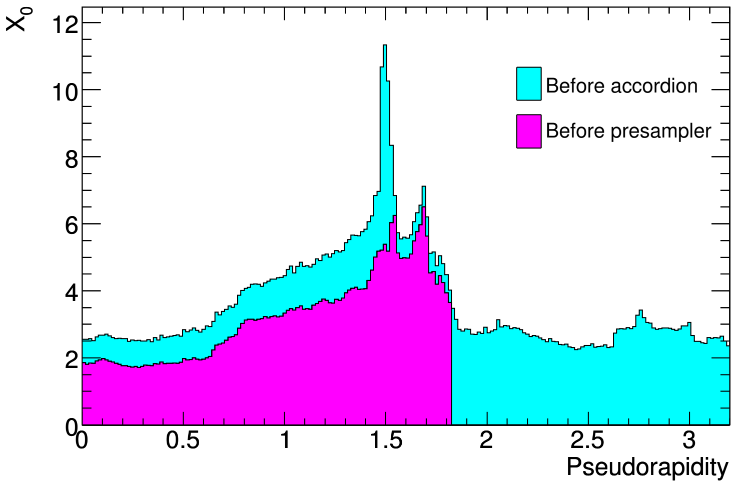

Figure 3.4: Cumulative amount of material in front of the calorimeter given in units of radiation length X_0 and as a function of the pseudo-rapidity, separately shown for the presampler and the electromagnetic calorimeter. From [59].

Hadronic calorimeter

The hadronic calorimeter is separated into a barrel and an endcap part. In contrast to the electromagnetic calorimeter, different technologies are used for the two calorimeter parts. The hadronic barrel calorimeter is built using steel as absorber and scintillating tiles as active material with a volume ratio between these materials of 4.7 : 1. It consists of three parts, the central barrel covering the region $|\eta| < 1.0$, and two extended barrels covering $0.8 < |\eta| < 1.7$. The total thickness of the hadronic barrel calorimeter in units of the interaction length, λ, is approximately $7.4\,\lambda$. The scintillators are connected via wave-length shifting fibers to the photomultiplier tubes. The fibers are grouped such that a longitudinal segmentation into three layers and a lateral segmentation into an approximately projective geometry in pseudo-rapidity with a typical granularity of 0.1 in $\Delta\eta$ and $\Delta\phi$ is achieved.

The hadronic endcap calorimeter is based on copper absorbers with liquid argon as active material. Each endcap consist of two adjacent wheels, the front- and rear-wheel, that differ in the ratio of active to absorber material. The granularity is 0.1×0.1 in $\Delta\eta \times \Delta\phi$ for the region $1.5 < |\eta| < 2.5$, and 0.2×0.2 for larger $|\eta|$.

Forward calorimeter

The forward calorimeter consists of three modules mounted about 4.7 m away from the interaction point, and covers the region $3.1 < |\eta| < 4.9$, which corresponds to a radius of approximately 40 cm. The active material for all modules is liquid argon. The module closest to the interaction point uses copper as absorber, while the two outer modules use tungsten, due to its high absorption length.

3.2.3 Muon spectrometer

The muon spectrometer is the outermost system of the ATLAS detector and measures the trajectories of charged particles that exit the calorimeters. Due to the large radiation and interaction length of the calorimeters, these are mostly muons. The muon spectrometer, which covers the region $|\eta| < 2.7$, is designed to provide an adequate momentum resolution for particles with momenta up to 3 TeV without the information from other parts of the detector. This is achieved by a variety of different tracking detectors placed over a large volume, immersed in a strong toroidal magnetic field.

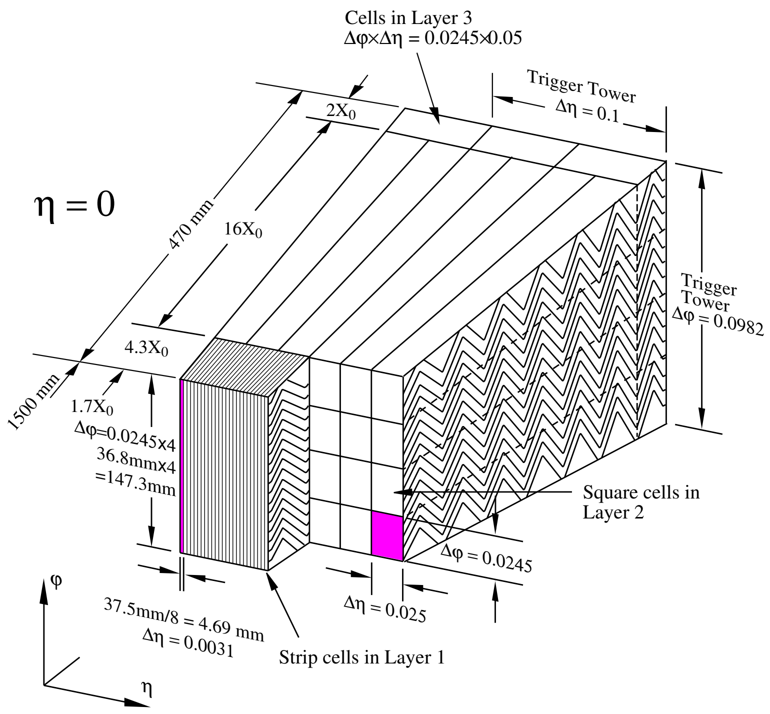

Figure 3.5: Sketched layout of one part of the electromagnetic barrel calorimeter. The accordion-shaped geometry as well as the different layers and their respective cell granularity are shown. In addition, the thickness in units of the radiation length X_0 is indicated. From [59].

The toroidal field is generated by three superconducting air-core toroids, consisting of eight coils each. The barrel toroid covers the region $|\eta| < 1.4$ and the two endcap toroids cover the region $1.6 < |\eta| < 2.7$. In the transition region both fields overlap. The geometry of the coils that generate the toroidal magnetic field is shown in Figure 3.6. The eight barrel coils and the interleaved eight endcap coils as well as the tile calorimeter and the return yoke are shown.

In total, four different tracking detectors are used in the muon spectrometer. The Monitored drift tube chambers (MDT) and Cathode strip chambers (CSC) are designed to provide high precision space point measurements of a particle passing through them. They are complemented by two fast tracking devices, the Resistive-plate chambers (RPC) and Thin-gap chambers (TGC), which deliver information

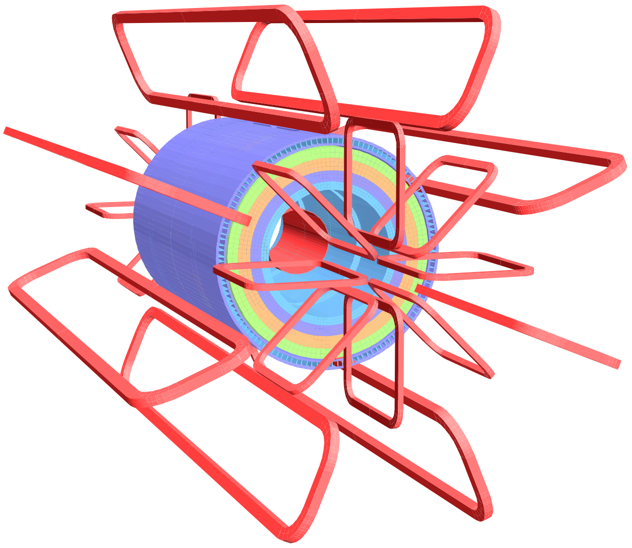

Figure 3.6: Geometry of the coils generating the toroidal field. In addition, the tile calorimeter with an outside return yoke is shown. From [59].

in a few nanoseconds. They are used to trigger on muons and to provide information about the position perpendicular to the bending plane.

In the barrel, the precision tracking chambers are placed on three cylindrical shells located on and between the coils. In the endcap, three discs perpendicular to the beam axis are equipped with the tracking chambers. MDTs are used in the region $|\eta| < 2.7$, except for the endcap disc closest to the interaction point, where CSCs are used in the region $|\eta| < 2.0$. In the barrel, $|\eta| < 1.05$, the RPCs are used as fast tracking devices, while for the endcap, $1.05 < |\eta| < 2.4$, TGCs are used. The region $2.4 < |\eta| < 2.7$ is not equipped with fast tracking devices. The layout of the muon spectrometer is shown in Figure 3.7.

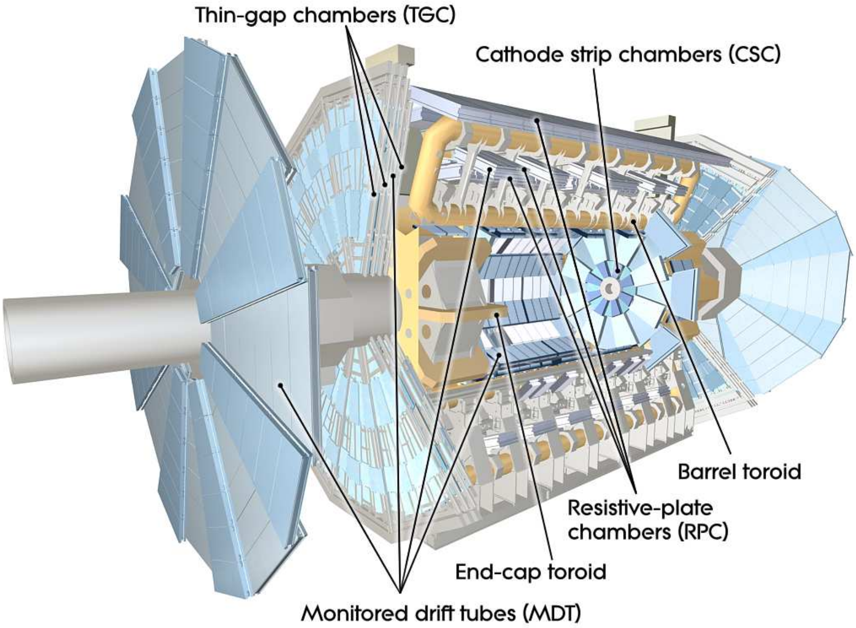

Figure 3.7: The layout of the muon spectrometer. From [59].

A Monitored drift tube chamber consist of several layers of Monitored drift tubes. Each aluminum tube has a diameter of approximately 30 mm and is operated with a gas mixture of argon and carbon dioxide at pressure of 3 bar. In the center of the tubes a tungsten-rhenium anode wire with a diameter of 50 µm is strained and operated at about 3 kV. The position resolution in the plane perpendicular to the tube is about 80 µm for a single tube and about 40 µm for a chamber. MDTs can only be safely operated for rates up to $150\,\mathrm{Hz\,cm^{-2}}$, which is exceeded in the first layer in a region $|\eta| > 2.0$. Therefore Cathode strip chambers, which can withstand rates of up to $1000\,\mathrm{Hz\,cm^{-2}}$ are used for the region $2.0 < |\eta| < 2.7$. The Cathode strip chambers are multi-wire proportional chambers with 30 µm diameter anode wires oriented in the radial direction. The charge induced on the cathodes, which are aligned perpendicular to the wires, is read out and the position resolution achieved in the bending plane is 60 µm.

The fast tracking devices are designed to achieve a time resolution well below the bunch crossing rate of 25 ns, such that they can be used to identify the bunch-crossing and provide fast information for the trigger decision. Their momentum resolution must be sufficient to keep the trigger rate due to mis-measured muon momenta at a reasonable level. The Resistive-plate chambers which are used in the barrel are gaseous parallel electrode-plate detectors, operated in avalanche mode and read out via capacitive coupling. The Thin-gap chambers are multi-wire proportional chambers like the CSCs. They are however, operated in saturation-mode to achieve the necessary time resolution.

3.2.4 Trigger system

The typical size of an event containing information from all sub-detectors is above 1 MB. At the design bunch-crossing rate of 40 MHz the recorded data rate would exceed 40 PB s^{-1}, which is orders of magnitudes larger than what current state-of-the-art storage technologies can handle. However, it is not necessary to store every event permanently. The vast majority of collisions has a negligible momentum transfer compared to the processes which constitute the physics program of ATLAS. This is illustrated in Figure 3.8, where the cross-sections for various Standard Model processes as a function of the center-of-mass energy are displayed. The total inelastic cross-section is several orders of magnitude higher than, for example, the Higgs boson production cross-section.

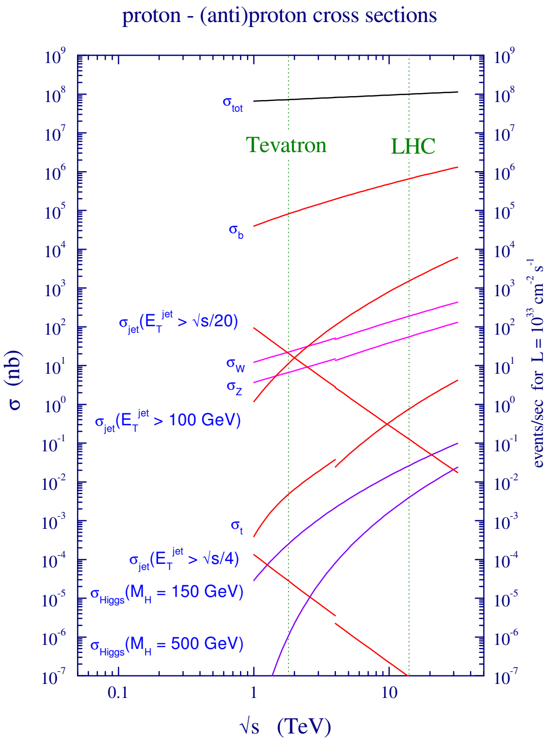

Figure 3.8: Cross section of various Standard Model processes at the TeVatron and LHC colliders as function of the center-of-mass energy $\sqrt{s}$. For $\sqrt{s} < 4$ TeV the cross-sections are calculated for a $p\bar{p}$-collider, and for $\sqrt{s} > 4$ TeV for a pp-collider. From [23].

The final event rate to permanent storage is a few hundred Hz. Thus a rejection factor on the order of 10^6 is needed. This is achieved by a trigger system, which is designed to filter all but the most interesting events. The criteria that an event has to fulfill to be kept are typically formulated in terms of p_{T} thresholds for certain particle types.

The ATLAS trigger system consists of three levels, which subsequently refine the decision of the previous level. The first trigger level (L1) reduces the input rate to roughly 75 kHz using custom-made electronics. The second (L2) and third (Event Filter, EF) trigger levels, which reduce the rate to 3.5 kHz and 200 Hz, respectively, are built using commercially available computers.

The L1 trigger uses custom hardware, which identifies signatures of high-p_{T} electrons, photons, muons, jets and missing transverse energy. The decision must be available within 2.5 µs. Thus only reduced granularity input from the subdetector systems and fast algorithms can be used. Muons are identified using the input from the RPCs and TGCs of the muon system. Electrons, photons and jets are identified using a sliding window algorithm on projective towers with a granularity of 0.1×0.1 ($\Delta\eta\times\Delta\phi$) in most parts of the detector. In addition to the decision whether or not an event should be processed further, the L1 system provides information about detector regions containing possibly interesting high-p_{T}

objects to the next trigger level. These regions are called Regions-of-Interest (RoI).

The second level trigger has access to the full detector granularity in the RoIs identified by the L1 trigger. It can therefore use more complex, software based algorithms to refine the decision of the first level trigger. The average computing time per event is about 40 ms yielding an output rate of approximately 3.5 kHz to the third trigger level. The event filter has access to the full detector information and granularity. The algorithms employed at the EF are very similar to the algorithms used for the offline reconstruction (cf. Chapter 5). The average time the EF takes to reach a decision for a particular event is about 4 s.

To reduce the rate of an individual trigger either the trigger threshold can be raised, or a so called *prescale factor* can be applied. A *prescaled trigger* with prescale P only selects one in P events that passed the trigger requirement. The prescale factors can be set or changed during the data taking with the ATLAS detector.

3.2.5 Luminosity measurement

The precise determination of the luminosity the LHC delivered is a challenging and important measurement. It affects most of the analyses that are carried out at ATLAS. Thus several detectors are employed to measure the instantaneous luminosity. One of them, BCM[5], served as the default device for the measurements of the integrated luminosity in 2011 and 2012. BCM measures the rate of incident particles, which is proportional to the luminosity, using diamond sensors. It is placed 184 cm away from the interaction point on both sides of the ATLAS detector.

Since the BCM system only measures the relative luminosity, the absolute luminosity must be calibrated at least once. This is done a few times per year using dedicated running conditions of the LHC. The measurement of the luminosity is based on the following formula, which expresses the instantaneous luminosity, L_{inst}, as a function of the beam parameters

$$L_{\mathrm{inst}} = \frac{n_c f_r n_a n_b}{2\pi \Sigma_x \Sigma_y} \, . \tag{3.1}$$

Here, n_c is the number of bunches travelling with a revolution frequency f_r around the ring. n_a and n_b are the number of protons in each of the beams and Σ_x and Σ_y are the convoluted beam widths in x and y direction, respectively. The numerator of Equation 3.1 is either given by the LHC (f_r) or can be measured by special instruments (n_a, n_b and n_c). The beam profiles have to be determined using a dedicated measurement, known as the *van-der-Meer scan* [64, 65]. In a van-der-Meer scan, the interaction rate is measured as a function of the beam separation, when one beam is scanned through the other in the transverse plane.

Once the rate measured with LUCID is calibrated to the instantaneous luminosity, the total integrated luminosity can be determined using the relative luminosity measurements. The systematic uncertainties that affect the luminosity determination can be split into two categories. The first affects the determination of the instantaneous luminosity with the van-der-Meer scan, while the other is an uncertainty on the stability of the relative luminosity measurement over time. For the data taken in the year 2012 the relative uncertainty on the luminosity measurement is 2.8 %. More details on the methods used can be found in [66].

---

[5] **B**eam **C**onditions **M**onitor

CHAPTER 4

Monte Carlo simulation

The precise simulation of physics processes using *Monte Carlo* (MC) methods is one of the most important aspects in modern particle physics. The features of particular signal processes can be studied in order to understand how to separate them from other processes constituting the background. In addition, the simulation allows the comparison between data and theoretical predictions. Other uses of simulations include the calibration and performance study of reconstruction algorithms and benchmarks for design of new experiments.

The importance of simulation can also be seen when considering that the most referenced journal publication authored by CERN is that of the `Geant4` toolkit [67], cited over 4000 times [68]. The `Geant4` toolkit describes the passage of particles through matter, which is one of the three steps that have to be simulated to describe an event from the collision to the response of the detector.

At first, the simulation of the collision will be discussed, then the ATLAS simulation infrastructure is introduced. At last, the Monte Carlo samples used in this analysis are listed.

4.1 Simulation of the collision

The simulation of the proton-proton collision can be separated in four distinct steps. The first of them is the hard-scatter, whose simulations includes the calculation of the matrix element and the phase-space integration. Afterwards, the parton shower and hadronization of quarks and gluons is simulated. The last step is the proper treatment of the *underlying event*, i.e. the interaction of the proton remnant.

For simple topologies, the hard-scatter can be calculated analytically, but in general, the necessary multi-dimensional integration is done numerically using Monte Carlo methods. The calculation is done at fixed order in perturbation theory, typically at leading or next-to-leading order in QCD. So-called *multi-leg* generators can calculate matrix elements with additional partons in the final state. This typically yields a better description of the differential distributions, although the calculation of the total cross-section can not be thought of as "improved leading order result", since it might be farther away from the next-to-leading order result [69].

The quarks participating in the hard scatter can emit gluons, $q \to qg$, and the participating gluons can split, $g \to gg$, or create a quark-antiquark pair, $g \to q\bar{q}$. This is modelled by the *parton-shower* simulation, which describes the evolution of a parton at the time-like scale, t_{max}, set by the hard scatter, down to a cut-off scale, t_0, by successive branching. In case of incoming partons the evolution is done backwards, also starting from the hard scatter. The cut-off scale is chosen as the scale at which QCD becomes strongly interacting and the splitting functions which are based on perturbative calculations are not valid anymore ($\sim 1\,\text{GeV}$). Different choices for the scale exist, most notably the p_{T} of the parton (p_{T}-ordered shower) or the angle between the splittings (angular-ordered shower). An additional complication arises for multi-leg generators. As the first branching of an outgoing parton can not be distinguished from a real emission calculated in the matrix element, special care has to be taken to avoid over- or under-counting of additional jets. For example, an event with $(N + 1)$-jets in the final state can be either obtained by simulating an $(N + 1)$-parton final state, or by an N-parton final state with a successive wide-angle radiation in the parton-shower. Several schemes are available that match the matrix element calculation to the parton-shower (*ME-PS matching*) and try to resolve the ambiguity, for example CKKW [70] or MLM [71]. These matching schemes essentially provide an event-by-event prescription whether the matrix element or the parton shower is used to obtain an additional jet.

The hadronization step turns color-charged quarks and gluons into colorless hadrons. It is described by phenomenological models tuned to data, since at the scales relevant for this process, QCD is strongly interacting and cannot be treated perturbatively anymore. The two schemes used typically for the transition from partons to hadrons are the *Lund string* [72] and the *cluster hadronization* model [73, 74]. Both describe the hadronization as a probabilistic, iterative process.

The last step is the embedding of the hard-scatter into the underlying event, which has two main aspects, the proton remnant and multiple parton interactions. The proton remnant, i.e. the particles that appear after the proton is broken up by the hard scatter, is color connected to the rest of the event and thus may give rise to additional hadrons in the final state. Multiple parton interactions occur if more than one constituent pair of the protons interacts. Normally these additional interactions are soft, but sometimes an additional hard-, or semi-hard interaction will occur.

Several different programs, so-called *Monte Carlo generators*, exist that cover some or all of the aforementioned steps. The following generator programs are used in this thesis.

SHERPA is a multipurpose multi-leg generator [75]. It includes the simulation of parton-shower, hadronization and the underlying event and uses an extension of the CKKW approach for ME-PS matching [76]. The hadronization is implemented using a cluster fragmentation scheme based on the description in [77]. It can simulate the $W\gamma\gamma$ process up to three additional partons and includes photons from fragmentation and radiation.

ALPGEN is a multi-leg generator [78], which simulates only the hard scatter. It is typically interfaced to HERWIG [79, 80] for the parton-shower and hadronization and JIMMY [81] for the underlying event. However, any simulation program that supports interfacing can be used.

PYTHIA is a multipurpose simulation program, that includes several $2 \rightarrow 2$ processes at leading order [82, 83]. It provides a full treatment of the parton-shower, hadronization and underlying event. A p_{T}-ordered prescription is used to model the parton shower, and the hadronization is based on the Lund string model.

MC@NLO is a next-to-leading order generator [84], which simulates the hard-scatter and the parton-shower. The matching is done using the MC@NLO technique. As in the case for ALPGEN, the hadronization and the underlying event are typically simulated using HERWIG and JIMMY, respectively.

POWHEG is a next-to-leading order program [85], that simulates the matrix element and the parton-shower. Normally, PYTHIA is used for the hadronization and the underlying event simulation. The ME-PS matching is done using the POWHEG method.

The result of the simulation of one proton-proton collision by these programs is typically a list of stable particles that were produced, where a stable particle is defined as having a lifetime of $c\tau > 10\,\text{mm}$. To be able to compare data and simulation, the interactions of these particles with the detector material and the electronics of the detectors have to be simulated.

4.2 ATLAS simulation framework

The ATLAS collaboration employs a multi-stage simulation infrastructure [86]. This means that the simulation process is split into several consecutive steps, starting with the *event generation*, i.e. the simulation of a hard scatter as described above. Afterwards, the interactions of the particles with the detector material is simulated with the `Geant4` program [67]. The result of this step are energy deposits in the sensitive detector material (*hits*) which are subsequently passed to the simulation of the electronics. This step, the *digitization*, converts the *hits* to the detector signal, e.g. voltage or current, of the particular sub-detector. After the digitization, the simulated events can be passed to the exact same reconstruction algorithms used for real collision data. This ensures that both data and simulation are treated completely identically. One notable exception is the *truth record* stored for simulated events, which contains information about the process and final-state particles of the hard scatter as well as links between energy depositions and incident particles that can be used for performance studies.

The presence of *pile-up* is taken into account in the simulation as described in [87]. Two types of pile-up can be distinguished and are included differently. The first, *in-time pile-up*, i.e. additional particles from multiple collisions in the same bunch crossing, is simulated by overlaying the *hits* from minimum bias events before the digitization. The minimum bias events are simulated with Pythia 8. The effect of collisions in neighbouring bunches, *out-of-time pile-up*, is considered by simulating proton bunches which are organized in four trains of 36 bunches. The spacing between the bunches was set to 50 ns in agreement with the bunch spacing used during the data taking.

The number of minimum-bias events overlaid in each simulated event is drawn from a Poisson distribution, whose mean is the average number of interactions per bunch crossing, $\langle\mu\rangle$. Since the value of $\langle\mu\rangle$ decreases during an LHC fill, the distribution of $\langle\mu\rangle$ should be used in the simulation to determine the number of overlay events. However, the simulation of events started well before the first collision was recorded and the distribution of $\langle\mu\rangle$ was yet unknown. Therefore values of $\langle\mu\rangle$ between 1 and 40 have been simulated to cover the expected range of $\langle\mu\rangle$ values at the LHC. To ensure a good pile-up description, the simulated events are reweighted on an event-by-event basis to restore the distribution of $\langle\mu\rangle$ observed in data.

4.3 Signal process simulation

The correction of the acceptance and efficiency of the event selection is determined using simulated $W\gamma\gamma$ events. The signal process has been simulated using Sherpa and AlpGen, the latter interfaced with Herwig and Jimmy for the simulation of the parton-shower, hadronization and underlying event. The sample simulated with Sherpa was chosen as the nominal sample, since the analysis of the $W\gamma$ process showed that Sherpa provides a better description of the data [88]. The nominal sample is used to derive the central value of the acceptance and efficiency correction. The sample simulated with AlpGen is used to assess the systematic uncertainties on this corrections. The total number of events, N, the cross-section, σ, and the integrated luminosity, $L_{\text{int}} = N/\sigma$, of the two samples is shown in Table 4.1. The cross-section for the comparison of data to theory is provided by VbfNlo [35].

	N	σ [fb]	L_{int} [fb^{-1}]
Sherpa	$350 \cdot 10^3$	162.4	2155.2
AlpGen	$360 \cdot 10^3$	62.59	5751.7

Table 4.1: The total number of events, N, the cross-section, σ, and the integrated luminosity, $L_{\text{int}} = N/\sigma$, of the signal samples.

CHAPTER 5

Object reconstruction

The energy depositions in the detector subsystems are used to reconstruct particle candidates. Ideally, these candidates would have the same kinematic properties as the incident particle depositing the energy. However, due to detector effects and stochastic fluctuations in the particle's energy depositions, this is in general not achievable. In addition, the particle type can only be determined with a probabilistic approach leading to a trade-of between the reconstruction efficiency and the rejection of other particles mimicking their signature.

The reconstruction algorithms are part of the Athena [89] software framework and maintained centrally. This ensures that all results obtained within the ATLAS collaboration use consistent algorithms. Furthermore, the development and performance studies of the algorithms are simplified. This chapter provides details about the algorithms used to reconstruct and identify the particles relevant to this analysis, namely: photons, muons, jets and the missing transverse momentum.

5.1 Photons

The photon reconstruction and identification proceeds in two distinct steps: at first a list of photon candidates is reconstructed. In the second step various identification criteria are applied to these candidates. The advantage is that each analysis can apply identification criteria specific to their needs. In the following the reconstruction and identification of photons will be briefly summarized, while more details can be found in [63, 90, 91].

5.1.1 Photon reconstruction

Photons interact electromagnetically, hence their signature is a collimated energy deposition in the electromagnetic compartment of the calorimeter. Since they do not carry charge, no track that points to the energy deposition is expected. As the inner detector of ATLAS has a large material budget (cf. Section 3.2), about 40 % of all photons undergo a conversion into an electron-positron pair (*converted photons*) before they reach the calorimeter. Typically, the opening angle between the electron and the positron is so small that they cannot be reconstructed separately. Using the above signature would therefore exclude a large fraction of photons from being reconstructed because the electron-positron pair might leave a track pointing to the energy deposition in the calorimeter. In order to recover converted photons, energy deposition in the electromagnetic calorimeter which have an associated track originating from a vertex within the volume of the tracker are also considered as photon candidates.

The photon signature is reconstructed in three steps: at first the energy deposition in the calorimeter is reconstructed using a clustering algorithm. Then tracks from vertices within the tracker volume are reconstructed [63]. At last the tracks are associated to the clusters. After the discussion of these three steps in the following sections, the performance of the reconstruction chain will be presented.

Cluster reconstruction

Photons deposit their energy in many calorimeter cells. The combination cells such that their energy reflects that of the incident photon is done by clustering algorithms. ATLAS uses the *sliding window* clustering algorithm [92] to reconstruct photon candidates.It consists of two steps:

- **Tower building:** the electromagnetic calorimeter is divided into a grid of 51 200 towers of size 0.025×0.025 in η-ϕ space. The tower energy is defined as the sum of the energy in all cells inside the tower. If a cell spans multiple towers its energy is divided among the towers according to their fractional area.
- **Seed Finding:** a window of 3×5 towers is moved across each tower in the η-ϕ grid. If the sum of the transverse energies of all towers in the window is a local maximum above 2.5 GeV a cluster is formed. The η and ϕ position of the cluster is calculated as the energy-weighted barycenter of all cells contained in the inner 3×3 towers to be less sensitive to noise. After all cluster have been formed duplicate cluster are removed: if two clusters are closer to each other than 0.05×0.05 in η-ϕ only the cluster with the larger transverse energy is kept.

Conversion vertex reconstruction

If the photon undergoes a conversion into an electron-positron pair inside the tracker, the location of the conversion can be reconstructed by the intersection of the electron and positron track. The reconstruction of conversion vertices therefore starts by selecting pairs of tracks with opposite sign and a small opening angle in ϕ. The tracks considered need to have a minimum transverse momentum of $p_{\mathrm{T}} > 0.5\,\mathrm{GeV}$ and the transverse and longitudinal impact parameters must be compatible with the primary vertex of the event. In addition, electron-like tracks are selected by requiring a large ratio of high-threshold TRT hits. The combinatorial background for two track pairs is further reduced by requiring that the minimal distance between both tracks is small. The track pairs remaining after this selections are used in a vertex fit with the additional constraint that both tracks should have the same initial azimuthal and polar angle, which reflects that the photon is a mass-less particle. The goodness-of-fit of this vertex fit allows to further reduce the background from track pairs not originating from a photon conversion vertex. All vertices passing the goodness-of-fit selection are called *double-track conversion vertices* and are stored for later cluster matching.

A further complication arises since a significant number of converted photons leave only one track in the inner detector. This can happen either because the electron-positron pair has an asymmetric momentum distribution rendering one of the two tracks as unreconstructable, or because the conversion happens so late that the individual tracks cannot be resolved. In order to recover these *single-track conversions* tracks that are not assigned to a double-track conversion vertex are selected if they do not have a hit in the pixel vertexing layer and the ratio of high-threshold TRT hits is high. The position of the single track conversion vertex is set to the innermost energy deposition associated with the track. The importance of considering single-track conversions is shown in Figure 5.1. It shows the reconstruction efficiency for converted photons with $p_{\mathrm{T}} > 20\,\mathrm{GeV}$ as function of the pseudo-rapidity obtained from simulated events. The single-track conversions contribute between 20 % and 40 % to the total reconstruction efficiency rendering them very important for the reconstruction of converted photons.

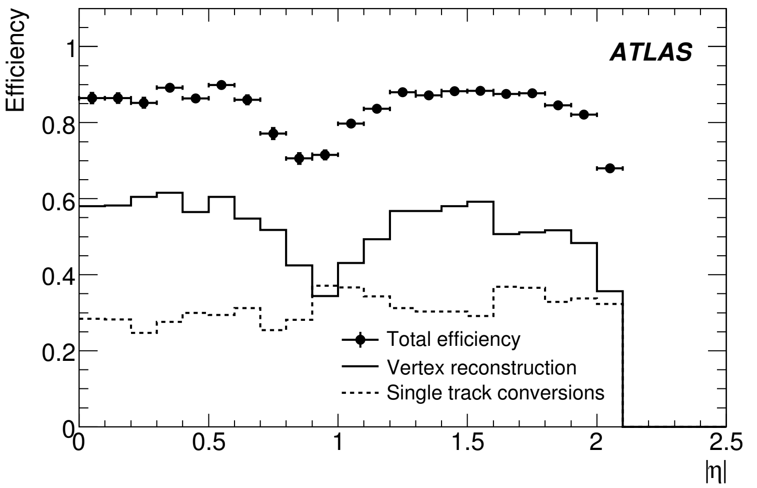

Figure 5.1: Reconstruction efficiency for converted photons with $p_T > 20\,\mathrm{GeV}$ as function of the pseudo-rapidity. In addition to the total efficiency, the contribution from single-track conversions and double-track conversions (denoted "Vertex reconstruction") is shown. From [63].

Photon classification

Clusters that do not have an associated track either from the primary tracking or from a conversion vertex are considered as *unconverted photon candidates*. In order to resolve the ambiguity between electrons and converted photons, further steps are necessary. If the cluster is matched to a conversion vertex it is generally considered as a *converted photon candidate*, otherwise it is considered as an electron candidate[1].

The association between calorimeter clusters and conversion vertices is based on the distance in η-ϕ space. Therefore the tracks from the conversion are extrapolated from their last hit to the second sampling of the electromagnetic calorimeter. The vertex is called matched if the extrapolated track is closer than 0.05 in η-ϕ to the cluster position. The window is extended to 0.1 in ϕ on the side of the cluster where bremsstrahlung losses are expected due to the bending of the track in the magnetic field. Double-track conversion vertices where one of the tracks has a momentum, which is smaller by at least a factor of four, are handled differently: a straight-line extrapolation from the conversion vertex position with the track direction obtained from the vertex fit is used to determine the impact point in the calorimeter and the same matching windows as above is used.

At this stage so-called *cleaning cuts* are applied to all photon candidates. Their purpose is to remove photon candidates from non-collision energy depositions, e.g. cells with sporadic noise bursts which produce a signal larger than 2.5 GeV and thus giving rise to a photon cluster. These clusters are removed if more than 98 % of the cluster energy are deposited in the second layer of the electromagnetic calorimeter, or more than 90 % for any other layer.

Photon calibration

The energy measurement of the photons is calibrated using simulated events. The simulation has been validated and improved by performing a series of measurements with the calorimeter and the tracker [93, 94] with test beams. The energy determination comprises three different contributions each calibrated separately: the energy deposited in front of the calorimeter and in the presampler E_{front}, the energy in the electromagnetic calorimeter E_{cal} and the energy that leaked into the hadronic calorimeters E_{back}. Each of these contributions is parametrized as function of the energy deposited, the position inside the detector, and the particle type (i.e. converted or unconverted photon). For example, E_{front} is given as a

---

[1] Some exceptions exists, full details can be found in [90].

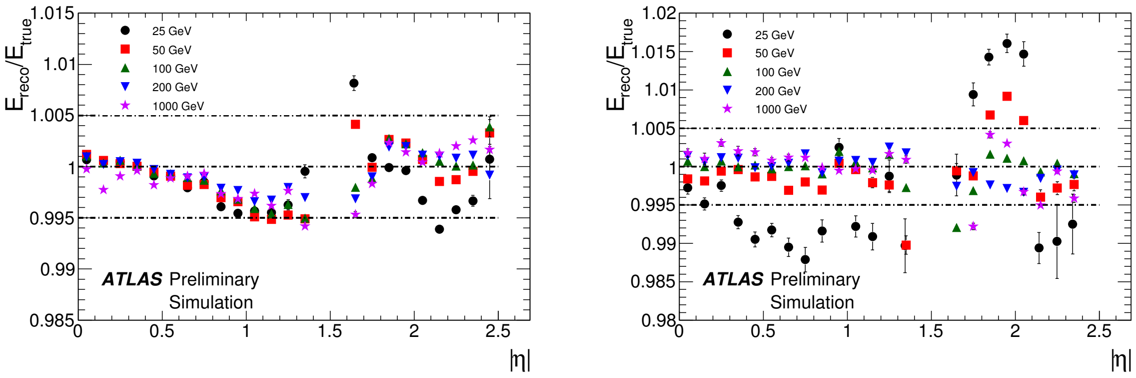

(a)

(b)

Figure 5.2: Expected ratio of reconstructed to true energy for unconverted (a) and converted (b) photons from simulated events as function of the pseudo-rapidity and photon p_{T} after the energy calibration has been applied. Figure from [95].

second order polynomial in the energy deposited in the presampler E_{ps}, where the coefficients have been parametrized as a function of the deposited energy in the calorimeter, E_{cal}, and the pseudo-rapidity, η,

$$E_{\mathrm{front}} = a\,(E_{\mathrm{cal}}, \eta) + b\,(E_{\mathrm{cal}}, \eta)\,E_{\mathrm{ps}} + c\,(E_{\mathrm{cal}}, \eta)\,E_{\mathrm{ps}}^{2}\,. \tag{5.1}$$

The sum of all three contributions, E_{front}, E_{cal} and E_{back} yields the total cluster energy. The ratio between the reconstructed and the true particle energy is shown in Figure 5.2 for unconverted (a) and converted (b) photons as a function of the pseudo-rapidity and photon p_{T}. The deviation from zero is within $\pm 1\,\%$ for most of the simulated samples. Only in the region $1.7 < |\eta| < 2.2$ for low photon transverse momenta, the difference from zero reaches up to $1.5\,\%$ for converted photons.

Performance of the photon reconstruction

The performance of the photon reconstruction has been determined using a simulated $H \to \gamma\gamma$ decays. Only photons with $p_{\mathrm{T}} > 20\,\mathrm{GeV}$ and within $|\eta| < 2.37$ are considered for this study. The overall reconstruction efficiency, defined as the ratio of the number of reconstructed to true photons, is found to be $(97.82 \pm 0.03)\,\%$. Photons, which fall into the transition region between the barrel and end-cap cryostat ($1.37 < |\eta| < 1.52$) are not considered in the calculation. The reconstruction efficiency for unconverted photons amounts to $(99.83 \pm 0.01)\,\%$ and is slightly higher than for converted photons, where it is $(94.33 \pm 0.09)\,\%$. The photon reconstruction efficiency as function of the transverse momentum and pseudo-rapidity of the true, simulated photon is shown in Figure 5.3 for unconverted and converted photons as well as the combination of both types. The efficiency is almost flat in p_{T} and the structure in η reflects the material budget in front of the calorimeters.

5.1.2 Photon identification

After the photon reconstruction step only a small percentage of photon candidates stems from prompt photons. Most photon candidates originate from neutral hadron decays (e.g. $\pi^0 \to \gamma\gamma$) due to the abundance of hadrons at a pp-collider. In addition, a small fraction of the photon candidates stems from narrow jets of charged hadrons. These *fake photons* need to be distinguished from prompt photons in order to properly select the $W\gamma\gamma$ process. In ATLAS, this separation is achieved using selections on

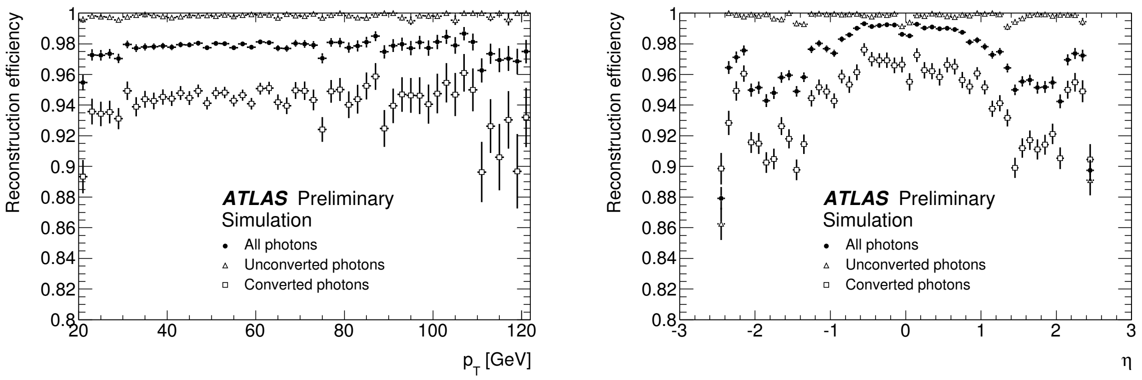

(a)

(b)

Figure 5.3: Photon reconstruction efficiency as function of the transverse momentum (a) and pseudo-rapidity (b) of the true, simulated photon. In addition, the reconstruction efficiency is shown separately for converted- and unconverted photons. The plots are from [90].

variables computed from the energy depositions in the calorimeter. In the following, these variables and three specific selections, namely `LOOSE`, `TIGHT` and `ANTITIGHT`, will be described.

Calorimeteric variables

In total, nine variables are defined to discriminate prompt from fake photons. They can be divided into three different categories:

Hadronic Leakage R_{had} Showers from real photons are contained in the electromagnetic calorimeter, while fake photons are often accompanied by other hadrons penetrating the electromagnetic calorimeter and depositing energy in the hadronic calorimeter. The ratio, R_{had}, of the transverse energy in the first sampling[2] of the hadronic calorimeter to the transverse energy of the photon cluster, thus separates prompt from fake photons. The considered energy in the hadronic compartment is the sum of all cells in a window of 0.24×0.24 in η-ϕ around the cluster center. The separation can be seen in Figure 5.4a showing the normalized distribution of R_{had} for prompt photons and fake photons for reconstructed photon candidates before any selection. As expected, the distribution of R_{had} for photon candidates from prompt photons shows a peak around zero and a negligible tail, while the distribution for fake photon candidates shows a significant tail towards higher values.

Middle layer variables The following variables are calculated using the second longitudinal layer of the electromagnetic calorimeter. They make use of the fact that fake photons are often accompanied by other hadrons and tend to yield broader showers, similarly to the hadronic leakage described above.

- **R_η:** The ratio of energy deposited in the central window of 3×7 cells around the cluster position with respect to the energy deposited in a window of 7×7 cells.
- **R_ϕ:** The ratio of energy deposited in the central window of 3×3 cells around the cluster position with respect to the energy deposited in a window of 3×7 cells.

---

[2] For photon candidates with $0.8 < |\eta| < 1.37$ all layers of the hadronic calorimeter are used.

- **w_2:** The energy weighted lateral width of the shower calculated using the central window of 3×5 around the cluster position. The energy weighted lateral width is defined as

$$w_2 = \sqrt{\frac{\sum_i E_i \left(\eta_i - \eta_{\text{cluster}}\right)^2}{\sum_i E_i}}\,, \tag{5.2}$$

  where E_i and η_i are the energy and pseudo-rapidity of cell i, respectively.

The first variable (R_η) is shown in Figure 5.4b for prompt and fake photons. As expected, the distribution for prompt photons show a sharp peak around 1.0 confirming that the shower is contained in the inner 3×7 cells. The distribution of fake photons shows a large tail towards smaller values confirming that they yield broader showers.

Strip layer variables The first layer of the electromagnetic calorimeter is finely segmented in η (cf. Section 3.2) and therefore can be used to discriminate directly between prompt photons and neutral hadron decays. Fake photons are often found to have two maxima due to e.g. $\pi^0 \to \gamma\gamma$ decays. Therefore the following variables operate on the cell with second highest energy found in a window of η-ϕ = 0.125×0.2 around the cell with the largest energy deposition.

- **ΔE:** The magnitude of the dip between the two maxima is computed as the energy difference between the cell with the minimal energy and the cell with the largest energy. The cell with the smallest energy between the two cells with the largest energy is considered as minimum.
- **E_{ratio}:** The ratio of the energy difference between the cells containing the two highest energies over the sum of the energies. The distribution of E_{ratio} is shown in 5.4c and it shows a clear peak around 1.0 for real photons while the distribution for fake photons show a large tail towards zero.

In addition, three more variables are calculated using the cells around the cell with the highest energy deposition to cover cases where the two photons of the neutral hadron do not create two distinct maxima:

- **w_{s3}:** The energy weighted lateral shower width as defined above, calculated using three cells around the cell with the largest deposited energy.
- **w_{stot}:** The energy weighted later shower width calculated using all cells in the cluster.
- **F_{side}:** The fraction of the energy deposited outside the core of the cluster. The cluster core is defined as the three cells containing the cell with the largest energy deposition.

Photon selections

Using these *discriminating variables* two different selections are defined , one high-efficiency selection (`LOOSE`) and one high-purity selection (`TIGHT`). Both will be briefly introduced in the following. In addition, a special selection (`ANTITIGHT`) will be presented. The detailed selection criteria used for each of these selections are given in [90].

The `LOOSE` selection

The `LOOSE` selection is based on the variables defined in the middle layer of the electromagnetic calorimeter (R_η, R_ϕ and w_2) and the hadronic leakage (R_{had}). The values have been optimized using simulations. To account for differences in the showers shapes due to differences in the material in front of the

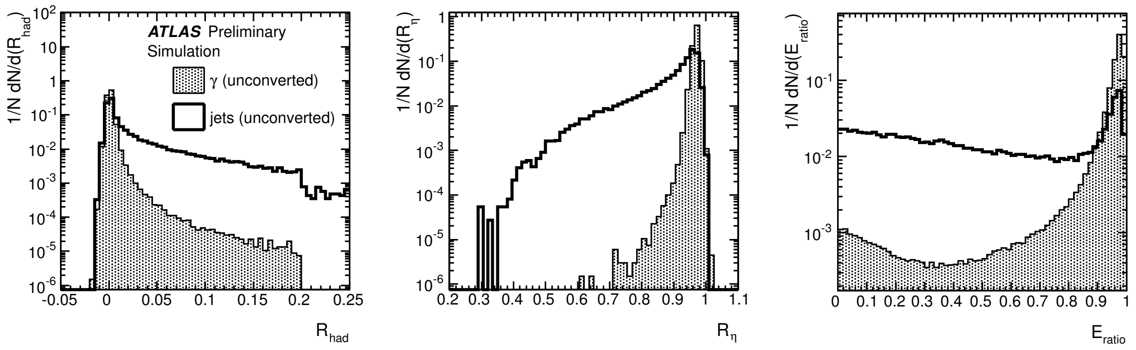

(a) (b) (c)

Figure 5.4: Distribution of calorimeteric variables used to discriminate between prompt (labelled γ) and fake photons (labelled jets): (a) the distribution of R_{had}, (b) the distribution of R_η and (c) the distribution of E_{ratio}. From [90].

calorimeter, the optimization is done nine different $|\eta|$ regions. In addition, the selections are optimized separately for converted and unconverted photons. The `LOOSE` selection provides an excellent efficiency and moderate fake photon rejection. In the analysis presented in this work it is mainly used for the preselection to reduce the amount of data that needs to be considered.

The `TIGHT` selection

The `TIGHT` selection is optimized to suppress the fake photons from jets containing high-energetic isolated π^0. It uses tighter selections on the variables used by the `LOOSE` selection and additionally includes the variables defined in the strip-layer (ΔE, E_{ratio}, w_{s3}, w_{stot} and F_{side}). The selection criteria are separately optimized for seven $|\eta|$ regions and for converted and unconverted photon candidates. For example, this takes into account the larger shower width in ϕ since the electron-positron pair is bent in different directions by the solenoidal magnetic field. The `TIGHT` selection is used throughout this work to identify photons from the $W\gamma\gamma$ process.

The `ANTITIGHT` selection

The `ANTITIGHT` selection is special compared to the `LOOSE` and `TIGHT` selections. Its purpose is to select fake photons without biasing their properties, in particular the isolation described later, which will be important to estimate the number of fake photons passing the `TIGHT` selection (cf. Section 7.1). This is achieved by requiring that the photon candidates pass all selections imposed on `TIGHT` photon candidates except that they have to fail at least one of the selections on F_{side}, w_{s3}, ΔE and E_{ratio}. The reason for inverting these variables is that they only operate on the inner strip cells which are excluded from the isolation calculation. Therefore to first order the isolation is independent from these variables. In addition to the nominal `ANTITIGHT` selection, which inverts four selections, two similar definitions are used for the study of systematic uncertainties later. The first one only inverts three selections, namely F_{side}, w_{s3} and E_{ratio}, and is therefore denoted as L_3'. The second definition inverts the selection on all five strip variables and is denoted as L_5'.

5.1.3 Photon isolation energy

Beside the photon identification criteria mentioned above another possibility of separating prompt from fake photons is the so-called *photon isolation*. The photon isolation does not operate on the shower properties of the photon candidate, but makes use of the event topology instead. The photon isolation energy of a photon candidate, $E_{\mathrm{T}}^{\mathrm{iso}}$, is calculated as the sum of the transverse energies of *topological clusters* [92] within a cone of $\Delta R < 0.4$ around the cluster center.

In contrast to the sliding window clustering described above, the topological clustering groups neighbouring calorimeter cells which have a significant energy deposition compared to their expected noise. At first the cells are categorized by significance of their energy deposition $|E|/\sigma$, where E is the energy deposited in the cell and σ is the expected noise. The clustering starts with cells having $|E|/\sigma > 4$, then all neighbouring cells, lateral and longitudinal, with $|E|/\sigma > 2$ are added to the cluster. If no more neighbouring cell exceeding $|E|/\sigma > 2$ can be found, cells with $|E|/\sigma > 0$ are added. In a last step the cluster is split into sub-clusters according to local energy maxima. Each local energy maximum above 500 MeV is used as seed for a new iteration of the topological clustering algorithm. The splitting step improves the assignment of clusters to incident particles. The cluster energy is determined by the sum of the energy of all cells contained in the cluster, and its direction is given by the energy weighted barycenter of the calorimeter cells.

All topological clusters within a cone of $\Delta R < 0.4$ around the cluster center are considered for the photon isolation energy and the energy of the photon itself is removed. This is done by subtracting the energy deposited in the central 5×7 (in η-ϕ) cells around the photon barycenter. At this stage the photon isolation energy shows a small dependence on the p_{T} of the photon due to lateral leakage of the photon energy outside the central core. This is corrected by measuring the leakage as function of the photon p_{T} using simulated samples and removing it from the isolation energy.

Energy depositions from particles from the underlying event or pile-up may spoil the isolation energy for real photons. Therefore the isolation energy is corrected for these effects using the *ambient energy correction* [96], which is based on an *in-situ* measurement of the *ambient transverse energy density* from underlying event and pile-up. It is computed from jets formed by a k_{t} jet-finding [97, 98] algorithm using topological clusters as input and without an explicit requirement on the jet transverse momentum. Each jet is assigned an area such that every point inside the jet area is closer to the axis of the current jet than to any other jet (Voroni tessellation). Then the ambient transverse energy density is taken as the median of the transverse energy density of the jets computed as the ratio between the energy of the jet and their area. Finally, the ambient transverse energy inside the photon isolation cone is calculated by multiplying the area of the cone with the ambient transverse energy density and subtracted from the photon isolation energy.

5.1.4 Corrections applied to the simulation

It is important that the ATLAS detector simulation models the distribution of the identification variables well. Comparisons of the identification variables in data and simulation show that some differences exists. These are corrected with the χ^2 method which is described in [99]. A short overview is given here.

The discrepancy between data and simulation is resolved by shifting the distribution in simulation by a fixed amount, such that the agreement between data and simulation is maximized. Since the distribution of the discriminating variables varies with the transverse momentum and the pseudo-rapidity of the photon the shifts are derived in bins of p_{T} and $|\eta|$. The simplest approach is to choose the value of the shift such, that the mean of the distribution agrees, $\Delta\mu = \langle \mathrm{data} \rangle - \langle \mathrm{MC} \rangle$. However, the mean of a variable is very sensitive to the tails of the distribution and so is the correction, $\Delta\mu$. Therefore the optimal shift is determined such that it minimizes the value of a χ^2 test between the distributions. The value of χ^2 test between two histograms, H_{data} and H_{MC}, is defined as

$$\chi^2 = \sum_b \frac{(H^b_{\text{data}} - H^b_{\text{MC}})}{\sqrt{\sigma^2_{\text{data},b} + \sigma^2_{\text{MC},b}}}\,, \tag{5.3}$$

where H^b is the value of bin b of the histogram H and σ_b is the corresponding uncertainty. The optimal correction, $\Delta\mu$, is obtained as the value which minimizes χ^2 and is applied to the simulation.

5.1.5 Performance of the photon identification for isolated photons

The photon identification efficiency for isolated photons has been measured in data using three different methods [91]. In the following, one of the methods and the results will be briefly summarized.

The photon identification efficiency is determined using events with a very small fake-photon contamination selected from radiative decays of the Z boson, i.e. $Z \to ll\gamma$. The selection of the photon candidates is not based on the variables used for identifying photons described above, but on kinematic quantities characterizing the three final state particles. Thus the selection allows for an unbiased estimate of the photon identification efficiency.

Events are selected by requiring two isolated light leptons[3] with opposite electric charge and an isolated photon candidate with $E_{\text{T}}^{\text{iso}} < 5\,\text{GeV}$. In radiative Z decays the photon is radiated from one of the leptons. Since the photon is carrying away momentum, the di-lepton invariant mass is required to be in a window $40\,\text{GeV} < m_{ll} < 83\,\text{GeV}$ below the mass of the Z boson, and the three-body invariant mass must lie within $80\,\text{GeV} < m_{ll\gamma} < 96\,\text{GeV}$ around the Z mass. A bias on the identification variables of the photon from overlapping showers in the calorimeter is avoided by requiring a minimal distance of $\Delta R > 0.2$ (0.4) between the photon and the muons (electrons). The purity of the photon candidates after applying all selection criteria is estimated in data. It is found to be $(98.3 \pm 0.2)\,\%$ in the muon- and $(97.4 \pm 0.2)\,\%$ int the electron channel [91].

The identification efficiency ϵ_{ID} is defined as the fraction of photon candidates identified as `TIGHT` among all photons. The weighted mean of the data-driven photon identification efficiency measurements together with the simulation is shown in Figure 5.5 for unconverted photon candidates as function of E_{T} in four different η regions. In all η regions an overall increase of the efficiency with E_{T} is observed. The difference between data and simulation is larger for larger η, but mostly below 5 % excluding the region $|\eta| > 1.81$ where the simulation overestimates the efficiency by up to 8 %. New measurements of the photon identification efficiency using the dataset recorded in 2012 show that the agreement is improved to be within 2.5 % [100]. The remaining difference is taken as a systematic uncertainty.

5.2 Muons

Muons traverse the ATLAS calorimeter without significant energy loss but deposit energy in the inner detector and the muon spectrometer. The reconstruction of muons is thus based on tracks reconstructed in these sub-detectors, which are combined to build the muon candidate. For this analysis, the tracks in the muon spectrometer are reconstructed using the MuonBoy [101] algorithm, and the combination with tracks from the inner detector is based on the *sta*tistical *co*mbination (STACO [102]) algorithm.

Track reconstruction in the muon spectrometer starts from a *region of activity* (ROA) identified by the trigger system. Its size is roughly 0.4×0.4 in η-ϕ. All muon chambers overlapping with ROAs are considered for the reconstruction of straight track segments connecting hits in two adjacent MDT

---

[3] Light lepton only refers to electron and muons, due to experimental difficulties that arise in the reconstruction of τ leptons.

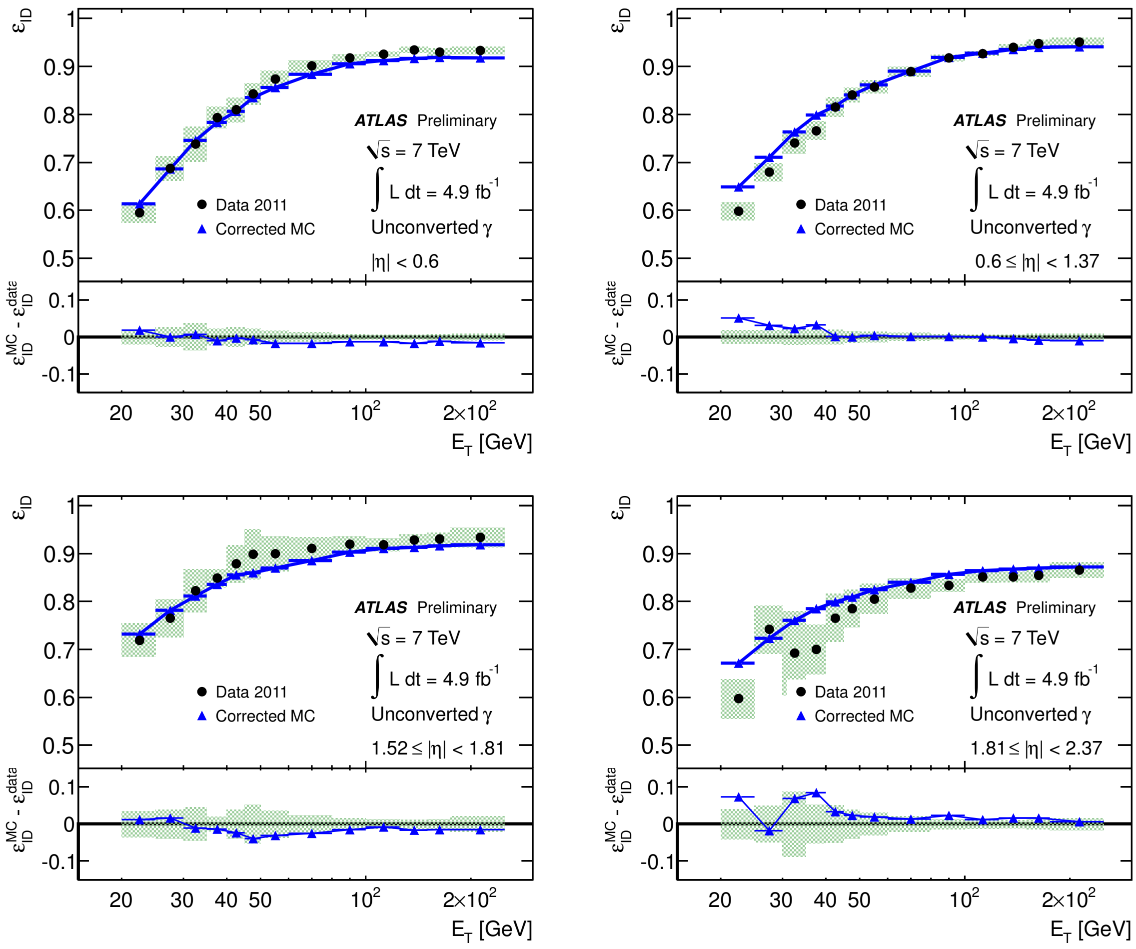

Figure 5.5: The photon identification efficiency obtained from data and simulation in different rapidity regions. The green band corresponds to the uncertainty of the measurement in data containing statistical and systematic sources. For the simulation only statistical uncertainties are shown. From [91].

multi-layers. The close proximity of the hits and the reduced complexity legitimates the use of straight tracks. In order to reject the contribution of track segments induced by noise the segments have to point to the interaction point. The next step is to combine the track segments to a muon track taking into account the influence of magnetic field on the muon. The track parameters are then determined by a fit to the individual hits comprising the segments used to define the track. This two step procedure, finding a track by combining straight track segments and measuring its parameters using the individual hits, makes use of the full available information and at the same time reduces the computational complexity required for a standard track reconstruction over the large distances covered by the muon system.

The combination of tracks from the inner detector (ID) and the muon spectrometer (MS) yields a *combined muon candidate*. Instead of refitting the hits of both tracks, the STACO algorithm treats both tracks as independent measurements of the same muon and combines their results statistically. The algorithm starts by making pairs of ID- and MS-tracks based on a loose matching in η-ϕ. For each of these pairs the track parameters are the sum of the ID- and MS-track parameters weighted by their respective uncertainty:

$$P = \left(C_{\mathrm{ID}}^{-1} + C_{\mathrm{MS}}^{-1}\right)^{-1} \cdot \left(C_{\mathrm{ID}}^{-1} \cdot P_{\mathrm{ID}} + C_{\mathrm{MS}}^{-1} \cdot P_{\mathrm{MS}}\right) .$$

Here, P is the parameter vector for the combined track, P_{ID} (P_{MS}) is the parameter vector of the ID (MS) track with the covariance matrices C_{ID} (C_{MS}). This definition ensures that each sub-detector is used in the momentum regime it performs best, i.e. for $p_{\mathrm{T}} < 80\,\mathrm{GeV}$ ($p_{\mathrm{T}} < 20\,\mathrm{GeV}$ in the endcap) the ID dominates the measurement, while for $p_{\mathrm{T}} \gtrsim 100\,\mathrm{GeV}$ the MS dominates [103]. The quality of the combination is determined by the quadratic difference of the initial track parameters to the combined track parameter weighted by their respective uncertainty:

$$\chi^2 = (P - P_{\mathrm{ID}})^T \cdot C_{\mathrm{ID}}^{-1} \cdot (P - P_{\mathrm{ID}}) = (P - P_{\mathrm{MS}})^T \cdot C_{\mathrm{MS}}^{-1} \cdot (P - P_{\mathrm{MS}}) .$$

The match is accepted if the χ^2 value is below 30. In case multiple combinations are possible the one with the lowest χ^2 value is chosen. A few additional quality criteria are applied to the inner detector track to take into account the status of the Pixel- and SCT system in the inner detector; for completeness they are summarized in appendix A.1.

Besides combined muon candidates another type of muon is reconstructed by the STACO algorithm. These *segment tagged* muons are reconstructed from the combination of an inner detector track to a track segment. Using a track segment instead of a full muon spectrometer track improves the reconstruction efficiency for muons in poorly instrumented detector regions or at low transverse momenta [103].

5.2.1 Performance of the muon reconstruction

The performance of the muon reconstruction has been measured in data [104]. In the following the method and the results will be briefly summarized.

The determination of a reconstruction efficiency is based on a sample of events with prompt muons. The selection of these events must provide a high-purity of real muons on the one hand and, on the other hand, must not use the tested reconstruction algorithm in order to obtain an unbiased measurement. The *tag-and-probe* method provides one way of such a selection. For this method, $Z \to \mu^+\mu^-$ decays are selected by requiring two oppositely charged muon candidates whose di-muon invariant mass is close to that of the Z boson. One of the muons, the so-called *tag*, is required to be a *combined* muon, i.e. a muon where the combination of ID- and MS- tracks was successful. The other muon, denoted *probe*, is selected using only information from the inner detector (muon spectrometer) if the efficiency of the MS-(ID-)track reconstruction is to be measured. The efficiency of reconstructing an MS-track, ϵ_{MS}, can then be defined as the ratio of probe muons with a reconstructed track to all probe muons:

$$\epsilon_{\mathrm{MS}} = \frac{\text{number of probe muons with reconstructed MS track}}{\text{number of probe muons}} .$$

The efficiency of the track reconstruction for the inner detector, ϵ_{ID}, is defined similarly.

The muon reconstruction consist of three distinct steps, the ID-track reconstruction, the MS-track reconstruction and the matching between ID- and MS-tracks. The total efficiency is obtained by multiplying the efficiencies of these individual steps. The resulting muon reconstruction efficiency is shown as a function of p_{T} and η in Figure 5.6. It does not depend on p_{T}, but varies with η. The efficiency drop observed at $|\eta| \sim 0$ and $|\eta| \sim 1.2$ corresponds to poorly instrumented regions of the muon system. The agreement between data and simulation is within 2 % except the transition region between barrel and endcap $1.1 \leq |\eta| \leq 1.3$ where it is within 3 %. The simulation is corrected for the observed differences as explained below.

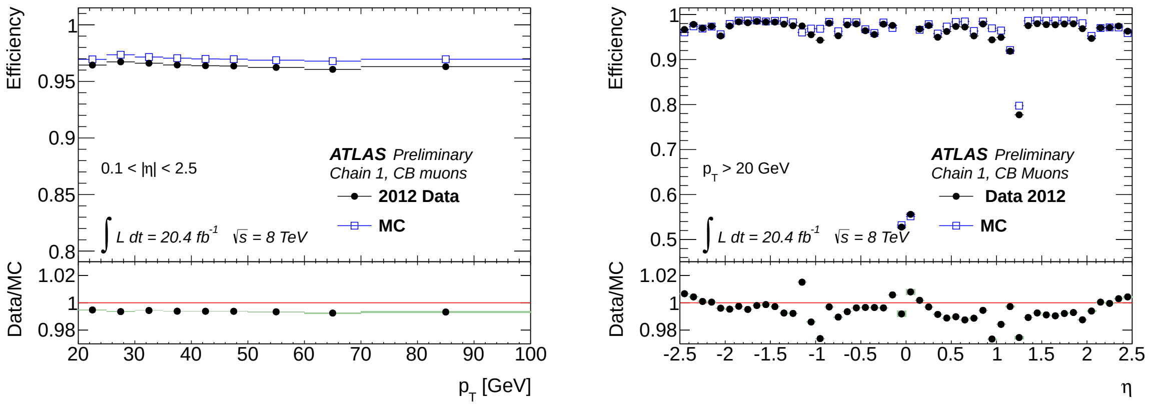

(a) (b)

Figure 5.6: Reconstruction efficiency for combined muons as a function of p_{T} (a) and η (b). Shown is the reconstruction efficiency from data and simulation. From [104].

5.2.2 Corrections to the simulation

The simulation describes the data on the level of a few percent. However the remaining differences would bias the estimation of the acceptance and efficiency for the $W\gamma\gamma$ process (cf. Chapter 8). Therefore the difference between the reconstruction efficiency measured in data and simulation shown in Figure 5.6 is corrected for by reweighting the distribution from simulation to match the one in data. In addition, the muon momentum scale and resolution have been measured using the Z pole in $Z \to \mu\mu$ events in data and simulation. Figure 5.7a shows the di-muon invariant mass distribution for isolated combined muons with $p_{\mathrm{T}} > 25\,\mathrm{GeV}$ measured in data and in the uncorrected simulation. The invariant mass spectrum in simulation is slightly shifted towards larger masses and the width is smaller than the one measured in data. The shift is treated by applying a scale correction to the momentum of the muons from the simulation, and the resolution is worsened by smearing the momentum measurement such that it matches the one in data. The effect of the corrections can be seen in Figure 5.7b, which shows the di-muon invariant mass for data and the corrected simulation. A clear improvement, especially in the ratio of data to simulation, can been seen in the region around the Z pole.

5.3 Jets

Quarks and gluons can not be observed directly, since they fragment and hadronize almost directly after being produced. This leads to a collimated spray of hadrons, called a jet. Jets are defined using a *jet definition* which gives a prescription on how to group particles into jets (the *jet algorithm*) and how to assign a four-momentum to the jet (the *recombination scheme*). Jet definitions can normally be applied to experimental measurements (e.g. calorimeter clusters or tracks) as well as the output of parton-shower simulation and partonic calculations [105].

5.3.1 Jet definition

The jet algorithm used to define jets in this analysis is the anti-k_{t} algorithm [106] implemented in the ATHENA framework using the FASTJET [107, 108] software package. Since the anti-k_{t} algorithm is both

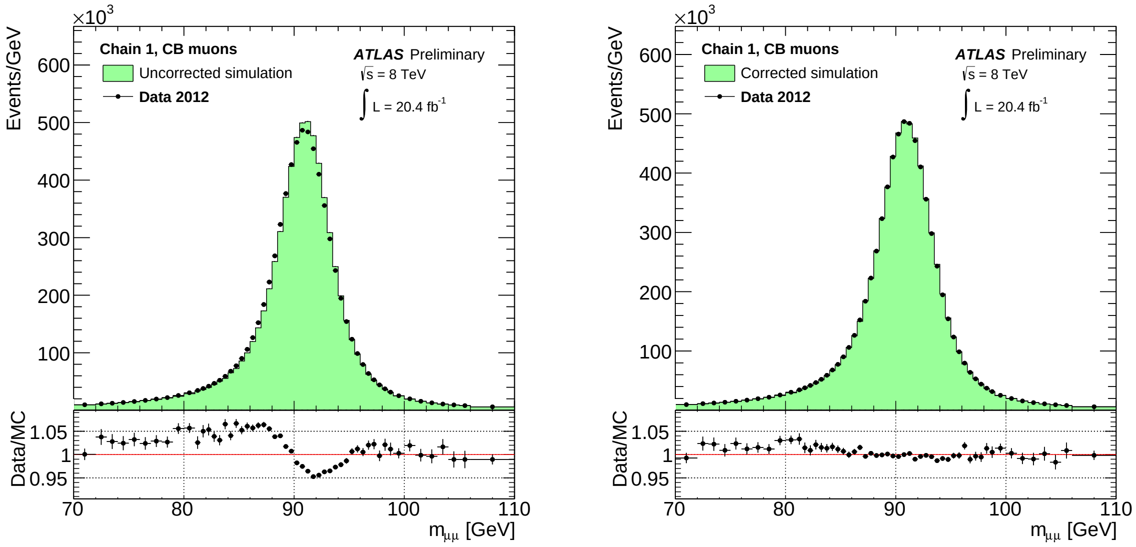

(a)

(b)

Figure 5.7: Di-muon invariant mass for isolated muons with $p_{\mathrm{T}} > 25\,\mathrm{GeV}$ for 2012 data and uncorrected (a) and corrected (b) simulation. The lower panel shows the ratio between data and simulation. From [104].

collinear (i.e. the collinear splitting of a particle leads to the same jets) and infrared safe (i.e. the emission of soft gluons leads to the same jets) it is the standard jet algorithm used in ATLAS and CMS.

The anti-k_{t} algorithm is a *sequential recombination algorithm*, meaning the jet is build by repeatedly combining the closest pairs of objects until a stop condition is met. The combination of two objects reduces the total number of objects by one. The measure of the distance d_{ij} between two objects i and j is defined as:

$$d_{ij} = \min\left(p_{\mathrm{T},i}^{-2}, p_{\mathrm{T},j}^{-2}\right) \frac{\Delta R_{i,j}^2}{R^2}\,, \tag{5.4}$$

where $p_{\mathrm{T},i}$ denotes the transverse momentum of object i, R is the distance parameter and $\Delta R_{i,j}$ is given by $\Delta R_{i,j}^2 = \left(y_i - y_j\right)^2 + \left(\phi_i - \phi_j\right)^2$. The recombination starts from the pair with the smallest distance d_{ij} and is repeated until the smallest distance is larger than $d_{iB} = p_{\mathrm{T},i}^{-2}$ in which case the object i is declared as jet. Two objects are combined by adding their four vectors, thus the four-momentum of the jet is defined as the sum of the four-momenta of all the objects that have been combined to form the jet. As soon as all objects have been declared as jets the algorithm stops.

Because of the negative exponents in $\min\left(p_{\mathrm{T},i}^{-2}, p_{\mathrm{T},j}^{-2}\right)$ and the weighting factor $\frac{\Delta R_{i,j}^2}{R^2}$, the anti-$k_{\mathrm{t}}$ algorithm starts by combining close-by, large transverse momentum objects, i.e. the jet grows outwards around hard "seeds" [105]. The resulting jet is almost circular in $y - \phi$ space [106] and thus overcomes the experimental problems the other algorithm of the sequential recombination family (e.g. k_{t} [98] or C/A [109]) face due to their irregular shape.

The jets used in this analysis were reconstructed with a distance parameter $R = 0.4$ using topological clusters built from calorimeter cells as input (cf. 5.1).

Jet calibration

The largest challenge of jet measurements is the determination of the *jet energy scale* (JES) calibration and its uncertainty. The JES correction brings the energy measured in the calorimeter to the energy of the particles forming the jet. The following section will shortly introduce how the JES corrections was performed in ATLAS. More details can be found in [110], which presents the JES measurement for the data collected in 2011 with $\sqrt{s} = 7\,\text{TeV}$. The procedure for the data used in this analysis is identical.

The JES correction is necessary since the topo-clusters used as input to the jet algorithm are calibrated at the *electromagnetic scale* (EM), i.e. the energy measurement of particles interacting electromagnetically with the material in the calorimeter is correct. Due to the non-compensating nature of the ATLAS calorimeter, the response to hadronic interactions is lower and has to be corrected. In addition, further corrections are necessary to account for energy deposited in non-instrumented regions of the calorimeter or particles that are not stopped in the calorimeters or particles that deposit their energy outside of the jet.

The calibration procedure is based on correction factors derived from Monte Carlo simulation. These correction factors are derived by comparing the energy of reconstructed jets to the true jet energy[4] in bins of E^{jet} and η^{jet}. Afterwards, the remaining differences between data and simulation are assessed by measuring *in-situ* the double-ratio

$$\mathfrak{R} = \frac{\left\langle p_{\text{T}}^{\text{jet}} / p_{\text{T}}^{\text{ref}} \right\rangle_{\text{data}}}{\left\langle p_{\text{T}}^{\text{jet}} / p_{\text{T}}^{\text{ref}} \right\rangle_{\text{MC}}} \tag{5.5}$$

exploiting the transverse momentum balance between a jet ($p_{\text{T}}^{\text{jet}}$) and a reference object ($p_{\text{T}}^{\text{ref}}$). The overall correction applied to the jets in data is obtained by a weighted average of the results of various *in-situ* techniques. The weights are proportional to the inverse of the squared uncertainties of these measurements.

The *in-situ* measurements include for example the *di-jet balance* used to achieve an uniform response over the full η-range of the ATLAS detector. In this case the reference object is a central jet (i.e. $|\eta| < 0.8$) while the probe jet must be non-central. Another example of such a measurement is the Z–jet measurement, which provides the overall energy scale. In this case the reference object is the Z boson balanced by a recoiling probe-jet.

The uncertainty of the JES correction is determined by adding the uncertainty of the absolute calibration and the *in-situ* measurements in quadrature. The resulting fractional uncertainty as a function of $p_{\text{T}}^{\text{jet}}$ is shown for two values of η in Figure 5.8. It is as low as $1\,\%$ for central jets in the range $55\,\text{GeV} < p_{\text{T}}^{\text{jet}} < 500\,\text{GeV}$ and goes up to $6\,\%$ for forward low p_{T} jets ($p_{\text{T}}^{\text{jet}} \simeq 25\,\text{GeV}$, $|\eta| \simeq 4.0$). For jets above 1 TeV, the uncertainty increases since the statistical uncertainty of the *in-situ* measurements is too high to give reliable results.

The calibration scheme outlined above achieves an average response close to unity for jets that are well separated from other jets. However, the calorimeter response of jets changes if jets are nearby. In addition, the jet response depends on the flavor of the initial parton due to changes in the parton shower and fragmentation. The total uncertainty is almost doubled for low p_{T} jets from semileptonic $t\bar{t}$ decays, but is negligible for transverse momenta greater than 200 GeV.

---

[4] The energy of jets is built from stable simulated particles. In general particles with a lifetime of $c\tau > 10\,\text{mm}$ are considered stable. To ensure the calibration to the *visible energy* in the detector, muons and neutrinos are excluded from the particles used to build the jet.

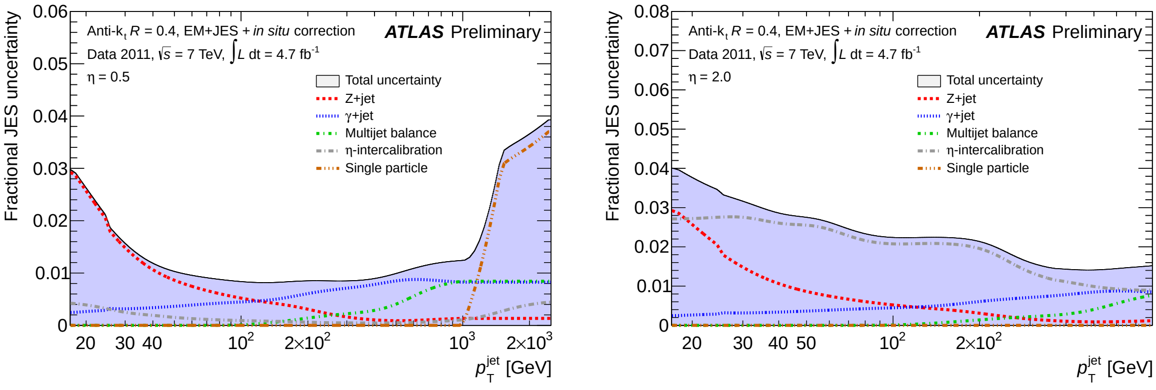

(a) (b)

Figure 5.8: The fractional jet energy scale uncertainty as a function of $p_\mathrm{T}^\mathrm{jet}$ for $\eta = 0.5$ (a) and $\eta = 2.0$ (b). From [110].

5.4 Missing transverse momentum

The presence of weakly interacting particles (e.g. neutrinos from leptonic decays of W bosons) in the final state of the hard-scatter gives rise to a momentum imbalance.The missing transverse momentum is defined as the momentum imbalance in the transverse plane, i.e. the plane transverse to the beam axis. In contrast to e^+e^- colliders only the momentum in the transverse plane is well defined for pp colliders due to the unknown momentum fraction of the proton the partons involved in the interaction carry. The vectorial momentum imbalance is determined by the negative vector sum of the momenta of all particles detected in a collision. The missing transverse momentum vector (comprising only an x- and y-coordinate) is denoted as $\boldsymbol{E}_\mathrm{T}^\mathrm{miss}$ with magnitude $E_\mathrm{T}^\mathrm{miss}$ and azimuthal angle ϕ^miss. The details of reconstruction and performance of the missing transverse momentum in ATLAS is described in [111].

The missing transverse momentum reconstruction is based on reconstructed and calibrated particles. It is calculated as the sum of several $E_\mathrm{T}^\mathrm{miss}$ components, $\boldsymbol{E}_{\mathrm{T},i}$, each calculated considering only particles of a specific type, i. The total transverse momentum imbalance can be written as

$$\boldsymbol{E}_\mathrm{T}^\mathrm{miss} = \boldsymbol{E}_{\mathrm{T},e}^\mathrm{miss} + \boldsymbol{E}_{\mathrm{T},\gamma}^\mathrm{miss} + \boldsymbol{E}_{\mathrm{T},\tau}^\mathrm{miss} + \boldsymbol{E}_{\mathrm{T},\mu}^\mathrm{miss} + \boldsymbol{E}_{\mathrm{T,jet}}^\mathrm{miss} + \boldsymbol{E}_{\mathrm{T,soft}}^\mathrm{miss}\,. \tag{5.6}$$

The particles must be above a certain transverse momentum threshold in order to be considered for the calculation. This ensures that the particles are only used in a p_T regime, where their calibration is available, e.g. $p_\mathrm{T} > 20\,\mathrm{GeV}$ for jets. Since neglecting low p_T particles can give rise to a sizable transverse momentum imbalance the last term in equation (5.6) contains all energy deposition in the calorimeters and tracks from the inner detector not associated to any reconstructed particle.

CHAPTER 6

Event selection

Generally the event selection aims at picking events which originated from the studied process, while rejecting events from other processes or spurious detector signals. For some inclusive analyses a sufficient background rejection can already be achieved by very basic requirements on e.g. the operating conditions of the detector. For the analysis presented here, however, the large difference between the total proton-proton cross-section and the expected $W\gamma\gamma$ production cross-section requires a background rejection on the order of $O(10^8)$. Given this huge rejection, the selection stability has to be carefully monitored to ensure, that the changing data taking conditions do not bias the result.

At first, the dataset used for this analysis is presented. The selection criteria are introduced in the second part of this chapter. The last part of this chapter is devoted to the studies carried out to ensure that the selection is stable.

6.1 Collision data

The data used for the analysis presented in this thesis have been recorded by the ATLAS detector during the year 2012 in proton-proton collisions at a center of mass energy $\sqrt{s} = 8\,\text{TeV}$. The LHC has delivered an integrated luminosity of $22.8\,\text{fb}^{-1}$ of which the ATLAS experiment recorded $21.3\,\text{fb}^{-1}$ during the same time. This corresponds to a data-taking efficiency of more than 93 %. The small inefficiency arises mostly from the time it takes until the tracking detectors operate at their nominal high-voltage and the detector dead time.

During data-taking some detector component occasionally becomes unavailable rendering it unable to record data. For example the readout electronics might have to be reset. Although this degrades the quality of the data, data taking still continues, as not all physics analyses need all components of the detector to be functional. Therefore all defects are stored such that their impact can be evaluated afterwards [112]. The time granularity used to store the defects is the so called *luminosity block* (LB), which normally lasts sixty seconds and is characterized by stable luminosity and detector conditions.

In this analysis all detector components are required to be fully functional. Technically this is achieved by only considering data from luminosity blocks without known defects. This list (*Good Runs List* [114]) is provided by the ATLAS Data Quality Group [115]. In total about $1\,\text{fb}^{-1}$ of data is not considered, leading to a total luminosity of $20.3\,\text{fb}^{-1}$ used for this analysis. A summary of the performance of the LHC and the ATLAS detector is presented in Figure 6.1. It shows the luminosity delivered, recorded and recorded without detector defects as a function of time.

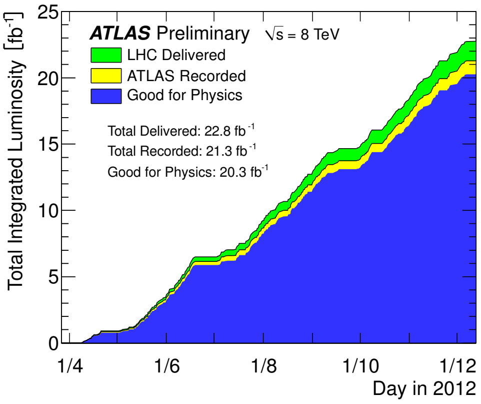

Figure 6.1: The total integrated luminosity delivered by the LHC (green) and recorded by the ATLAS detector (yellow) excluding detector defects (blue) as a function of time for proton-proton collision at $\sqrt{s}$ = 8 TeV during the year 2012. Figure from [113]

A prescaled trigger cannot be used for the selection of the $W\gamma\gamma$ process due to the low cross-section. Therefore the only available triggers are a single-muon trigger with a threshold of 24 GeV or a di-photon trigger with a threshold of 40 GeV. The high thresholds associated with these triggers will reduce the number of observed events making an observation of the $W\gamma\gamma$ final state more difficult. Therefore a new trigger was developed and studied during the course of this thesis specifically for the $W\gamma\gamma$ analysis. It selects data by requiring one muon and two photons[1]. The advantage over the existing trigger is that the three-object trigger runs *unprescaled* with lower transverse momentum thresholds of 18 GeV for the muon and 10 GeV for the photons.

The benefits of this trigger have been studied using simulated $W\gamma\gamma$ events. The author showed, that the usage of the three-object trigger increases the number of selected events by 27 % compared to the available triggers [116]. This is a significant improvement of the total rate, which boosts the sensitivity of the measurement presented here. In addition, the expected rate of the new trigger has been studied with pp-collisions recorded in 2011 at $\sqrt{s}$ = 7 TeV. Since the expected rate was well below 1 Hz and the improvement for the analysis significant the trigger was endorsed for the 2012 data taking period. It ran unprescaled for the whole year with an average rate of about 0.7 Hz and is the primary trigger used for this measurement.

6.2 Analysis selection

The selection criteria employed can be broadly separated into two categories: event-based and object-based. The event-based criteria ensure that the studied event is a genuine collision event recorded at a time when the detector was fully operational. The object-based criteria are applied to objects, which are reconstructed as described in Chapter 5.

6.2.1 Event-based selection criteria

Collision vertex

To ensure that the energy depositions originate from a proton-proton collision, the event is required to contain a well-measured primary collision vertex [117]. It is defined as the vertex which has the maximum sum of the p_{T} of the associated tracks among all vertices reconstructed. The primary vertex is considered as well-measured if at least three tracks with $p_{\mathrm{T}} > 500$ MeV are associated to it.

Detector defects in single events

In addition to the detector defects spanning multiple events described above, data corruption can occur on an event-by-event basis, for example short noise bursts in the calorimeters. It would be very ineffi-

---

[1] The trigger item is called `EF_mu18_2g10_medium`.

cient to reject the whole luminosity block containing such an event. Therefore the status of the major detector components is stored for each event. For this analysis only completely recorded events not corrupted by LAr noise bursts or readout problems of the tile calorimeter are considered.

6.2.2 Object-based selection criteria

The object-based selection criteria select the $W\gamma\gamma$ final state, where the W bosons decays into a muon and a neutrino. In addition, one or more jets may be present due to contributions from real radiation in QCD. The muon, photons and jets are reconstructed from energy deposition in the different detector subsystems as described in Chapter 5. The neutrino cannot be reconstructed directly, but it gives rise to a transverse momentum imbalance (cf. Section 5.4).

Spurious jet rejection

The data contain a small fraction of jets which are reconstructed from cosmic ray showers, beam-induced background or localized noise bursts in the calorimeters. These *fake jets* will lead to a substantial transverse momentum imbalance although the hard scatter did not contain any invisible particles. Therefore events containing fake jets with $p_{\mathrm{T}} > 20\,\mathrm{GeV}$ are not considered for this analysis. Details on the identification of fake jets are given in appendix A.2.

W boson selection

Events are selected by requiring a *combined muon* (cf. Section 5.2) with $p_{\mathrm{T}} > 20\,\mathrm{GeV}$ and within the acceptance of the inner detector $|\eta| < 2.5$. In addition, the events are required to have $E_{\mathrm{T}}^{\mathrm{miss}} > 25\,\mathrm{GeV}$ to account for the neutrino escaping detection. The p_{T} threshold of the muon is chosen such that the efficiency of the trigger reaches the plateau as this facilitates the treatment of the trigger efficiency. Events that contain a muon and transverse momentum imbalance from other sources than the decay of a W boson are suppressed by requiring that the *transverse mass* m_{T} is above 40 GeV. The transverse mass of the muon-neutrino system is commonly used at hadron colliders to replace the invariant mass when invisible particles are involved[2]. For this analysis it is defined as

$$m_{\mathrm{T}} = 2 p_{\mathrm{T}}^{\mu} E_{\mathrm{T}}^{\mathrm{miss}} \left(1 - \cos\Delta\phi\right) , \tag{6.1}$$

where p_{T}^{μ} is the transverse momentum of the muon and $\Delta\phi$ is the difference in azimuthal angle between the muon and the direction of the missing transverse energy. Figure 6.2a shows the distribution of m_{T} for simulated W boson and di-jet production. One can clearly see the separation between these two samples above about 40 GeV.

A selection on the muon isolation as well as the muon impact parameter helps to further reduce events containing non-prompt muons, e.g. muons from the decay of a B meson. The lifetime of B mesons is orders of magnitude larger than that of W bosons, which allows them to travel a measurable distance from the interaction point before they decay. In addition, muons from hadron decays are accompanied by other hadrons from the decay that leave additional energy deposits in the vicinity of the muon. These properties of non-prompt muons are exploited as follows: first the transverse impact parameter, d_0, and

---

[2] As explained in Section 5.4 the z-component of the momentum imbalance is unknown at hadron colliders rendering the invariant mass useless if invisible particles are involved.

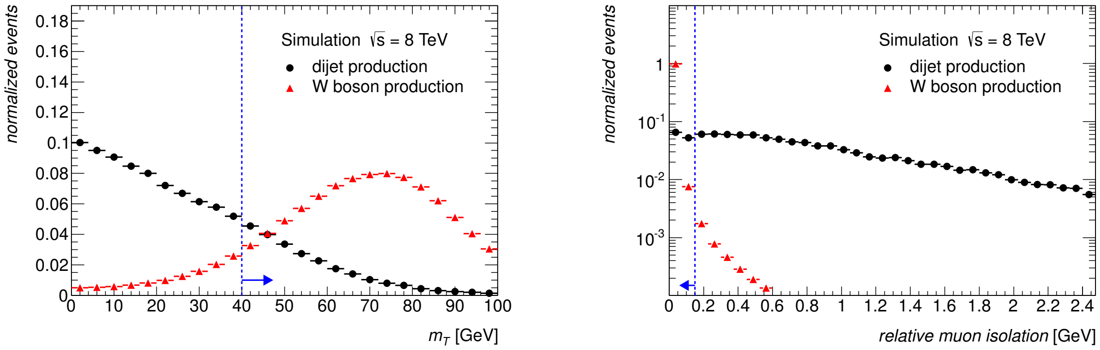

(a) (b)

Figure 6.2: Transverse mass (a) and relative muon isolation (b) distribution for simulated W boson and di-jet production. The cut value is indicated by the vertical blue line and the arrow indicates the events that are kept after the respective selection.

the longitudinal impact parameter, z_0, are required to be compatible with the primary vertex

$$d_0 < 3\sigma_{d_0} \tag{6.2}$$

$$z_0 \sin(\theta) < 0.5\,, \tag{6.3}$$

where σ_{d_0} is the uncertainty of d_0 obtained from the track fit and θ is the angle between the muon track and the beam direction. And secondly, the p_{T} sum of all tracks within a cone with an opening angle of 0.2 in η-ϕ around the muon track is required to be less than 15 % of the muon momentum. That is

$$p_{\mathrm{T},\mu}^{\mathrm{iso}} = \sum_i p_{\mathrm{T}}^i < 0.15 p_{\mathrm{T}}^{\mu}\,, \tag{6.4}$$

where i runs over all tracks inside the cone.

Figure 6.2b shows how well the muon isolation separates prompt and non-prompt muons. It displays the relative muon isolation for events with muons passing the kinematic selection and the $E_{\mathrm{T}}^{\mathrm{miss}}$ and m_{T} requirements outlined above. The separation between non-prompt muons from simulated di-jet production and prompt muons from the decay of a W boson is clearly visible.

Additional muon veto

Events that contain at least one additional muon with $p_{\mathrm{T}} > 7\,\mathrm{GeV}$ and $|\eta| < 2.5$ are rejected if they are compatible with the primary vertex using the criteria on the transverse and longitudinal impact parameters as described above. Not considering events with additional muons suppresses events where the muon stems from the decay of a Z boson or where multiple weak bosons have been produced simultaneously, for instance WW or WZ production. In contrast to the W boson selection above, *segment tagged muons* (cf. Section 5.2) are also considered. This increases the rejection of Z boson decays even further and does not reject events from $W\gamma\gamma$ production.

Photon selection

Two `TIGHT` photons with $E_{\mathrm{T}} > 20\,\mathrm{GeV}$ and within $|\eta| < 2.37$ are required. Photons in the transition region between the barrel and endcap calorimeter ($1.37 < |\eta| < 1.52$) are excluded, since the additional non-instrumented material in front of the calorimeter does not allow for a sufficiently precise photon reconstruction. The E_{T} threshold is set to $20\,\mathrm{GeV}$, to use the same phase-space region as the measurement of $W\gamma\gamma$ in the electron decay channel of the W boson. Both photons are required to be isolated, i.e. $E_{\mathrm{T}}^{\mathrm{iso}} < 4\,\mathrm{GeV}$, to obtain a further reduction of non-prompt photons from neutral hadron decays. To avoid an overlap between the isolation cones of the two photons the distance in η-ϕ space between them must be larger than $\Delta R > 0.4$.

As discussed earlier, a significant part of the photons is radiated from the charged lepton. Since the probability of photon radiation decreases quickly with the angle between the muon and photon directions, only events where both photons are well separated from the muon are considered. This ensures that the measured cross-section is not dominated by the well known bremsstrahlung process and is sensitive to the more interesting gauge boson interactions. The value of the distance cut was set to $\Delta R > 0.7$ in order to cover a similar phase-space region as measurements of the $W\gamma$ and $Z\gamma$ cross-section published earlier [88, 118, 119].

Inclusive and exclusive selection

As discussed earlier, the theoretical prediction of the $W\gamma\gamma$ final state may be affected by large NNLO QCD corrections [120]. Since perturbative calculations at NNLO precision in the strong coupling are not yet available, this cannot be accounted for properly. On the other hand neglecting these large corrections may lead to a spurious claim for new physics phenomena.

To account for this, the analysis is carried out using two different jet selections. The *inclusive selection* does not restrict the number of jets and is therefore susceptible to the large corrections mentioned above. The *exclusive selection* requires that no jet is present in the event. In this case the NNLO contribution to the *exclusive cross-section* is reduced to virtual two-loop corrections, which are expected to be smaller as discussed in Chapter 2.

The jets considered in this analysis are required to have $p_{\mathrm{T}} > 30\,\mathrm{GeV}$, $|\eta| < 4.4$ and are required to be well separated from the muon and the photons, $\Delta R(\mathrm{j}, \mu/\gamma) > 0.3$. To further suppress jets originating from another interaction during the same bunch crossing (i.e. from *in-time pile-up*) a significant fraction of the jet energy carried by charged particles is required to originate from the primary interaction. This is measured using tracking and vertexing information from the inner detector. The sum over the p_{T} of all tracks associated to the jet originating from the primary vertex must be at least 50 % of the sum over the p_{T} of all tracks associated to the jet. This *jet vertex fraction* requirement is only applied to jets within $|\eta| < 2.4$, since tracks can only be reconstructed within the η coverage of the inner detector.

6.2.3 Summary

From the events the ATLAS detector recorded in 2012, 112 events remain after the inclusive selection described above has been applied. After the additional jet veto, which defines the exclusive selection, 54 events are selected. The number of events rejected by the individual selection criteria and the number of events remaining are listed in Table 6.1 for both selections. The selection only keeps about 1×10^{-5} % of the recorded events. The rejection is dominated by the trigger requirements which alone rejects about 7×10^{8} events.

Selection	Events remaining	Events rejected
Recorded (egamma stream)	732026805	—
Good Runs List	701620359	30406446
Collision vertex	700616152	1004207
Trigger	1340764	699275388
Detector status	1337941	2823
Spurious jet veto	1332289	5652
μ selection	175236	1157053
$E_{\mathrm{T}}^{\mathrm{miss}}$, m_T selection	69123	106113
Additional muon veto	63575	5548
One photons	4116	59459
Two photons	112	4004
Inclusive selection	112	—
Exclusive selection	54	58

Table 6.1: The number of events remaining and rejected after the application of the different selection criteria.

6.3 Selection stability

A selection has to be very carefully monitored. For example already a small change in the muon reconstruction caused by the varying data taking conditions will affect the cross-section measurement if it remains unnoticed. Therefore the event yield, i.e. the number of events per integrated luminosity, has been studied as function of different observables that characterize the data-taking.

The ATLAS data-taking is organized in periods, which represent time windows of continuous running. During 2012, eleven periods have been defined, of which ten have been used in this analysis. The event yield normalized to one fb^{-1} for these ten periods is shown in Figure 6.3 after the inclusive (a) and the exclusive (b) selection. The data shows no hints for a time dependence. To quantify this qualitative observation a χ^2-test has been used to test the compatibility of the data with a time independent event yield. Values of $\chi^2/\mathrm{NDF} = 8.1/9$ for the inclusive and $\chi^2/\mathrm{NDF} = 4.3/9$ for the exclusive selection have been found. They confirm the initial observation of a time-independent selection efficiency.

The stability of the selection was monitored using the average number of interactions per bunch crossing ($\langle\mu\rangle$), as a measure for the *pile-up*. Figure 6.4 shows the event yield per fb^{-1} for the inclusive (a) and exclusive (b) selection as a function of $\langle\mu\rangle$. Again, a χ^2-test was confirms the data are independent of $\langle\mu\rangle$, with a value of $\chi^2/\mathrm{NDF} = 3.0/4$ for the inclusive and $\chi^2/\mathrm{NDF} = 3.8/4$ for the exclusive selection.

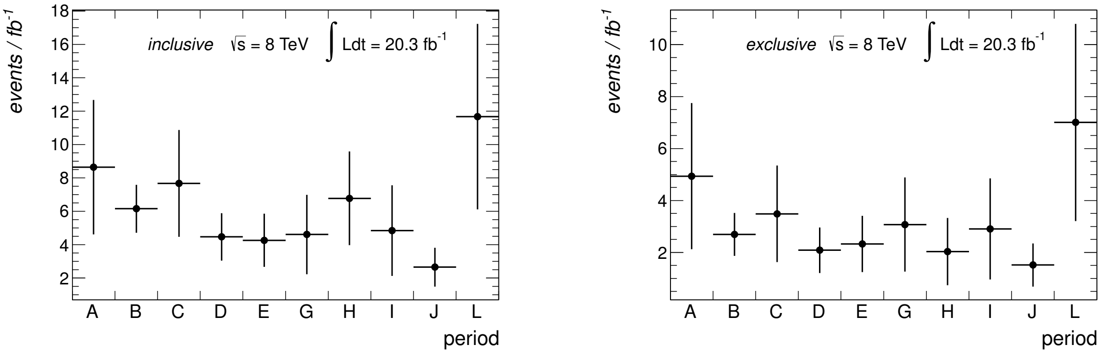

(a)

(b)

Figure 6.3: The event yield as function of the data-taking period after the inclusive (a) and exclusive (b) selection has been applied.

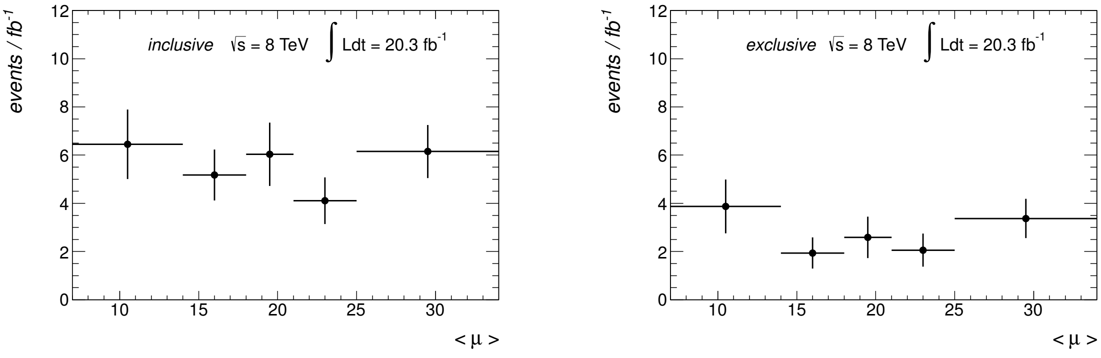

(a)

(b)

Figure 6.4: The event yield as function of the average number of interaction per bunch crossing, $\langle\mu\rangle$, after the inclusive (a) and exclusive (b) selection has been applied.

CHAPTER 7

Background estimation

The object reconstruction and the event selection is a compromise between the selection efficiency of events from the signal process and the rejection of events from other processes. It is in general not possible to select a pure sample of signal events with a reasonable efficiency. The remaining contribution from background processes has to be estimated and then subtracted from the number of observed events to obtain a meaningful measurement of the cross-section.

For the measurement presented in this thesis, the background events that remain after the selection described in Chapter 6 can be broadly classified into three categories:

- Events that contain mis-identified photons. The dominant background source are $W(\gamma)$+jets events where one or both of the selected photon candidates stem from the decay of a neutral meson produced as part of a jet. For the photon to pass the identification criteria, the meson has to carry most of the jet momentum. For this rare topology, the fragmentation functions of quarks and gluons into hadrons are poorly constrained by experiments. Therefore estimating this background contribution using simulated events is not feasible due to the large uncertainties associated with the fragmentation functions. Instead it is estimated using the data as detailed in Section 7.1.

- Events where the muon comes from the fragmentation of a heavy-flavour quark. Although these events do not contain genuine $E_{\mathrm{T}}^{\mathrm{miss}}$, the large production cross-section of $\gamma\gamma$+jets compared to $W\gamma\gamma$ final states results in a sizable amount of background events. As above, the use of simulated events to estimated this background contribution is not appropriate, since the modelling of fake $E_{\mathrm{T}}^{\mathrm{miss}}$ in the simulation is difficult. Therefore it is also estimated from data. The method and results of this estimation are described in Section 7.2.

- Events that contain two photons and a muon that do not originate from a $W\gamma\gamma$ process. For example $Z\gamma\gamma$ events, where one of the muons is not reconstructed or $t\bar{t}$ events with two real photons. The contribution from this type of background processes is estimated using simulated events. This is justified, because it only contains real photons and muons. The details for this background estimation are given in Section 7.3.

Finally, the measured number of signal and background events will be presented in Section 7.4 together with the comparison of kinematic properties between the data and simulated $W\gamma\gamma$ events.

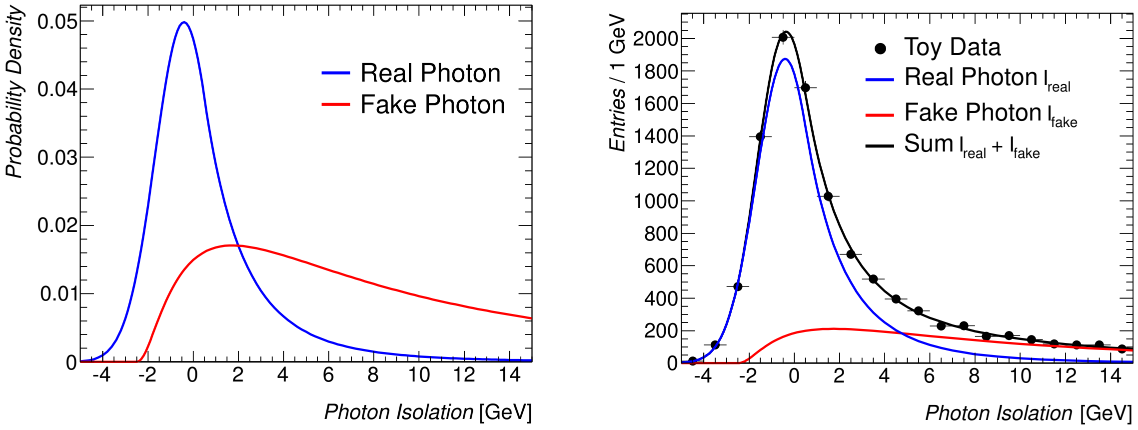

(a)

(b)

Figure 7.1: (a): Typical distribution of the transverse isolation energy for real and fake photons. (b): Illustration of the idea of the template-fit in one dimension.

7.1 Mis-identified photon background

Jets can fake a photon signature in rare cases, giving rise to *fake photons*. Events that contain fake photons cannot be suppressed entirely by applying tighter selection criteria on the photon. Therefore the number of events that contain one or two fake photons and pass all selection criteria has to be estimated. Due to the large uncertainties associated with the simulation of this rare fake-photon topology, the estimation is done using a data-driven method. It exploits that the distribution of the transverse isolation energy is different for real and fake photons, where the latter tend to be less isolated.

Typical isolation distributions of real and fake photons are shown in Figure 7.1a. The distributions are clearly distinct, but because of the large overlap they cannot be used to separate real from fake photons on an event-by-event basis, without removing most of the real photon contribution. Instead, a probabilistic approach, the *template-fit*, is adapted to estimate the contribution of fake photons in data. If the distributions of the transverse isolation energy for real and fake photons are known by some auxiliary measurement, their respective normalization can be varied such that the best agreement with the data is obtained. Since the isolation distributions are considered as fixed and only their normalization is varied, they are called *templates*. This idea is illustrated in Figure 7.1b, where an example using toy-data and the isolation distributions of Figure 7.1a is shown. For the normalization of the isolation distributions chosen here, the sum of both describes the toy data best. In this example, 25 % of all events can be accounted to a fake photon.

Since the final-state considered in this analysis consists of two photons, the template-fit method has to be extended to two dimensions. This method was first developed for the ATLAS di-photon cross-section measurement [121, 122]. At first, the general method is described. Afterwards, the determination of the templates and corrections to account for the contamination of the fake-photon templates with real photons are discussed. At last, the results of the method and the assessment of the statistical and systematic uncertainties are provided.

7.1.1 General method

The selection of the photon candidates described in Section 6.2, contains a requirement on the transverse isolation energy, $E_{\mathrm{T}}^{\mathrm{iso}} < 4\,\mathrm{GeV}$. Since this method exploits the differences of the isolation distribution between real and fake photons, which are most prominent at larger values of $E_{\mathrm{T}}^{\mathrm{iso}}$, the isolation requirement is relaxed for the estimation of the fake photon background contribution. Thus all events passing the nominal selection, excluding the isolation requirement of the two photon candidates, are considered for the method. These events can be divided into four different categories according to the origin of the photon candidates. Events with two real photons are denoted as $\gamma\gamma$, while events with one photon candidate stemming from a jet are denoted $\gamma\mathrm{j}$ ($\mathrm{j}\gamma$) when the leading (subleading) photon is real. The last category consists of events where both photons stem from a jet. These events are denoted jj throughout this document. By using this categorization, the two-dimensional $E_{\mathrm{T}}^{\mathrm{iso}}$ distribution, $I(E_{\mathrm{T}}^{\mathrm{iso},1}, E_{\mathrm{T}}^{\mathrm{iso},2})$, can be modelled by the sum of four isolation templates, F, each normalized with the number of events in the respective category, W,

$$\begin{aligned} I(E_{\mathrm{T}}^{\mathrm{iso},1}, E_{\mathrm{T}}^{\mathrm{iso},2}) =& W_{\gamma\gamma}F_{\gamma\gamma}(E_{\mathrm{T}}^{\mathrm{iso},1}, E_{\mathrm{T}}^{\mathrm{iso},2}) + W_{\gamma\mathrm{j}}F_{\gamma\mathrm{j}}(E_{\mathrm{T}}^{\mathrm{iso},1}, E_{\mathrm{T}}^{\mathrm{iso},2}) + \\ &+ W_{\mathrm{j}\gamma}F_{\mathrm{j}\gamma}(E_{\mathrm{T}}^{\mathrm{iso},1}, E_{\mathrm{T}}^{\mathrm{iso},2}) + W_{\mathrm{jj}}F_{\mathrm{jj}}(E_{\mathrm{T}}^{\mathrm{iso},1}, E_{\mathrm{T}}^{\mathrm{iso},2})\,. \end{aligned} \tag{7.1}$$

When properly normalized, the templates can be considered as two-dimensional probability density functions (p.d.f.) of the transverse isolation energies.

Equation 7.1 can be simplified using the observation that the isolation energy of the two photons is independent for events with at most one fake photon [122]. This allows to write the corresponding p.d.f.'s as the product of two one-dimensional p.d.f.'s, i.e. $F_{\gamma\gamma} = F_{\gamma,1} \cdot F_{\gamma,2}$. For events with two fake photons the isolation energy of the two photons is not independent due to the potential color connection between the jets which fake the photons. Thus the corresponding p.d.f. cannot be factorized in order to take into account the correlation. Hence, Equation 7.1 can be re-written as:

$$\begin{aligned} I(E_{\mathrm{T}}^{\mathrm{iso},1}, E_{\mathrm{T}}^{\mathrm{iso},2}) =& W_{\gamma\gamma}F_{\gamma,1}(E_{\mathrm{T}}^{\mathrm{iso},1}, E_{\mathrm{T}}^{\mathrm{iso},2})F_{\gamma,2}(E_{\mathrm{T}}^{\mathrm{iso},1}, E_{\mathrm{T}}^{\mathrm{iso},2}) \\ &+ W_{\gamma\mathrm{j}}F_{\gamma,1}(E_{\mathrm{T}}^{\mathrm{iso},1}, E_{\mathrm{T}}^{\mathrm{iso},2})F_{\mathrm{j},2}(E_{\mathrm{T}}^{\mathrm{iso},1}, E_{\mathrm{T}}^{\mathrm{iso},2}) \\ &+ W_{\mathrm{j}\gamma}F_{\mathrm{j},1}(E_{\mathrm{T}}^{\mathrm{iso},1}, E_{\mathrm{T}}^{\mathrm{iso},2})F_{\gamma,2}(E_{\mathrm{T}}^{\mathrm{iso},1}, E_{\mathrm{T}}^{\mathrm{iso},2}) \\ &+ W_{\mathrm{jj}}F_{\mathrm{jj}}(E_{\mathrm{T}}^{\mathrm{iso},1}, E_{\mathrm{T}}^{\mathrm{iso},2})\,, \end{aligned} \tag{7.2}$$

where $F_{\gamma,1}$ and $F_{\gamma,2}$ are the one-dimensional real photon isolation p.d.f.'s for the leading and subleading photon, $F_{\mathrm{j},1}$ and $F_{\mathrm{j},2}$ are the one-dimensional isolation p.d.f.'s for a jet faking the leading or the subleading photon, respectively, and F_{jj} is the two-dimensional jj isolation p.d.f. used when both photon candidates are fake.

The signal ($W_{\gamma\gamma}$) and background ($W_{\gamma\mathrm{j}}$, $W_{\mathrm{j}\gamma}$, W_{jj}) yields can be obtained by fitting $I(E_{\mathrm{T}}^{\mathrm{iso},1}, E_{\mathrm{T}}^{\mathrm{iso},2})$ to the data, i.e. by maximizing the agreement between the observed two-dimensional isolation distribution and $I(E_{\mathrm{T}}^{\mathrm{iso},1}, E_{\mathrm{T}}^{\mathrm{iso},2})$. This is done by searching the values of $\vec{\theta} = (W_{\gamma\gamma}, W_{\gamma\mathrm{j}}, W_{\mathrm{j}\gamma}, W_{\mathrm{jj}})$ for which the likelihood $\mathcal{L}(\vec{\theta}\,|\,\vec{x}_1, \vec{x}_2, \ldots)$ is a maximum, given the observed data $\vec{x}_i = (E_{\mathrm{T},\,i}^{\mathrm{iso},1}, E_{\mathrm{T},i}^{\mathrm{iso},2})$, where i runs over all observed events. The likelihood contains two terms:

$$\mathcal{L}(\vec{\theta}\,|\,\vec{x}_1, \vec{x}_2, \ldots) = P_{W_{\mathrm{tot}}}(N) \cdot \prod_{i=0}^{N} F_{\mathrm{tot}}(\vec{x}_i|\vec{\theta}) \tag{7.3}$$

with

$$W_{\mathrm{tot}} = W_{\gamma\gamma} + W_{\gamma \mathrm{j}} + W_{\mathrm{j}\gamma} + W_{\mathrm{jj}} \tag{7.4}$$

$$F_{\mathrm{tot}}(E_{\mathrm{T}}^{\mathrm{iso},1}, E_{\mathrm{T}}^{\mathrm{iso},2}) = \frac{I(E_{\mathrm{T}}^{\mathrm{iso},1}, E_{\mathrm{T}}^{\mathrm{iso},2})}{\iint I(E_{\mathrm{T}}^{\mathrm{iso},1}, E_{\mathrm{T}}^{\mathrm{iso},2}) \mathrm{d}E_{\mathrm{T}}^{\mathrm{iso},1} \mathrm{d}E_{\mathrm{T}}^{\mathrm{iso},2}} \,. \tag{7.5}$$

Here, $F_{\mathrm{tot}}(E_{\mathrm{T}}^{\mathrm{iso},1}, E_{\mathrm{T}}^{\mathrm{iso},2})$ is the normalized, two-dimensional $E_{\mathrm{T}}^{\mathrm{iso}}$ distribution.

The first term in Equation 7.3, $P_{W_{\mathrm{tot}}}(N)$, is the Poisson probability of observing N events when W_{tot} events were expected. It is sensitive to the overall normalization. The second term, $\prod_{i=0}^{N} F_{\mathrm{tot}}(\vec{x}_i|\vec{\theta})$, describes the shape of the isolation distribution and is sensitive to the relative contribution of the different event categories.

As explained above the data considered for the fit is selected without the $E_{\mathrm{T}}^{\mathrm{iso}} < 4\,\mathrm{GeV}$ requirement for the two photons. The result of the fit is therefore the number of events for each category which pass the full selection without considering the photon isolation. The cross-section will be presented in a phase-space region with isolated photons, the fraction of events which fulfill $E_{\mathrm{T}}^{\mathrm{iso}} < 4\,\mathrm{GeV}$ has to be obtained. Since the isolation p.d.f.'s are known, the number of events considered for the calculation of the cross-section can be easily obtained, as

$$W^{\mathrm{sig}} = W \cdot \iint_{-\infty}^{4\,\mathrm{GeV}} F \, \mathrm{d}E_{\mathrm{T}}^{\mathrm{iso},1} \mathrm{d}E_{\mathrm{T}}^{\mathrm{iso},2} \,. \tag{7.6}$$

With this approach the estimation of the fake photon background contribution has been reduced to the determination of the isolation distribution for real and fake photons. The method used to determine the templates is not relevant as long as the template describes the data well. Thus it is possible to determine the templates for real photons from simulation, while the templates for fake photons are determined from data. Consequently the fake photon background estimation does not rely on the description of fake photons in the simulation.

7.1.2 Determination of the templates

The maximum likelihood fit in the form given above is an *unbinned* fit, i.e. the templates F must be available in their functional form. The advantage of an unbinned is that it performs better than binned fits if the number of events is small, whereas the functional form of the templates has to be extracted from the histogrammed data. This is done by with a fit assuming a functional form which has been found to describes the data well.

Real photon templates

The photon isolation p.d.f.'s $F_{\gamma,1}$ and $F_{\gamma,2}$ are determined using simulated $W\gamma\gamma$ events. All events passing the analysis selection without the $E_{\mathrm{T}}^{\mathrm{iso}}$ requirement are considered. The $E_{\mathrm{T}}^{\mathrm{iso}}$ distribution is found to be well described by a Crystal-Ball line-shape [123], which is therefore used as the functional form of the template. Figure 7.2a and (b) shows the $E_{\mathrm{T}}^{\mathrm{iso}}$ distribution for the leading (a) and subleading (b) photon. In addition, the fitted Crystal-Ball line-shape, which describes the simulation well, is shown.

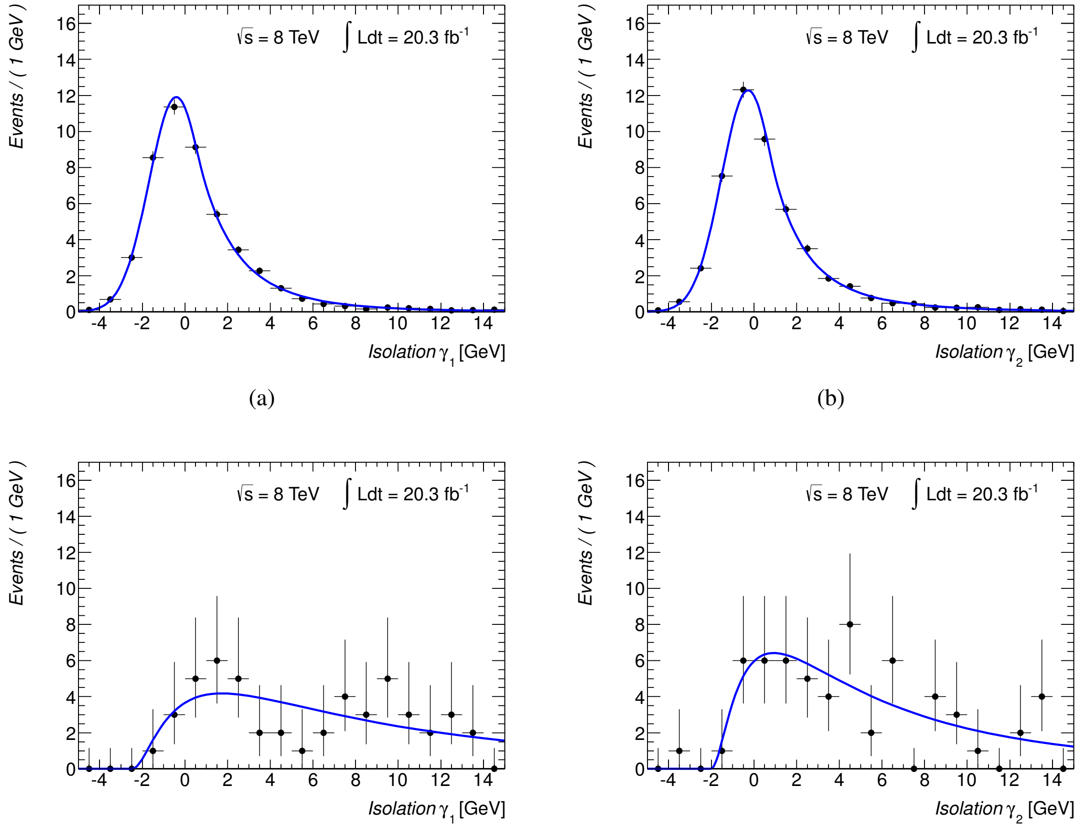

(a) (b)

(c) (d)

Figure 7.2: The $E_{\mathrm{T}}^{\mathrm{iso}}$ distribution for the leading (left) and subleading (right) photon selected using the inclusive selection from simulated $W\gamma\gamma$ events (top) and data (bottom). The solid line shows the photon isolation p.d.f.'s. The corresponding distributions for the exclusive selection are shown in Figure A.5 and A.6.

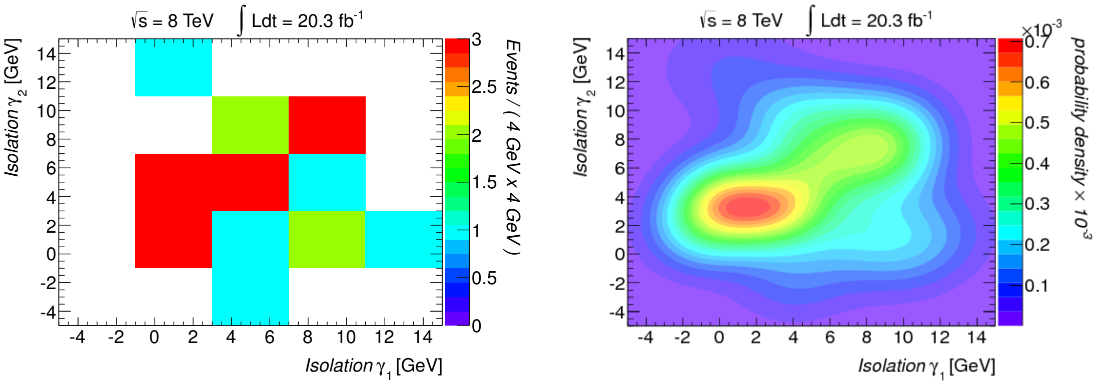

(a) (b)

Figure 7.3: The two-dimensional $E_{\mathrm{T}}^{\mathrm{iso}}$ distribution for the jj-p.d.f. selected using the inclusive selection, (a) in the AA sample, and (b), the corresponding smoothed p.d.f. F_{jj}. The two-dimensional $E_{\mathrm{T}}^{\mathrm{iso}}$ distribution obtained using the exclusive selection and the corresponding p.d.f. are shown in Figure A.7.

Fake photon templates

The isolation p.d.f. for jets that fake a photon signature $F_{\mathrm{j},1}$ ($F_{\mathrm{j},2}$) is determined from data control regions enriched in events where the leading (subleading) photon candidate is a fake photon. In order to obtain such a control region, the `TIGHT` (T) identification requirement for the photon candidate under study is replaced by the `ANTITIGHT` (A) requirement. As explained in Section 5.1, the `ANTITIGHT` selection was specially designed to select fake photons without biasing the calorimeteric isolation. In the following, events with both photons passing the `TIGHT` identification requirement are denoted as TT, while events with the leading (subleading) photon candidate passing `TIGHT` and the other one passing `ANTITIGHT` will be denoted as TA (AT).

The events used for the extraction of the isolation p.d.f. are required to pass all selections up to the photon identification, but for the leading (subleading) candidate the AT (TA) sample is used instead of the TT sample. The events are selected using the unprescaled single muon triggers with the lowest transverse momentum threshold[1], since the nominal trigger requires the photon candidates to pass a quality selection which biases the `ANTITIGHT` definition.

The $E_{\mathrm{T}}^{\mathrm{iso}}$ distributions of $\gamma\mathrm{j}$ and $\mathrm{j}\gamma$ events are modelled by a Novosibirsk function[124]. The $E_{\mathrm{T}}^{\mathrm{iso}}$ distributions for both samples are shown in Figure 7.2c and (d) together with the template.

Finally, the two-dimensional jj-p.d.f. is derived from data using the AA sample, i.e. both photon candidates are required to fulfill the `ANTITIGHT` criteria. Given the limited statistics available, the two-dimensional $E_{\mathrm{T}}^{\mathrm{iso}}$ distribution is smoothed using an adaptive kernel estimate technique implemented in the RooFit framework [125]. The two-dimensional $E_{\mathrm{T}}^{\mathrm{iso}}$ distribution and the resulting smoothed p.d.f. are shown in Figure 7.3.

7.1.3 Signal-leakage corrections

The control regions used for the jet template extraction contain a small but non-negligible amount of real photons. This *signal-leakage* into the control regions has to be corrected for, otherwise it would change the templates such that the number of events with two real photons would be underestimated. The fraction of real photons passing the `ANTITIGHT` selection can be estimated using simulated events and then taken into account by correcting the yields accordingly. The data used to obtain the fake photon templates contains real and fake photons. Therefore the isolation templates do not coincide with the fake photon p.d.f.'s, but instead are the sum of real and fake photon p.d.f.'s. This is taken into account by re-expressing the templates obtained from the control regions, $F_{\mathrm{b},1}$, $F_{\mathrm{b},2}$ and F_{bb}, as the sum of the real- and fake photon p.d.f's

$$\begin{aligned} F_{\mathrm{b},i} =& \alpha_i F_{\gamma,i} + (1-\alpha_i) F_{\mathrm{j},i} \qquad\qquad i \in \{1,2\}\,, & (7.7)\\ F_{\mathrm{bb}} =& (1-\alpha'_1-\alpha'_2-\alpha'_3) F_{\mathrm{jj}} + \alpha'_1 F_{\gamma,1} F_{\mathrm{j},2} + \alpha'_2 F_{\mathrm{j},1} F_{\gamma,2} + \alpha'_3 F_{\gamma,1} F_{\gamma,2}\,, & (7.8)\end{aligned}$$

where α_1 is the fraction of $\gamma\gamma$ events in the AT control region and α_2 is the same fraction in the TA control region. The fraction of events containing real photons in the AA control region is denoted as α'_1 for events where the subleading photon is real, α'_2 for events where the leading photon is real and α'_3 for events with two real photons.

To use the fit with the templates obtained from the control regions as explained before, the two dimensional isolation distribution of equation (7.2) has to be written in terms of the measured background

---

[1] `EF_mu24i_tight` OR `EF_mu36_tight`

templates. After reordering the different terms, one obtains

$$W_{\text{tot}}F_{\text{tot}} = w_{\gamma\gamma}F_{\gamma,1}F_{\gamma,2} + w_{\gamma\text{j}}F_{\gamma,1}F_{\text{b},2} + w_{\text{j}\gamma}F_{\text{b},1}F_{\gamma,2} + w_{\text{jj}}F_{\text{bb}} \tag{7.9}$$

with

$$\begin{aligned}
w_{\gamma\gamma} &= W_{\gamma\gamma} \\
&\quad - \frac{\alpha'_3}{1-\alpha'_1-\alpha'_2-\alpha'_3}W_{\text{jj}} \\
&\quad - \frac{\alpha_1}{1-\alpha_1}\left(W_{\gamma\text{j}} - \frac{\alpha'_1}{1-\alpha'_1-\alpha'_2-\alpha'_3}W_{\text{jj}}\right) \\
&\quad - \frac{\alpha_2}{1-\alpha_2}\left(W_{\text{j}\gamma} - \frac{\alpha'_2}{1-\alpha'_1-\alpha'_2-\alpha'_3}W_{\text{jj}}\right) \\
w_{\gamma\text{j}} &= \frac{1}{1-\alpha_1}\left(W_{\gamma\text{j}} - \frac{\alpha'_1}{1-\alpha'_1-\alpha'_2-\alpha'_3}W_{\text{jj}}\right) \\
w_{\text{j}\gamma} &= \frac{1}{1-\alpha_2}\left(W_{\text{j}\gamma} - \frac{\alpha'_2}{1-\alpha'_1-\alpha'_2-\alpha'_3}W_{\text{jj}}\right) \\
w_{\text{jj}} &= \frac{1}{1-\alpha'_1-\alpha'_2-\alpha'_3}W_{\text{jj}}\,.
\end{aligned}$$

The fraction of real photon events α can be written as a function of the yields W together with the efficiency of the `ANTITIGHT` selection from simulated events

$$\alpha_1 = \left(\frac{N^{\text{AT}}_{\gamma\gamma}}{N^{\text{TT}}_{\gamma\gamma}}\right)_{\text{MC}} \frac{W_{\gamma\gamma}}{N^{\text{AT}}}, \quad \alpha_2 = \left(\frac{N^{\text{TA}}_{\gamma\gamma}}{N^{\text{TT}}_{\gamma\gamma}}\right)_{\text{MC}} \frac{W_{\gamma\gamma}}{N^{\text{TA}}} \tag{7.10}$$

$$\alpha'_1 = \left(\frac{N^{\text{AA}}_{\gamma\text{j}}}{N^{\text{TT}}_{\gamma\text{j}}}\right)_{\text{MC}} \frac{W_{\gamma\text{j}}}{N^{\text{AA}}}, \quad \alpha'_2 = \left(\frac{N^{\text{AA}}_{\text{j}\gamma}}{N^{\text{TT}}_{\text{j}\gamma}}\right)_{\text{MC}} \frac{W_{\text{j}\gamma}}{N^{\text{AA}}}, \quad \alpha'_3 = \left(\frac{N^{\text{AA}}_{\gamma\gamma}}{N^{\text{TT}}_{\gamma\gamma}}\right)_{\text{MC}} \frac{W_{\gamma\gamma}}{N^{\text{AA}}}\,. \tag{7.11}$$

Here $N^X_{ij,\text{MC}}$ is the number of events of category ij in the sample X measured in Monte Carlo simulated events and N^X is the number of events in the sample X measured in the data.

The inputs used for the signal-leakage corrections are shown in Table 7.1 for simulated $W\gamma\gamma$ events and in Table 7.2 for simulated $W\gamma$ events. For the former, the results from Sherpa and AlpGen are shown, while for the latter only AlpGen was available, as explained in Section 4.1. The `ANTITIGHT` ratios obtained from different Monte Carlo samples agree within their statistical uncertainties. Table 7.3 lists the number of events measured in the control regions using the inclusive and exclusive selection.

7.1.4 Results of the template-fit method

The results of the two-dimensional fit, performed on the 181 (78) events in the TT sample selected using the inclusive (exclusive) selection, are shown in Table 7.4. The event yields in the signal region are provided as well. Projections of the resulting two-dimensional $E_{\text{T}}^{\text{iso}}$ distributions on the transverse isolation energies of the two photon candidates are shown in Figure 7.4. As explained above events with two real photons, i.e. the $\gamma\gamma$ component, does not correspond to the $W\gamma\gamma$ signal at this stage, since events from other process can contain two real photons as well.

coefficient	*inclusive*		*exclusive*	
	SHERPA	ALPGEN	SHERPA	ALPGEN
$\left(\frac{N_{\gamma\gamma}^{\mathrm{AT}}}{N_{\gamma\gamma}^{\mathrm{TT}}}\right)_{\mathrm{MC}}$	0.035 ± 0.003	0.030 ± 0.003	0.034 ± 0.005	0.035 ± 0.005
$\left(\frac{N_{\gamma\gamma}^{\mathrm{TA}}}{N_{\gamma\gamma}^{\mathrm{TT}}}\right)_{\mathrm{MC}}$	0.059 ± 0.004	0.061 ± 0.004	0.066 ± 0.007	0.070 ± 0.008
$\left(\frac{N_{\gamma\gamma}^{\mathrm{AA}}}{N_{\gamma\gamma}^{\mathrm{TT}}}\right)_{\mathrm{MC}}$	0.003 ± 0.001	0.001 ± 0.001	0.004 ± 0.002	0.002 ± 0.001

Table 7.1: Input for the signal-leakage correction derived from simulated $W\gamma\gamma$ events using the inclusive selection. The results are shown for the two Monte Carlo generators available. The uncertainties shown are statistical only.

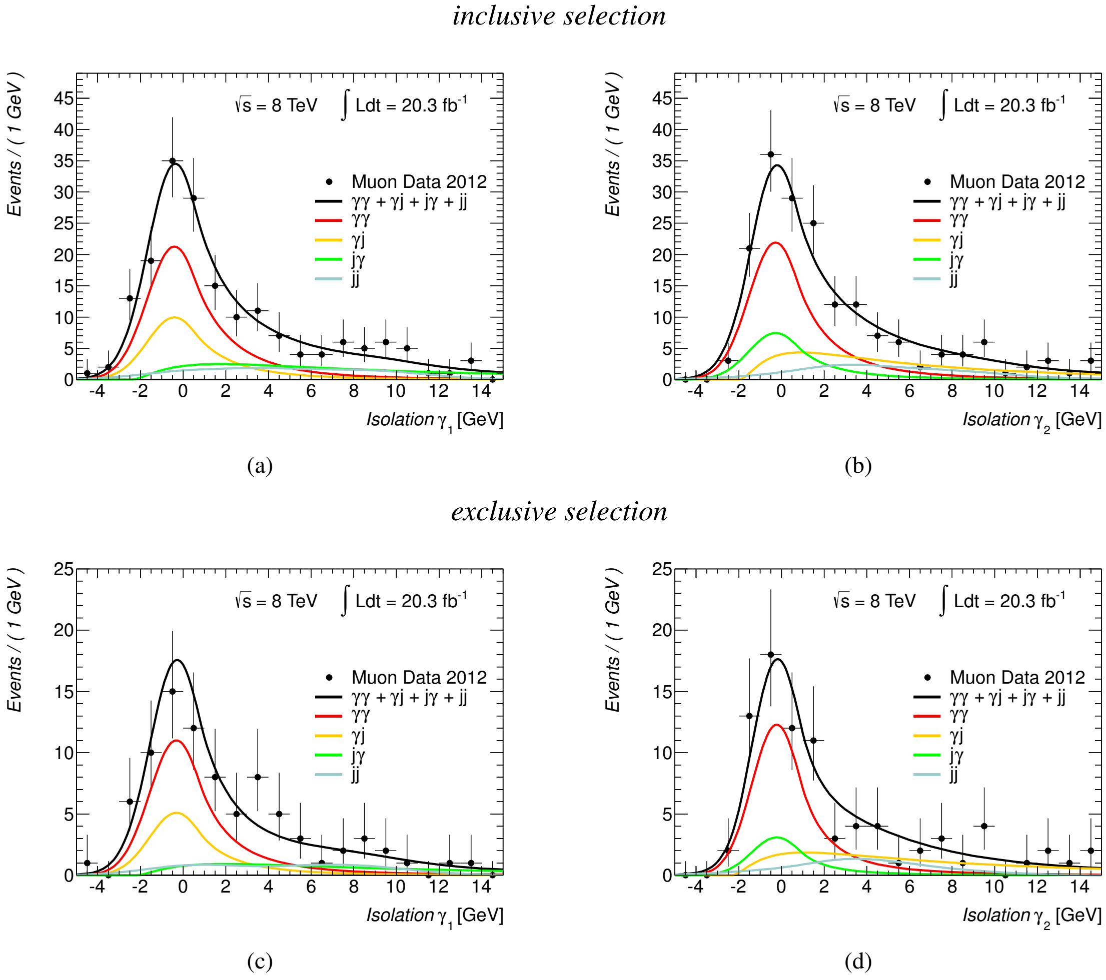

Figure 7.4: Projection of the two-dimensional isolation distributions on the transverse isolation energy of the leading (left) and subleading (right) photon candidate for the inclusive (top) and exclusive (bottom) selection. The black dots represent the data selected using the inclusive selection. The black line shows the result of the fit and the colored lines show the contributions from the different event categories.

coefficient	*inclusive*	*exclusive*
$\left(\frac{N_{\gamma\mathrm{j}}^{\mathrm{AA}}}{N_{\gamma\mathrm{j}}^{\mathrm{TT}}}\right)_{\mathrm{MC}}$	0.025 ± 0.010	0.029 ± 0.015
$\left(\frac{N_{\mathrm{j}\gamma}^{\mathrm{AA}}}{N_{\mathrm{j}\gamma}^{\mathrm{TT}}}\right)_{\mathrm{MC}}$	0.040 ± 0.011	0.050 ± 0.018

Table 7.2: Inputs for the signal-leakage correction derived from simulated $W\gamma$ + jets events with the AlpGen generator. The uncertainties shown are statistical only.

control region	**number of events**	
	inclusive	*exclusive*
AT	49	26
TA	59	27
AA	21	12

Table 7.3: Number of events in the control regions used for the calculation of the signal-leakage corrections.

7.1.5 Estimate of the statistical uncertainties

The statistical uncertainty on the event yields is calculated using the Minos algorithm [126] taking into account both, non-linearities of the likelihood function and correlations between the parameters. To better understand how the Minos algorithm estimates the uncertainty it is advisable to shorty recall the traditional approach. The minimum of the negative log-likelihood function, $-\ln\mathcal{L}(\theta)$, is characterized by a specific value of the parameter, denoted as $\hat{\theta}$. This value is called the maximum-likelihood estimator (MLE) of the parameter θ, since it maximises the likelihood, $\mathcal{L}$, or conversely minimizes the negative log-likelihood, $-\ln\mathcal{L}$. The uncertainty on the parameter is given by the value of θ, which changes the negative log-likelihood by 0.5. That is the uncertainty on θ, σ_θ, is given by

$$\sigma_\theta = \theta' - \hat{\theta}\,, \tag{7.12}$$

category	*inclusive*		*exclusive*	
	W	W^{sig}	W	W^{sig}
$\gamma\gamma$	92 ± 16	76 ± 14	46 ± 10	39 ± 9
γj	36 ± 13	17 ± 6	19 ± 8	8 ± 4
jγ	29 ± 11	11 ± 4	9 ± 7	3 ± 3
jj	20 ± 9	5 ± 2	10 ± 6	3 ± 2

Table 7.4: Results of the 2D fit method. For each category the result of the fit and the number of events where both photons pass the isolation criterion is given. The uncertainties are statistical only. Details on how the statistical uncertainties are obtained can be found below.

where θ' fulfills

$$0.5 = \ln \mathcal{L}(\hat{\theta}) - \ln \mathcal{L}(\theta') \,. \tag{7.13}$$

The condition of Equation 7.13 is fulfilled by two values of θ, giving the lower uncertainty and upper uncertainty on $\hat{\theta}$.

The Minos algorithm extends this procedure to likelihoods with more than one parameter. Then the likelihood has the form $\mathcal{L}(\theta, \vec{\nu})$, where θ is the parameter whose uncertainty is to be evaluated, and $\vec{\nu}$ are the remaining parameters. The maximum of the likelihood is now characterized by $\mathcal{L}(\hat{\theta}, \hat{\vec{\nu}})$, where $\hat{\theta}$ and $\hat{\vec{\nu}}$ are the MLEs of θ and $\vec{\nu}$, respectively. Now the condition of Equation 7.13 changes to

$$0.5 = \ln \mathcal{L}(\hat{\theta}, \hat{\vec{\nu}}) - \ln \mathcal{L}(\theta', \hat{\hat{\vec{\nu}}}) \,. \tag{7.14}$$

The "double-hat", $\hat{\hat{\vec{\nu}}}$, indicates that the log-likelihood is minimized after the tested value of θ has been fixed. Since the value of the negative log-likelihood will always be smaller after it has been minimized with respect to the other parameters, the Minos algorithm yields larger uncertainty intervals.

Extensive studies have been done during the course of this thesis to understand the validity of the Minos uncertainties and to assess the bias of the parameter estimates due to the small number of events available. The studies are based on the evaluation of a large number of *pseudo-experiments*. Each pseudo-experiment consist of two steps: at first *pseudo-data* are generated and then the pseudo-data are fitted.

The generation of the pseudo-data is done by sampling the two dimensional isolation distribution which minimizes the likelihood with respect to the data. The number of generated events is fluctuated according to a Poisson distribution whose mean is set to the number of events measured in data.

Each of these pseudo-datasets is then fitted as described above, and the event yields with their corresponding uncertainties are extracted. Since the parameter values that have been used in the generation of the pseudo-data are known (exactly the parameter that minimize the likelihood with respect to the data, i.e. the results given in Table 7.4) the fit performance can be evaluated. This is quantified by the pull p_W which is calculated for each event yield W as

$$p_W = \frac{W_{\text{pe}} - W_{\text{gen}}}{\sigma_{\text{pe}}} \,, \tag{7.15}$$

where W_{gen} is the value used in the generation of the pseudo-data and $W_{\text{pe}} \pm \sigma_{\text{pe}}$ is the fit result.

The distribution of pulls for a sufficiently large number of pseudo-experiments is expected to be a Gaussian distribution with mean zero and width one, provided that the parameter estimation is not biased and the uncertainty σ_{pe} is correctly calculated. Since the estimation of parameters using the maximum likelihood method is only unbiased in the limit of infinite number of events, the obtained pull distribution may not be Gaussian. Any deviation from a Gaussian pull distribution is taken as an additional uncertainty, as follows. If the mean of the pull distribution is shifted from zero, the resulting uncertainty σ_{bias} is calculated as

$$\sigma_{\text{bias}} = \mu_{\text{pull}} \cdot \sigma_{\text{fit}} \,, \tag{7.16}$$

where μ_{pull} is the mean of the pull distribution and σ_{fit} is the uncertainty of the fit as given by Minos. If the width of the pull distribution is different from one, the uncertainty of the fit is given by

$$\sigma_{\text{width}} = \sigma_{\text{pull}} \cdot \sigma_{\text{fit}} \,, \tag{7.17}$$

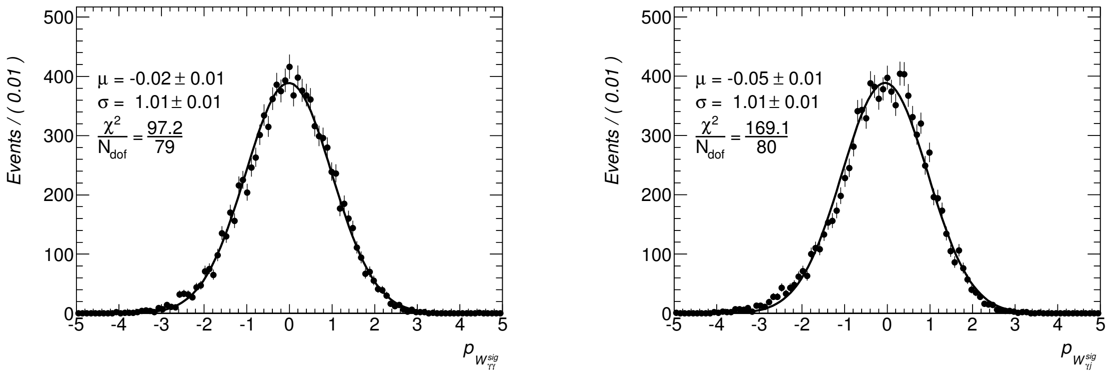

(a) $W_{\gamma\gamma}$ (b) $W_{\gamma\mathrm{j}}$

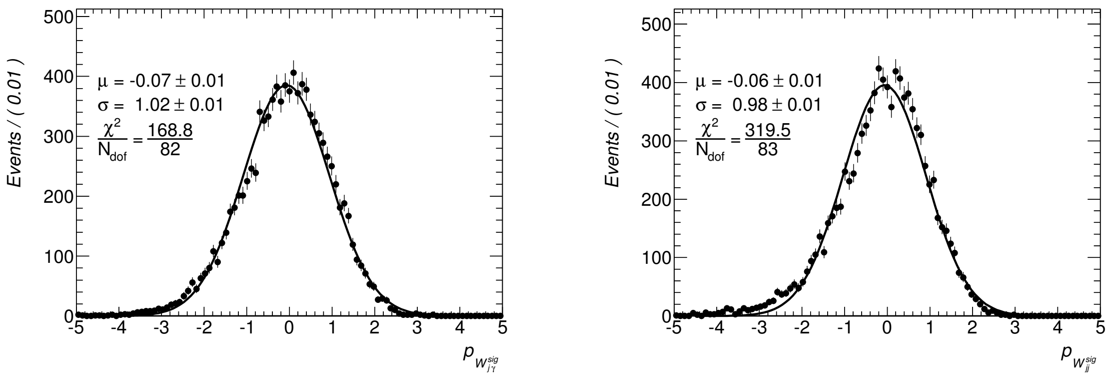

(c) $W_{\mathrm{j}\gamma}$ (d) W_{jj}

Figure 7.5: Pull distributions for the four event yields in the signal region from 10000 pseudo-experiments. In addition the mean, width and goodness-of-fit, as χ^2/NDF, of a Gaussian function fitted to these distributions is shown. The same distributions for the exclusive selection are shown in Figure A.8.

where σ_{pull} is the width of the pull distribution and σ_{fit} is the same as above. The total uncertainty on the event yield N is the square-root of the quadratic sum of the two terms,

$$\sigma_N = \sqrt{\sigma^2_{\text{bias}} + \sigma^2_{\text{width}}}\,. \tag{7.18}$$

Figure 7.5 shows the pull distribution of the event yields in the signal region after generating 10000 pseudo-experiments. The distributions are fitted with a Gaussian function with mean μ and width σ whose values are also given in the figure. For all these distributions the width of the Gaussian is compatible with one within uncertainties, although they show a small tendency towards negative values.

The three background components γj, jγ and jj show non-Gaussian tails towards negative values. This behaviour comes from the small statistics available in the control regions. This has been verified by performing the same pseudo-experiments as above, but generating fifty times more events than observed in data per pseudo-experiment. The pull distributions obtained in this case are shown in Figure 7.6. As expected, the Gaussian behaviour is restored, confirming that the bias is caused by the limited number of events.

The mean and the sigma parameters of a Gaussian function fitted to the pull distribution can only be used if the pull distribution is described well be a Gaussian function. Since this is not the case, the mean

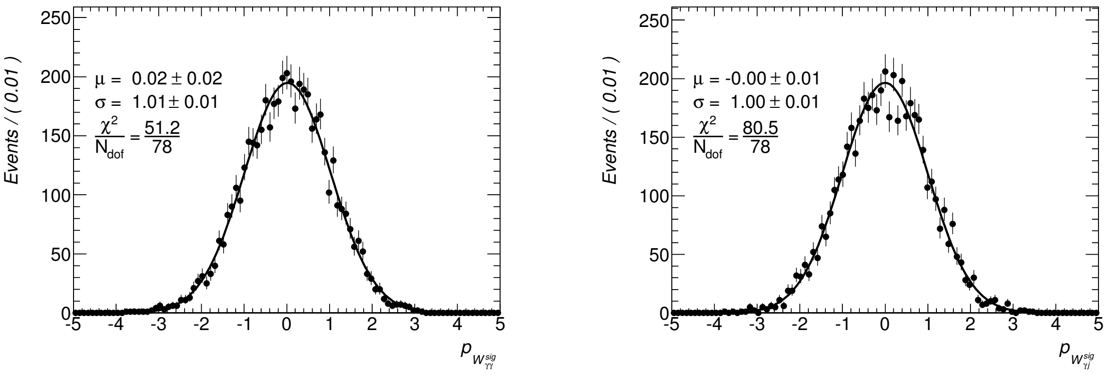

(a) $W_{\gamma\gamma}$ (b) $W_{\gamma \mathrm{j}}$

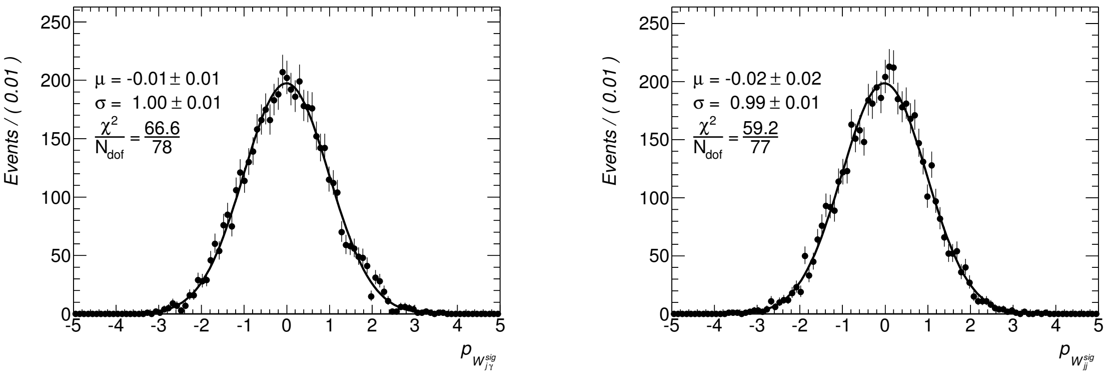

(c) $W_{\mathrm{j}\gamma}$ (d) W_{jj}

Figure 7.6: Pull distributions for the four event yields in the signal region from 10000 pseudo-experiments using fifty times more events than observed in data per pseudo-experiment.

and the width of the pull distribution are obtained differently. The mean is taken as the 50 %-quantile, i.e. the median, of the distribution. The lower and upper one sigma uncertainty values are taken as the 15.8 %-quantile and 84.1 %-quantile, respectively. To avoid asymmetric uncertainties the larger of the two deviations is taken as the uncertainty.

The resulting statistical uncertainties are summarized in Table 7.4. The relative uncertainties range from 17 % in case of the $\gamma\gamma$-events up to 48 % for the jj-category. The maximum corrections to the uncertainties given by Minos is applied in the jj-category and is below 10 %.

7.1.6 Estimate of the systematic uncertainties

In addition to the statistical uncertainties it is important to correctly estimate the size of the systematic uncertainties the template-fit method is exposed to. These include uncertainties due to choices that have been made, for example the functional form used to model the background templates, or using the values from the Sherpa generator instead of AlpGen. Moreover, it also includes the effect of the small number of events in the control regions limiting the knowledge of the templates.

More specifically the following sources of systematic uncertainties have been considered:

- limited statistics in the control regions

- functional form used for modelling the background distribution
- definition of the control regions
- dependence on Monte Carlo generator
- statistical uncertainty on signal-leakage

The effect of each source of systematic uncertainty is evaluated using pseudo-experiments very similar to what was described above. Now, however, the distribution used for the pseudo-data generation and the subsequent fit are not the same. In general this will lead to a bias and an increased width of the pull distribution, reflecting the additional uncertainty. If the equations described above are used to determine the systematic uncertainty of one effect, the statistical uncertainty will be considered twice. Therefore the statistical uncertainty is subtracted from the uncertainty obtained by pseudo-experiments, i.e.

$$\sigma_{\mathrm{syst}} = \sqrt{(\sigma_{\mathrm{bias}} + \sigma_{\mathrm{width}})^2 - \sigma_{\mathrm{stat}}^2}\,, \tag{7.19}$$

where σ_{bias} and σ_{stat} are the uncertainties obtained from the pull distribution, σ_{stat} is the statistical uncertainty as described above and σ_{syst} is the resulting systematic uncertainty. In the following, the procedure for each systematic uncertainty is described, and the results are provided.

In this section, only some figures for the inclusive selection will be shown. The remaining figures are available in Appendix A.3. The results obtained for the exclusive selection are qualitatively similar and can be found in Appendix A.4.

Limited control regions statistics

This uncertainty arises from the imperfect knowledge of the functional form of the templates due to the limited number of events in the control regions as well as in the Monte Carlo samples. In order to estimate it, the pseudo-data is generated using the nominal functional form and is fitted using a functional form obtained by varying the parameters within their uncertainties. The pull distributions for these pseudo-experiments are shown in Figure 7.7. This relative systematic uncertainty amounts to 5 % on the $\gamma\gamma$-yield and about 30 % on the

Background model

The choice of the functional form of the fake photon template F_{b} is arbitrary, hence the uncertainty related to the specific choice needs to be estimated. This uncertainty is evaluated by using templates with a different functional form to fit the pseudo-datasets generated using the nominal choice. The two alternate functions considered are a Crystal-Ball line-shape [123] and the sum of a Gaussian and a Novosibirsk [124] function with the same mean parameter. The corresponding pull distributions are shown in Figure 7.8 and Figure A.1, respectively. The effect of this uncertainty is small, as can be seen. This uncertainty hardly affects the number of events in the $\gamma\gamma$ category, but amounts to just below 10 % for the background events.

Selection of the control regions

The choice of the `ANTITIGHT` photon selection may influence the fake photon templates F_{b} and F_{bb}. In order to estimate the impact of this choice, two alternate `ANTITIGHT` definition have been tested. The first inverts the selections on three instead of four strip variables (L_3'). The second inverts the selection

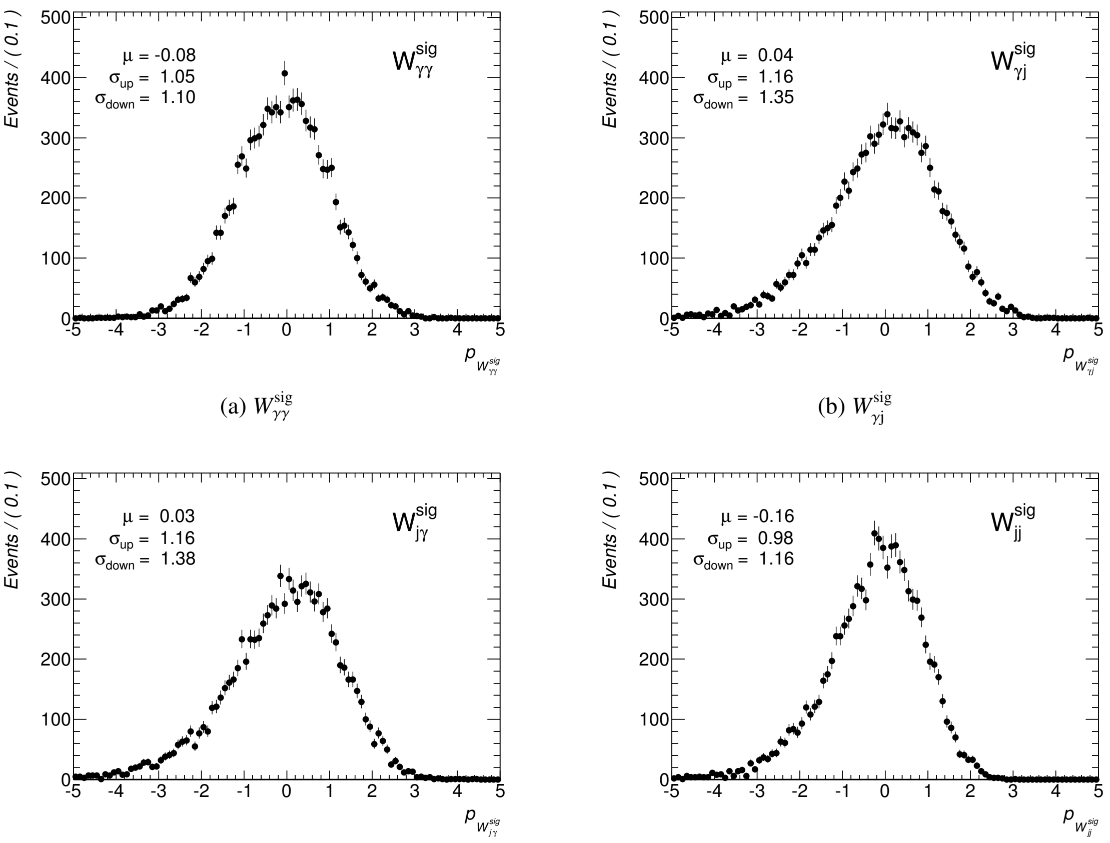

(a) $W^{\text{sig}}_{\gamma\gamma}$ (b) $W^{\text{sig}}_{\gamma\text{j}}$

(c) $W^{\text{sig}}_{\text{j}\gamma}$ (d) $W^{\text{sig}}_{\text{jj}}$

Figure 7.7: Pull distributions from pseudo-experiments used to evaluate the systematic uncertainty due to limited control region statistics (see text) for the inclusive selection. The corresponding distributions for the exclusive selection can be found in Figure A.9.

one all five strip variables (L'_5). More details on these alternative `ANTITIGHT` definitions have been given in Section 5.1.

Alternative functional forms of the fake photon templates have been extracted from the data in the control regions obtained using the alternate `ANTITIGHT` definitions. These templates have been used in the generation of the pseudo-data, which was fitted using the nominal templates. The corresponding pull distributions are shown in Figure A.2 and in Figure 7.9 for the L'_5 and L'_3 `ANTITIGHT` definitions, respectively. The effect of this uncertainty on the yield amounts to 2 % for the $\gamma\gamma$ category and about 10 % for the background category.

Monte Carlo generator dependence

Since the real-photon templates, $F_{\gamma,1}$ and $F_{\gamma,2}$, are taken events simulated with the Sherpa Monte Carlo generator, the effect of a different Monte Carlo program used to obtain the templates has to be tested. The pseudo-data for this test is generated using the templates obtained from events simulated with AlpGen. This also takes into account differences in the description of the signal-leakage parameters shown in Table 7.1. The corresponding pull distributions are shown in Figure A.3 for the inclusive selection and Figure A.14 for the exclusive selection. The uncertainty is around 1 % on $W^{\text{sig}}_{\gamma\gamma}$ and 10 % on $W^{\text{sig}}_{\text{bkg}}$.

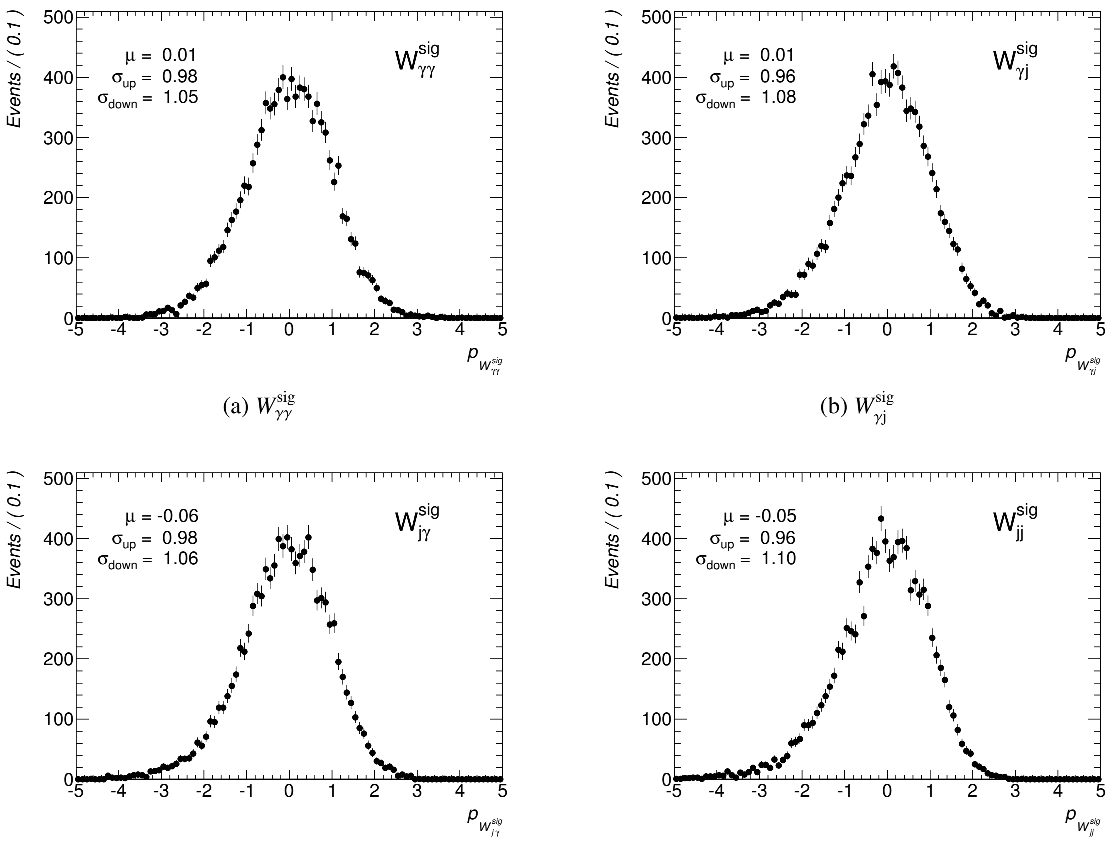

(a) $W^{\text{sig}}_{\gamma\gamma}$ (b) $W^{\text{sig}}_{\gamma\text{j}}$

(c) $W^{\text{sig}}_{\text{j}\gamma}$ (d) $W^{\text{sig}}_{\text{jj}}$

Figure 7.8: Pull distributions from pseudo-experiments used to evaluate the systematic uncertainty due to the choice of the background model for the inclusive selection. The pseudo-data has been generated using the nominal template and it has been fitted using a Crystal-Ball function as fake photon template, F_b. The corresponding distributions for the exclusive selection can be found in Figure 7.8.

Signal-leakage inputs

The parameters used to correct the leakage of real photons into the fake photon control region have associated uncertainties, whose effect on the fit result needs to be tested. The events in the control regions N^{AT}, N^{TA} and N^{AA} and the leakage parameters α are subject to statistical fluctuations. In addition the systematic uncertainty on the photon identification efficiency [91] are taken into account. The corresponding pull distributions are shown in Figure A.4 for the inclusive selection and Figure A.15 for the exclusive selection. The uncertainty amounts to roughly 8 % for the background yield and does hardly affect the yield of $\gamma\gamma$ events.

Resulting systematic uncertainties

The systematic uncertainties on the event yields in the signal region are given in Table 7.5 for the inclusive selection and in Table 7.6 for the exclusive selection. These values are obtained by carrying out pseudo-experiments and analyzing the corresponding pull distributions as described above. The statistical uncertainty dominates the determination of the number of events containing two real photons.

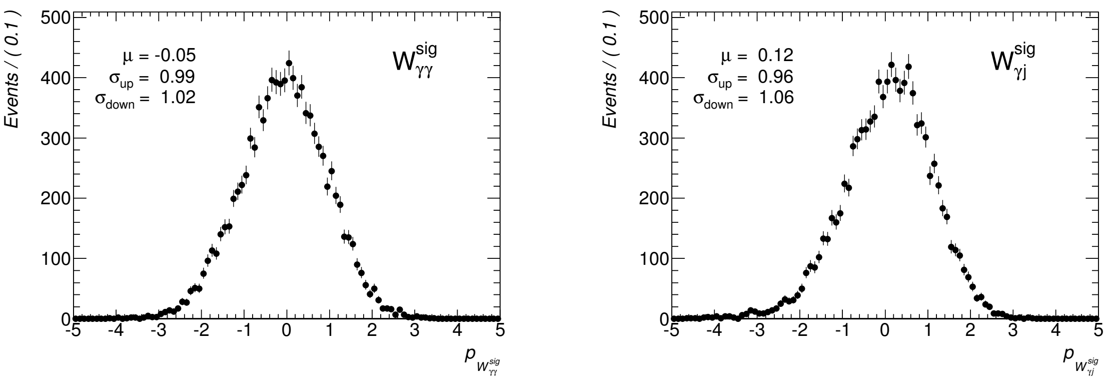

(a) $W^{\mathrm{sig}}_{\gamma\gamma}$ (b) $W^{\mathrm{sig}}_{\gamma \mathrm{j}}$

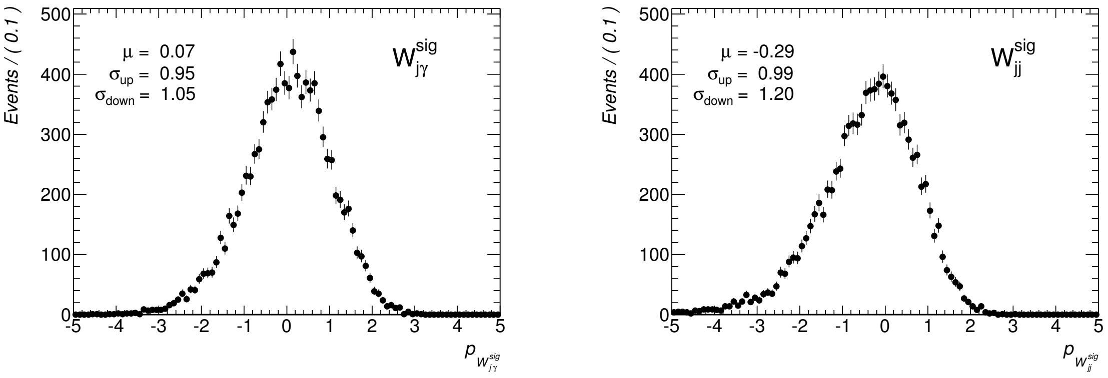

(c) $W^{\mathrm{sig}}_{\mathrm{j}\gamma}$ (d) $W^{\mathrm{sig}}_{\mathrm{jj}}$

Figure 7.9: Pull distributions from pseudo-experiments used to evaluate the systematic uncertainty due to the definition of the fake photon control region for the inclusive selection. The pseudo-data has been generated with a template obtained using the L'_3 control region definition and was fitted using the nominal template. The corresponding distribution for the exclusive selection can be found in Figure A.13.

For events containing fake photons, the statistical and systematic uncertainties are of the same size. The dominant systematic effect is the uncertainty on the background templates due to the small number of events observed in the control regions.

7.2 Non-prompt muon background

The non-prompt muon background events arise from muons produced in the fragmentation of a quark. A data-driven approach known as the *2-D sideband method*[2] is used to estimate the non-prompt muon background contribution in this work. At first the method will be introduced, and afterwards the results of the non-prompt muon background estimation are presented.

---

[2] Sometimes also called the ABCD method.

source	$W^{\mathrm{sig}}_{\gamma\gamma}$	$W^{\mathrm{sig}}_{\gamma\mathrm{j}}$	$W^{\mathrm{sig}}_{\mathrm{j}\gamma}$	$W^{\mathrm{sig}}_{\mathrm{jj}}$
Central Value	76 ± 14 (stat.)	17 ± 6 (stat.)	11 ± 4 (stat.)	5 ± 2 (stat.)
Control Region Statistics	±4	±5	±3	±1
Background Model	0	±2	0	±1
CR Definition	±2	±3	±1	±2
MC Generator	±1	±2	0	0
Signal-Leakage Inputs	0	±1	0	±1
total systematic uncertainty	±4	±7	±4	±2

Table 7.5: Systematic uncertainties on the number of events in each category for the inclusive selection.

source	$W^{\mathrm{sig}}_{\gamma\gamma}$	$W^{\mathrm{sig}}_{\gamma\mathrm{j}}$	$W^{\mathrm{sig}}_{\mathrm{j}\gamma}$	$W^{\mathrm{sig}}_{\mathrm{jj}}$
Central Value	39 ± 9 (stat.)	8 ± 4 (stat.)	3 ± 3 (stat.)	3 ± 2 (stat.)
Control Region Statistics	±3	±3	±2	±1
Background Model	0	±1	±1	0
CR Definition	±2	0	0	±1
MC Generator	±1	±1	±1	0
Signal-Leakage Inputs	0	±1	0	±1
total systematic uncertainty	±4	±4	±2	±1

Table 7.6: Systematic uncertainties on the number of events in each category for the exclusive selection.

7.2.1 General method

The 2-D sideband method is a powerful tool to obtain the number of background events in the signal region that can be used if certain conditions are met. The method has been used in the measurement of the $W\gamma$ cross-section [88] (among others). The main advantages are that the background properties can be measured directly in the data and that no precise knowledge of the signal is required. This section will describe the implementation of the method in this analysis.

The method uses two sidebands to estimate the number of background events in the signal region. A sideband is defined by reverting one of the selection criteria used to obtain the signal region. For example, a requirement of $p_{\mathrm{T},\mu}^{\mathrm{iso}} > 0.15 \cdot p_{\mathrm{T}}^{\mu}$ instead of $p_{\mathrm{T},\mu}^{\mathrm{iso}} < 0.15 \cdot p_{\mathrm{T}}^{\mu}$ would define a sideband in the muon isolation. Using a second selection criterion allows to define four regions: one that coincides with the signal region (i.e. both selections are passed), and three control regions where either one or both of the selections are inverted.

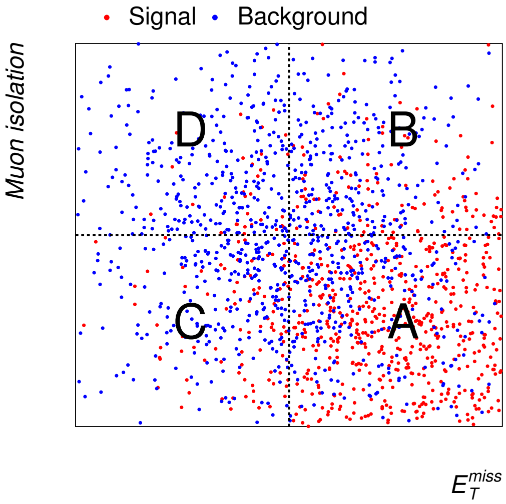

Figure 7.10: A sketch presentation of the signal region (A) and three control regions (B, C and D) used in the 2-D sideband method. Hypothesized signal and background distributions are indicated.

In general, the events where the muon comes from the decay of a real W boson are characterized by a isolated muon and high missing transverse energy ($E_{\mathrm{T}}^{\mathrm{miss}}$). Hence the control regions are defined by inverting the muon isolation and the $E_{\mathrm{T}}^{\mathrm{miss}}$ requirements. Figure 7.10 shows a sketch of the four regions and their definitions. In addition, a hypothesized signal and background distribution is overlaid.

Under the assumption that the selection requirement on $E_{\mathrm{T}}^{\mathrm{miss}}$ is independent from the muon isolation for non-prompt muons, the number of events with non-prompt muons, N, observed in the four regions, satisfies

$$\frac{N_{\mathrm{A}}}{N_{\mathrm{B}}} = \frac{N_{\mathrm{C}}}{N_{\mathrm{D}}} . \tag{7.20}$$

Therefore one can write the number of non-prompt muon events in region A, $N_{\mathrm{A}}^{\mathrm{F}}$, as

$$N_{\mathrm{A}}^{\mathrm{F}} = \frac{N_{\mathrm{B}} N_{\mathrm{C}}}{N_{\mathrm{D}}} . \tag{7.21}$$

This only holds if no other background process contributes to the four regions. In general this is not true and has to be considered. Therefore the number of events measured in each region is corrected for the number of events that other background processes contribute. This number is estimated from simulated events from $W\gamma$, $Z\gamma$ and $t\bar{t}$ production. Now the number of non-prompt muons in region A may be expressed as

$$N_{\mathrm{A}}^{\mathrm{F}} = \left(N_{\mathrm{C}} - N_{\mathrm{C}}^{\mathrm{EW}}\right) \cdot \left(\frac{N_{\mathrm{B}} - N_{\mathrm{B}}^{\mathrm{EW}}}{N_{\mathrm{D}} - N_{\mathrm{D}}^{\mathrm{EW}}}\right) \tag{7.22}$$

where $N_{\mathrm{i}}^{\mathrm{EW}}$ is the number of events in region i from $W\gamma$, $Z\gamma$ and $t\bar{t}$ production.

Monte Carlo studies show that the amount of real muons from $W\gamma\gamma$ in the control regions is small but not negligible. To account for this, the number of events is corrected using the signal-leakage of real muons into the control regions as determined from simulated $W\gamma\gamma$ events. Therefore 7.22 may be written

$$N_{\mathrm{A}}^{\mathrm{F}} = \left(N_{\mathrm{C}} - N_{\mathrm{C}}^{\mathrm{EW}} - c_{\mathrm{C}} N_{\mathrm{A}}^{\mathrm{S}}\right) \cdot \left(\frac{N_{\mathrm{B}} - N_{\mathrm{B}}^{\mathrm{EW}} - c_{\mathrm{B}} N_{\mathrm{A}}^{\mathrm{S}}}{N_{\mathrm{D}} - N_{\mathrm{D}}^{\mathrm{EW}} - c_{\mathrm{D}} N_{\mathrm{A}}^{\mathrm{S}}}\right), \tag{7.23}$$

where c_{i} is the signal leakage into region i, with $i \in \{\mathrm{A, B, C}\}$. It is derived from Monte Carlo as

$$c_{\mathrm{i}} = \left(\frac{N_{\mathrm{i}}^{W\gamma\gamma}}{N_{\mathrm{A}}^{W\gamma\gamma}}\right)_{\mathrm{MC}} . \tag{7.24}$$

A central assumption of this method is that the two variables used to define the sidebands are independent for background events. Since a selection of a pure sample of background events in the four regions is not possible, this assumption has to be tested on simulated events. In order to quantify the effect of a small correlation between the isolation and the $E_{\mathrm{T}}^{\mathrm{miss}}$ requirement an additional factor, R, is introduced. It is defined as

$$R = \frac{N_{\mathrm{D}}^{\mathrm{F}} \cdot N_{\mathrm{B}}^{\mathrm{F}}}{N_{\mathrm{A}}^{\mathrm{F}} \cdot N_{\mathrm{C}}^{\mathrm{F}}} \tag{7.25}$$

and derived from simulated events. If R is close to 1.0, the distribution of the two variables is uncorrelated, while other values indicate the contrary. Since the simulated $W\gamma\gamma$ sample does not contain enough events in the control regions to derive R, a sample of simulated di-photon events has been used, because it is expected to have the same background properties.

The R factor is set to 1.0 for the calculation of the central value of the non-prompt muon background contribution. The estimation of the R factor is not reliable in simulation due to large statistical uncertainties in the simulation. A conservative systematic uncertainty is applied by varying the R factor from one to the value obtained from simulated events.

The analytical solution of equation (7.23) for the number of events with non-prompt muons in the signal region $N_{\mathrm{A}}^{\mathrm{F}}$ is:

$$N_{\mathrm{A}}^{\mathrm{F}} = N_{\mathrm{A}} - N_{\mathrm{A}}^{\mathrm{EW}} - \frac{E \cdot (-1 + \sqrt{1 + F})}{G} \tag{7.26}$$

with E, F and G defined as

$$E = N_{\mathrm{C}} - N_{\mathrm{C}}^{\mathrm{EW}} + c_{\mathrm{C}}(N_{\mathrm{A}} - N_{\mathrm{A}}^{\mathrm{EW}}) - \frac{c_{\mathrm{B}}}{R}(N_{\mathrm{D}} - N_{\mathrm{D}}^{\mathrm{EW}}) - \frac{c_{\mathrm{D}}}{R}(N_{\mathrm{B}} - N_{\mathrm{B}}^{\mathrm{EW}}) \tag{7.27}$$

$$F = \frac{4}{E^2}(\frac{c_{\mathrm{B}} c_{\mathrm{C}}}{R} - c_{\mathrm{C}})((N_{\mathrm{A}} - N_{\mathrm{A}}^{\mathrm{EW}})(N_{\mathrm{C}} - N_{\mathrm{C}}^{\mathrm{EW}}) - \frac{1}{R}(N_{\mathrm{B}} - N_{\mathrm{B}}^{\mathrm{EW}})(N_{\mathrm{D}} - N_{\mathrm{D}}^{\mathrm{EW}})) \tag{7.28}$$

$$G = 2(\frac{c_{\mathrm{B}} c_{\mathrm{C}}}{R} - c_{\mathrm{D}}) \tag{7.29}$$

7.2.2 Definition of the control regions

In order to enhance the fraction of muons stemming from B-meson decays the events in region C and D are required to contain muons well separated from the primary vertex. Therefore the transverse impact parameter significance of the muon track is required to be $d_0^{\mathrm{sig}} = \frac{d_0}{\sigma(d_0)} > 4$. Since the final selection contains an requirement on the transverse mass, m_{T}, in addition to the $E_{\mathrm{T}}^{\mathrm{miss}}$ requirement, the definition of the control regions C and D is slightly changed, such that it inverts the m_{T} requirement in addition. The exact definition of the four regions is summarized in Table 7.7.

Requirement	A (Signal region)	B	C	D
Muon isolation	isolated	non-isolated	isolated	non-isolated
$E_{\mathrm{T}}^{\mathrm{miss}}$ [GeV]	> 25	> 25	< 25	< 25
m_{T} [GeV]	> 40	> 40	< 40	< 40
d_0^{sig}	< 3	< 3	> 4	> 4

Table 7.7: Definition of signal (A) and control regions (B, C, D) using muon isolation, missing transverse energy and transverse mass. The significance of the muon transverse impact parameter, d_0^{sig} is inverted in control regions C and D to enrich the muon contribution from the decay of heavy flavor mesons.

	A	B	C	D
$W\gamma$	35.4 ± 2.5	0.4 ± 0.2	< 0.1	< 0.1
$Z\gamma\gamma$	4.0 ± 0.2	$\pm < 0.1$	0.1 ± 0.1	< 0.1
$t\bar{t}$	8.3 ± 2.7	3.7 ± 1.9	< 0.1	0.9 ± 0.9
$\tau\nu\gamma\gamma$	1.0 ± 0.1	0.1 ± 0.1	< 0.1	< 0.1
WW, WZ, ZZ	2.658 ± 0.6	< 0.1	< 0.1	< 0.1
Total EW events (N^{EW})	51.8 ± 3.7	4.1 ± 1.9	0.1 ± 0.1	0.9 ± 0.9
Observed events	112	46	13	52

Table 7.8: The number of observed events in data and the contribution from $W\gamma$, $Z\gamma$ and $t\bar{t}$ processes (N^{EW}) predicted from simulated events in regions A, B, C and D for the inclusive selection. The estimation from simulated events is normalized to the process cross-section and luminosity.

7.2.3 Results

The number of events observed in each of the control regions as well as the number of events expected from Monte Carlo are summarized in Table 7.8 and Table 7.9 for the inclusive and the exclusive selection, respectively. Table 7.10 shows the signal-leakage parameters used to calculate the fake-muon background contribution in region A. Since the signal-leakage into regions C and D is zero, the calculation of G in Equation 7.29 diverges. This is a artifact of the mathematical methods and can be circumvented by setting c_{C} and c_{D} to zero before solving equation (7.23). This yields then

$$N_{\mathrm{A}}^{\mathrm{F}} = \frac{\left(N_{\mathrm{C}} - N_{\mathrm{C}}^{\mathrm{EW}}\right)\left(c_{\mathrm{B}} N_{\mathrm{A}} - \left(N_{\mathrm{B}} - N_{\mathrm{B}}^{\mathrm{EW}}\right)\right)}{c_{\mathrm{B}}\left(N_{\mathrm{C}} - N_{\mathrm{C}}^{\mathrm{EW}}\right) - \left(N_{\mathrm{D}} - N_{\mathrm{D}}^{\mathrm{EW}}\right)} \tag{7.30}$$

Using the results from Table 7.8 and 7.10, the number of fake-muon events in the signal region and its uncertainty due to the limited number of events available in data and the simulated samples can be calculated.

In order to evaluate the systematic uncertainty due to correlations between the muon isolation and $E_{\mathrm{T}}^{\mathrm{miss}}$ and m_{T}, their correlation has been checked using a sample of di-photon events simulated with Sherpa. The muon isolation distribution for non-prompt muons from this sample of simulated events can be seen in Figure 7.11 for all four regions. If no correlations between the muon isolation and $E_{\mathrm{T}}^{\mathrm{miss}}$ and m_{T} exists, the distribution for both regions should be identical. Given the large statistical uncertainties this seems plausible. The R factor of 1.50 ± 0.75 is also compatible with one within the

	A	B	C	D
$W\gamma$	20.5 ± 1.9	0.1 ± 0.1	< 0.1	< 0.1
$Z\gamma$	2.8 ± 0.2	< 0.1	< 0.1	< 0.1
$t\bar{t}$	< 0.1	< 0.1	< 0.1	< 0.1
$\tau\nu\gamma\gamma$	0.4 ± 0.1	< 0.1	< 0.1	< 0.1
WW, WZ, ZZ	1.0 ± 0.3	< 0.1	< 0.1	< 0.1
Total EW events (N^{EW})	24.6 ± 2.0	0.1 ± 0.1	< 0.1	< 0.1
Observed data	54	5	3	3

Table 7.9: The number of observed events in data and the contribution from $W\gamma$, $Z\gamma$ and $t\bar{t}$ processes (N^{EW}) predicted from simulated events in regions A, B, C and D for the exclusive selection. The estimation from simulated events is normalized to the process cross-section and luminosity.

	inclusive selection	exclusive selection
c_{B}	0.006 ± 0.002	0.001 ± 0.001
c_{C}	< 0.001	< 0.001
c_{D}	< 0.001	< 0.001

Table 7.10: Signal leakage parameters obtained from simulated $W\gamma\gamma$ events.

uncertainties. Nevertheless the difference between the nominal estimate (i.e. $N^{\mathrm{F}}_{\mathrm{A}}|_{R=1}$) and the estimate using the larger R-factor (i.e. $N^{\mathrm{F}}_{\mathrm{A}}|_{R=1.5}$) is taken as a systematic uncertainty. Therefore the final estimate of the number of fake-muon background events is $N^{\mathrm{F}}_{\mathrm{A}} = 10.5 \pm 3.8\,(\text{stat.}) \pm 3.5\,(\text{sys.})$ for the inclusive selection, and $N^{\mathrm{F}}_{\mathrm{A}} = 4.8 \pm 4.5\,(\text{stat.}) \pm 1.6\,(\text{sys.})$ for the exclusive selection.

7.3 Other backgrounds

Events from other processes than $W\gamma\gamma$ containing a real muon and two photons that do not stem from a jet are estimated using the simulation. The processes considered are in decreasing order of importance:

$Z\gamma\gamma$ production This process has the same signature as the signal process, if one of the two muons from the decay of the Z boson is out of the acceptance of the ATLAS detector and thus gives rise to missing transverse momentum.

$t\bar{t}$ production The top quark decays almost always into a b quark and a W bosons. One of the W boson decays into a muon and a neutrino, while the other decays into an electron and a neutrino, and the electron is mis-identified as a photon.

WW, WZ, ZZ production Typically the photons are mis-identified electrons and the muon either stems from a genuine $W \to \mu\nu$ decay or from the decay of a τ lepton.

$W(\to \tau\nu)\gamma\gamma$ production This process has the same signature as the signal process if the τ lepton decays into a muon and two neutrinos.

The number of events from each of these processes passing the inclusive and exclusive selection is summarized in Table 7.11. The systematic uncertainties on the background estimates for these processes

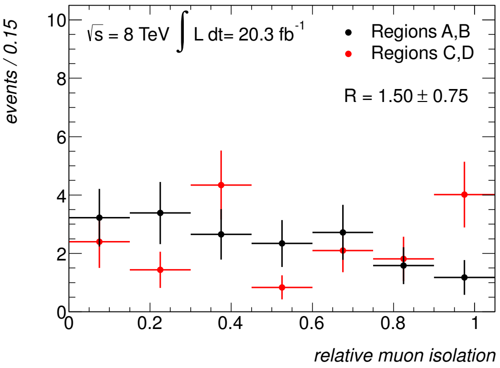

Figure 7.11: Muon isolation distribution for the different regions from simulated di-photon events. In addition, the R-value is given.

process	**number of events**	
	inclusive	*exclusive*
$Z\gamma\gamma$	4.1 ± 0.2 (stat.) ± 0.2 (sys.)	2.9 ± 0.2 (stat.) ± 0.2 (sys.)
$W(\to \tau\nu)\gamma\gamma$	1.0 ± 0.1 (stat.) ± 0.1 (sys.)	0.4 ± 0.1 (stat.) ± 0.1 (sys.)
$t\bar{t}$	3.7 ± 2.0 (stat.) ± 0.8 (sys.)	< 0.1
WW, WZ, ZZ	2.6 ± 0.6 (stat.) ± 0.4 (sys.)	0.9 ± 0.3 (stat.) ± 0.1 (sys.)
total	11 ± 2 (stat.) ± 1 (sys.)	4.2 ± 0.4 (stat.) ± 0.3 (sys.)

Table 7.11: Number of background events with a real muon and two real photons passing the inclusive and exclusive selection.

are derived in the same way as described in Section 8.3 for the efficiency estimate. Basic properties of the simulated background processes are listed in Appendix A.5.

7.4 Total background estimate

With the results of the background estimates, the number of measured signal events N_{sig} can be calculated by subtracting the number of background events from the number of candidate events measured in the data. The result is shown in Table 7.12 for the inclusive and exclusive selection. The purity, i.e. the fraction of $W\gamma\gamma$ events in the selected sample, is (50 ± 20) % for the inclusive, and (60 ± 20) % for the exclusive selection.

7.5 Comparisons between data and simulations

The validity of the background estimation is assessed by comparing kinematic properties between data and the simulation. Thus the shape of the properties for the different background components must be known. However, the method used for the background estimation only yields the overall normalization of the background events as a result. One possibility to obtain information about the shape is to carry out the background estimation in several bins of the corresponding variable. This is not feasible due to low statistics available for this analysis. Instead the shape is taken from control regions for the data-driven

	number of events	
	inclusive	*exclusive*
Data	112	54
Fake photon background	34 ± 8 (stat.) ± 9 (sys.)	15 ± 6 (stat.) ± 6 (sys.)
Non-prompt muon background	10 ± 4 (stat.) ± 4 (sys.)	5 ± 5 (stat.) ± 2 (sys.)
Other background	11 ± 2 (stat.) ± 1 (sys.)	4.2 ± 0.4 (stat.) ± 0.3 (sys.)
N_{bkg}	55 ± 9 (stat.) ± 10 (sys.)	24 ± 7 (stat.) ± 6 (sys.)
N_{sig}	57 ± 14 (stat.) ± 10 (sys.)	31 ± 10 (stat.) ± 6 (sys.)

Table 7.12: The number of events passing the full selection and the number of events for the different background contributions. In addition the measured signal determined as $N_{\text{obs}} - N_{\text{bkg}}$ is presented.

background estimates and from simulated events for the background estimates based on Monte Carlo simulation.

The shape of the kinematic distributions for events that contain one or more fake photons is taken from the same control region used to derive the templates used in the 2D isolation fit. For example the AT control region is used to determine the shape for events where the leading photon is fake. The kinematic distributions for the non-prompt muon background events are obtained from a control region B of the ABCD method, i.e. non-isolated muons. The distributions are normalized and then scaled according to the data-driven background estimate. The statistical uncertainty due to the limited number of events in the control regions is taken as shape uncertainty and added in quadrature to the uncertainty on the overall normalization.

The transverse momentum distribution for the leading photon and the di-photon invariant mass distribution, are shown in Figure 7.12 for the inclusive selection. In the upper panel the background estimates are shown as stacked histograms. The normalization of the signal component is scaled to match the number of observed signal events in data. The $E_{\text{T}}^{\text{miss}}$ and N_{jets} distributions for the inclusive selection are shown in Figure 7.13. The agreement between data and simulation is generally good and the small differences can be attributed to fluctuations. This indicates that the background estimates provide reasonable results and can be used in the calculation of the cross-section. In addition, the good agreement, especially at high momenta and invariant masses, shows that no signs of physics beyond the Standard Model are present in the observed data. Kinematic distributions for the exclusive selection can be found in Appendix A.6.

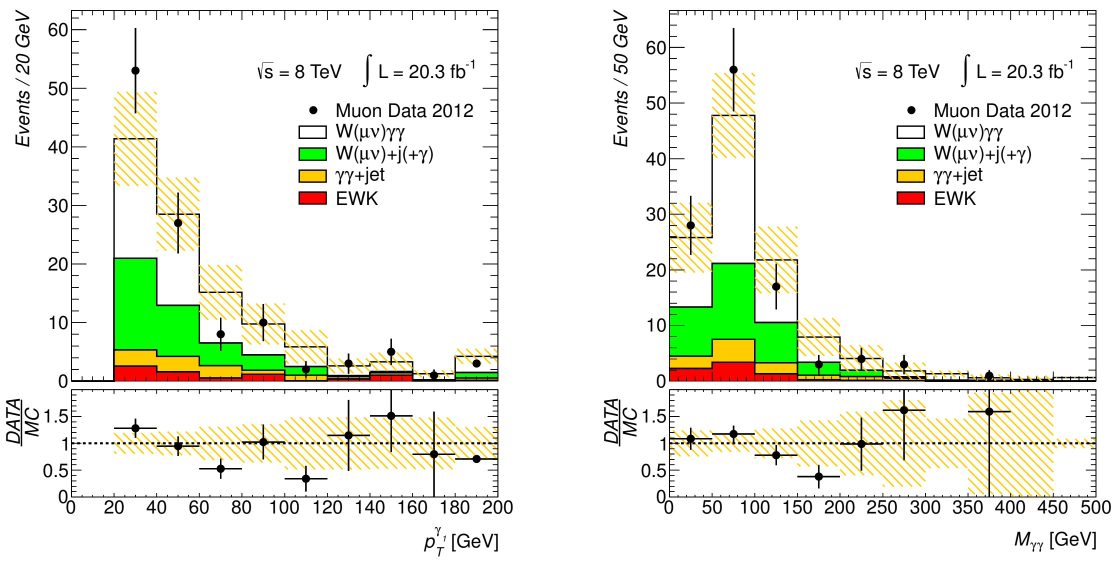

(a) (b)

Figure 7.12: The transverse momentum distribution of the leading photon (a) and the di-photon invariant mass (b) in the signal region for the inclusive selection. The prediction from the simulation is shown as a stacked histogram with the uncertainties indicated by the yellow hatched band. The rightmost bin is an overflow bin. The prediction for the $W\gamma\gamma$ process is normalized to the number of signal events observed in data.

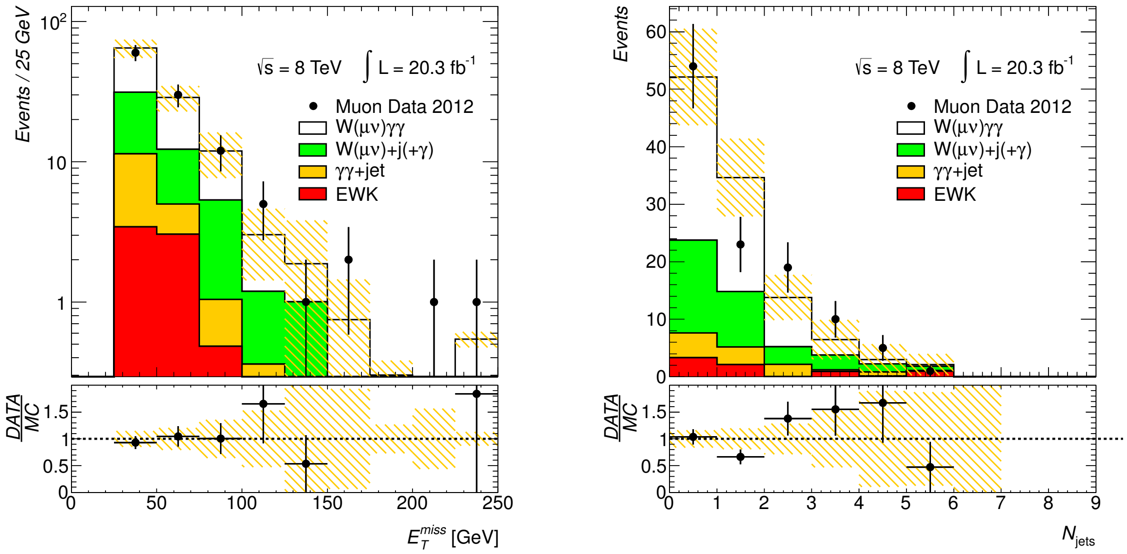

(a) (b)

Figure 7.13: The $E_{\mathrm{T}}^{\mathrm{miss}}$ (a) and N_{jets} (b) distribution for the inclusive selection in the signal region. The prediction from the simulation is shown as a stacked histogram with the uncertainties indicated by the yellow hatched band. The rightmost bin is an overflow bin. The prediction for the $W\gamma\gamma$ process is normalized to the number of signal events observed in data.

CHAPTER 8

Cross-section measurement

In particle physics cross-section measurements are an important test of the Standard Model. Any deviation from the predicted cross-section might point to contributions of physics beyond the Standard Model, that affect the process under study. In addition, the $W\gamma\gamma$ process is an irreducible background for the HW associated production with a subsequent $H \rightarrow \gamma\gamma$ decay, and the cross-section measurement helps to constrain this background.

Experimentally, the cross-section can be determined using the well known equation

$$\sigma = \frac{N_{\text{obs}} - N_{\text{bkg}}}{A \cdot \epsilon \cdot \mathcal{B} \cdot L_{\text{int}}} . \tag{8.1}$$

Here, $N_{\text{obs}} - N_{\text{bkg}}$ is the difference between the observed number of selected events and the estimated number of background events and hence corresponds to the number of signal events observed. The acceptance, A, corrects for the events that fall outside the geometric and kinematic constraints of the selection. The selection efficiency, ϵ, describes which percentage of the events within the acceptance are actually reconstructed. The branching ratio, $\mathcal{B}$, is the fraction of W boson that decay into muons. Since only W boson that subsequently decay into a muon and a muon-neutrino are considered in this analysis, the branching ratio is set to one, $\mathcal{B} = 1$, and the cross-section for the $pp \rightarrow \mu\nu\gamma\gamma$ is presented as the result. Finally, L_{int} is the integrated luminosity that is used to collect N_{obs} events.

In this chapter the components necessary for the calculation of the cross-section, the results obtained from the measurement and the comparison of the cross-section to Standard Model predictions will be presented.

8.1 Definition of the cross-section

This thesis presents the measurement of the $W\gamma\gamma$ production cross-section in two restricted phase-space regions, which are identical to the inclusive and exclusive selection defined in Chapter 6. Thus the extrapolation of the measured to the total cross-section is omitted and the theoretical uncertainties of the acceptance correction do not come into play. To facilitate the comparison to theory calculations an *extended fiducial* cross-section $\sigma_{\text{ext-fid}}$ will be measured. For this measurement the phase-space region is extended such that it includes photons that fall into region $1.37 < |\eta| < 1.52$ and a different isolation requirement, $\epsilon_h < 0.5$, for the photons that is better suited for particle level calculations. The relative

Muon	p_{T}^{μ}	$>$	20 GeV
	$\lvert\eta^{\mu}\rvert$	$<$	2.5
	p_{T}^{ν}	$>$	25 GeV
W boson	m_{T}	$>$	40 GeV
Photon	E_{T}^{γ}	$>$	20 GeV
	$\lvert\eta^{\gamma}\rvert$	$<$	2.37
	$\Delta R(\mu,\gamma)$	$>$	0.7
	$\Delta R(\gamma,\gamma)$	$>$	0.4
	ϵ_h	$<$	0.5

Table 8.1: Definition of the extended fiducial phase-space region for the evaluation of the cross-section.

Jet	anti-k_{t} $R = 0.4$		
	$p_{\mathrm{T}}^{\mathrm{jet}}$	$>$	30 GeV
	$\left\lvert\eta^{\mathrm{jet}}\right\rvert$	$<$	4.4
	$\Delta R(\mu,\mathrm{jet})$	$>$	0.3
	$\Delta R(\gamma,\mathrm{jet})$	$>$	0.3

Table 8.2: Definition of particle level jets for the exclusive selection.

photon isolation, ϵ_h, is defined as

$$\epsilon_h = \frac{E_{\mathrm{iso}}}{E_{\gamma}}\,, \tag{8.2}$$

where E_{iso} is the energy deposited by other particles than the photon in a cone with radius, $R = 0.4$, around the photon. The extended fiducial phase-space region used for the cross-section measurement is summarized in Table 8.1.

For the measurement using the exclusive selection, the definition of the extended fiducial phase-space region is modified such, that no additional particle-level jet with $p_{\mathrm{T}} > 30\,\mathrm{GeV}$ and $|\eta| < 4.4$ is allowed. In addition, the jet is required to be well separated from the muon, $\Delta R(\mu,\mathrm{jet}) > 0.3$, and the photons, $\Delta R(\gamma,\mathrm{jet}) > 0.3$. The jet definition used is summarized in Table 8.2.

8.2 Acceptance correction

The acceptance correction extrapolates the cross-section measured in the fiducial phase-space region to the extended fiducial phase-space region. It is defined as the fraction of events in the fiducial volume N_{fid} with respect to all events in the extended fiducial volume $N_{\text{ext-fid}}$, i.e.

$$A = \frac{N_{\mathrm{fid}}^{\mathrm{part}}}{N_{\text{ext-fid}}^{\mathrm{part}}}\,. \tag{8.3}$$

The additional superscript, *part*, indicates that the acceptance correction is done entirely at particle level and has to be determined using from simulated $W\gamma\gamma$ events. The central value of the acceptance

Source (%)	inclusive	exclusive
PDF	± 0.1	± 0.1
Scales	± 1.5	± 3.9
Parton Shower	± 0.9	± 1.9
Total	± 1.8	± 4.4

Table 8.3: The systematic uncertainties on the acceptance correction for the inclusive and exclusive selection.

corrections is derived using events simulated by the Sherpa program.

The acceptance correction is only susceptible to so-called *theory uncertainties*, which are independent of the detector. The uncertainties arise from the uncertainties on the PDF, the choice of the factorization and renormalization scale, μ_F and μ_R, respectively, and the modelling of the parton shower. The PDF uncertainties are evaluated using the difference between the nominal and an alternate PDF. The nominal choice is CT10 [29], and as alternate PDF MSTW2008 [28] was chosen. The scale uncertainties are taken as the maximum change in the acceptance correction derived from events simulated with different scales. The factorization and renormalization scale are independently varied by a factor of two around their nominal value with the constraint $0.5 \leq \mu_\mathrm{F}/\mu_\mathrm{R} \leq 2.0$, to exclude the two extreme choices. The difference between the acceptance correction calculated using events simulated by Sherpa and AlpGen is used as the uncertainty due to the parton shower modelling. Since the programs were configured with different PDFs to describe the proton structure, the events in the AlpGen sample are reweighted to the PDF used in the Sherpa sample using LhaPdf [127]. This avoids double-counting the uncertainty due to the choice of the PDF.

The value of the acceptance correction from the fiducial to the extended fiducial volume for the inclusive selection is

$$A_\mathrm{incl} = (89.2 \ \pm 0.3\,(\mathrm{stat.}) \ \pm 1.8\,(\mathrm{sys.}))\,\%\,.$$

For the exclusive selection it results in

$$A_\mathrm{excl} = (89.8 \ \pm 0.4\,(\mathrm{stat.}) \ \pm 4.4\,(\mathrm{sys.}))\,\%\,.$$

The total systematic uncertainty is obtained as the square root of the quadratic sum of the individual uncertainties. The breakdown of the uncertainties is given in Table 8.3. The dominant uncertainty for both selections is the scale dependence. In general the exclusive selection is more susceptible to these theory uncertainties due to the additional selection on the jets.

8.3 Efficiency correction

The efficiency correction ϵ transforms the cross-section from the detector to the particle level. It includes corrections for inefficiencies of the trigger and reconstruction algorithms, as well as inefficiencies due to the detector resolution. Thus the efficiency correction is given as the number of events passing the fiducial selection at detector level, $N_\mathrm{fid}^\mathrm{det}$, divided by the number of events in the fiducial phase-space region at particle level, $N_\mathrm{fid}^\mathrm{part}$, i.e.

$$\epsilon = \frac{N_\mathrm{fid}^\mathrm{det}}{N_\mathrm{fid}^\mathrm{part}}\,. \tag{8.4}$$

Similarly to the acceptance, the efficiency is determined using simulated $W\gamma\gamma$ events. Therefore it relies on the correct description of the actual reconstruction efficiency and energy scale and resolution in the simulation. Although the simulation is corrected such that it reproduces the data as explained in Chapter 5, a difference between data and simulation might remain due to the uncertainty on the corrections. Therefore the uncertainties on the simulation corrections are propagated to an uncertainty on the efficiency.

The individual sources of uncertainties on the efficiency correction considered are

Trigger efficiency The trigger used for this analysis requires that one muon above a transverse momentum threshold of $p_{\mathrm{T}} > 18\,\mathrm{GeV}$ and two photons with $p_{\mathrm{T}} > 10\,\mathrm{GeV}$ are present. The efficiency of all three requirements is considered to be independent and can therefore be estimated separately. The muon trigger efficiency in data is estimated using events that contain a $Z \to \mu^+\mu^-$ decay. It is compared to the trigger efficiency obtained from Monte Carlo simulation and the residual differences are corrected in the simulation. The uncertainty associated with this corrections is considered as the systematic uncertainty due to the muon trigger. The photon trigger efficiency is determined from data using events from radiative Z boson decays, i.e. $Z \to l^+l^-\gamma$, and is found to be $(99.63 \pm 0.06)\,\%$ [128]. The uncertainty on the efficiency of the photon trigger is applied as systematic uncertainty.

Muon momentum scale and resolution As mentioned in Section 5.2, the momentum scale and the resolution of muons obtained from simulation are adjusted to match the ones observed in data. The main systematic uncertainties of these corrections arise from a possible momentum dependence on the correction. Since the corrections are derived from $Z \to \mu^+\mu^-$ events, the majority of the muons has a transverse momentum between 20 GeV and 50 GeV. The momentum dependence has been tested with muons from lower di-muon mass resonances, e.g. $J/\psi \to \mu^+\mu^-$ [104]. The difference was found to be small and a systematic uncertainty of 0.2 % has been assigned.

Muon reconstruction efficiency The reconstruction efficiency of muons observed in data and simulation is slightly different. The residual differences are corrected for in the simulation. The systematic uncertainties associated to this correction originates mainly from residual backgrounds in the $Z \to \mu^+\mu^-$ sample used to derive the corrections, and from the definition of the probe muons used in the tag-and-probe analysis (cf. Section 5.2). It was found that a systematic uncertainty of 0.2 % is sufficient to cover the difference [129].

Photon energy scale and resolution The agreement of the energy scale and resolution of photons between data and simulation is measured indirectly using electrons from $Z \to e^+e^-$ decays. The main systematic uncertainty of this measurement is the imperfect knowledge of the amount of material in front of the calorimeters and varies from about −2 % to 1 % [130].

Photon identification efficiency The photon identification efficiency has been determined in data using several methods. These methods include the use of radiative Z boson decays and extrapolation from electron to photon showers, among others. The main systematic uncertainties arise from the limited statistics available to derive the identification efficiency in data and the imperfect knowledge of the amount of material in front of the calorimeter. In addition, the background contamination and the difference between the methods yield systematic uncertainties of similar size. In total the uncertainty is 2.5 % for photons with transverse momentum below 40 GeV and 1.5 % for those above with the exception of unconverted photons with $p_{\mathrm{T}} > 40\,\mathrm{GeV}$ and $|\eta| > 1.81$, whose uncertainty is 2.5 %. The uncertainty is fully correlated between the two photons of the $W\gamma\gamma$ final state, if they are both in the same detector region and of the same category, i.e. both converted or unconverted. Otherwise the uncertainty is split into different categories whose correlations are assessed individually. For example the uncertainty due to additional material in front of the calorimeter is fully correlated among all measurements in the same η bin. The combined uncertainty due to the differences between data and simulation for the photon identification efficiency is given as

$$\sigma_{\mathrm{ID}} = \sqrt{\sigma^2_{\gamma,1}\sigma^2_{\gamma,2} + 2C \cdot \sigma_{\gamma,1} \cdot \sigma_{\gamma,2}}\,, \tag{8.5}$$

where $\sigma_{\gamma,i}$ is the uncertainty for the leading and subleading photon, respectively, and C is the correlation between both uncertainties.

Jet energy scale and resolution As explained in Section 5.3, the jet energy scale uncertainty is between 1 % and 6 % depending on the jet momentum and rapidity. The jet energy resolution is measured in data, and the simulation is corrected to match the resolution in data. The dominant systematic uncertainties of this measurement are the differences between two independent measurements and residual differences between the data and the simulation. The systematic uncertainty on the resolution varies between 10 % and 20 %.

Missing transverse momentum imbalance scale The uncertainty on the scale of the transverse momentum imbalance is composed of several parts. First, the energy scale and resolution uncertainties on the muon, photon and jets are propagated to the calculation of the $E_{\mathrm{T}}^{\mathrm{miss}}$. In addition, the scale and resolution uncertainty due to the *soft energy term* is considered. The soft energy term covers the contribution of particles with transverse momentum below 20 GeV, which are not included by other uncertainties. Its uncertainty is assessed by studying the agreement of $E_{\mathrm{T}}^{\mathrm{miss}}$ between data and simulation in leptonic decays of Z bosons with no additional jet with $p_{\mathrm{T}} > 20\,\mathrm{GeV}$. The uncertainty on the soft term from these studies is found to be 3.6 % for the scale, and 2.3 % for the resolution of the soft term.

Pileup description Since the distribution of average interactions per bunch-crossing, $\langle\mu\rangle$, was not known at the time the Monte Carlo simulation started, a triangular distribution was assumed to cover the different scenarios for the expected LHC performance. As the $\langle\mu\rangle$-distribution is known now, after the data-taking has finished, the simulated events are reweighted to obtain the distribution in data. The uncertainty associated with this reweighting is taken as systematic uncertainty on the pile-up description of the simulation.

For each of the above mentioned uncertainty sources, the efficiency is calculated according to Equation 8.4 for the nominal value and for the values corresponding to one standard-deviation in both directions. The larger difference to the nominal value is taken as systematic uncertainty

The resulting efficiency correction for the inclusive selection is

$$\epsilon_{\mathrm{incl}} = (47.7\ \pm 0.8\,(\mathrm{stat.})\ \pm 2.0\,(\mathrm{sys.}))\,\%\,.$$

For the exclusive selection it amounts to

$$\epsilon_{\mathrm{excl}} = (46.4\ \pm 1.2\,(\mathrm{stat.})\ \pm 2.4\,(\mathrm{sys.}))\,\%\,.$$

All sources of uncertainty are considered as uncorrelated, and the total uncertainty is the square root of the quadratic sum of all sources. A breakdown of the uncertainties is given in Table 8.4. The dominant systematic uncertainty is the uncertainty due to the modelling of the photon identification efficiency. It amounts to ±1.5 % for both channels. As expected, the jet energy scale uncertainty is only significant in the exclusive channel (±1.1 %), where it is the second largest uncertainty. This can be understood, since the jet veto is very sensitive to the energy measurement of the jets due to the steeply falling p_{T}

Source (%)	inclusive	exclusive
$E_{\mathrm{T}}^{\mathrm{miss}}$ soft term resolution	± 0.3	± 0.4
$E_{\mathrm{T}}^{\mathrm{miss}}$ soft term scale	± 0.4	± 0.3
Jet energy resolution	± 0.3	± 0.4
Jet energy scale	± 0.1	± 1.1
Jet pileup suppression	± 0.0	± 0.1
Muon efficiency	± 0.1	± 0.1
Muon energy scale	± 0.1	± 0.2
Muon resolution ID	± 0.1	± 0.1
Muon resolution MS	± 0.0	± 0.0
Photon efficiency	± 1.5	± 1.5
Photon energy resolution	± 0.1	± 0.3
Photon energy scale	± 0.5	± 0.6
Pileup modelling	± 0.2	± 0.4
MC generator	± 0.8	± 1.0
Total	± 2.0	± 2.4

Table 8.4: The relative systematic uncertainties on the efficiency correction for the inclusive and exclusive selection.

distribution. In total the relative systematic uncertainty is 3.9 % (4.7 %) for the inclusive (exclusive) selection and thus considerably smaller than the uncertainties on the background estimates presented in the previous chapter.

8.4 Cross-section extraction

The extended fiducial cross-section is calculated considering only $W \to \mu\nu$ decays of the W boson. As discussed in Section 8.1, the extended fiducial cross-section is defined as

$$\sigma_{\text{ext-fid}}^{pp\to W(\to\mu\nu)\gamma\gamma} = \frac{N_{\text{obs}}^{\mu\nu\gamma\gamma} - N_{\text{bkg}}}{A \cdot \epsilon \cdot L_{\text{int}}}\,, \tag{8.6}$$

where $N_{\text{obs}}^{\mu\nu\gamma\gamma}$ is the total number of events observed after the selection described in Chapter 6. N_{bkg} is the number of background events estimated as described in Chapter 7 and A and ϵ are the acceptance and efficiency corrections described earlier in this chapter. The integrated luminosity is obtained with the procedure described in Section 3.2 and amounts to $(20.3 \pm 0.6)\,\text{fb}^{-1}$. All inputs needed for the cross-section extraction are summarized in Table 8.5.

The result of the extended fiducial cross-section for the $pp \to W(\to \mu\nu)\gamma\gamma$ process with two isolated photons with $E_{\mathrm{T}} > 20\,\text{GeV}$ measured at $\sqrt{s} = 8\,\text{TeV}$ is

$$\sigma_{\text{ext-fid}}^{pp\to W(\to\mu\nu)\gamma\gamma} = (6.5\ \pm 1.6\,(\text{stat.})\ \pm 1.1\,(\text{sys.})\ \pm 0.2\,(\text{lumi.}))\,\text{fb}^{-1}\,.$$

When no jets with $p_{\mathrm{T}} > 30\,\text{GeV}$ and $|\eta| < 4.4$ are allowed the cross-section is reduced to

$$\sigma_{\text{ext-fid}}^{pp\to W(\to\mu\nu)\gamma\gamma} = (3.6\ \pm 1.2\,(\text{stat.})\ \pm 0.8\,(\text{sys.})\ \pm 0.1\,(\text{lumi.}))\,\text{fb}^{-1}\,.$$

Input	inclusive	exclusive
$N^{\text{obs}}_{\mu\nu\gamma\gamma}$	112	54
$N^{\text{bkg}}_{\mu\nu\gamma\gamma}$	55 ± 9 (stat.) ± 10 (sys.)	24 ± 7 (stat.) ± 6 (sys.)
A	(89.2 ± 0.3 (stat.) ± 1.8 (sys.)) %	(89.8 ± 0.4 (stat.) ± 4.4 (sys.)) %
ϵ	(47.7 ± 0.8 (stat.) ± 2.0 (sys.)) %	(46.4 ± 1.2 (stat.) ± 2.4 (sys.)) %
L_{int}	$(20.3 \pm 0.6)\,\text{fb}^{-1}$	

Table 8.5: The values used for the calculation of the cross-section.

8.5 Comparison to Standard Model predictions

The results are compared to Standard Model predictions at next-to-leading order in perturbative QCD. The predictions are obtained using VBFNLO[1] [35]. It allows to specify arbitrary cuts and is thus well suited to calculate the cross-section in the extended fiducial phase-space region used in this measurement. The calculation has been done using the MSTW2008 NLO PDF set, interfaced to VBFNLO using the LHAPDF library. The factorization and renormalization scales have been set to the invariant mass of the $W\gamma\gamma$ system. A detailed listing of all settings used to calculate the cross-section can be found in Appendix A.7.

Uncertainties on the theory calculation

As uncertainties on the theory prediction, the factorization and renormalization scale uncertainties, the parton distribution function uncertainty and the uncertainty on the value of the strong coupling constant α_S have been considered. The factorization and renormalization scale uncertainties are evaluated by varying them independently by a factor two. The two extreme cases $\mu_R = 4\mu_F$ and $\mu_F = 4\mu_R$ are excluded. The difference from the nominal cross-section is taken as the uncertainty. The combination of the factorization and normalization uncertainties are in the following referred to as *scale dependence*.

The MSTW2008 parton distribution functions are obtained by a global fit to multiple datasets of hard-scattering data [28]. The experimental uncertainty on these datasets is propagated to the fit parameters used to determine the PDF. After diagonalizing the covariance matrix of the parameters, the up-and-down variations of each orthogonal eigenvector are used to obtain a modified version of the nominal PDF, called an *error set*. Since the parametrization used for MSTW2008 contains 20 free parameters, the PDF contains 40 error PDFs, one up and one down variation of each parameter.

The uncertainty on the PDF is propagated to the uncertainty on the theory calculation by calculating the cross-section for each of the 40 error PDFs. The difference between the up-and-down variation of one eigenvector i is used as uncertainty by this eigenvector. By construction the eigenvectors are independent, and the total uncertainty is obtained by the quadratic sum of the uncertainties of all eigenvectors. Using the symmetric prescription of the uncertainty [131] this yields

$$\Delta\sigma = \frac{1}{2}\sqrt{\sum_{i=1}^{20}(\sigma^i_+ - \sigma^i_-)^2}\,, \tag{8.7}$$

where i runs over all eigenvectors and σ^i_+ (σ^i_-) is the cross-section obtained when using the up (down) variation of eigenvector i. The factor $^1/_2$ appears since the difference between the up and the down

---

[1] Version 2.7.0beta4

Theory uncertainties [%]		
	inclusive	exclusive
Scale dependence	7.3	3.4
PDF	2.2	1.8
α_S	1.9	1.0
Total	7.9	4.9

Table 8.6: The breakdown of the uncertainties on the theory calculation of the cross-section of the $W(\to \mu\nu)\gamma\gamma$ process for the inclusive and exclusive cross-section.

variation corresponds to twice the uncertainty. The error sets used for the calculation correspond to the 90 % confidence level on the eigenvectors to be consistent with the current policy within the ATLAS collaboration.

The value of $\alpha_S(M_Z)$ has to be obtained from experimental measurements, thus it is subject to experimental uncertainties. The impact of the uncertainties on the theory prediction is evaluated as follows. The MSTW2008 PDF set provides two PDFs in which the value of $\alpha_S(M_Z)$ is changed according to its 90 % confidence level. The cross-section is calculated using each of these PDFs and the largest change is taken as uncertainty. The `ALFA_S` parameter, which defines the value of the strong coupling at the Z mass used in the VBFNLO calculation is set to the same value used by the MSTW2008 PDF.

The breakdown of all sources of theory uncertainties is given in Table 8.6. The dominant uncertainty is the scale dependence. This indicates that the inclusion of higher orders in the strong coupling constant will have a measurable impact on the prediction. The PDF and α_S uncertainties are on the order of 2 % and small compared to the scale dependence.

The total result of the parton level cross-section calculation for the $W(\to \mu\nu)\gamma\gamma$ process obtained from VBFNLO, is for the inclusive channel

$$\sigma_{\text{ext-fid}}^{\text{VBFNLO}} = (3.0 \pm 0.2)\,\text{fb}\,,$$

and for the exclusive channel

$$\sigma_{\text{ext-fid}}^{\text{VBFNLO}} = (1.8 \pm 0.1)\,\text{fb}\,.$$

8.5.1 Parton-to-particle level corrections

Since VBFNLO is a parton level Monte Carlo program, the calculated cross-section has to be corrected to the particle level to allow for a meaningful comparison with data. The correction from parton to particle level will mostly affect the photon isolation and the jet definition, due to the fragmentation and hadronization of quarks and gluons. It is applied as a multiplicative correction factor,

$$\sigma_{\text{ext-fid}}^{\text{theory}} = \sigma_{\text{ext-fid}}^{\text{VBFNLO}} \cdot C^{\text{parton}\to\text{particle}}\,, \tag{8.8}$$

where $\sigma_{\text{ext-fid}}^{\text{theory}}$ is the theory prediction for the cross-section at particle level, $\sigma_{\text{ext-fid}}^{\text{VBFNLO}}$ is the parton level cross-section obtained from VBFNLO and $C^{\text{parton}\to\text{particle}}$ is the parton to particle level correction.

The photon isolation correction covers differences of the isolation of photons between parton and particle level. This is necessary since the parton shower and hadronization turns the original quark or gluon into a broad object. Even if the parton falls outside the isolation cone of the photons it might well be that some of the particles produced in the hadronization fall inside and spoil the isolation of the

Parton-to-particle level correction		
	inclusive	exclusive
$C^{\text{parton}\to\text{particle}}$	1.11 ± 0.01 (stat.) ± 0.01 (sys.)	1.11 ± 0.02 (stat.) ± 0.03 (sys.)

Table 8.7: The parton to particle level corrections factors for jet production and photon isolation as obtained from SHERPA.

photon. In addition the different parton and particle level input to the jet algorithm is corrected for. At parton level the quark or gluon present in the final state due to real emissions from NLO diagrams is used as input. At particle level the jet algorithm operates on the stable particles after the fragmentation and hadronization of the parton. Since the inclusive extended fiducial phase-space region has no explicit dependence on jets, this will only affect the prediction for the exclusive measurement.

$C^{\text{parton}\to\text{particle}}$ is determined using $W\gamma\gamma$ events simulated by SHERPA. Since SHERPA is a multi-leg generator, the real emissions of quarks and gluons are simulated at parton level and, after the subsequent parton shower, at particle level. Therefore it is well suited to derive the correction. The correction is defined as the ratio of events inside the extended fiducial phase-space region between particle and parton level,

$$C^{\text{parton}\to\text{particle}} = \frac{N^{\text{particle}}_{\text{ext-fid}}}{N^{\text{parton}}_{\text{ext-fid}}}\,. \tag{8.9}$$

Here, $N^{\text{parton}}_{\text{ext-fid}}$ is the number of events falling inside the extended fiducial phase-space region at parton level, and $N^{\text{particle}}_{\text{ext-fid}}$ is the number of events inside the extended fiducial phase-space region at particle level.

The value of the correction factor depends on the modelling of the parton shower. Therefore the correction factor has also been derived using events simulated with ALPGEN, which uses a different parton shower model. The difference between the correction factor obtained from SHERPA and ALPGEN is used as systematic uncertainty. The result for $C^{\text{parton}\to\text{particle}}$ is given in Table 8.7 for the inclusive and exclusive extended fiducial phase-space region.

After applying the corrections described above, the particle level cross-section for the $W(\to\mu\nu)\gamma\gamma$ process in the extended fiducial phase-space region for the inclusive selection is

$$\sigma^{\text{theory}}_{\text{ext-fid}} = (3.4 \pm 0.3)\,\text{fb}$$

and for the exclusive selection

$$\sigma^{\text{theory}}_{\text{ext-fid}} = (1.9 \pm 0.1)\,\text{fb}\,.$$

8.5.2 Cross-section comparison

The measured production cross-sections for the extended fiducial phase-space region given in Table 8.1 are compared to anNLO prediction made by the VBFNLO generator. The results are listed in Table 8.8 for the inclusive and exclusive selection, respectively. The measured cross-sections are found to be higher than the VBFNLO predictions. The probability that a discrepancy like the one observed or worse happens due to fluctuations, i.e. the *p-value*, is 7.5 % for the inclusive and 11.3 % for the exclusive measurement. Although both measurements have small p-values this does not allow to conclude that the Standard Model prediction is not in agreement with the data. Both measurements are fully correlated since

	$\sigma_{\text{ext-fid}}^{pp\to W(\to\mu\nu)\gamma\gamma}$[fb]	$\sigma_{\text{ext-fid}}^{\text{theory}}$[fb]
inclusive	6.5 ± 1.6 (stat.) ± 1.1 (sys.) ± 0.2 (lumi.)	3.4 ± 0.3
exclusive	3.6 ± 1.2 (stat.) ± 0.8 (sys.) ± 0.1 (lumi.)	1.9 ± 0.1

Table 8.8: Measured cross-section for the $pp \to W(\to \mu\nu)\gamma\gamma$ process at $\sqrt{s} = 8\,\text{TeV}$ in the extended fiducial phase-space region defined in the text. Also shown are the Standard Model predictions from VBFNLO calculated at NLO. The predictions by VBFNLO are corrected to the particle level using the parton to particle level corrections described in the text.

the extended fiducial phase-space region of the exclusive selection is a proper subset of the inclusive selection. Another possible reason for the difference is that the VBFNLO program does not include the fragmentation of quarks or gluons to photons. This effectively lowers the predicted cross-section. In addition, higher order QCD corrections are expected to have a non-negligible effect on the predicted cross-section even for the exclusive selection.

This is the first direct measurement of the three weak gauge boson production cross-section $pp \to W(\to \mu\nu)\gamma\gamma$. It is in reasonable agreement with the Standard Model. Therefore the measurement is used to constrain physics beyond the Standard Model as discussed in the next chapter.

CHAPTER 9

Limits on anomalous quartic gauge couplings

The cross-section measurements presented in Chapter 8 show that the observed cross-section and the theory predictions are statistically consistent. Therefore, the measurement is used to place constraints on new physics using the framework of anomalous quartic gauge couplings discussed in Section 2.4. The constraints will be presented as 95 % frequentist $\mathrm{CL_S}$ confidence level intervals on the couplings of the dimension-8 operators that introduce anomalous couplings for the $WW\gamma\gamma$ vertex.

The limits on anomalous couplings are set using the exclusive selection. As discussed earlier, the theory prediction for the $W\gamma\gamma$ process suffers from potentially large NNLO corrections (cf. Section 2.3) leading to artificially small predictions if only NLO corrections are considered. Hence, the discrepancy between data and prediction that results from disregarded NNLO corrections could be mistaken for a new physics signal or could lead to limits on anomalous couplings that do not reflect the current knowledge [120]. The contribution of NNLO corrections to a final state without jets is restricted to pure-virtual two-loop corrections, which are expected to be small.

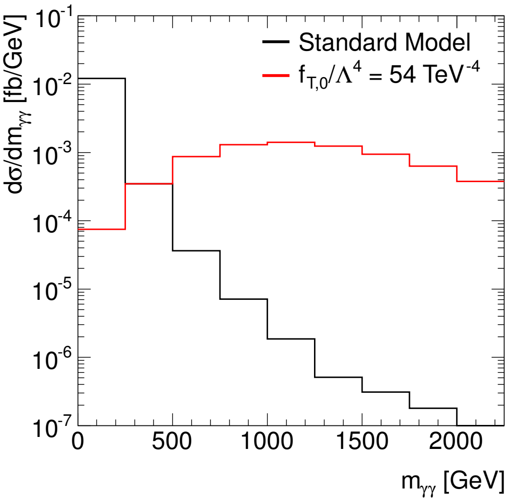

Figure 9.1: Predicted cross-section as function of the di-photon invariant mass for the SM (black line) and the operator $F_{\mathrm{T},0}$ with a coupling of $f_{\mathrm{T},0}\,/\Lambda^4 = 54\,\mathrm{TeV}^{-4}$ (red line).

For the limit setting an optimized phase-space region is used. Only events above a certain di-photon invariant mass threshold are considered, because deviations between the Standard Model and new physics phenomena are expected to occur at high energies compared to the typical energies of the Standard Model. This is exemplified due to the cross-section as a function of the di-photon invariant mass shown in Figure 9.1 for the Standard Model and the operator $F_{\mathrm{T},0}$ with a coupling of $f_{\mathrm{T},0}\,/\Lambda^4 = 54\,\mathrm{TeV}^{-4}$. The excess of the cross-section by the anomalous coupling is clearly visible above about 300 GeV, while for small masses the contribution from the Standard Model exceeds the new physics signal.

Since many different operators that modify the $WW\gamma\gamma$ vertex exist, the frequentist confidence intervals are not directly set on the couplings of those operators. Instead, the measurement is used to calculate an upper limit on the cross-section of new physics phenomena. This can be converted into a frequentist confidence interval on the coupling of a specific operator by evaluating at which value of the anomalous coupling the predicted cross-section of the operator exceeds the limit. In this thesis, the limits on one particular operator, $F_{\mathrm{T},0}$, will be presented. The VBFNLO program is used to calculate the cross-section prediction for the anomalous couplings.

The chapter is organized as follows: At first, the statistical method used to determine the frequentist confidence intervals is discussed. Then, the inputs to the methods and the optimization of the phase-space are shown. At last, the resulting frequentist confidence intervals are presented.

9.1 Statistical method

Frequentist confidence intervals of a parameter are constructed in such a way that they include the *true* value of the parameter with a probability greater as or equal than to a desired level. This probability is called the coverage probability and is conventionally set to 95 %. The intervals are constructed with a procedure according to Neyman [132], which is described below. The discussion in this section follows [1].

9.1.1 Neyman construction

The Neyman construction starts from a probability density function (p.d.f.), $f(x\,|\,\theta)$, that describes the probability of observing the value x, given the parameter θ, whose confidence interval is to be determined. For each value of θ the intervals $[x_1, x_2]$ that contain 95 % of the total probability are given by

$$\int_{x_1}^{x_2} f(x\,|\,\theta)\,\mathrm{d}x = 0.95\,. \tag{9.1}$$

The intervals $[x_1, x_2]$ are not unique, typical choices are the *central interval* constructed such that the probabilities below x_1 and above x_2 are equal. Another choice, more suited for upper limit setting, is the one-sided interval for which the probability below x_1 is set to zero.

The concept of the Neyman construction is illustrated in Figure 9.2 which shows the central intervals $[x_1, x_2]$ for some parameters θ as horizontal lines. The union of all those intervals for every parameter value of θ is called the *confidence belt*. The confidence interval on θ is determined by drawing a vertical line at the observed value x_{obs}. The intersection of this line with the confidence belt yields the confidence interval $\left[\theta_{\mathrm{min}}^{95\,\%\,\mathrm{CL}}, \theta_{\mathrm{max}}^{95\,\%\,\mathrm{CL}}\right]$. By construction, this interval contains the *true* value, θ_0, with a probability of 95 %.

Typically some function of the measured value is used instead of the measured value itself. The function is called a *test statistic*. In this analysis, the $\mathrm{CL_S}$ prescription of the test statistic is used. It is defined using the p-values of a background-only and a new physics hypothesis. The p-value is defined as the probability that a fluctuation yields a discrepancy as large or larger than the one observed in data. Typically, the signal hypothesis is parametrized using a parameter μ that is proportional to the signal cross-section. Therefore the background-only hypothesis is given by $\mu = 0$. The $\mathrm{CL_S}$ test statistic is defined as

$$\mathrm{CL_S} = \frac{p_\mu}{p_0}\,. \tag{9.2}$$

Here, p_0 is the p-value of the background-only hypothesis, and p_μ is the p-value of the new-physics hypothesis with a strength parameter μ. The parameter point μ_1 is excluded at a 95 % confidence level if $\mathrm{CL_S}(\mu_1) < 5\,\%$. The more traditional use of $\mathrm{CL_{S+B}}$ as the test statistic will lead to an exclusion if the

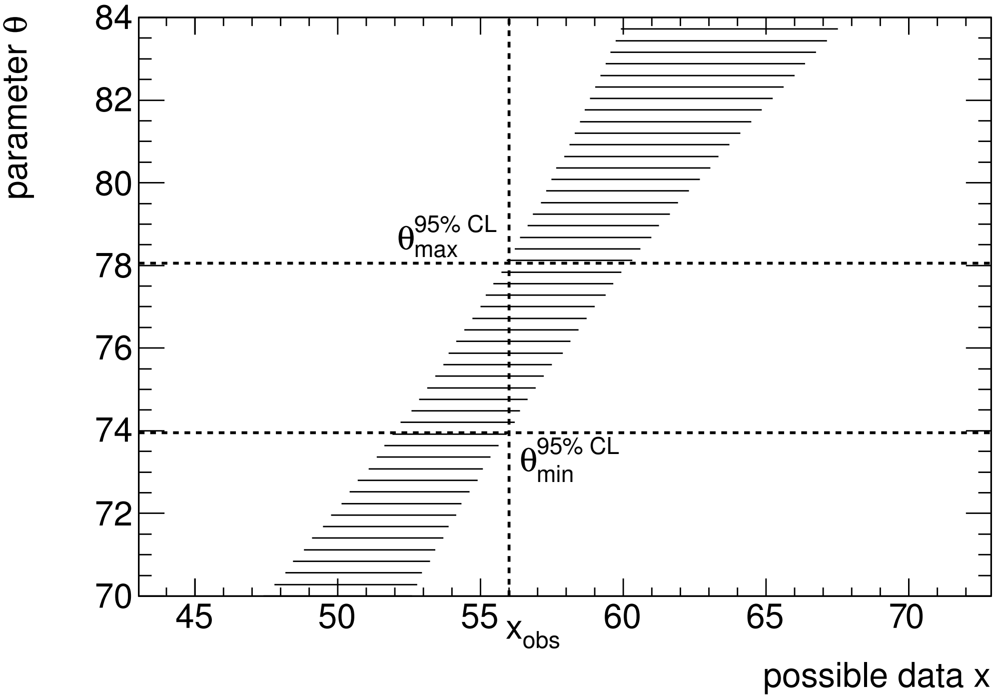

Figure 9.2: Illustration of the Neyman construction. The solid horizontal lines indicate the 95 % confidence intervals for a specific value of θ. The vertical dashed line indicates the observed data, and the horizontal dashed lines indicate the 95 % confidence interval for the parameter θ.

experiment has no sensitivity to the tested model and the data fluctuated downward. Therefore the $\mathrm{CL_S}$ test statistic puts a penalty of p_0 on the p-value of the signal hypothesis.

The p-value is evaluated using the *profile likelihood ratio*, since it simplifies the treatment of systematic uncertainties. They are often introduced in terms of *nuisance parameters*, i.e. parameters whose values are known with some limited accuracy, but the actual value of these nuisance parameters is not of interest. One example for this kind of parameters is the jet energy scale. The profile likelihood ratio, λ_p, is defined via the ratio of the profile likelihood L_p to the (traditional) likelihood L,

$$\lambda_\mathrm{p} = -2 \ln \frac{L_\mathrm{p}(\mu \,|\, x)}{L(\hat{\mu}, \hat{\nu} \,|\, x)} \,. \tag{9.3}$$

Here, x is the data, μ is the parameter of interest and ν are the nuisance parameters. $\hat{\mu}$ and $\hat{\nu}$ are the maximum likelihood estimators, i.e. the values of μ and ν which maximize the likelihood $L(\mu, \nu \,|\, x)$. The profile likelihood is defined as

$$L_\mathrm{p}(\mu \,|\, x) = L(\mu, \hat{\hat{\nu}} \,|\, x) \,, \tag{9.4}$$

where the nuisance parameters $\hat{\hat{\nu}}$ maximize the likelihood for fixed μ. The p-values inferred from the profile likelihood ratio do not provide proper coverage for all values of the nuisance parameters, but for cases of practical interest the coverage is sufficient [133].

9.1.2 Likelihood for the measurement

At this stage, everything for the calculation of the confidence intervals is in place, except the likelihood. For each parameter value μ that is tested, the $\mathrm{CL_S}$ statistic is evaluated by calculating p_0 and p_μ. If the value of the $\mathrm{CL_S}$ test statistic is below 5 %, μ is outside of the confidence interval. The only missing piece is the functional form of the likelihood L, which is used to calculate p-values using the profile likelihood ratio λ_p. The likelihood gives the probability for a particular μ given the data.

For this measurement, the likelihood is generally given by the probability of observing N_obs events, when N_exp events were expected. That is, it equals the Poisson probability

$$\mathcal{L} = \mathcal{P}_{N_\mathrm{exp}}(N_\mathrm{obs}) = \frac{N_\mathrm{exp}^{N_\mathrm{obs}}}{N_\mathrm{obs}!} e^{-N_\mathrm{exp}} . \tag{9.5}$$

The number of expected events is the sum of events from background, $W\gamma\gamma$ and new-physics processes,

$$N_\mathrm{exp} = N_\mathrm{bkg} + \underbrace{N_{W\gamma\gamma} + N_\mathrm{aQGC}}_{(1+\mu)\cdot N_{W\gamma\gamma}} . \tag{9.6}$$

Here, N_aQGC is the number of events from processes involving anomalous quartic couplings, $N_{W\gamma\gamma}$ is the number of events from the $W\gamma\gamma$ process predicted by the Standard Model, and N_bkg is the number of events from other Standard Model processes. The topology of events from the Standard Model $W\gamma\gamma$ process and possible new physics phenomena from anomalous quartic gauge couplings are expected to be very similar, i.e. new physics phenomena only enhance the number of events at high masses. Therefore the acceptance and efficiency corrections are similar and the number of events can be combined to

$$N_{W\gamma\gamma} + N_\mathrm{aQGC} = (1+\mu)\cdot N_{W\gamma\gamma} , \tag{9.7}$$

where μ is the signal-strength parameter. If the most likely value of μ for a given N_obs, $\hat{\mu}$, is close to 0, no new physics signal is present. If on the other hand, $\hat{\mu}$ is much larger than 0, an excess of events compared to the Standard Model prediction is observed. In agreement with the notation used above, the null hypothesis that no new phenomena contribute to the observed data, is given by $\mu = 0$, which yields the Standard Model prediction $N_{W\gamma\gamma}$.

As described above, the strategy of this measurement is to set an upper limit on the cross-section of a potential new physics signal and then calculate confidence intervals on the coupling parameters. Therefore $N_{W\gamma\gamma}$ is replaced by the cross-section formula given in 8.6, yielding

$$N_\mathrm{exp} = N_\mathrm{bkg} + (1+\mu)\cdot\left(\sigma_\mathrm{SM}^{pp\to W(\to\mu\nu)\gamma\gamma}\cdot A\cdot\epsilon\cdot L_\mathrm{int}\right) , \tag{9.8}$$

where $\sigma_\mathrm{SM}^{pp\to W(\to\mu\nu)\gamma\gamma}$ is the predicted cross-section for the Standard Model process and A, ϵ and L_int are the acceptance, efficiency and the integrated luminosity, respectively. At this stage, the likelihood would describe the measurement if all terms that enter the calculation of N_exp are known without uncertainty. This is never the case for a real measurement. Therefore, the uncertainties have to be incorporated into the likelihood to obtain a meaningful result.

The uncertainties are integrated into the likelihood by adding additional parameters from auxiliary measurements, for example, the integrated luminosity measurement. The result of this measurement is $L_\mathrm{int} = (20.3 \pm 0.6)\,\mathrm{fb}^{-1}$, which in the frequentist interpretation is equivalent to the statement that the interval $\left[19.7\,\mathrm{fb}^{-1}, 20.9\,\mathrm{fb}^{-1}\right]$ includes the true value with a 68 % probability. Since the number of expected events obviously depends on the true value of the luminosity, L_int is replaced with $L_\mathrm{int}^\mathrm{true}$ in

Equation 9.8. The same argument can be applied to the other terms, leading to

$$N_{\text{exp}} = N_{\text{bkg}}^{\text{true}} + (1+\mu) \cdot \left(\sigma_{\text{SM}}^{pp\to W(\to\mu\nu)\gamma\gamma,\text{true}} \cdot A^{\text{true}} \cdot \epsilon^{\text{true}} \cdot L_{\text{int}}^{\text{true}}\right) . \tag{9.9}$$

The knowledge about the true parameter values obtained from the auxiliary measurements is included in the likelihood by additional *constraint terms*

$$\mathcal{G}\left(L_{\text{int}}^{\text{true}} \,\middle|\, L_{\text{int}}^{\text{meas}}, \sigma_{L_{\text{int}}}\right) , \tag{9.10}$$

where $\mathcal{G}$ denotes the Gaussian p.d.f. with mean $L_{\text{int}}^{\text{meas}}$ and width $\sigma_{L_{\text{int}}}$.

For each auxiliary measurement such a constraint is added to the likelihood such that the likelihood, $\mathcal{L}(\mu, \vec{\nu} \,|\, N_{\text{obs}})$ for the parameter of interest μ, given that N_{obs} events have been observed, can be written as

$$\mathcal{L}\left(\mu, \vec{\nu} \,\middle|\, N_{\text{obs}}\right) = \mathcal{P}_{N_{\text{exp}}}\left(N_{\text{obs}}\right) \cdot \prod_{\nu \in \vec{\nu}} \mathcal{G}\left(\nu^{\text{true}} \,\middle|\, \nu^{\text{meas}}, \sigma_{\nu}\right) . \tag{9.11}$$

Here, $\vec{\nu}$ is a vector that contains all nuisance parameters ν.

The likelihood describes the measurement presented in this work. It is used to calculate the p-value for a certain value of μ given the observed data. The p-values are calculated using the profile likelihood ratio λ_{p} as described in the next section.

9.1.3 P-value determination

In the limit of large numbers of observed events, the p-value can be calculated according to Wilk's theorem [134]. It states that for large N, the likelihood ratio is distributed like a χ^2-distribution with one degree of freedom. Therefore, the value of μ that corresponds to a p-value of 5 % can be derived using the well known cumulative distribution function of the χ^2-distribution. However, for this analysis the asymptotic formula cannot be used, as the number of expected events is to small to justify the approximations used in Wilk's theorem. Instead, the p-value is calculated using pseudo-experiments. For each tested value of μ, the likelihood is used to randomly draw the number of (pseudo-)observed events. This is repeated 100000 times per parameter point and as a result the distribution of λ_{p}^{μ} is obtained. One example for such a distribution is shown in Figure 9.3 together with the value of the profile likelihood ratio obtained from data. The p-value, p_{μ}, is the fraction of events with larger profile likelihood ratios than the one observed in data. The pseudo-experiments that end up in the tail can be thought of as measurements of a model with a hypothesized signal strength μ, where as many as or less events than measured in data are observed due to a downwards fluctuation.

The generation of pseudo-experiments is repeated for every tested value of μ. In addition, pseudo-experiments are carried out with a value of $\mu = 0$ to obtain the p-value for the null hypothesis, p_0, needed for the calculation of CL_{S}. If the CL_{S} value for a fixed value of μ is smaller than 5 %, the point is outside the confidence interval, and inside otherwise.

9.2 Inputs and optimization

The inputs needed for the calculation of the frequentist 95 % CL_{S} upper limit on the cross-section are similar to those needed in the computation of the cross-section. The only difference is that the phase-space used in the limit setting procedure includes a selection on the invariant mass of the diphoton system. As explained earlier, this enhances the sensitivity to anomalous quartic couplings, whose

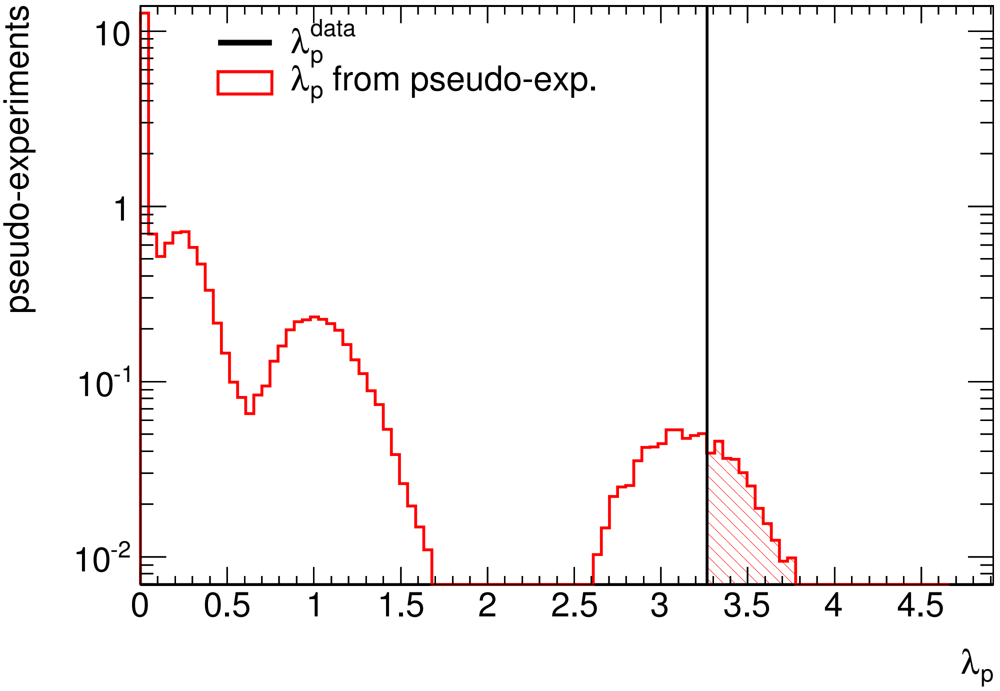

Figure 9.3: Profile likelihood ratio distribution for 100000 pseudo-experiments generated with a fixed value of μ (red histogram) and the value of the profile likelihood ratio obtained from data (black line). The hatched area indicates the fraction of pseudo-experiments that yield a profile likelihood ratio equal or larger than that obtained in data.

contribution is expected at high mass. This additional requirement affects especially the central values and uncertainties of the background estimation and the reconstruction efficiency.

The expected number of background events is extrapolated into the high mass region, since the small number of events does not allow to redo the background estimates. The extrapolation is done using the di-photon invariant mass distribution obtained from a control region for the data-driven backgrounds and from simulation for the other backgrounds. Details on how the shape of the kinematic distributions is obtained can be found in Section 7.4. An additional systematic uncertainty of 100 % is assigned due to the uncertainties inherent to the extrapolation.

The acceptance and efficiency corrections are derived as described in Section 8.2 and Section 8.3 as a function of the minimum di-photon invariant mass requirement. The resulting distributions are shown in Figure 9.4. The acceptance correction shows no significant dependence on the minimum $m_{\gamma\gamma}$ requirement, whereas the efficiency correction shows a strong dependence. A potential explanation is the photon identification efficiency, which rises for larger photon transverse momenta. A requirement on large $m_{\gamma\gamma}$ shifts the average photon transverse momentum to higher values and therefore increases the overall identification efficiency.

The dataset used for the calculation of the confidence intervals is the same as for the cross-section measurement. Thus the luminosity and its uncertainty are the same as in the previous chapter, $L_{\text{int}} = 20.3 \pm 0.6\,\text{fb}^{-1}$. The uncertainties on the theory prediction show only a small dependence on the di-photon invariant mass. The scale dependence of the $m_{\gamma\gamma}$ distribution is shown in Figure 2.6a in Chapter 2. Therefore, a conservative uncertainty of 15 % will be used for the determination of the confidence interval.

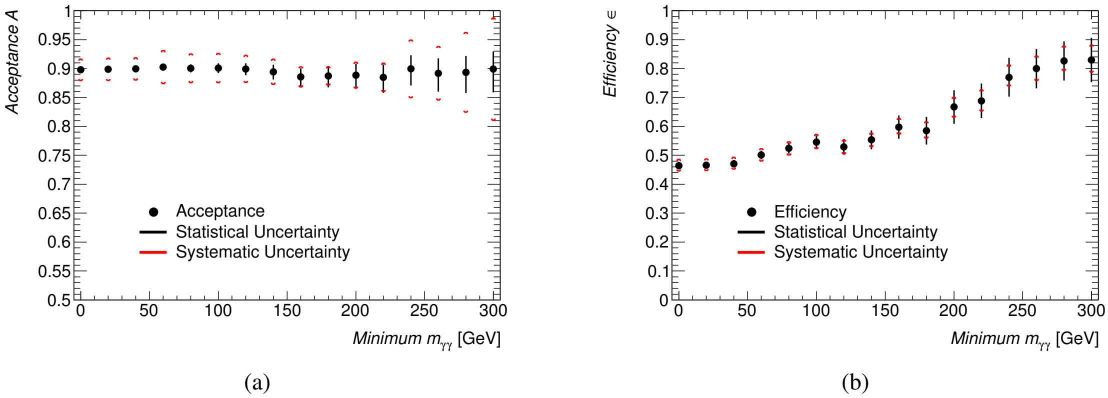

(a) (b)

Figure 9.4: The acceptance (left) and efficiency correction (right) as a function of the minimum requirement on the di-photon invariant mass. The statistical uncertainties are indicated as black lines and the systematic uncertainties are indicated as red bars.

9.2.1 Optimization of the phase-space

The phase-space used to set the limits on the cross-section is optimized by a scan of the expected 95 % $\mathrm{CL_S}$ confidence interval on the anomalous coupling $f_{\mathrm{T},0}/\Lambda^4$ as a function of the minimum $m_{\gamma\gamma}$ requirement. The optimization is performed without knowledge about the observed data. This is important in order to avoid choosing a phase-space region that artificially tightens the limit due to a statistical fluctuation in the data. The calculation of the expected limit is identical to that of the observed limit, but instead of the number of observed events, N_{obs}, the number of expected events, N_{exp}, is used. Therefore, the expected limit gives the median limit that can be obtained by this particular measurement, if only the known Standard Model processes contribute.

The confidence interval on $f_{\mathrm{T},0}/\Lambda^4$ is calculated in two steps. At first, the expected upper limit on the cross-section of anomalous couplings, $\sigma^{95\,\%}_{\mathrm{aQGC}}$, is calculated using the statistical methods described above. Afterwards, the value of $f_{\mathrm{T},0}/\Lambda^4$ at which the additional cross-section of the operator, $\sigma_{\mathrm{T},0}$, equals the upper limit is determined, i.e.

$$\sigma_{\mathrm{T},0}\left(\frac{f_{\mathrm{T},0}}{\Lambda^4}\right) = \sigma^{95\,\%}_{\mathrm{aQGC}}\,. \tag{9.12}$$

The calculation of the cross-section for a single parameter point using VBFNLO takes from a few hours to a few days depending on the precision of the results needed. Therefore it is not possible to calculate the cross-section for the whole parameter space. Instead, the cross-section is parametrized as a function of the value of the anomalous coupling. Figure 9.5 shows the predicted cross-section for the $W\gamma\gamma$ process in the extended-fiducial phase-space defined in Section 8.1 for various parameters of $f_{\mathrm{T},0}/\Lambda^4$. The uncertainty on the cross-section is the uncertainty due to the numerical calculation reported by VBFNLO. The cross-section shows a clear parabolic dependence on the value of the coupling parameter. This justifies the parametrization with a second order polynomial, which is fitted to the cross-section. The estimated parameters are given in the figure as well as the χ^2/NDF value, which confirms that the fit describes the cross-section well. The parabola is not fully symmetric around zero due to interference effects. Using the parabolic parametrization of $\sigma_{\mathrm{T},0}$ it is easy to find the value of $f_{\mathrm{T},0}/\Lambda^4$ that satisfies Equation 9.12.

The scan of the expected limit is done in steps of 20 GeV of the minimum $m_{\gamma\gamma}$ requirement. For each

	Parameter	Relative uncertainty
N_{bkg}	0.02	±116 %
$\sigma^{\text{theory}}_{\text{ext-fid}}$	0.06 fb	±15 %
L_{int}	$20.3\,\text{fb}^{-1}$	±2.8 %
A	0.90	±11 %
ϵ	0.82	±11 %
N_{obs}	0	—

Table 9.1: The parameters used to extract the upper 95 % CL_S limit on the cross-section from the process that modifies the quartic gauge coupling of the $WW\gamma\gamma$ vertex.

step the parametrization of the cross-section is obtained from a parabolic fit. Instead of using pseudo-experiments, the p-value is calculated using the asymptotic formulas. The better coverage obtained by using pseudo-experiments does not justify the extra computational cost, since the absolute value of the expected limit will not be used later. The expected 95 % CL_S confidence interval on $f_{\text{T},0}/\Lambda^4$ as a function of the minimum $m_{\gamma\gamma}$ requirement is shown in Figure 9.6. For a given value of $m_{\gamma\gamma}$, everything above the upper and below the lower line is excluded.

The optimization shows that a high minimum $m_{\gamma\gamma}$ requirement yields the best expected limits. However, in this phase-space region the number of expected events from background processes is zero, which makes it difficult to include the uncertainty in a proper way into the statistical method. In addition, the sample of simulated $W\gamma\gamma$ events that is used to derive the acceptance and efficiency corrections has not enough events above $m_{\gamma\gamma} \sim 300\,\text{GeV}$ to provide a reliable estimate. Since the change in the expected limit on $f_{\text{T},0}/\Lambda^4$ between $m_{\gamma\gamma} > 300\,\text{GeV}$ and $m_{\gamma\gamma} > 500\,\text{GeV}$ is small, the limits will be set with a minimum di-photon invariant mass requirement of $m_{\gamma\gamma} > 300\,\text{GeV}$.

9.3 Results without unitarization

The parameters used to obtain 95 % CL_S upper limits on the cross-section from processes that give rise to anomalous quartic $WW\gamma\gamma$ couplings are given in Table 9.1. The limit is obtained in the extended-fiducial region defined in Chapter 8 with the additional requirement that the di-photon invariant mass $m_{\gamma\gamma}$ is above 300 GeV. The observed values of the CL_S test statistic as a function of the signal strength parameter μ of a hypothesized anomalous quartic gauge couplings are shown in Figure 9.7. In addition, the expected value and its uncertainty is shown. Every value of μ that leads to a CL_S value below 0.05 is excluded with a confidence level of 95 %.

The upper 95 % CL_S limit on the cross-section from processes giving rise to anomalous quartic couplings, σ_{aQGC}, is the point where the observed CL_S value goes below 0.05. This point is determined by linear interpolation between the two closest μ values. It is found to be

$$\sigma^{95\,\%\text{ C.L.}}_{\text{excluded}} = 0.19\,\text{fb}\,. \tag{9.13}$$

The expected limit which is given by the intersection of the median expected CL_S value with the horizontal line $\text{CL}_\text{S} = 0.05$ is

$$\sigma^{95\,\%\text{ C.L., expected}}_{\text{excluded}} = (0.23\,^{+0.08}_{-0.04})\,\text{fb} \tag{9.14}$$

and thus slightly weaker. This is expected since no data was observed in the phase-space region used

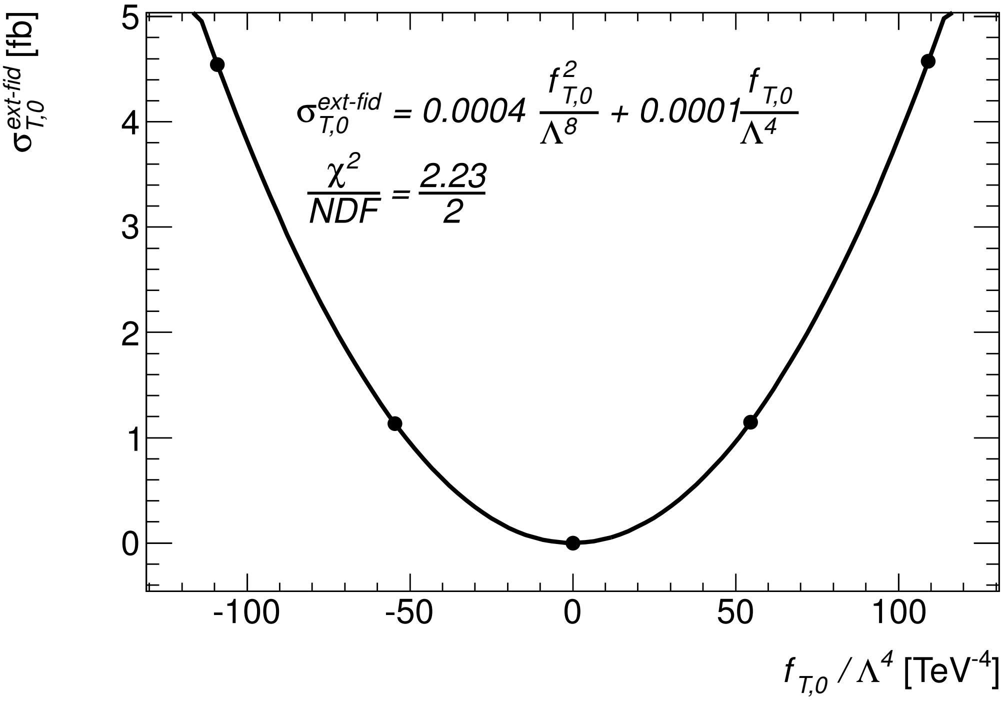

Figure 9.5: Cross-section of the $W\gamma\gamma$ process in the extended-fiducial region as function of the anomalous quartic coupling $f_{\mathrm{T},0}\,/\Lambda^4$. A fit with a parabola is overlaid.

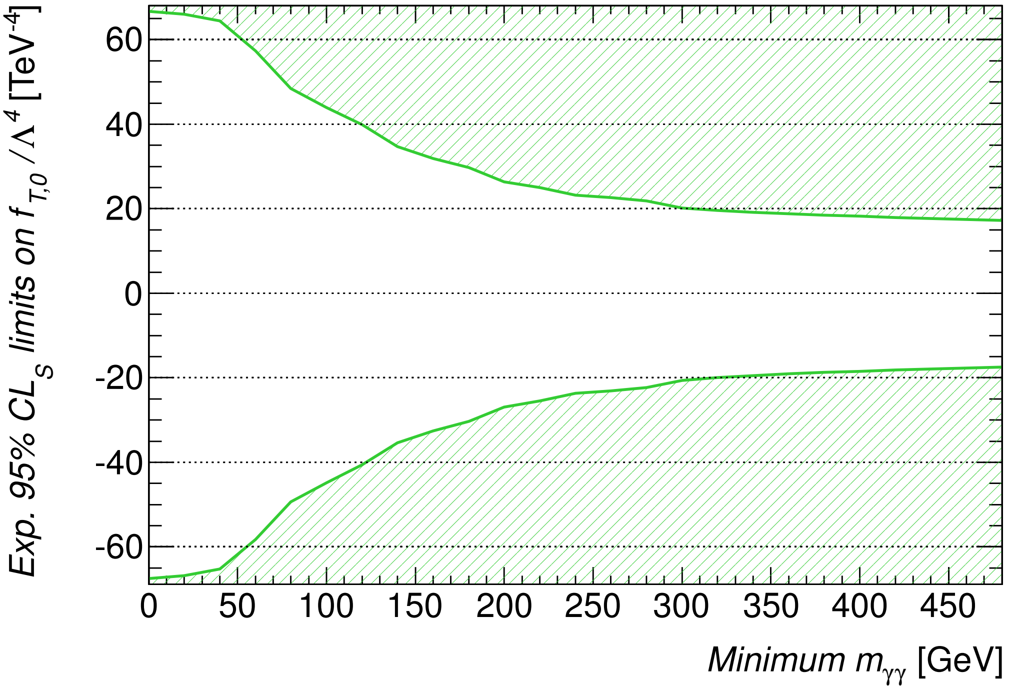

Figure 9.6: The expected limit on the cross-section of new-physics processes as a function of the minimum $m_{\gamma\gamma}$ requirement. The green hatched area is excluded.

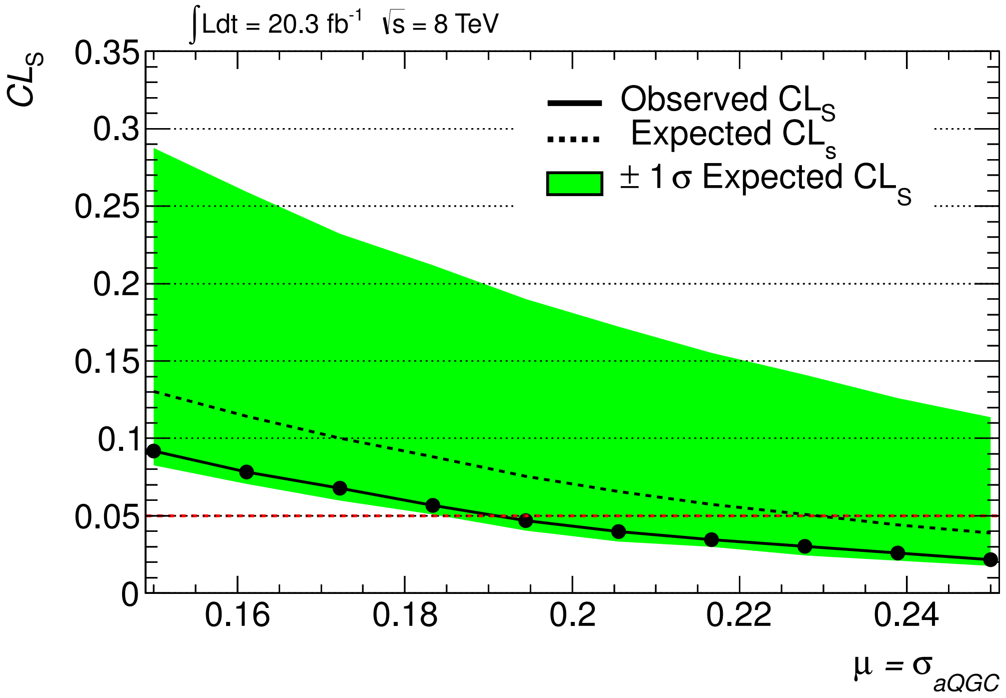

Figure 9.7: The value of the $\mathrm{CL_S}$ test statistic as a function of the signal strength parameter μ of a hypothesized model. The observed values as well as the expected values are shown. The green band indicates the ± $1\,\sigma$ uncertainty on the expected $\mathrm{CL_S}$ values. All values of μ yielding $\mathrm{CL_S} < 0.05$ (indicated by the red horizontal line) are excluded with a confidence level of 95 %.

for the limit setting. The observed and the expected limit are compatible within one standard deviation.

The upper limit on the cross-section of processes involving anomalous $WW\gamma\gamma$ couplings can be expressed in terms of the coupling of the operator $F_{\mathrm{T},0}$ by using the parametrization from Figure 9.5. The limit is visualized in Figure 9.8, where the ratio of the excluded cross-section to that predicted by the $F_{\mathrm{T},0}$-operator is shown as a function of the coupling parameter $f_{\mathrm{T},0}/\Lambda^4$. The couplings for which the ratio is larger than 1.0 are excluded at 95 % confidence level. The observed confidence interval is

$$-22.5\,\mathrm{TeV}^{-4} < \frac{f_{\mathrm{T},0}}{\Lambda^4} < 22.2\,\mathrm{TeV}^{-4}\,.$$

The median expected limit and its uncertainty band are also shown in Figure 9.8. The expected confidence interval is

$$(-24.7\,^{+2.9}_{-5.3})\,\mathrm{TeV}^{-4} < \frac{f_{\mathrm{T},0}}{\Lambda^4} < (24.3\,^{+5.3}_{-2.9})\,\mathrm{TeV}^{-4}\,.$$

The observed and the expected confidence intervals agree within one standard deviation.

9.4 Results with unitarization

As discussed in Section 2.4, the current limit on the couplings are so weak that unitarity might be violated at scales well below 8 TeV and therefore in the reach of the LHC. The unitarity bound as a function of the coupling, $f_{\mathrm{T},0}/\Lambda^4$, displayed in Figure 2.10a in Chapter 2 shows that for couplings

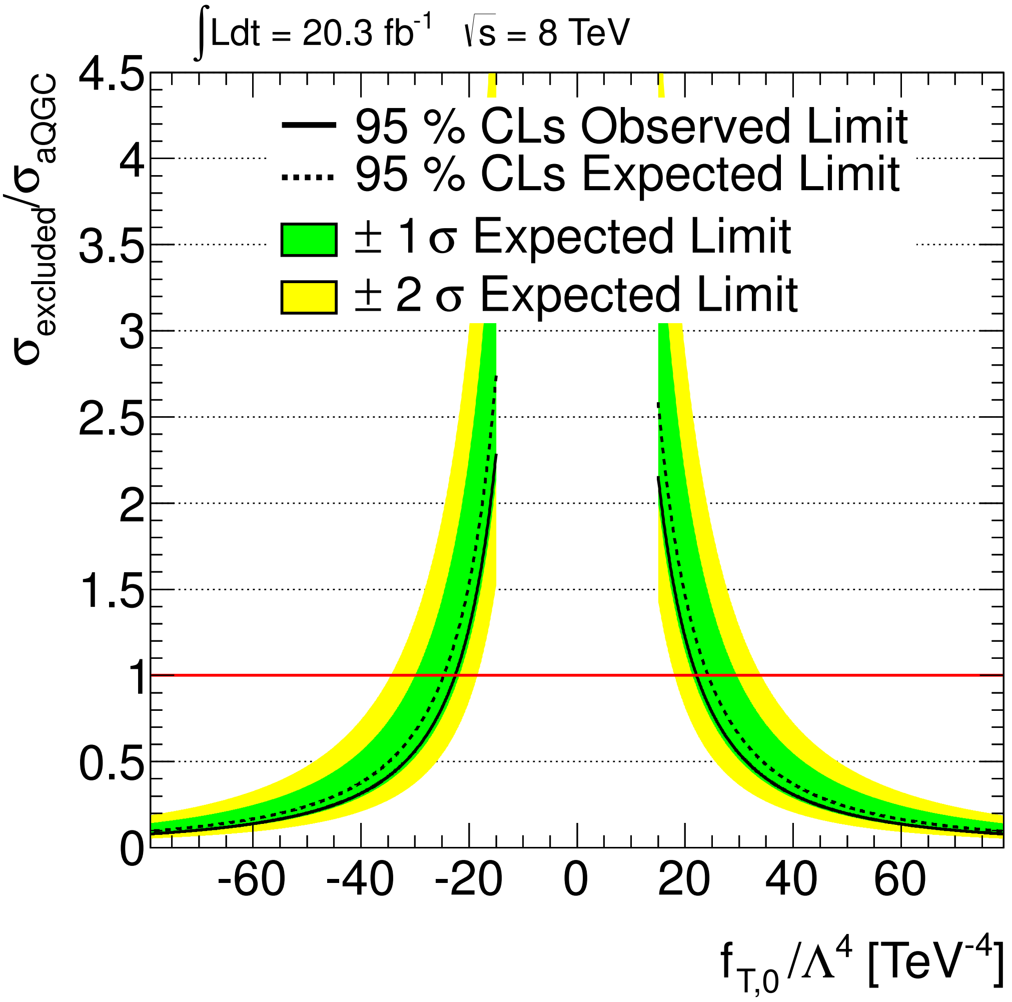

Figure 9.8: The ratio of the observed excluded cross-section to the cross-section of the $F_{\mathrm{T},0}$ operator as a function of its coupling $f_{\mathrm{T},0}\,/\Lambda^4$ (solid black line). In addition, the median limits (dashed black line) and the $\pm\,1\,\sigma$ and $\pm\,2\,\sigma$ uncertainty bands are shown in green and yellow, respectively.

parameters around $20\,\mathrm{TeV}^{-4}$, the unitarity bound is at $\sqrt{\hat{s}} = 0.6\,\mathrm{TeV}$. Thus a dipole form-factor,

$$\left(1+\frac{s}{\Lambda_{\mathrm{FF}}^2}\right)^{-2}, \tag{9.15}$$

is applied to ensure unitarity. The form-factor scale, Λ_{FF}, is chosen as the smallest scale for which unitarity is conserved up to $\sqrt{\hat{s}} = 8\,\mathrm{TeV}$, for an anomalous coupling which equals the expected limit given above. The calculation of the scale is done by a tool provided by the VbfNlo authors [56], already described earlier. The resulting form-factor scale is found to be $\Lambda_{\mathrm{FF}} = 0.622\,\mathrm{TeV}^{-4}$.

Since the dipole form-factor depends on the scale of the interaction, s, it can not be applied as a multiplicative factor to the differential cross-section as function of the di-photon invariant mass. Instead, the theory predictions have to be recalculated with dipole form-factor applied. This requires that the parametrization of the cross-section as function of the coupling and the optimization of the phase-space

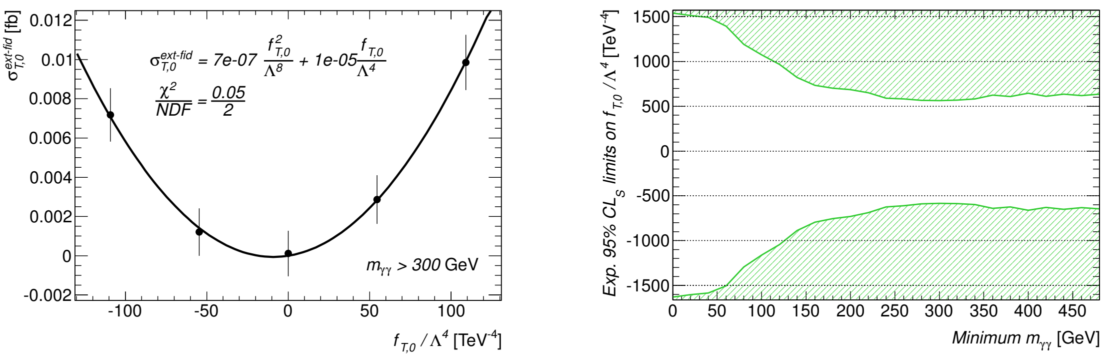

(a) (b)

Figure 9.9: (a): The parametrization of the cross-section as function of the coupling $f_{\mathrm{T},0}/\Lambda^4$ for the $F_{\mathrm{T},0}$ operator. The cross-section has been calculated with a dipole form-factor with $\Lambda_{\mathrm{FF}} = 622\,\mathrm{GeV}$. (b): The expected limit on $f_{\mathrm{T},0}/\Lambda^4$ as function of the minimum di-photon invariant mass requirement calculated using a dipole form-factor with $\Lambda_{\mathrm{FF}} = 622\,\mathrm{GeV}$.

region used for the limit setting have to be redone. One example of the parametrization obtained for events with $m_{\gamma\gamma} > 300\,\mathrm{GeV}$ is shown in Figure 9.9a. The suppression of the cross-section compared to the case without form-factor is clearly visible. For example for a hypothesized coupling of $f_{\mathrm{T},0}/\Lambda^4 = 100\,\mathrm{TeV}^{-4}$, the expected cross-section decreases from around 4 fb to only 0.1 fb when applying the dipole form-factor unitarization.

Since the form-factor might change the optimal phase-space region for the calculation of the limit, the phase-space is optimized as described above using the parametrization obtained from the theory predictions with the dipole form-factor applied. The resulting expected limit on $f_{\mathrm{T},0}/\Lambda^4$ is shown in Figure 9.9b as a function of the minimum di-photon invariant mass requirement. As before, the optimal phase-space for the limit is given by an additional $m_{\gamma\gamma} > 300\,\mathrm{GeV}$ requirement.

The observed and median expected 95 % $\mathrm{CL_S}$ confidence interval on the coupling $f_{\mathrm{T},0}/\Lambda^4$ of the $F_{\mathrm{T},0}$ operator, obtained using a dipole form-factor unitarization with a scale of $\Lambda_{\mathrm{FF}} = 622\,\mathrm{GeV}$ are visualized in Figure 9.10. It shows the ratio of the excluded to the predicted cross-section of the $F_{\mathrm{T},0}$ operator. Everything above one is excluded at a 95 % confidence level. The confidence interval observed is

$$-527\,\mathrm{TeV}^{-4} < \frac{f_{\mathrm{T},0}}{\Lambda^4} < 508\,\mathrm{TeV}^{-4}\,.$$

The median expected limit and its uncertainty band are also shown in Figure 9.8. The expected confidence interval is

$$(-576\,^{+67}_{-123})\,\mathrm{TeV}^{-4} < \frac{f_{\mathrm{T},0}}{\Lambda^4} < (558\,^{+123}_{-67})\,\mathrm{TeV}^{-4}\,.$$

The observed and the expected confidence intervals agree within one standard deviation. The observed limit obtained using the unitarized prescription of the $F_{\mathrm{T},0}$ operator is around a factor 20 weaker than the one obtained without applying unitarization.

9.5 Comparison to previous measurements

Anomalous quartic couplings have been previously constrained in several measurements carried out at LEP [45–48] and TeVatron [49], but these do not cover the $F_{\mathrm{T},0}$ operator considered in this analysis.

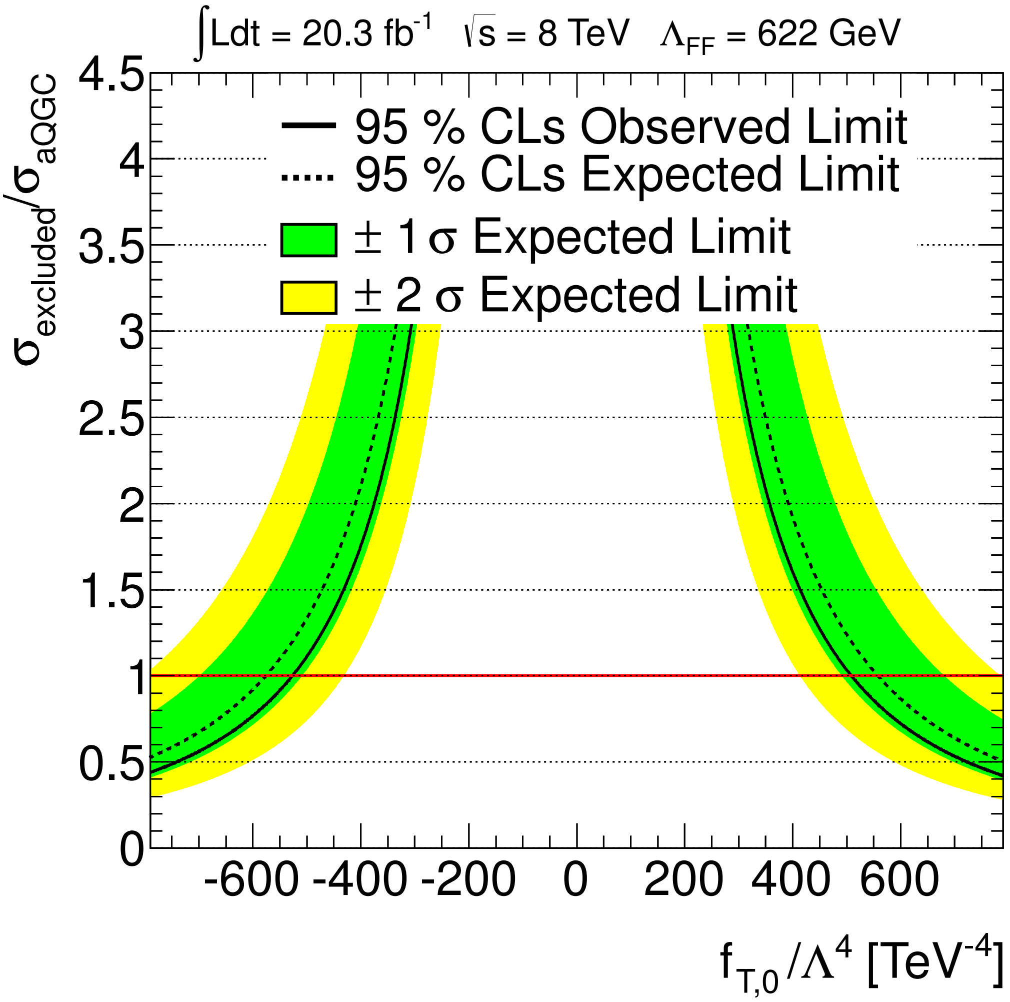

Figure 9.10: The ratio of the observed excluded cross-section to the cross-section of the $F_{\mathrm{T},0}$ operator as a function of its coupling $f_{\mathrm{T},0}/\Lambda^4$ (solid black line) obtained using a dipole form-factor unitarization with a scale of $\Lambda_{\mathrm{FF}} = 622\,\mathrm{GeV}$. In addition, the median limits (dashed black line) and the $\pm 1\,\sigma$ and $\pm 2\,\sigma$ uncertainty bands are shown in green and yellow, respectively.

Recently, the CMS Collaboration published the first ever 95 % confidence interval on $f_{\mathrm{T},0}/\Lambda^4$ [55], obtained from a measurement of the three boson production processes $WW\gamma$ and $WZ\gamma$. The published confidence interval is only presented without unitarization applied. It is found to be $-25\,\mathrm{TeV}^{-4} < f_{\mathrm{T},0}/\Lambda^4 < 24\,\mathrm{TeV}^{-4}$ and thus slightly weaker than the confidence interval presented in this work.

In summary, the measurement of the $W\gamma\gamma$ production cross-section is found to be in agreement with the Standard Model predictions. It has therefore been used to constrain physics beyond the Standard Model. A model-independent approach, consisting of effective Lagrangians that give rise to anomalous quartic couplings, was conducted to quantify the deviations from the Standard Model excluded by this measurement. The coupling of one exemplary effective operator, $F_{\mathrm{T},0}$, has been constrained by an upper limit of about $\left|f_{\mathrm{T},0}/\Lambda^4\right| < 22\,\mathrm{TeV}^{-4}$. This limit improves the previous limit by around $2\,\mathrm{TeV}^{-4}$. In addition, the upper limit on the coupling has been derived using a dipole form-factor with a scale of $\Lambda_{\mathrm{FF}} = 622\,\mathrm{GeV}$ to ensure the unitarity up to $\sqrt{\hat{s}} = 8\,\mathrm{TeV}$, the center-of-mass energy at which the data was recorded. In this case the 95 % frequentist $\mathrm{CL_S}$ upper limit obtained is around $\left|f_{\mathrm{T},0}/\Lambda^4\right| < 515\,\mathrm{TeV}^{-4}$.

CHAPTER 10

Summary

After two years of LHC data taking no evidence for physics beyond the Standard Model has been found. This thesis presents a complementary approach to the searches for direct production of new particles. A yet unmeasured three weak gauge boson production process is used for a generic test of the electroweak gauge structure.

The first measurement of the three vector boson production process, $pp \rightarrow \mu\nu\gamma\gamma$, is presented in this study. The measurement was performed using 20.3 fb^{-1} of proton-proton collision data at $\sqrt{s}$ = 8 TeV recorded with the ATLAS detector. The cross-section was extracted in two restricted phase-space regions and compared to predictions at next-to-leading order QCD. The events are selected by requiring a W boson that decays into a muon and its neutrino in association with two isolated photons with transverse energies above 20 GeV. The main challenge of this work was the estimation of the background contributions, primarily from jets which fake a photon signature or non-prompt muons from the decay of a heavy-flavor hadron.

These backgrounds have been estimated using data-driven methods. The fake photon background is determined using the 2D template fit method, which exploits the difference of the transverse energy in a cone around the photon candidates. The non-prompt muon background is estimated by defining three control-regions used to constrain the number of events with non-prompt muons. From 112 selected candidate events, 57 ± 14 (stat.) ± 10 (sys.) signal events remain after the subtraction of the backgrounds.

The cross-section has been calculated in two restricted phase-space regions well covered by the ATLAS detector. The inclusive phase-space poses no requirement on jets, while in the exclusive phase-space a veto on anti-k_t jets with transverse momentum above 30 GeV is applied. The cross-section is found to be (6.5 ± 1.6 (stat.) ± 1.1 (sys.) ±0.2 (lumi.)) fb, and (3.6 ± 1.2 (stat.) ±0.8 (sys.) ±0.1 (lumi.)) fb in the inclusive and exclusive phase-space regions, respectively. The measured cross-sections are compatible with predictions at next-to-leading order QCD by the VBFNLO program, but slightly larger, which can be attributed to non-negligible higher order perturbative effects and the missing inclusion of fragmentation photons for the prediction.

The measurement in the exclusive phase-space is used to constrain anomalous quartic gauge boson couplings. In this thesis the coupling parameter of one exemplary operator has been constraint. An optimization of the sensitivity has been performed, and only events at large di-photon invariant masses are considered. No evidence for physics beyond the Standard Model is observed. The 95 % frequentist CL$_\mathrm{S}$ limits obtained for the coupling parameter, is found to be $-22.5\,\mathrm{TeV}^{-4} < \frac{f_{\mathrm{T},0}}{\Lambda^4} < 22.2\,\mathrm{TeV}^{-4}$ improving previous limits published by the CMS collaboration. A second limit is derived using a dipole form-factor to avoid unitarity violation at high energies. In this case the obtained limit is $-527\,\mathrm{TeV}^{-4} < \frac{f_{\mathrm{T},0}}{\Lambda^4} < 508\,\mathrm{TeV}^{-4}$.

APPENDIX A

Supplementary material

A.1 Additional quality criteria for muons

This section lists the add additional quality criteria that are applied to the inner detector track of a combined muon to take into account the status of the Pixel- and SCT-systems. The following quality criteria are applied [135]:

- At least one hit in the pixel detector, except the track crossed a module which is known to be defect.
- At least four hits in the SCT detector. If the track crosses SCT modules which are known to be defect, this SCT module is assigned as a hit.
- At most three modules which are known to be defect are crossed by the track.
- If a TRT track is expected (in the region $0.1 < |\eta| < 1.9$) it must be sufficiently well measured.

A.2 Fake jet identification

To suppress jets from cosmic-ray showers, beam-induced background or short localized noise bursts in the calorimeter, the following variables are used [136]:

f_{EM}: The fraction of the total jet energy deposited in the electromagnetic compartment of the calorimeter.

f_{HEC}: The fraction of the total jet energy deposited in the hadronic endcap calorimeter.

f_{max}: The maximum energy fraction deposited in a single calorimeter layer.

$\langle Q \rangle$: The weighted average of the quality measure Q_{cell} of all cells that constitute a jet. The cell-level quality is a function of the difference between the measured pulse-shape to a nominal pulse-shape obtained from simulation of the calorimeter front-end electronics.

$f_{\mathrm{Q}}^{\mathrm{LAr}}$: The fraction of cells constituting the jet, which are in the LAr calorimeters that have a bad quality pulse-shape.

$f_{\mathrm{Q}}^{\mathrm{HEC}}$: The fraction of cells constituting the jet, which are in the HEC that have a bad quality pulse-shape.

f_{ch}: The charged energy fraction of the total jet energy. This is determined from the transverse momentum sum of tracks within a cone of $\Delta R \leq 0.4$ around the jet direction.

E_{neg}: Sum of the energy of all cells constituting the jets which have negative energy.

The selections applied to all jets with transverse momentum above 20 GeV are listed in Table A.1.

Source	Selection criteria
Non-collision background	($f_{\mathrm{EM}} < 0.05$ and $f_{\mathrm{ch}} < 0.05$ and $\lvert\eta\rvert < 2$) or ($f_{\mathrm{max}} < 0.05$ and $\lvert\eta\rvert < 2$) or ($f_{\mathrm{EM}} < 0.05$ and $\lvert\eta\rvert > 2$) or
Coherent noise bursts in the electromagnet calorimeters	$f_{\mathrm{EM}} > 0.95$ and $f_{\mathrm{Q}}^{\mathrm{LAr}} > 0.8$ and $\langle Q \rangle > 0.8$ and $\lvert\eta\rvert < 2.8$
Noise bursts in the hadronic endcap calorimeters	($f_{\mathrm{HEC}} > 0.5$ and $\left\lvert f_{\mathrm{HEC}}^{\mathrm{Q}} \right\rvert > 0.5$ and $\langle Q \rangle > 0.8$) or $\left\lvert E_{\mathrm{neg}} \right\rvert > 60\,\mathrm{GeV}$

Table A.1: Selection criteria used to suppress jets from different background sources.

A.3 Figures for the study of systematic uncertainties using the inclusive selection

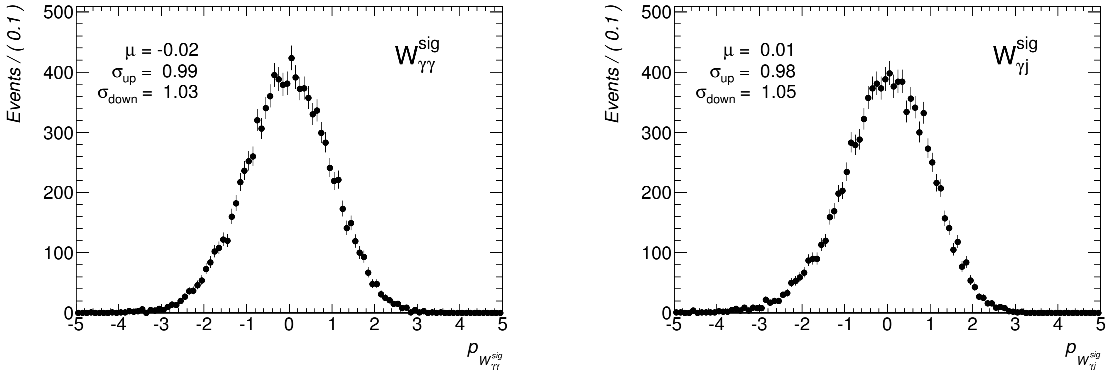

(a) $W_{\gamma\gamma}$ (b) $W_{\gamma \mathrm{j}}$

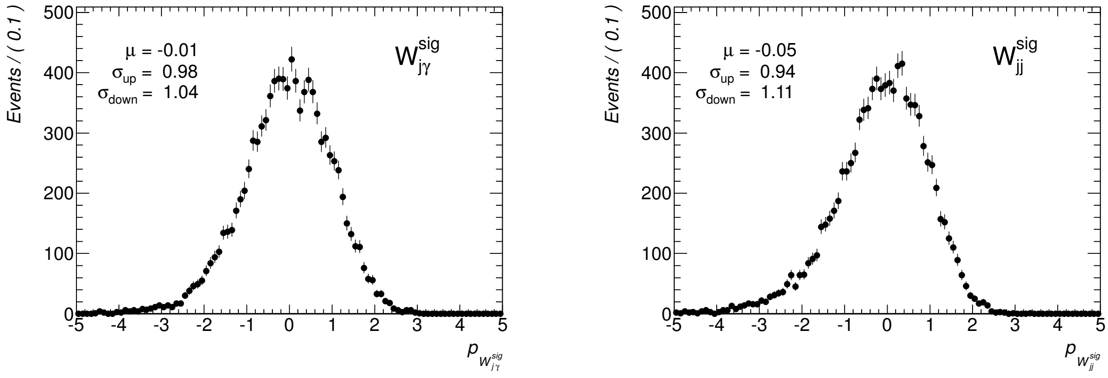

(c) $W_{\mathrm{j}\gamma}$ (d) W_{jj}

Figure A.1: Pull distributions from pseudo-experiments used to evaluate the systematic uncertainty due to the choice of the background model for the inclusive selection. The pseudo-data has been generated using the nominal template and it has been fitted using the sum of a Gaussian and a Novosibirsk function with the same mean parameter, as fake-photon template F_{b}. The corresponding distributions for the exclusive selection can be found in Figure A.10.

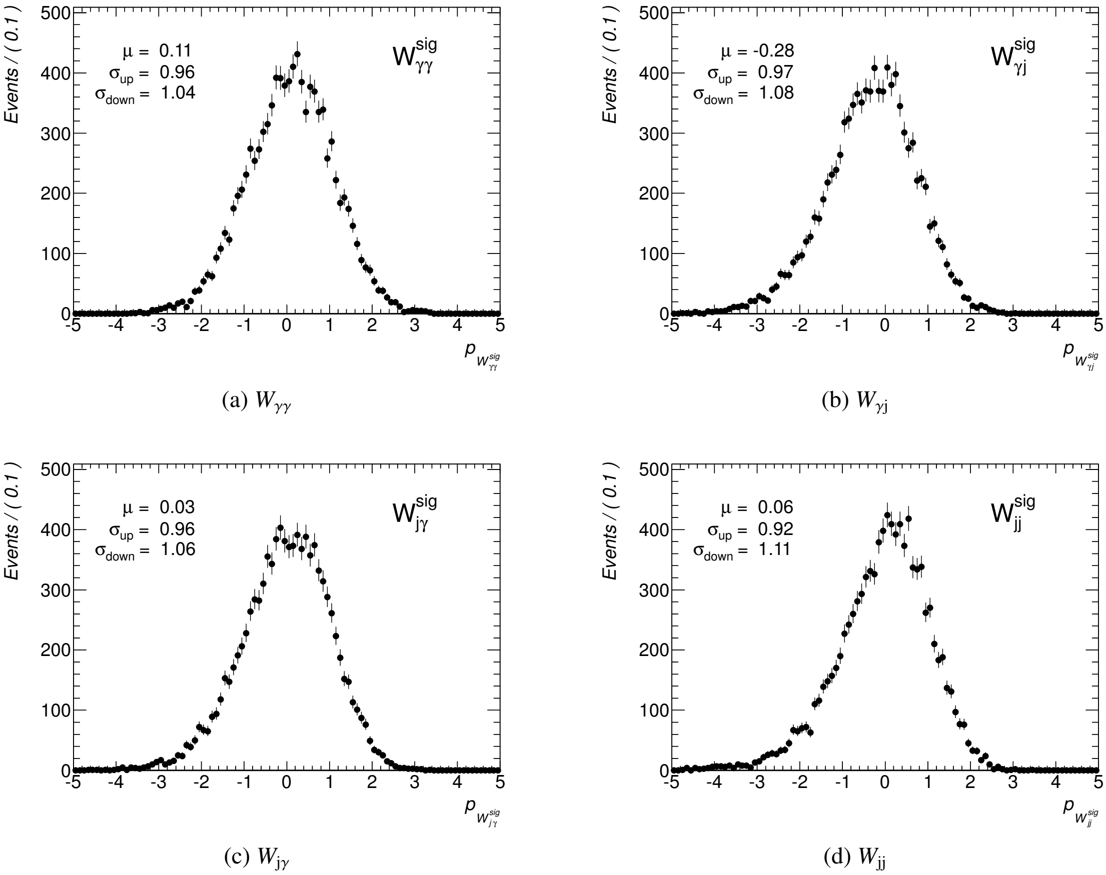

(a) $W_{\gamma\gamma}$

(b) $W_{\gamma \mathrm{j}}$

(c) $W_{\mathrm{j}\gamma}$

(d) W_{jj}

Figure A.2: Pull distributions from pseudo-experiments used to evaluate the systematic uncertainty due to the definition of the fake-photon control region for the inclusive selection. The pseudo-data has been generate using a template obtained using the L'_5 control region definition and was fitted using the nominal template. The distributions for the exclusive selection are shown in Figure A.12.

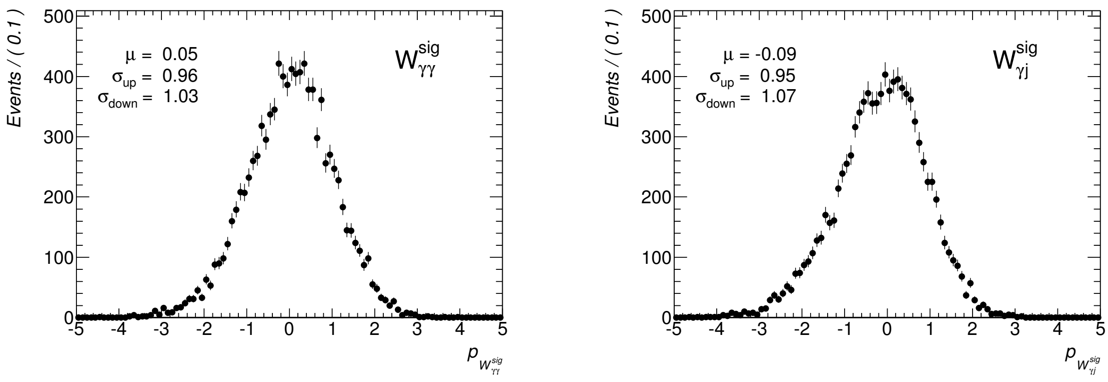

(a) $W_{\gamma\gamma}$ (b) $W_{\gamma \mathrm{j}}$

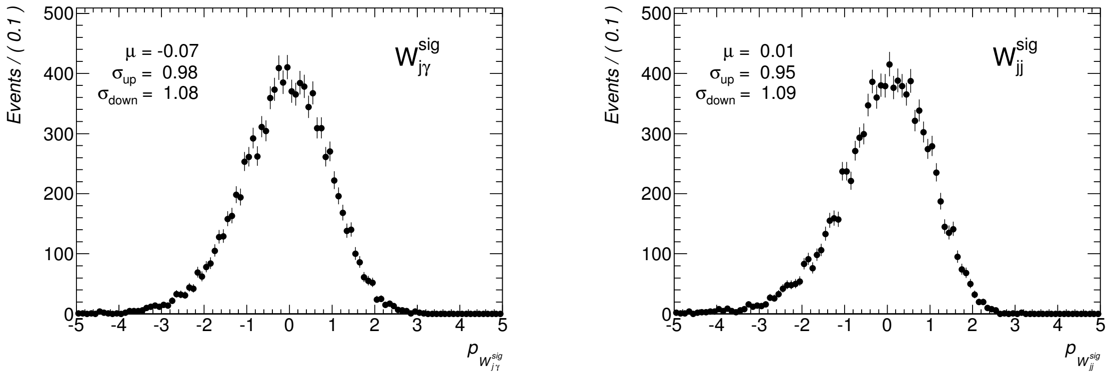

(c) $W_{\mathrm{j}\gamma}$ (d) W_{jj}

Figure A.3: Pull distributions from pseudo-experiments used to evaluate the systematic uncertainty due to the choice of the Monte Carlo generator for the inclusive selection. The corresponding distributions for the exclusive selection can be found in Figure A.14.

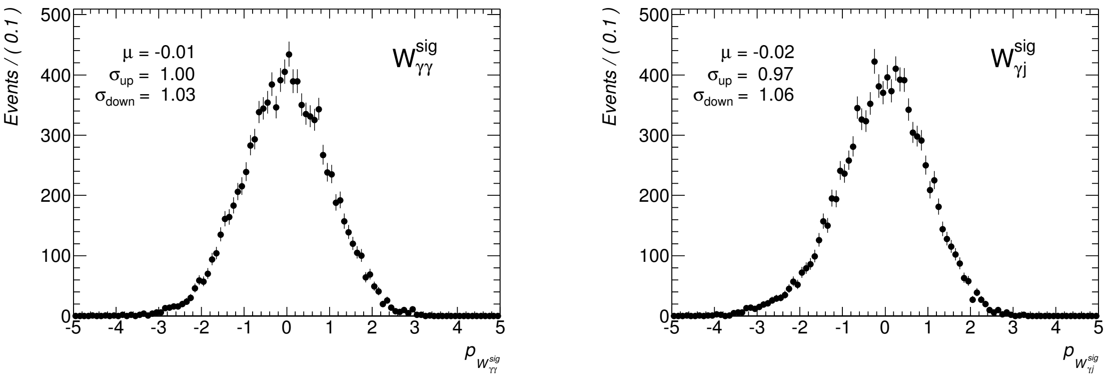

(a) $W^{\text{sig}}_{\gamma\gamma}$ (b) $W^{\text{sig}}_{\gamma\text{j}}$

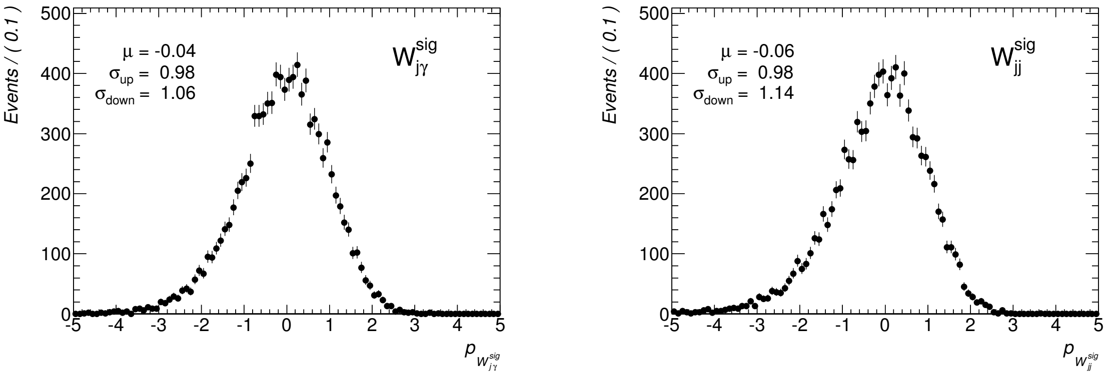

(c) $W^{\text{sig}}_{\text{j}\gamma}$ (d) $W^{\text{sig}}_{\text{jj}}$

Figure A.4: Pull distributions from pseudo-experiments used to evaluate the systematic uncertainty due to the signal-leakage correction for the inclusive selection. The corresponding distributions for the exclusive selection can be found in Figure A.15.

A.4 Figures for the photon background estimates using the exclusive selection

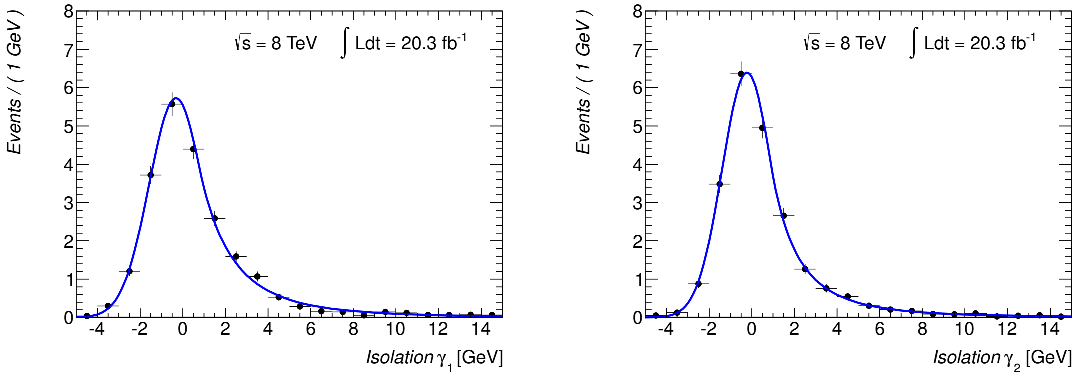

(a) (b)

Figure A.5: The $E_{\mathrm{T}}^{\mathrm{iso}}$ distribution and the photon isolation p.d.f.'s for the leading (a) and subleading (b) photon from simulated $W\gamma\gamma$ events selected using the exclusive selection. The distribution for the inclusive selection is shown in Figure 7.2

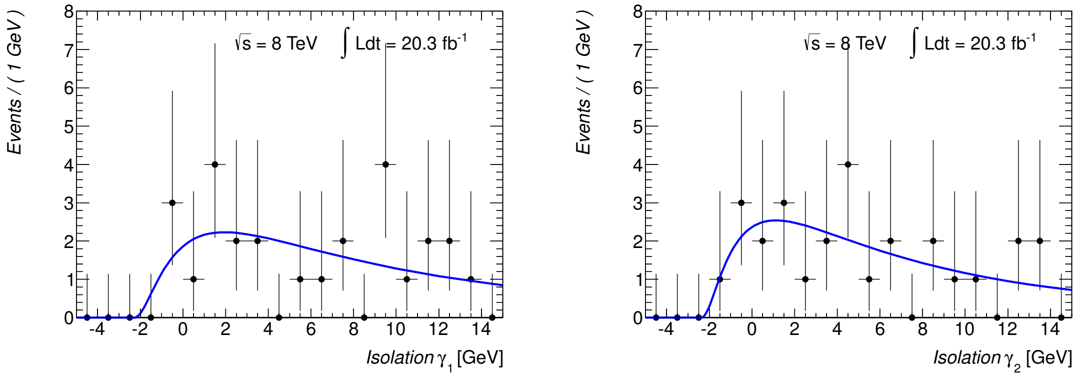

(a) (b)

Figure A.6: The jet $E_{\mathrm{T}}^{\mathrm{iso}}$ distribution for the leading (c) and subleading (d) photon candidate extracted from the data using the exclusive selection. The solid line shows the resulting jet isolation p.d.f.'s $F_{\mathrm{j},1}$ and $F_{\mathrm{j},2}$. The distribution and the template for the inclusive selection is shown in Figure 7.2.

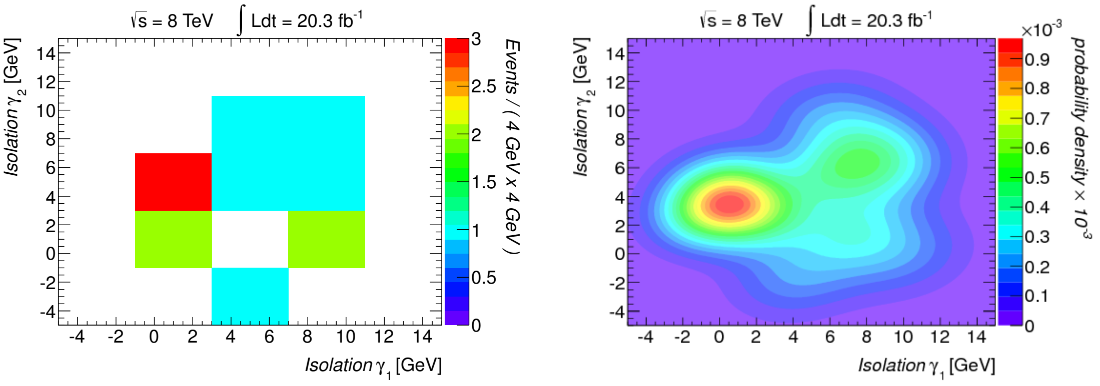

(a)

(b)

Figure A.7: The two-dimensional $E_{\mathrm{T}}^{\mathrm{iso}}$ distribution for the jj-p.d.f. selected using the exclusive selection. (a): $E_{\mathrm{T}}^{\mathrm{iso}}$ distribution in the AA sample. (b): Corresponding smoothed p.d.f. F_{jj}. The two-dimensional $E_{\mathrm{T}}^{\mathrm{iso}}$ distribution obtained using the inclusive selection and the corresponding p.d.f. are shown in Figure 7.3

.

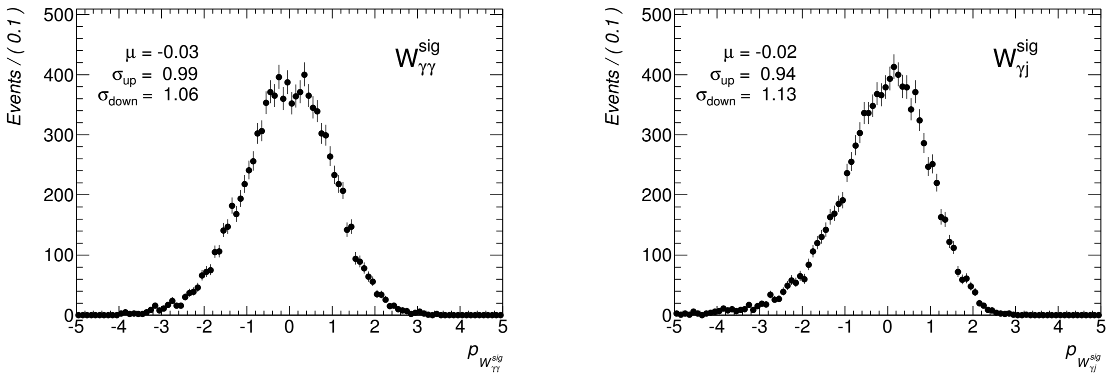

(a) $W_{\gamma\gamma}$ (b) $W^{\mathrm{sig}}_{\gamma\mathrm{j}}$

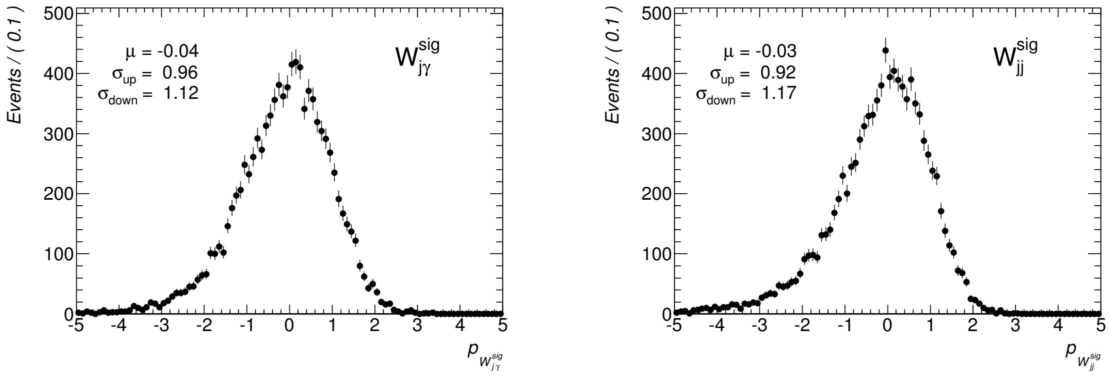

(c) $W^{\mathrm{sig}}_{\mathrm{j}\gamma}$ (d) $W^{\mathrm{sig}}_{\mathrm{jj}}$

Figure A.8: Pull distributions for the four event yields in the signal region from 10000 pseudo-experiments. In addition the mean, width and goodness-of-fit of a Gaussian fitted to these distributions is shown. The same distributions for the inclusive selection are shown in Figure 7.5.

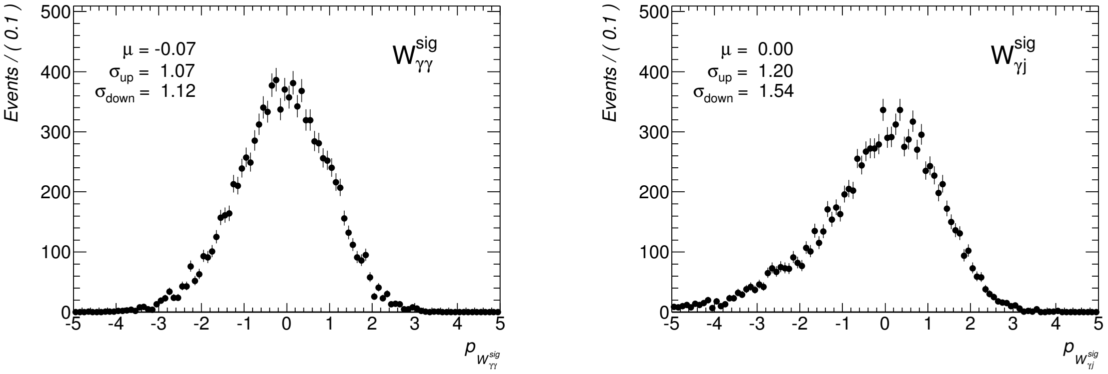

(a) $W^{\mathrm{sig}}_{\gamma\gamma}$ (b) $W^{\mathrm{sig}}_{\gamma\mathrm{j}}$

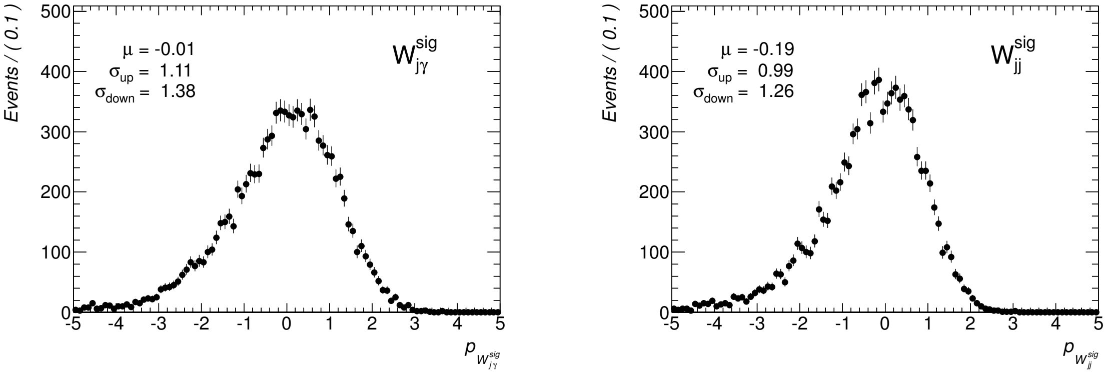

(c) $W^{\mathrm{sig}}_{\mathrm{j}\gamma}$ (d) $W^{\mathrm{sig}}_{\mathrm{jj}}$

Figure A.9: Pull distributions from pseudo-experiments used to evaluate the systematic uncertainty due to limited control region statistics.

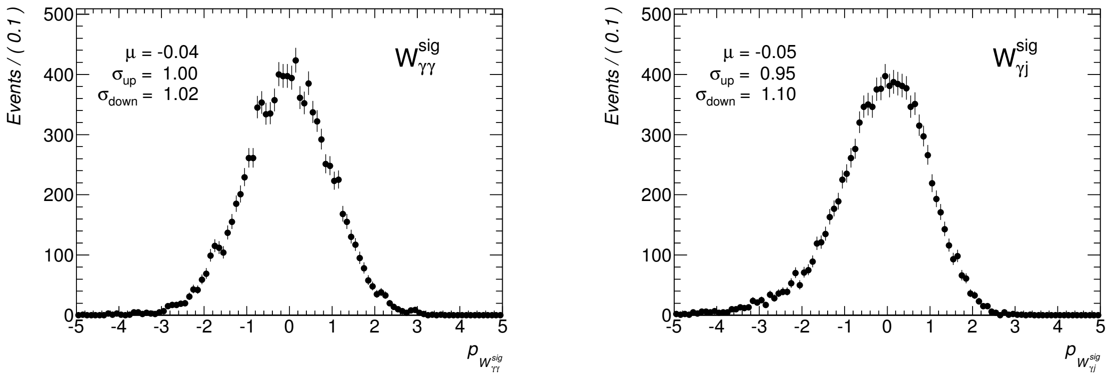

(a) $W^{\mathrm{sig}}_{\gamma\gamma}$ (b) $W^{\mathrm{sig}}_{\gamma\mathrm{j}}$

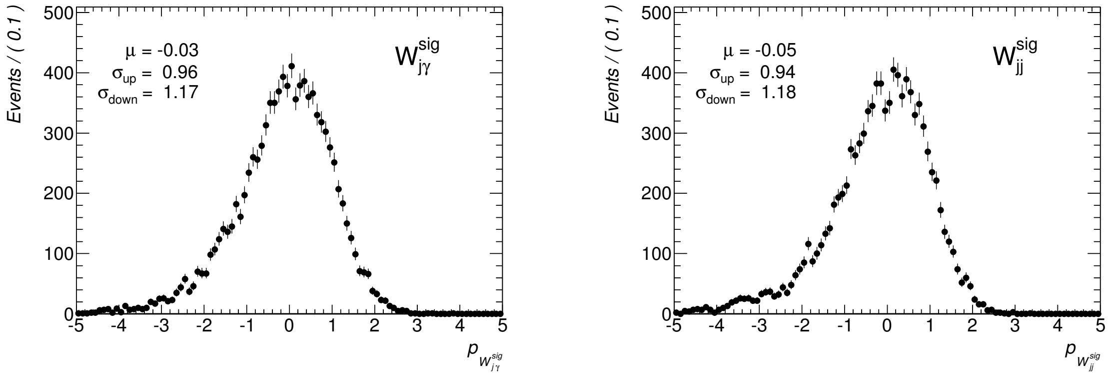

(c) $W^{\mathrm{sig}}_{\mathrm{j}\gamma}$ (d) $W^{\mathrm{sig}}_{\mathrm{jj}}$

Figure A.10: Pull distributions from pseudo-experiments used to evaluate the systematic uncertainty due to the choice of the background model for the exclusive selection. The pseudo-data has been generated using the nominal template and it has been fitted using the sum of a Gaussian and a Novosibirsk function with the same mean parameter, as fake-photon template F_{b}. The corresponding distributions for the inclusive selection can be found in Figure A.10.

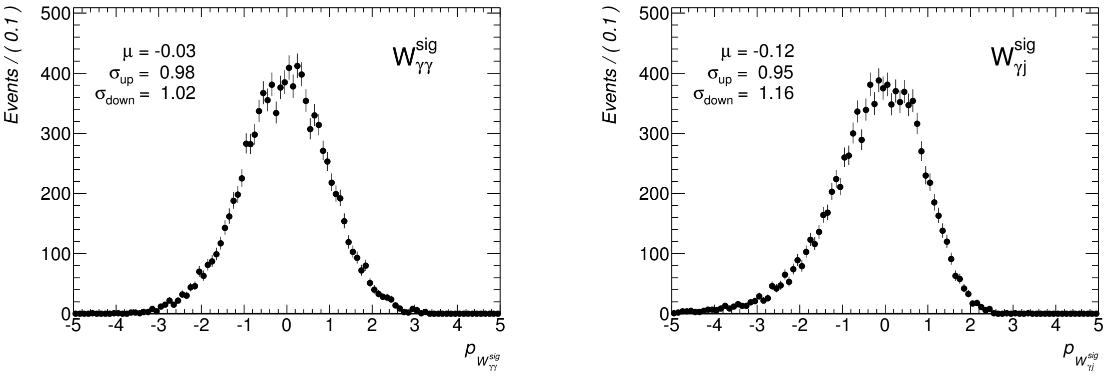

(a) $W^{\mathrm{sig}}_{\gamma\gamma}$ (b) $W^{\mathrm{sig}}_{\gamma \mathrm{j}}$

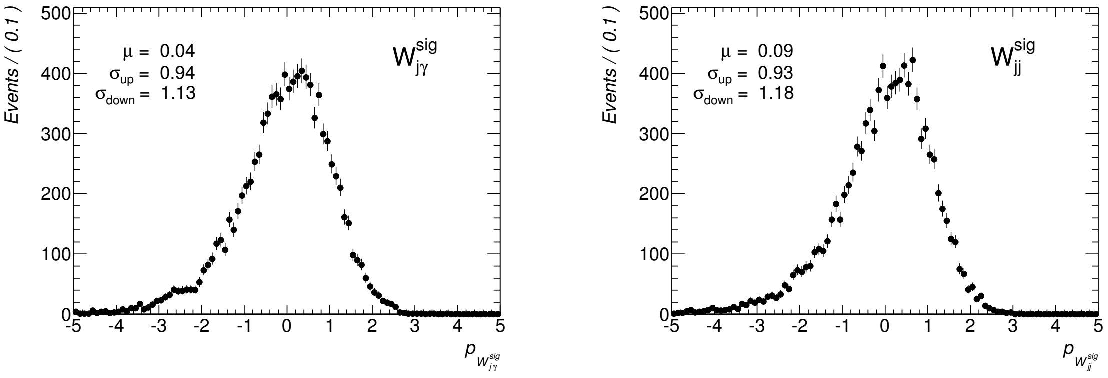

(c) $W^{\mathrm{sig}}_{\mathrm{j}\gamma}$ (d) $W^{\mathrm{sig}}_{\mathrm{jj}}$

Figure A.11: Pull distributions from pseudo-experiments used to evaluate the systematic uncertainty due to the choice of the background model for the exclusive selection. The pseudo-data has been generated using the nominal template and it has been fitted using a Crystal-Ball function as fake-photon template F_{b}. The corresponding distributions for the inclusive selection can be found in Figure A.11.

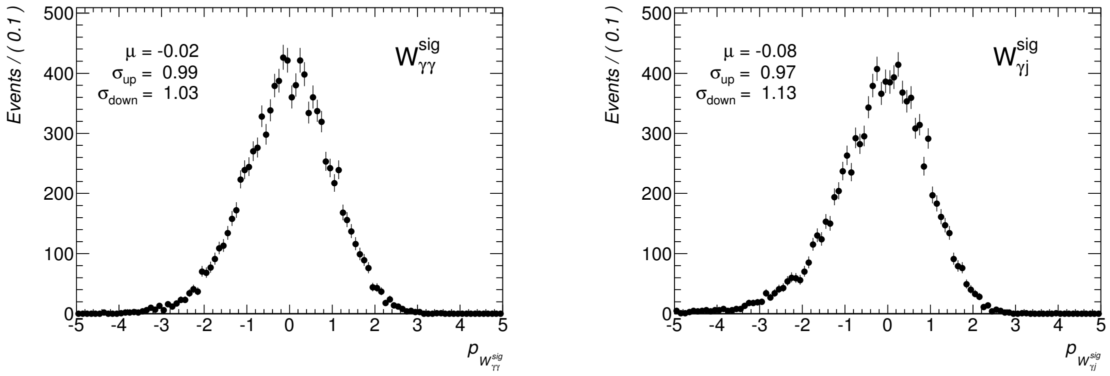

(a) $W^{\mathrm{sig}}_{\gamma\gamma}$

(b) $W^{\mathrm{sig}}_{\gamma \mathrm{j}}$

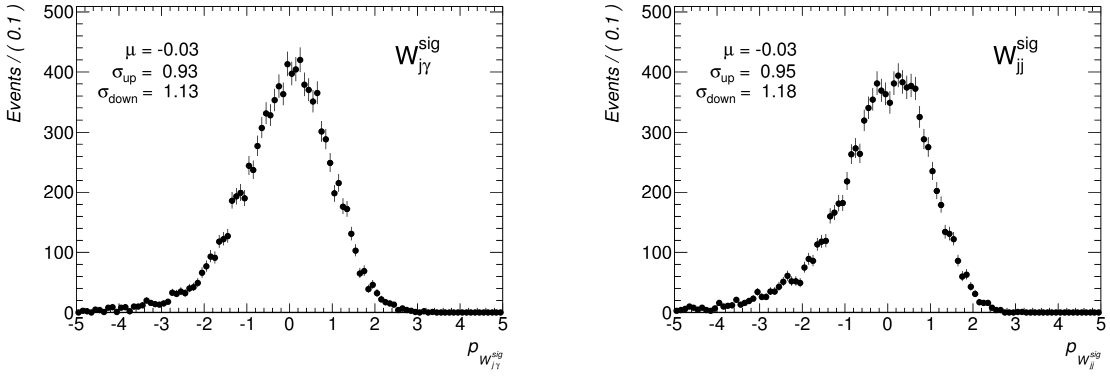

(c) $W^{\mathrm{sig}}_{\mathrm{j}\gamma}$

(d) $W^{\mathrm{sig}}_{\mathrm{jj}}$

Figure A.12: Pull distributions from pseudo-experiments used to evaluate the systematic uncertainty due to the definition of the fake-photon control region for the exclusive selection. The pseudo-data has been generated with a template obtained using the L_5' control region definition and was fitted using the nominal template. The corresponding distribution for the inclusive selection can be found in Figure A.12.

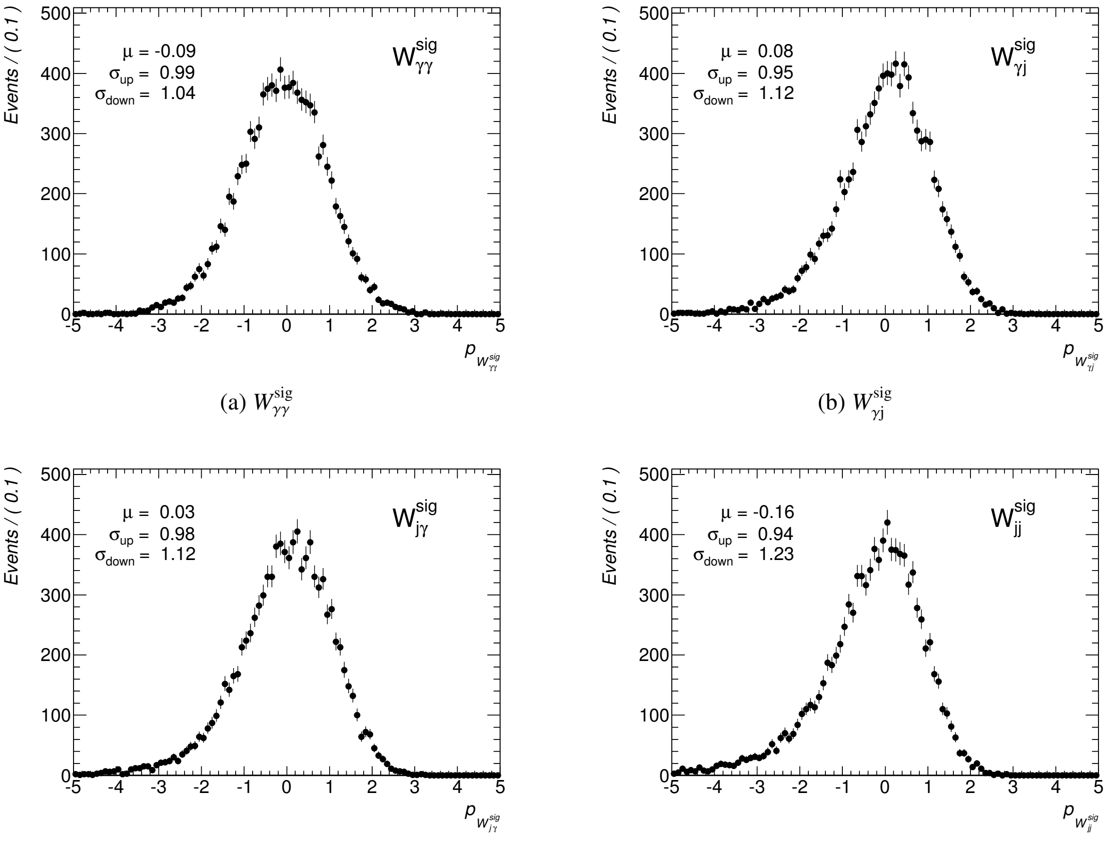

(a) $W^{\mathrm{sig}}_{\gamma\gamma}$

(b) $W^{\mathrm{sig}}_{\gamma\mathrm{j}}$

(c) $W^{\mathrm{sig}}_{\mathrm{j}\gamma}$

(d) $W^{\mathrm{sig}}_{\mathrm{jj}}$

Figure A.13: Pull distributions from pseudo-experiments used to evaluate the systematic uncertainty due to the definition of the fake-photon control region for the exclusive selection. The pseudo-data has been generated with a template obtained using the L'_3 control region definition and was fitted using the nominal template. The corresponding distribution for the inclusive selection can be found in Figure 7.9.

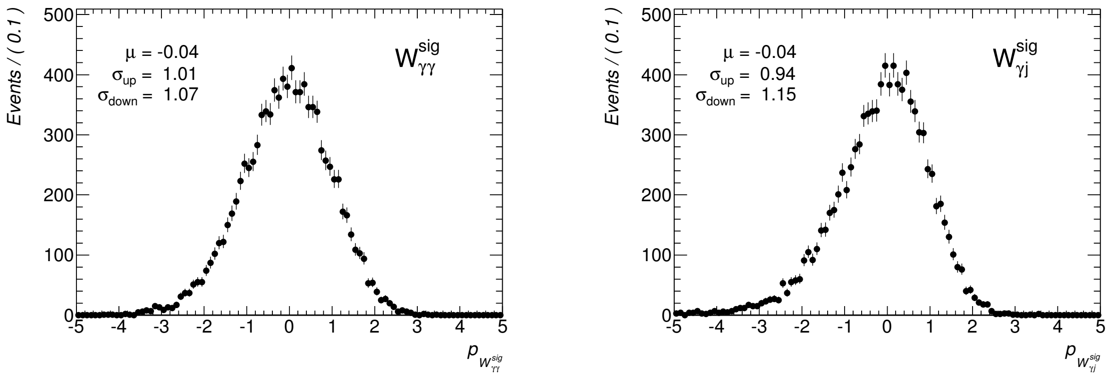

(a) $W_{\gamma\gamma}^{\mathrm{sig}}$ (b) $W_{\gamma\mathrm{j}}^{\mathrm{sig}}$

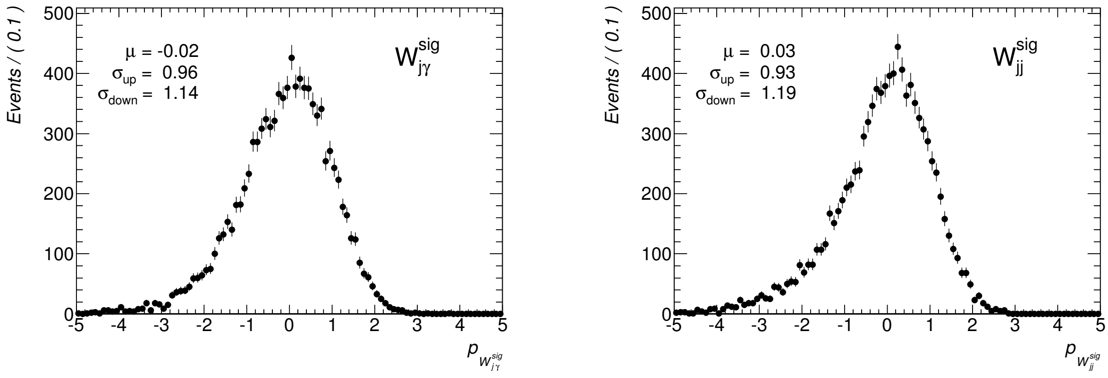

(c) $W_{\mathrm{j}\gamma}^{\mathrm{sig}}$ (d) $W_{\mathrm{jj}}^{\mathrm{sig}}$

Figure A.14: Pull distributions from pseudo-experiments used to evaluate the systematic uncertainty due to the choice of the Monte Carlo generator for the exclusive selection. The corresponding distribution for the inclusive selection can be found in Figure A.3.

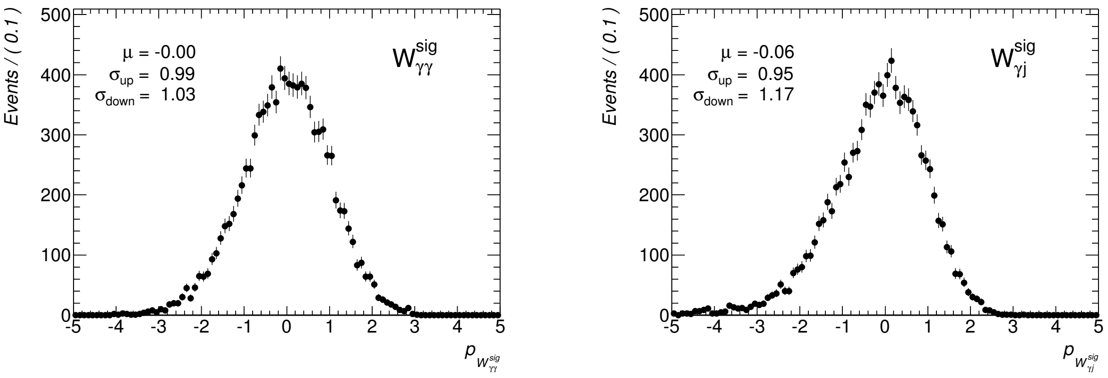

(a) $W^{\text{sig}}_{\gamma\gamma}$ (b) $W^{\text{sig}}_{\gamma\text{j}}$

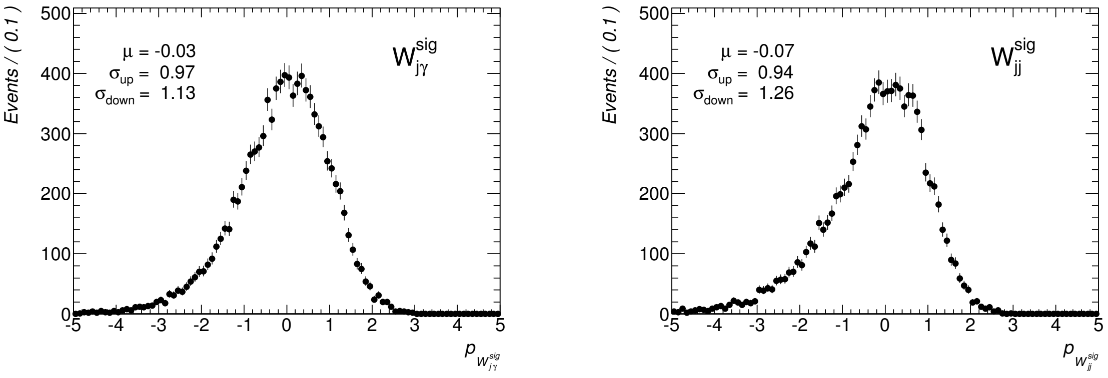

(c) $W^{\text{sig}}_{\text{j}\gamma}$ (d) $W^{\text{sig}}_{\text{jj}}$

Figure A.15: Pull distributions from pseudo-experiments used to evaluate the systematic uncertainty due to the signal-leakage correction for the exclusive selection. The corresponding distribution for the inclusive selection can be found in Figure A.4.

A.5 Simulation of background processes

The simulation of background processes is used for two different purposes in this thesis. First, it is used to develop and validate the methods used for the data-driven background estimates. Secondly, the contribution of irreducible background processes is directly estimated from Monte Carlo simulations. Table A.2 lists the background process and which program was used to simulate them.

Process	Generator	N	σ [fb]	L_{int} [fb^{-1}]
$pp \to W\gamma + X$	AlpGen	23×10^6	1.3×10^5	180
$pp \to W + X$	AlpGen	31×10^6	3.6×10^7	0.85
$pp \to Z\gamma\gamma + X$	Sherpa	1.2×10^6	417	2877
$pp \to t\bar{t} + X$	Mc@Nlo	9×10^6	130×10^3	70
$pp \to t + X$	Mc@Nlo	3.4×10^6	50×10^3	69
$pp \to W(\to \tau\nu)\gamma\gamma + X$	Sherpa	350×10^3	162	2155
$pp \to W^+W^- + X$	Mc@Nlo	1.6×10^6	4.9×10^3	322
$pp \to WZ + X$	Sherpa	2.7×10^6	9.8×10^3	277
$pp \to ZZ + X$	Powheg	5.3×10^6	580	9100

Table A.2: The processes, the program used for simulation, the total number of events, the cross-section and the corresponding integrated luminosity of the simulated background processes used in this thesis.

A.6 Kinematic distributions in the signal region for the exclusive selection

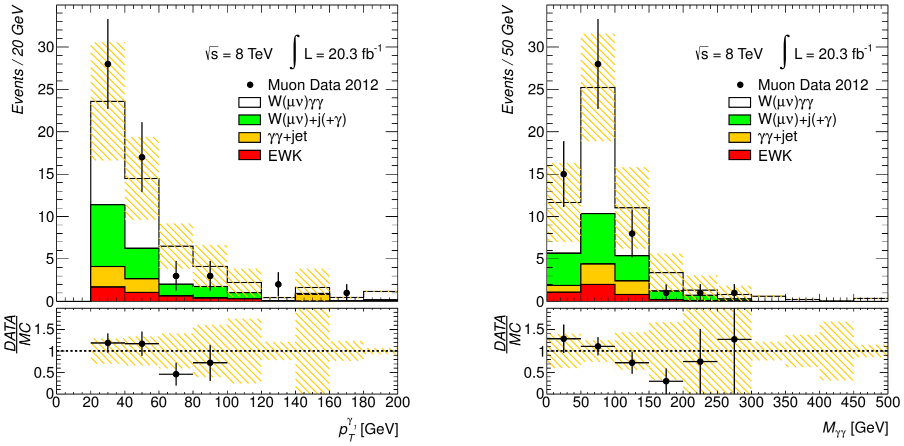

(a) (b)

Figure A.16: The transverse momentum distribution of the leading photon (a) and the di-photon invariant mass (b) in the signal region for the exclusive selection. The prediction from the simulation is shown as a stacked histogram with the uncertainties indicated by the yellow hatched band. The rightmost bin is an overflow bin. The prediction for the $W\gamma\gamma$ process is normalized to the number of signal events observed in data.

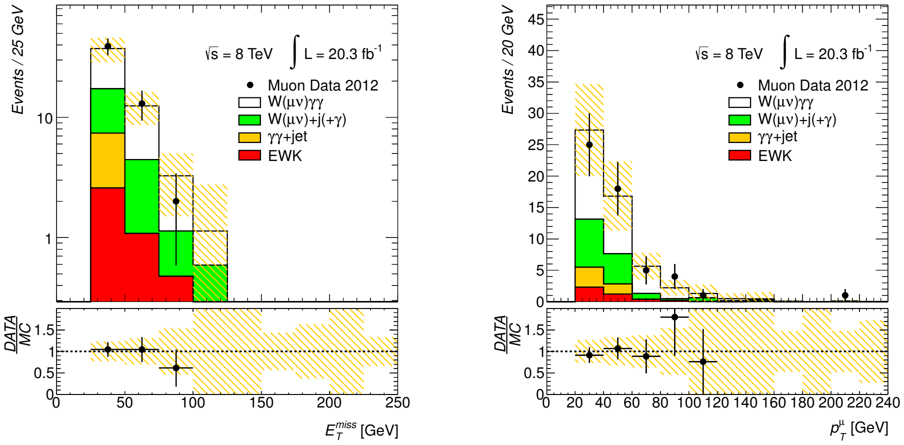

(a) (b)

Figure A.17: The $E_{\mathrm{T}}^{\mathrm{miss}}$ (a) and transverse momentum (b) distribution of the muon for the exclusive selection in the signal region. The prediction from the simulation is shown as a stacked histogram with the uncertainties indicated by the yellow hatched band. The rightmost bin is an overflow bin. The prediction for the $W\gamma\gamma$ process is normalized to the number of signal events observed in data.

A.7 VBFNLO parameters

```
!   Main input file for vbfnlo

!   General parameters of the calculation
!-------------------------------------------
PROCESS              = 500                  ! Identifier for process
LOPROCESS_PLUS_JET   = false                ! switch: LO process with 1 additional jet
LEPTONS              = 98               ! final state leptons
LO_ITERATIONS        = 3         ! number of iterations for LO calculation
NLO_ITERATIONS       = 3         ! number of iterations for real-emissions calc.
LO_POINTS            = 24        ! number of points for LO calculation (= 2^..)
NLO_POINTS           = 24        ! number of points for real-emissions calc. (= 2^..)
LO_GRID              = "grid2_1" "grid2_2" "grid2_3" "grid2_4" ! names of gridfiles for LO calculation
NLO_GRID             = "grid3_1" "grid3_2" "grid3_3" "grid3_4" ! names of gridfiles for real emissions calculation
PHTN_GRID            = "grid4_1" "grid4_2" "grid4_3" "grid4_4" ! names of gridfiles for photon emission calculation
FLOOP_GRID           = "grid5_1" "grid5_2" "grid5_3" "grid5_4" ! names of gridfiles for fermion loop calculation
NLO_SWITCH           = true      ! switch: nlo/lo calculation
EWCOR_SWITCH         = false     ! Whether electoweak corrections are included
FERMIONLOOP          = 3         ! Contribution of gluon-induced fermionic loops for diboson processes
ECM                  = 8000d0    ! collider center-of-mass energy
BEAM1                = 1         ! type of beam 1 (1=proton, -1 = antiproton)
BEAM2                = 1         ! type of beam 2 (1=proton, -1 = antiproton)
ID_MUF               = 4         ! ID for factorization scale
ID_MUR               = 4         ! ID for renormalization scale
MUF_USER             = 100.d0    ! user defined factorization scale, if MUF is set to 0
MUR_USER             = 100.d0    ! user defined renormalization scale, if MUR is set to 0
XIF                  = 1.0d0     ! scale factor xi for mu_F (not mu^2!!)
XIR                  = 1.0d0     ! scale factor xi for mu_R
!   Physics parameters
!------------------------
HMASS       = 126.0d0         ! Higgs mass
HTYPE       = 0               ! Type of Higgs produced:
                              !      0     SM Higgs with mass HMASS
MODEL       = 1               ! model: 1 for SM, 2 for MSSM
HWIDTH      = -999d0          ! Higgs width (set to -999d0 for internal calculation)
TOPMASS     = 172.4d0         ! Top mass
BOTTOMMASS  = 4.855d0         ! Bottom Pole mass
CHARMMASS   = 1.65d0          ! Charm Pole mass
TAU_MASS    = 1.77684D0       ! Tau mass
ALFA_S      = 0.1176d0        ! Strong coupling constant
EWSCHEME    = 3               ! Choose scheme for electroweak parameters (1,2,3,4)
EW_APPROX   = 0               ! Approximation used when calculating electroweak
FERMI_CONST = 1.16637d-5      ! Fermi Constant
ALFA        = 7.2973525376d-3 ! Fine-structure constant
SIN2W       = 0.23119d0       ! Weak mixing angle
WMASS       = 80.398d0        ! W mass
ZMASS       = 91.1876d0       ! Z mass
ANOM_CPL    = false           ! Anomalous couplings
KK_MOD      = false           ! Warped Higgsless Model
SPIN2       = false           ! Spin-2 model
!   Parameters for the LHA event output
!-----------------------------------------
LHA_SWITCH            = false    ! Les Houches interface only for LO calculation
LHA_FILE              = event.lhe  ! Name of Les Houches output file
HEPMC_SWITCH          = false      ! HepMC interface only for LO calculation
HEPMC_FILE            = event.hepmc ! Name of HepMC output file
UNWEIGHTING_SWITCH    = false    ! weighted/unweighted (T/F) events for LHA
PRENEVUNW             = 1000     ! number of events to calculate pre-maximal weight
TAUMASS               = false    ! Include mass of the tau lepton(s) in the LHA file for VBF processes
!   PDF set parameters
!------------------------
PDF_SWITCH    = 1       ! which pdfs to use: 1 = lhapdf, 0 = hard-wired cteq (default)
! choose pdfset and pdfmember here. Look at the LHAPDF manual for details.
LO_PDFNAME    = MSTW2008lo90cl.LHgrid
NLO_PDFNAME   = MSTW2008nlo90cl.LHgrid
LO_PDFMEMBER  = 0
NLO_PDFMEMBER = 0
```

Table A.3: Generation parameters for the VBFNLO program.g

Bibliography

[1] J. Beringer et al., *Review of Particle Physics*, *Phys. Rev.* D86 (2012 and 2013 partial update for the 2014 edition) 010001, DOI: `10.1103/PhysRevD.86.010001`.

[2] ATLAS Collaboration, *Observation of a new particle in the search for the Standard Model Higgs boson with the ATLAS detector at the LHC*, *Phys.Lett.* B716 (2012) 1–29, DOI: `10.1016/j.physletb.2012.08.020`, ARXIV: `1207.7214 [hep-ex]`.

[3] CMS Collaboration, *Observation of a new boson at a mass of 125 GeV with the CMS experiment at the LHC*, *Phys.Lett.* B716 (2012) 30–61, DOI: `10.1016/j.physletb.2012.08.021`, ARXIV: `1207.7235 [hep-ex]`.

[4] ATLAS Collaboration, *Measurements of $W\gamma$ and $Z\gamma$ production in pp collisions at $\sqrt{s} = 7\,\text{TeV}$ with the ATLAS detector at the LHC*, *Phys.Rev.* D87 (2013) 112003, DOI: `10.1103/PhysRevD.87.112003`, ARXIV: `1302.1283 [hep-ex]`.

[5] CMS Collaboration, *Measurement of the $W\gamma$ and $Z\gamma$ inclusive cross sections in pp collisions at $\sqrt{s} = 7\,\text{TeV}$ and limits on anomalous triple gauge boson couplings* (2013), ARXIV: `1308.6832 [hep-ex]`.

[6] ATLAS Collaboration, *Measurement of ZZ production in pp collisions at $\sqrt{s} = 7\,\text{TeV}$ and limits on anomalous ZZZ and $ZZ\gamma$ couplings with the ATLAS detector*, *JHEP* 1303 (2013) 128, DOI: `10.1007/JHEP03(2013)128`, ARXIV: `1211.6096 [hep-ex]`.

[7] A. Belyaev et al., *Strongly interacting vector bosons at the CERN LHC: Quartic anomalous couplings*, *Phys.Rev.* D59 (1999) 015022, DOI: `10.1103/PhysRevD.59.015022`, ARXIV: `hep-ph/9805229 [hep-ph]`.

[8] *Press release from the Royal Swedish Academy of Science*, 8th Oct. 2013, URL: `http://www.nobelprize.org/nobel_prizes/physics/laureates/2013/press.pdf`.

[9] S. Glashow, *Partial Symmetries of Weak Interactions*, *Nucl. Phys.* 22 (1961) 579.

[10] A. Salam, *Weak and Electromagnetic Interactions*, *Conf.Proc.* C680519 (1968) 367–377.

[11] S. Weinberg, *A Model of Leptons*, *Phys. Rev. Lett.* 19 (1967) 1264.

[12] F. Halzen and A. D. Martin, *Quarks and Leptons: An Introductory Course in Modern Particle Physics*, 1984, ISBN: 9780471887416.

[13] M. E. Peskin and D. V. Schroeder, *An introduction to quantum field theory*, Boulder, Colo.: Westview Press, 2007 XXII, 842 S. ISBN: 978-0-201-50397-5 ; 0-201-50397-2.

[14] N. Cabibbo, *Unitary Symmetry and Leptonic Decays*, *Phys.Rev.Lett.* 10 (1963) 531–533, DOI: `10.1103/PhysRevLett.10.531`.

[15] M. Kobayashi and T. Maskawa, *CP Violation in the Renormalizable Theory of Weak Interaction*, *Prog.Theor.Phys.* 49 (1973) 652–657, DOI: `10.1143/PTP.49.652`.

[16] F. Englert and R. Brout, *Broken Symmetry and the Mass of Gauge Vector Mesons*, *Phys. Rev. Lett.* 13 (9 Aug. 1964) 321–323, DOI: `10.1103/PhysRevLett.13.321`.

[17] P. Higgs, *Broken symmetries, massless particles and gauge fields*, *Phys. Lett.* 12.2 (1964) 132–133, ISSN: 0031-9163, DOI: `10.1016/0031-9163(64)91136-9`.

[18] P. W. Higgs, *Broken Symmetries and the Masses of Gauge Bosons*, *Phys. Rev. Lett.* 13 (16 Oct. 1964) 508–509, DOI: `10.1103/PhysRevLett.13.508`.

[19] G. S. Guralnik, C. R. Hagen and T. W. B. Kibble, *Global Conservation Laws and Massless Particles*, *Phys. Rev. Lett.* 13 (20 Nov. 1964) 585–587, DOI: `10.1103/PhysRevLett.13.585`.

[20] P. W. Higgs, *Spontaneous Symmetry Breakdown without Massless Bosons*, *Phys. Rev.* 145 (4 May 1966) 1156–1163, DOI: `10.1103/PhysRev.145.1156`.

[21] T. W. B. Kibble, *Symmetry Breaking in Non-Abelian Gauge Theories*, *Phys. Rev.* 155 (5 Mar. 1967) 1554–1561, DOI: `10.1103/PhysRev.155.1554`.

[22] R. Ellis, W. Stirling and B. Webber, *QCD and Collider Physics*, Cambridge Monographs on Particle Physics, Nuclear Physics and Cosmology, Cambridge University Press, 2003, ISBN: 9780521545891.

[23] J. M. Campbell, J. Huston and W. Stirling, *Hard Interactions of Quarks and Gluons: A Primer for LHC Physics*, *Rept.Prog.Phys.* 70 (2007) 89, DOI: `10.1088/0034-4885/70/1/R02`, ARXIV: `hep-ph/0611148 [hep-ph]`.

[24] L. Lipatov, *The parton model and perturbation theory*, *Sov.J.Nucl.Phys.* 20 (1975) 94–102.

[25] V. Gribov and L. Lipatov, *Deep inelastic e p scattering in perturbation theory*, *Sov.J.Nucl.Phys.* 15 (1972) 438–450.

[26] G. Altarelli and G. Parisi, *Asymptotic Freedom in Parton Language*, *Nucl. Phys.* B126 (1977) 298, DOI: `10.1016/0550-3213(77)90384-4`.

[27] Y. L. Dokshitzer, *Calculation of the Structure Functions for Deep Inelastic Scattering and e+ e- Annihilation by Perturbation Theory in Quantum Chromodynamics.*, *Sov.Phys.JETP* 46 (1977) 641–653.

[28] A. Martin et al., *Parton distributions for the LHC*, *Eur. Phys. J.* C63 (2009) 189–285, DOI: `10.1140/epjc/s10052-009-1072-5`, ARXIV: `0901.0002 [hep-ph]`.

[29] H.-L. Lai et al., *New parton distributions for collider physics*, *Phys.Rev.* D82 (2010) 074024, DOI: `10.1103/PhysRevD.82.074024`, ARXIV: `1007.2241 [hep-ph]`.

[30] F. Aaron et al., *Combined Measurement and QCD Analysis of the Inclusive $e^{\pm}$ p Scattering Cross Sections at HERA*, *JHEP* 1001 (2010) 109, DOI: `10.1007/JHEP01(2010)109`, ARXIV: `0911.0884 [hep-ex]`.

[31] U. Baur et al., *$W\gamma\gamma$ production at the Fermilab Tevatron collider: Gauge invariance and radiation amplitude zero*, *Phys.Rev.* D56 (1997) 140–150, DOI: `10.1103/PhysRevD.56.140`, ARXIV: `hep-ph/9702364 [hep-ph]`.

[32] U. Baur, D. Wackeroth and M. M. Weber, *Radiative corrections to $W\gamma\gamma$ production at the LHC*, *PoS* RADCOR2009 (2010) 067, ARXIV: `1001.2688 [hep-ph]`.

[33] G. Bozzi et al., *$W^{\pm}\gamma\gamma$ production with leptonic decays at NLO QCD*, *Phys. Rev.* D83 (2011) 114035, ARXIV: `1103.4613 [hep-ph]`.

[34] S. Frixione, *Isolated photons in perturbative QCD*, *Phys.Lett.* B429 (1998) 369–374, DOI: `10.1016/S0370-2693(98)00454-7`, ARXIV: `hep-ph/9801442 [hep-ph]`.

[35] K. Arnold et al., *VBFNLO: A parton level Monte Carlo for processes with electroweak bosons*, *Comput.Phys.Commun.* 180 (2009) 1661–1670, DOI: `10.1016/j.cpc.2009.03.006`, ARXIV: `0811.4559 [hep-ph]`, URL: `http://www.itp.kit.edu/~vbfnloweb/wiki/doku.php?id=overview`.

[36] V. Hankele and D. Zeppenfeld, *QCD corrections to hadronic WWZ production with leptonic decays*, *Phys.Lett.* B661 (2008) 103–108, DOI: `10.1016/j.physletb.2008.02.014`, ARXIV: `0712.3544 [hep-ph]`.

[37] F. Campanario et al., *QCD corrections to charged triple vector boson production with leptonic decay*, *Phys.Rev.* D78 (2008) 094012, DOI: `10.1103/PhysRevD.78.094012`, ARXIV: `0809.0790 [hep-ph]`.

[38] G. Bozzi et al., *NLO QCD corrections to $W^+W^-\gamma$ and $ZZ\gamma$ production with leptonic decays*, *Phys.Rev.* D81 (2010) 094030, DOI: `10.1103/PhysRevD.81.094030`, ARXIV: `0911.0438 [hep-ph]`.

[39] G. Bozzi et al., *NLO QCD corrections to $W^{\pm}Z\gamma$ production with leptonic decays*, *Phys.Lett.* B696 (2011) 380–385, DOI: `10.1016/j.physletb.2010.12.051`, ARXIV: `1011.2206 [hep-ph]`.

[40] R. W. Brown, K. Kowalski and S. J. Brodsky, *Classical Radiation Zeros in Gauge Theory Amplitudes*, *Phys.Rev.* D28 (1983) 624, DOI: `10.1103/PhysRevD.28.624`.

[41] F. Campanario et al., *Precise predictions for $W\gamma\gamma$+jet production at hadron colliders*, *Phys.Lett.* B704 (2011) 515–519, DOI: `10.1016/j.physletb.2011.09.072`, ARXIV: `1106.4009 [hep-ph]`.

[42] F. Campanario et al., *Di-boson and Tri-boson production at the LHC* (2013), ARXIV: `1307.2261 [hep-ph]`.

[43] W. Buchmueller and D. Wyler, *Effective lagrangian analysis of new interactions and flavour conservation*, *Nuclear Physics B* 268.3-4 (1986) 621–653, ISSN: 0550-3213, DOI: `10.1016/0550-3213(86)90262-2`.

[44] O. Eboli, M. Gonzalez-Garcia and J. Mizukoshi, *$pp \to jje^{\pm}\mu^{\pm}\nu\nu$ and $jje^{\pm}\mu^{\mp}\nu\nu$ at $O(\alpha_{em}^6)$ and $O(\alpha_{em}^4\alpha_S^2)$ for the study of the quartic electroweak gauge boson vertex at CERN LHC*, *Phys.Rev.* D74 (2006) 073005, DOI: `10.1103/PhysRevD.74.073005`, ARXIV: `hep-ph/0606118 [hep-ph]`.

[45] ALEPH Collaboration, *Constraints on anomalous QGCs in interactions from* 183 *to* 209 GeV, *Physics Letters B* 602.1 - 2 (2004) 31–40, ISSN: 0370-2693, DOI: `10.1016/j.physletb.2004.09.041`.

[46] DELPHI Collaboration, *Measurement of the $e^+e^- \to W^+W^-\gamma$ cross-section and limits on anomalous quartic gauge couplings with DELPHI*, *Eur. Phys. J.* C31 (2003) 139–147, DOI: `10.1140/epjc/s2003-01350-x`, ARXIV: `hep-ex/0311004 [hep-ex]`.

[47] L3 Collaboration, *Study of the $W^+W^-\gamma$ process and limits on anomalous quartic gauge boson couplings at LEP*, *Phys.Lett.* B527 (2002) 29–38, DOI: `10.1016/S0370-2693(02)01167-X`, ARXIV: `hep-ex/0111029 [hep-ex]`.

[48] OPAL Collaboration, *Measurement of the $W^+W^-\gamma$ cross-section and first direct limits on anomalous electroweak quartic gauge couplings*, *Phys.Lett.* B471 (1999) 293–307, DOI: `10.1016/S0370-2693(99)01357-X`, ARXIV: `hep-ex/9910069 [hep-ex]`.

[49] D0 Collaboration, *Search for anomalous quartic $WW\gamma\gamma$ couplings in dielectron and missing energy final states in $p\bar{p}$ collisions at $\sqrt{s} = 1.96$ TeV*, *Phys.Rev.* D88 (2013) 012005, DOI: `10.1103/PhysRevD.88.012005`, ARXIV: `1305.1258 [hep-ex]`.

[50] G. Belanger et al., *Bosonic quartic couplings at LEP-2*, *Eur. Phys. J.* C13 (2000) 283–293, DOI: `10.1007/s100520000305`, ARXIV: `hep-ph/9908254 [hep-ph]`.

[51] T. Han, *Workshop Summary*, Workshop Summary of the Anomalous Quartic Gauge Couplings Workshop 2013 in Dresden, 2nd Oct. 2013, URL: `https://indico.desy.de/getFile.py/access?contribId=19&sessionId=7&resId=1&materialId=slides&confId=7512`.

[52] E. Fermi, *Versuch einer Theorie der Betastrahlen*, *Zeitschrift für Physik* Bd. 88 (1934) 161.

[53] F. L. Wilson, *Fermi's Theory of Beta Decay*, *American Journal of Physics* 36.12 (1968) 1150–1160, DOI: `http://dx.doi.org/10.1119/1.1974382`.

[54] CMS Collaboration, *Study of exclusive two-photon production of W^+W^- in pp collisions at $\sqrt{s} = 7$ TeV and constraints on anomalous quartic gauge couplings*, *JHEP* 1307 (2013) 116, DOI: `10.1007/JHEP07(2013)116`, ARXIV: `1305.5596 [hep-ex]`.

[55] CMS Collaboration, *A Search for $WW\gamma$ and $WZ\gamma$ production in pp Collisions at $\sqrt{s} = 8$ TeV.*, CMS-PAS-SMP-13-009, CERN, 2013, URL: `https://cds.cern.ch/record/1563302`.

[56] *VBFNLO utility to calculate form factors*, Version 1.2.1, July 2013, URL: `http://www.itp.kit.edu/~vbfnloweb/wiki/doku.php?id=download:formfactor`.

[57] V. D. Barger et al., *Strong W^+W^+ scattering signals at pp supercolliders*, *Phys.Rev.* D42 (1990) 3052–3077, DOI: `10.1103/PhysRevD.42.3052`.

[58] L. Evans and P. Bryant, *LHC Machine*, *JINST* 3 (2008), ed. by L. Evans S08001, DOI: `10.1088/1748-0221/3/08/S08001`, URL: `http://cds.cern.ch/record/1129806`.

[59] ATLAS Collaboration, *The ATLAS Experiment at the CERN Large Hadron Collider*, *J. Instrum.* 3 (2008) S08003. 437 p, URL: `http://cds.cern.ch/record/1129811`.

[60] CMS Collaboration, *The CMS experiment at the CERN LHC. The Compact Muon Solenoid experiment*, *J. Instrum.* 3 (2008) S08004. 361 p, URL: `http://cds.cern.ch/record/1129810`.

[61] ALICE Collaboration, *The ALICE experiment at the CERN LHC. A Large Ion Collider Experiment*, *J. Instrum.* 3 (2008) S08002. 259 p, URL: `http://cds.cern.ch/record/1129812`.

[62] LHCb Collaboration, *The LHCb Detector at the LHC*, *J. Instrum.* 3.LHCb-DP-2008-001. CERN-LHCb-DP-2008-001 (2008) S08005, URL: `http://cds.cern.ch/record/1129809`.

[63] ATLAS Collaboration, *Expected performance of the ATLAS experiment: detector, trigger and physics*, CERN-OPEN-2008-20 (2009), ARXIV: `0901.0512 [hep-ex]`, URL: `https://cds.cern.ch/record/1125884`.

[64] S. van der Meer, *Calibration of the effective beam height in the ISR*, 1968.

[65] C. Rubbia, *Measurement of the luminosity of $p\overline{p}$ collider with a (generalized) Van der Meer Method*, CERN-pp-Note-38, CERN, Nov. 1977.

[66] G. Aad et al., *Improved luminosity determination in pp collisions at $\sqrt{s} = 7$ TeV using the ATLAS detector at the LHC*, *Eur. Phys. J.* C73 (2013) 2518, DOI: `10.1140/epjc/s10052-013-2518-3`, ARXIV: `1302.4393 [hep-ex]`.

[67] S. Agostinelli et al., *GEANT4: A Simulation toolkit*, *Nucl.Instrum.Meth.* A506 (2003) 250–303, DOI: `10.1016/S0168-9002(03)01368-8`.

[68] Thomson Reuters, *Web of Knowledge*, Oct. 2013, URL: `http://apps.webofknowledge.com`.

[69] SHERPA *Manual*, Oct. 2013, URL: `http://sherpa.hepforge.org/doc/SHERPA-MC-1.4.1.html`.

[70] S. Catani et al., *QCD matrix elements + parton showers*, *JHEP* 0111 (2001) 063, ARXIV: `hep-ph/0109231 [hep-ph]`.

[71] F. Caravaglios et al., *A New approach to multijet calculations in hadron collisions*, *Nucl.Phys.* B539 (1999) 215–232, DOI: `10.1016/S0550-3213(98)00739-1`, ARXIV: `hep-ph/9807570 [hep-ph]`.

[72] B. Andersson, *The Lund model*, *Camb.Monogr.Part.Phys.Nucl.Phys.Cosmol.* 7 (1997) 1–471.

[73] T. D. Gottschalk, *An Improved Description of Hadronization in the QCD Cluster Model for e^+e^- Annihilation*, *Nucl.Phys.* B239 (1984) 349, DOI: `10.1016/0550-3213(84)90253-0`.

[74] B. Webber, *A QCD Model for Jet Fragmentation Including Soft Gluon Interference*, *Nucl.Phys.* B238 (1984) 492, DOI: `10.1016/0550-3213(84)90333-X`.

[75] T. Gleisberg et al., *Event generation with SHERPA 1.1*, *JHEP* 0902 (2009) 007, DOI: `10.1088/1126-6708/2009/02/007`, ARXIV: `0811.4622 [hep-ph]`.

[76] S. Hoeche et al., *QCD matrix elements and truncated showers*, *JHEP* 0905 (2009) 053, DOI: `10.1088/1126-6708/2009/05/053`, ARXIV: `0903.1219 [hep-ph]`.

[77] J.-C. Winter, F. Krauss and G. Soff, *A Modified cluster hadronization model*, *Eur. Phys. J.* C36 (2004) 381–395, DOI: `10.1140/epjc/s2004-01960-8`, ARXIV: `hep-ph/0311085 [hep-ph]`.

[78] M. L. Mangano et al., *ALPGEN, a generator for hard multiparton processes in hadronic collisions*, *JHEP* 0307 (2003) 001, ARXIV: `hep-ph/0206293 [hep-ph]`.

[79] G. Corcella et al., *HERWIG 6: An Event generator for hadron emission reactions with interfering gluons (including supersymmetric processes)*, *JHEP* 0101 (2001) 010, DOI: `10.1088/1126-6708/2001/01/010`, ARXIV: `hep-ph/0011363 [hep-ph]`.

[80] M. Bahr et al., *Herwig++ Physics and Manual*, *Eur. Phys. J.* C58 (2008) 639–707, DOI: `10.1140/epjc/s10052-008-0798-9`, ARXIV: `0803.0883 [hep-ph]`.

[81] J. Butterworth et al., *JIMMY4: Multiparton Interactions in Herwig for the LHC*, Oct. 2013, URL: `http://projects.hepforge.org/jimmy/`.

[82] T. Sjostrand et al., *High-energy physics event generation with PYTHIA 6.1*, *Comput. Phys. Commun.* 135 (2001) 238–259, DOI: `10.1016/S0010-4655(00)00236-8`, ARXIV: `hep-ph/0010017 [hep-ph]`.

[83] T. Sjostrand, S. Mrenna and P. Z. Skands, *A Brief Introduction to PYTHIA 8.1*, *Comput. Phys. Commun.* 178 (2008) 852–867, DOI: `10.1016/j.cpc.2008.01.036`, ARXIV: `0710.3820 [hep-ph]`.

[84] S. Frixione and B. R. Webber, *Matching NLO QCD computations and parton shower simulations*, *JHEP* 0206 (2002) 029, ARXIV: `hep-ph/0204244 [hep-ph]`.

[85] S. Alioli et al., *A general framework for implementing NLO calculations in shower Monte Carlo programs: the POWHEG BOX*, *JHEP* 1006 (2010) 043, DOI: `10.1007/JHEP06(2010)043`, ARXIV: `1002.2581 [hep-ph]`.

[86] ATLAS Collaboration, *The ATLAS Simulation Infrastructure*, *Eur. Phys. J.* C70 (2010) 823–874, DOI: `10.1140/epjc/s10052-010-1429-9`, ARXIV: `1005.4568 [physics.ins-det]`.

[87] ATLAS Collaboration, *Performance of pile-up subtraction for jet shapes*, ATLAS-CONF-2013-085, CERN, 2013, URL: `http://cds.cern.ch/record/1572979`.

[88] ATLAS Collaboration, *Measurements of $W\gamma$ and $Z\gamma$ production in pp collisions at $\sqrt{s}$= 7 TeV with the ATLAS detector at the LHC*, arXiv:1302.1283. CERN-PH-EP-2012-345 (Feb. 2013), submitted to PRD, URL: https://cds.cern.ch/record/1513670.

[89] ATLAS Collaboration, *ATLAS Computing: Technical Design Report*, ATLAS-TDR-017, CERN-LHCC-2005-022 (2005), URL: https://cds.cern.ch/record/837738.

[90] ATLAS Collaboration, *Expected photon performance in the ATLAS experiment*, ATL-PHYS-PUB-2011-007, CERN, Apr. 2011, URL: https://cdsweb.cern.ch/record/1345329.

[91] ATLAS Collaboration, *Measurements of the photon identification efficiency with the ATLAS detector using 4.9 fb^{-1} of pp collision data collected in 2011*, ATLAS-CONF-2012-123, CERN, Aug. 2012, URL: https://cds.cern.ch/record/1473426.

[92] W. Lampl et al., *Calorimeter Clustering Algorithms: Description and Performance*, ATL-LARG-PUB-2008-002, CERN, Apr. 2008, URL: https://cds.cern.ch/record/1099735.

[93] M. Aharrouche et al., *Energy linearity and resolution of the ATLAS electromagnetic barrel calorimeter in an electron test-beam*, *Nucl.Instrum.Meth.* A568 (2006) 601–623, DOI: 10.1016/j.nima.2006.07.053, ARXIV: physics/0608012 [physics].

[94] M. Aharrouche et al., *Measurement of the response of the ATLAS liquid argon barrel calorimeter to electrons at the 2004 combined test-beam*, *Nucl.Instrum.Meth.* A614 (2010) 400–432, DOI: 10.1016/j.nima.2009.12.055.

[95] ATLAS Collaboration, *Electron and photon reconstruction and identification in ATLAS: expected performance at high energy and results at 900 GeV*, CERN, 2010, URL: http://cdsweb.cern.ch/record/1273197.

[96] ATLAS Collaboration, *Measurement of the inclusive isolated prompt photon cross section in pp collisions at sqrt(s) = 7 TeV with the ATLAS detector*, *Phys.Rev.* D83 (2011) 052005, DOI: 10.1103/PhysRevD.83.052005, ARXIV: 1012.4389 [hep-ex].

[97] S. D. Ellis and D. E. Soper, *Successive combination jet algorithm for hadron collisions*, *Phys. Rev. D* 48 (Apr. 1993) 3160–3166. 15 p, ARXIV: 9305266 [hep-ph].

[98] S. Catani et al., *Longitudinally invariant K_t clustering algorithms for hadron hadron collisions*, *Nucl.Phys.* B406 (1993) 187–224, DOI: 10.1016/0550-3213(93)90166-M.

[99] J. Saxon and H. H. Williams, *Neural Networks for Photon Identification in $H \rightarrow \gamma\gamma$*, ATL-COM-PHYS-2013-305, CERN, Mar. 2013, URL: https://cds.cern.ch/record/1524081.

[100] *Photon ID e/gamma recommendation for Moriond*, Internal presentation., 2013, URL: https://indico.cern.ch/getFile.py/access?contribId=2&resId=0&materialId=slides&confId=231190.

[101] R. Nicolaidou et al., *Muon identification procedure for the ATLAS detector at the LHC using Muonboy reconstruction package and tests of its performance using cosmic rays and single beam data*, *J. Phys Conf. Ser.* 219.3 (2010) 032052, DOI: 10.1088/1742-6596/219/3/032052.

[102] S. Hassani et al., *A muon identification and combined reconstruction procedure for the ATLAS detector at the LHC using the (MUONBOY, STACO, MuTag) reconstruction packages*, *Nucl.Instrum.Meth.* A572 (2007) 77–79, DOI: 10.1016/j.nima.2006.10.340, URL: http://inspirehep.net/record/754679.

[103] ATLAS Collaboration, *Muon reconstruction efficiency in reprocessed 2010 LHC proton-proton collision data recorded with the ATLAS detector*, ATLAS-CONF-2011-063, CERN, Apr. 2011, URL: https://cds.cern.ch/record/1345743.

[104] ATLAS Collaboration, *Preliminary results on the muon reconstruction efficiency, momentum resolution, and momentum scale in ATLAS 2012 pp collision data*, ATLAS-CONF-2013-088, CERN, Aug. 2013, URL: `https://cds.cern.ch/record/1580207`.

[105] G. P. Salam, *Towards Jetography*, *Eur. Phys. J.* C67 (2010) 637–686, DOI: `10.1140/epjc/s10052-010-1314-6`, ARXIV: `0906.1833 [hep-ph]`.

[106] M. Cacciari, G. P. Salam and G. Soyez, *The Anti-k(t) jet clustering algorithm*, *JHEP* 0804 (2008) 063, DOI: `10.1088/1126-6708/2008/04/063`, ARXIV: `0802.1189 [hep-ph]`.

[107] M. Cacciari, G. P. Salam and G. Soyez, *FastJet User Manual*, *Eur. Phys. J.* C72 (2012) 1896, DOI: `10.1140/epjc/s10052-012-1896-2`, ARXIV: `1111.6097 [hep-ph]`.

[108] M. Cacciari and G. P. Salam, *Dispelling the N^3 myth for the k_t jet-finder*, *Phys.Lett.* B641 (2006) 57–61, DOI: `10.1016/j.physletb.2006.08.037`, ARXIV: `hep-ph/0512210 [hep-ph]`.

[109] Y. L. Dokshitzer et al., *Better jet clustering algorithms*, *JHEP* 9708 (1997) 001, ARXIV: `hep-ph/9707323 [hep-ph]`.

[110] ATLAS Collaboration, *Jet energy measurement and its systematic uncertainty in proton-proton collisions at* $\sqrt{s} = 7$ TeV *with the ATLAS detector* (Aug. 2013), submitted to Eur. Phys. J. C.

[111] ATLAS Collaboration, *Performance of Missing Transverse Momentum Reconstruction in ATLAS studied in Proton-Proton Collisions recorded in 2012 at 8 TeV*, ATLAS-CONF-2013-082, CERN, Aug. 2013, URL: `http://cds.cern.ch/record/1570993`.

[112] T. Golling et al., *The ATLAS Data Quality Defect Database System*, arXiv:1110.6119. EFI-11-30 (Oct. 2011), Comments: 6 pages, 3 figures, submitted to EPJ C, URL: `https://cds.cern.ch/record/1394173`.

[113] *Luminosity Public Results*, 7th Oct. 2013, URL: `https://twiki.cern.ch/twiki/bin/view/AtlasPublic/LuminosityPublicResults`.

[114] *GoodRunList*, URL: `http://atlasdqm.web.cern.ch/atlasdqm/grlgen/All_Good/data12_8TeV.periodAllYear_DetStatus-v61-pro14-02_DQDefects-00-01-00_PHYS_StandardGRL_All_Good.xml`.

[115] M. Baak et al., *Data Quality Status Flags and Good Run Lists for Physics Analysis in ATLAS*, ATL-COM-GEN-2009-015, CERN, Mar. 2009, URL: `https://cds.cern.ch/record/1168026`.

[116] V. Scharf, *muon + 2gamma trigger proposal*, internal presentation, 9th Feb. 2012, URL: `https://indico.cern.ch/getFile.py/access?contribId=10&resId=0&materialId=slides&confId=177265`.

[117] K. Prokofiev for the ATLAS Collaboration, *Reconstruction of primary vertices in pp collisions at energies of 900 GeV and 7 TeV with the ATLAS detector*, arXiv:1010.1483. SNSN-323-63, Oct. 2010, URL: `https://cds.cern.ch/record/1298557`.

[118] ATLAS Collaboration, *Measurement of $W\gamma$ and $Z\gamma$ production in proton-proton collisions at $\sqrt{s} = 7$ TeV with the ATLAS Detector*, *J. High Energy Phys.* 09.arXiv:1106.1592. CERN-PH-EP-2011-079 (June 2011) 072. 46 p, URL: `https://cds.cern.ch/record/1357549`.

[119] ATLAS Collaboration, *Measurement of $W\gamma$ and $Z\gamma$ production cross sections in pp collisions at $\sqrt{s} = 7$ TeV and limits on anomalous triple gauge couplings with the ATLAS detector*, *Phys. Lett. B* 717.arXiv:1205.2531. CERN-PH-EP-2012-059 (May 2012) 49–69. 24 p, URL: `https://cds.cern.ch/record/1448274`.

[120] F. Campanario and S. Sapeta, *WZ production beyond NLO for high-pT observables*, *Phys.Lett.* B718 (2012) 100–104, DOI: `10.1016/j.physletb.2012.10.013`, ARXIV: `1209.4595 [hep-ph]`.

[121] G. Aad et al., *Measurement of the isolated di-photon cross-section in pp collisions at $\sqrt{s} = 7$ TeV with the ATLAS detector*, *Phys.Rev.* D85 (2012) 012003, DOI: `10.1103/PhysRevD.85.012003`, ARXIV: `1107.0581 [hep-ex]`.

[122] G. Aad et al., *Measurement of isolated-photon pair production in pp collisions at $\sqrt{s} = 7$ TeV with the ATLAS detector*, *JHEP* 1301 (2013) 086, DOI: `10.1007/JHEP01(2013)086`, ARXIV: `1211.1913 [hep-ex]`.

[123] Gaiser, J.E., *Charmonium Spectroscopy from Radiative Decays of the J/Psi and Psi-Prime*, PhD thesis: Stanford University, Aug. 1982 178.

[124] J. Lees et al., *Measurement of the Branching Fraction for $D_s^+ \to \tau^+ \nu_\tau$ and Extraction of the Decay Constant f_{D_s}* (2010), ARXIV: `1003.3063 [hep-ex]`.

[125] W. Verkerke et al., *The RooFit Toolkit for Data Modelling*, URL: `http://roofit.sourceforge.net`.

[126] F. James and M. Roos, *Minuit: A System for Function Minimization and Analysis of the Parameter Errors and Correlations*, *Comput.Phys.Commun.* 10 (1975) 343–367, DOI: `10.1016/0010-4655(75)90039-9`.

[127] M. Whalley, D. Bourilkov and R. Group, *The Les Houches accord PDFs (LHAPDF) and LHAGLUE* (2005), ARXIV: `hep-ph/0508110 [hep-ph]`, URL: `http://hepforge.cedar.ac.uk/lhapdf/`.

[128] P. Bell et al., *Measurement of $W\gamma\gamma$ production in proton-proton collisions at $\sqrt{s} = 8$ TeV with the ATLAS detector*, ATL-COM-PHYS-2013-910, ATLAS internal documentation, July 2013, URL: `https://cds.cern.ch/record/1560073`.

[129] ATLAS Collaboration, *Determination of the muon reconstruction efficiency in ATLAS at the Z resonance in proton-proton collisons at $\sqrt{s} = 7$ TeV*, ATLAS-CONF-2011-008, CERN, Feb. 2011.

[130] ATLAS Collaboration, *Electron performance measurements with the ATLAS detector using the 2010 LHC proton-proton collision data*, *Eur. Phys. J.* C72 (2012) 1909, DOI: `10.1140/epjc/s10052-012-1909-1`, ARXIV: `1110.3174 [hep-ex]`.

[131] J. Butterworth et al., *Single Boson and Diboson Production Cross Sections in pp Collisions at sqrts=7 TeV*, ATL-COM-PHYS-2010-695, ATLAS internal documentation, Aug. 2010, URL: `https://cds.cern.ch/record/1287902`.

[132] J. Neyman, *Outline of a Theory of Statistical Estimation Based on the Classical Theory of Probability*, *Phil. Trans. Royal Soc. London, Series A* 236 (Aug. 1937) 333–380, DOI: `10.1098/rsta.1937.0005`.

[133] W. A. Rolke, A. M. López and J. Conrad, *Limits and confidence intervals in the presence of nuisance parameters*, *Nucl. Inst. Meth.* A551 (Oct. 2005) 493–503, DOI: `10.1016/j.nima.2005.05.068`, eprint: `arXiv:physics/0403059`.

[134] S. S. Wilks, *The Large-Sample Distribution of the Likelihood Ratio for Testing Composite Hypotheses*, *The Annals of Mathematical Statistics* 9.1 (1938) pages, ISSN: 00034851, URL: `http://www.jstor.org/stable/2957648`.

[135] ATLAS Muon Combined Performance Working Group, *ATLAS Muon Combined Performance Guidelines for Analyses of 2012 Data*, internal documentation, URL: `https://twiki.cern.ch/twiki/bin/viewauth/AtlasProtected/MCPAnalysisGuidelinesData2012`.

[136] ATLAS Jet and Missing Et Group, *Recommendations for jet cleaning for data 2012*, internal documentation, URL: `https://twiki.cern.ch/twiki/bin/viewauth/AtlasProtected/HowToCleanJets2012`.

Acknowledgements

In almost six years as a member of the KIP ATLAS group, I had the opportunity to meet a lot of people, without whom this work would not have been possible.

First of all, I would like to thank Prof. Dr. Hans-Christian Schultz-Coulon for the possibility to carry out this thesis during an incredibly exciting time for physicists in our field. I am grateful for the freedom and support in physics as well as in non-physics matters. His honest advice and constructive criticism have been an invaluable motivation.

I want to thank Prof. Dr. André Schöning, who kindly agreed to be the second referee of this thesis.

I would like to thank Rainer and Monica for their supervision, all their advice and lively discussions about physics and methods. Thanks to Christoph, Felix, Thorsten, Michael and Sahill who have been great colleagues and are even closer friends. Without your support, this thesis would not have been possible. Additionally, I am grateful to Julia. Her collaboration made the fast progress in the last year possible. I would like to thank all colleagues of the ATLAS and ILC research groups for the enjoyable atmosphere in the group and the activities outside of our daily work.

I want to thank the $W\gamma\gamma$ subgroup at CERN, especially Paul Bell and Camilla Maiani, for their support, advice and effort, to push the analysis forward.

Thanks a lot to my family and all friends, who forgave me my absent-mindedness notably when it comes to appointments. Their support, trustfulness and faith in me have been invaluable.

Most importantly, I would like to thank my wife Saskia, for her patience, constant support and faith in me. She kept me going, especially in the mornings. Without her, this work would not have been possible.